Theoretical and Experimental Study of the Interaction of Small Molecules with Metal Oxide Surfaces for Sensing Applications

A thesis submitted in fulfilment of the requirements for the degree of Doctor of Philosophy

Kester W. J. Wong

BAppSci, RMIT University

BAppSci (Hons), RMIT University

School of Applied Sciences
Science, Engineering and Health Portfolio

RMIT University

Melbourne, Australia

June, 2013

Author's Declaration

I certify that except where due acknowledgement has been made, the work is that of the author alone; the work has not been submitted previously, in whole or in part, to qualify for any other academic award; the content of the thesis is the result of work which has been carried out since the official commencement date of the approved research program; any editorial work, paid or unpaid, carried out by a third party is acknowledged. Research ethics, occupational health and safety guidelines have been followed.

_____

Kester Wong
24th June 2013

Acknowledgements

Completing a research project is a process of acquiring a wonderful string of intellectual debts. I would like to thank my first supervisor, Dr. Michelle Spencer, whose high expectations and standards allowed me to grow as a research scientist. It is difficult to sum into words the enormous appreciation and respect I have for her extensive contribution to my research that goes beyond making this thesis possible. I am also truly indebted to my second supervisor Prof. Irene Yarovsky, who is also my research group leader, for the continuous support and trust bestowed upon me. I owe sincere and honest gratitude for my third supervisor, Prof. Kourosh Kalantar-zadeh for his guidance and patience. They all know my faults, of course, but for once, I can say truthfully that the lessons they taught will continue to resonate with me for a lifetime.

Some of the initial calculations were performed during my Honours study at RMIT University. The RMIT School of Applied Sciences, the Australian Research Council's *Discovery Projects* grant (project no. DP0666883), and the National Computational Infrastructure (NCI) are acknowledged for providing scholarship, financial and computational resources, respectively.

I am indebted to the members of RMIT Microscopy and Microanalysis Facility (RMMF), Microelectronics and Materials Technology Centre (MMTC), and Chemistry department, in no particular order, Mr. Paul Spizzirri, Mr. Paul E. Jones, A/Prof. Kay Latham, Prof. Dougal McCulloch, Mr. Phil Francis, Mr. Peter Rummel, Dr. Matthew Field, Mr. Frank Antolasic, Dr. Samuel Ippolito, Dr. Jian Zhen Ou, Dr. Mohd Hanif Yacob, and Mr. Shiva Balendhran for their technical assistance and guidance in my experimental work.

I would also like to extend my gratitude to past and present members from my research group and the department of Applied Physics, who have been supportive in my work. I will remember fondly about the group activities, seminars, house parties, cricket matches, as

well as the delightful moments of hearing announcement of newborn baby, engagement, wedding, and many more.

I would like to thank the RMIT HDR research coordinators Prof. Peter Daivis and Prof. Gary Bryant for their advices and academic support on my research performance, and the research administration officers Ms. Kaarina Liind, Ms. Louise Lutz, Mrs Lisa Dias, and Ms. Alexandra Radywonik for arranging my enrollment, visa, and scholarship applications.

I thank Dr. Michael Breedon, Dr. Akin Budi and Dr. Andrew Christofferson who provided invaluable research-related insights and future directions over lunch and coffee breaks. I am indebted to Mr. Michael Plazzer, Mr. Levy Yeung and Mr. Adam Makarucha for their tireless enthusiasm and devotion to proofread my writing, in pursuit of giving corrections to the grave and verbose writer.

To my parents Mau Lian and Elizabeth who have financially supported me in my pursuit of this degree, my older sister Kirstin, and my younger brother Kegan; your unconditional love is deeply appreciated. Special thanks go to Dr. Yii Min Lim, whose care and encouragement kept me going. Last but not least, I am grateful to my close friends (if you are going to skip reading half my thesis that means you) for always having supported my numerous and varying endeavours.

Table of Contents

Chapter 3
Computational Methodology and Surface Models

Chapter 4
N_2O Adsorption on ZnO ($10\bar{1}0$) and ($2\bar{1}\bar{1}0$) Surfaces

Chapter 5
Adsorption of Ethanol on the ZnO($10\bar{1}0$) Surface

Chapter 6
Adsorption of Ethanol on the ZnO($2\bar{1}\bar{1}0$) Surface

Chapter 7
Experimental Study of Gas Interaction in ZnO Nanomaterials

Chapter 8
Conclusions

List of Figures

List of Tables

Abstract

Stringent gas monitoring of harmful gases associated with industrial activities has received considerable attention lately with the research and development of novel nanostructured semiconducting gas sensors. Zinc oxide (ZnO) nanostructures have shown electrical properties highly suitable for gas sensing, and can be manipulated with specific properties for desired applications; however, the adsorption of different molecules on the non-polar ZnO surfaces remain poorly understood. *Ab-initio* density functional theory (DFT) and some experimental techniques were used to study the electronic and structural properties of different gases on ZnO surfaces for gas sensing applications.

The two low index non-polar ZnO surfaces, namely the $(10\bar{1}0)$ and $(2\bar{1}\bar{1}0)$ surfaces were studied as these are commonly found on different ZnO nanostructures. Nitrous oxide (N_2O) and ethanol (CH_3CH_2OH) were adsorbed on each surface and the effect of surface facet, gas coverage, and the presence of surface defects (oxygen vacancies) was investigated. It was found that nitrous oxide physisorbed on both stoichiometric surfaces at 1 ML coverage, with evidence of weak chemisorption on the $(2\bar{1}\bar{1}0)$ surface. Multiple stable structures were found with N_2O adsorbing via the O or the terminal N atom to a surface Zn atom. The calculated charge transfer for each surface indicated that N_2O behaves as a charge acceptor, withdrawing charge from the surface after adsorption, in line with other theoretical and experimental results.

Ethanol also adsorbed in multiple stable orientations on the stoichiometric and defect surfaces at ¼, ½ and 1 ML coverages, with the binding being stronger than for adsorbed N_2O. Ethanol can form two types of adsorbate-substrate interactions; one being between the ethanol O atom and a surface Zn atom; and the other being a hydrogen bond between the ethanol hydroxyl H atom and a surface O atom. The formation of a hydrogen bond stabilises the adsorbate-substrate interaction, and can be identified by a red shift in the adsorbate OH stretching mode. Due to the reduced number of surface oxygen atoms on

the defect surfaces, the binding was weaker as either a hydrogen bond could not form or it was not as strong as on the stoichiometric surfaces. In contrast to nitrous oxide, ethanol was calculated to donate charge to the surface, behaving as a reducing gas.

Experimentally, several characterisation techniques: Raman, Fourier Transform Infrared (FTIR) Spectroscopy and X-Ray Diffraction (XRD) were used to detect the presence of hydrogen gas (H_2) adsorbed on nanopowdered ZnO surfaces having a high proportion of the low index $(10\bar{1}0)$ surface. We propose that the interaction of hydrogen gas on the ZnO surfaces can lead to the formation of surface hydroxyl groups, as was indicated by the FTIR spectroscopy. The presence of hydrogen was not observed for highly crystalline ZnO nanopowders with larger grain sized, while for smaller grain sized powders, clear peak shifts confirm the presence of hydrogen.

Our theoretical and experimental findings have shed new light on the design and synthesis of potential nanostructured gas sensors and their interaction with different gases.

List of Publications

I. *Density functional theory modelling of ZnO(10$\bar{1}$0) and ZnO(2$\bar{1}\bar{1}$0) surfaces: structure, properties and adsorption of N_2O*

M. J. S. Spencer, K. W. J. Wong, I. Yarovsky, *Mater. Chem. Phys.* **119** 505-514 (2010)

II. *Surface defects on ZnO nanowires: implications for design of sensors*

M. J. S. Spencer, K. W. J. Wong, I. Yarovsky, *J. Phys. Condens. Matter* **24** 305001 (2012)

III. *Interaction of hydrogen with ZnO nanopowders – evidence of hydroxyl group formation*

K. W. J. Wong, M. R. Field, J. Z. Ou, K. Latham, M. J. S. Spencer, I. Yarovsky, K. Kalantar-zadeh, *Nanotechnology* **23** 015705 (2012)

Chapter 1

Introduction

1.1 Introduction

The prolonged concern over pollution and its effect on human health, as well as stringent gas monitoring of industrial activities involving harmful gases, has resulted in substantial research and development of semiconducting gas sensors [1].

Monitoring atmospheric concentrations of different gases is an important part of any scheme to help mitigate their effects. This involves the development and refinement of devices used in estimating gas emissions, and reducing uncertainties and errors in the monitoring process. Improved technologies in the monitoring of gas emissions and leakages can reduce the effect caused by these gases. Some of the drawbacks of commercially available gas sensors are the instrument size [2, 3], the requirement of preheating the sensor for long hours before they can be used [4], and their strong dependence on temperature and gas concentration [5]. The market is in need of better solutions for efficient gas monitoring.

Surface chemistry plays an important role in modern industries, with the gas-surface interaction affecting the operation of many electronic devices, including gas sensors. Realistically, metal oxide materials exist in multiple crystalline structures, also known as different surface terminations. Therefore, a lot of work is needed to improve our understanding of the structure and properties of single crystal surfaces at the molecular level. The aim of this dissertation is to study the adsorption of selected gas species on different zinc oxide (ZnO) surfaces that are present in materials used for gas sensors.

In this dissertation, ZnO is employed as the material of choice as it is already used in gas sensing devices. In order to study the adsorption mechanism on the ZnO surfaces, a solid understanding of the structure of each surface and its interaction with different molecules must be obtained. With computer resources becoming cheaper, and with more well-established computational codes being developed, the interaction of molecules with different crystal facets can be accurately modelled using electronic structure calculations. In this study, this is achieved using density functional theory (DFT) calculations along with some experimental characterisation techniques.

1.2 Gas Sensors

In general, gas sensors can be categorised into several types, including infrared [6], electrochemical [7, 8] and catalytic combustion sensors [9]. They are used in a range of applications from chemical engineering, to medicine, agriculture, architecture and others.

1.2.1 Metal Oxide Semiconductor Gas Sensors

Metal oxide based sensors commonly used include SnO_2, TiO_2, In_2O_3, and ZnO. It was discovered in the 1950s that common metal oxides change their electrical properties

when exposed to reducing gases, with the change being more apparent at elevated temperatures [10, 11]. About a decade later, Seiyama *et al* [12] used this phenomenon to propose the idea of constructing a ZnO thin film gas sensor. In the same year, the more commonly used metal oxide SnO_2 was also proposed as a gas sensing material, and was patented by Naoyoshi Taguchi, who later founded the gas sensor manufacturing facility Figaro Engineering [13-15]. The oxide based gas sensors were initially in the form of thick films; however, as they showed poor sensitivity [16], they were made thinner to produce increased sensitivity. Since then, thin film gas sensors have increased in popularity and are still used frequently today [17-19].

As will be discussed in Section **1.2.2**, ZnO nanostructures have been investigated for use as gas sensors. Their large surface areas with single crystal facets make them highly popular for these applications.

The presence of a gas is detected by measuring a change in conductivity when the gas adsorbs on the sensor surface. It has been shown that oxidising gases (such as O_2, N_2O and NO_2 [20]) withdraw charge from the surface and decrease the conductivity, while reducing gases (such as NH_3 [20] and H_2 [21]) donate charge to the surface causing an increase in conductivity [22]. Although the full sensing mechanism is not clear, it involves the interaction of the gas directly with the oxide surface or with pre-adsorbed oxygen atoms. The adsorbed oxygen (which comes from the surrounding environment) withdraws electrons from the oxide, trapping them at the surface. This leads to an electron depleted region or space charge layer. When an adsorbing molecule interacts directly with the surface, or with the adsorbed oxygen, it changes the free charge carrier density, which can lead to an increase or decrease in the sensor conductivity.

1.2.2 Recent Advances in Metal Oxide Gas Sensors

One of the most popular advances in metal oxide gas sensors has been the investigation of sensors using nanostructures. The Sberveglieri [23] and Wang [24] groups have been instrumental in shedding light on the gas sensing properties of metal oxide nanomaterials. The successful collaboration between the two groups in 2002 stemmed from the discovery of semiconducting zinc oxide nanowires and nanobelts by Wang *et al*. [24], and their ability to detect a variety of gas species including CO, NO_2, and ethanol [23, 25]. The gas detection was demonstrated by the measurement of significant current changes of SnO_2 nanowires towards target gases in synthetic air [23]. The group of Kalantar-zadeh *et al*. have also been instrumental in reporting the structural properties, synthesis, and applications of various metal oxide nanostructures, including ZnO [26-28], WO_X [29-32], MoO_3 [32], and TiO_2 [33], for gas sensing applications [21]. The interest in this area has since been growing rapidly due to relatively simple and inexpensive nanostructure fabrication methods.

The *Electronic Nose* sensing approach, inspired by the olfactory systems of humans and animals, is a commercially available technology that uses an array of metal oxides in a sensor device to measure the conductance of various gas species on the same chip. This approach discriminates different gas species by characterising the conductivity pattern of various metal oxides [34]. This electronic nose is used in identifying spoilt wine [35] and has also been proposed for potential applications including explosives detection [36]. This approach, however, is not very efficient in distinguishing different gas species because the reactions do not vary much between a specific target gas and the different oxide thin film surfaces. To overcome this issue, the *nanoelectronic nose* that employs a hybrid of nanostructures for sensitive gas discrimination has been used [36]. The sensor array contains individual sensors (In_2O_3 nanowires, SnO_2 nanowires, ZnO nanowires, and single-walled carbon nanotubes), with integrated micromachined hot plates for accurate

temperature control of each sensor. The assembled sensors on a chip successfully demonstrated a major improvement in gas selectivity when exposed to important industrial gases such as hydrogen, ethanol and nitrogen dioxide.

Another novel approach in gas sensing is the use of self-heated metal oxide nanowires as sensors. Essentially, the device consisting of single nanowire sensor is powered by heat (without the aid of a heater) from other electronic devices that are already generating heat surrounding the nanowire. The advantage of self-heated gas sensors is their efficiency in power consumption, using a mere 10^{-5} watt, compared to 10^{-2} watts of power in traditional sensors [37, 38]. Prades *et al*. [39] investigated the power consumption of gas sensors based on self-heated individual SnO_2 nanowires. The study showed that the gas sensor produced nearly identical results to sensors operated with an external microheater. The ultralow power consumption of the nanostructure sensors proved to be an advantage for mobile devices and has certainly stimulated interest in employing other metal oxide nanostructures for self-heated gas sensors.

Based on the above approaches, the next generation of gas sensors can be envisioned to be based on nanostructured materials. Although the sensing mechanisms are complicated and they are not well understood, metal oxide nanostructures have shown promising potential in the detection or monitoring of a target gas at higher efficiencies.

1.2.3 Sensitivity and Selectivity of Semiconductor Gas Sensors

The performance of metal oxide gas sensors can be characterised by their sensitivity, selectivity, response time, recovery time, and stability [14]. The measurable parameter in this type of sensor is the resistance of the semiconducting material, which corresponds to the sensitivity. The sensitivity of a sensor can be defined as R_{gas}/R_{air}, where R_{gas} and R_{air} are the resistance in the presence or absence of a gas species, respectively. The variable

resistivities (R_{gas}/R_{air}) enable the sensitivity of a material in reducing and oxidising gases at different concentrations to be compared. After exposure to a target gas, the higher (or lower) the measured resistance, the more sensitive the sensor is showing [40].

The selectivity of a gas sensor can be described as the sensitivity of one target gas compared to another under the same environment [2]. Often, metal oxide gas sensors exhibit poor selectivity toward specific gases since their reaction mechanism involves pre-adsorbed species such as oxygen or water [2, 14, 41-43]. Achieving an absolutely selective metal oxide gas sensor is usually complex, as most of the sensors are prone to detecting humidity and other gases (cross-sensitivity) that may be present in the working environment [3, 44]. An experimental study, however, has shown that quartz crystal microbalance (QCM) gas sensors coated with ZnO nanorods exhibit high selectivity toward NH_3 gas at room temperature over other gases such as liquefied petroleum gas (which consists of hydrocarbons like CH_4, C_3H_8, and C_4H_{10}), N_2O, NO_2, CO, and CO_2 [45].

The response time and recovery time are the time required to reach 90% of the final change in resistance following a change in the target gas concentration [46, 47]. Because the chemical reaction occurs very quickly, response times are often expressed in percentage values of the total time [47]. A sensor's response and recovery time are crucial factors in determining the applicability of the sensor. In general, sensors with shorter recovery time will have the advantage of broader applications in the market.

Another major characteristic of a gas sensor is the stability. An ideal sensor would be able to provide reproducible results over a certain period of time, while retaining the sensitivity, selectivity, response, and recovery time [48]. Some metal oxide gas sensor are known to have low stability, as evidenced by the nanotube and nanorod forms of SnO_2 [49, 50], that are prone to baseline resistance change over time, due to their degradation [48, 51]. Although sensor degradation/ageing is inevitable, the stability of a sensor can be

increased, to some extent, by the post-processing heat treatment, *i.e*. annealing. For example, greater current stability has been reported for multiple ZnO nanorod gas sensors in comparison with single nanorod ZnO sensor devices [51]. Doping of metal oxides is also a common practice to increase the stability of sensors [2, 52].

1.3 ZnO Nanostructures for Gas Sensing

1.3.1 Applications of ZnO

The history of ZnO is well-documented and the material has been used in a multitude of products for thousands of years, including medicinal ointments, body lotions and metal production [53]. Several emerging applications of ZnO in the more recent years are in the areas of dye-sensitized solar cells [54-56], piezoelectrics [57, 58], liquid crystal displays (LCD) [59] and light emitting diodes (LED) [60, 61] in optoelectronics [62], spintronics [63], and sensors and actuator devices [26, 27, 53, 54, 64]. ZnO has a wide band gap of 3.4 eV and a large exciton binding energy of ~60 meV, characteristics that make it highly attractive as a material for sensing and optoelectronic devices in particular [65, 66].

Unlike many of the materials which it competes against, ZnO is inexpensive, abundant, chemically stable, biocompatible [67] and is known to be non-toxic. As a result, the emergence of ZnO in numerous industries is not surprising, especially in the cosmetics and food packaging industries where ZnO provides protection against ultraviolet rays [68], sterilisation effects [69], and the ability to deactivate a number of harmful food pathogens [69, 70]. The use of ZnO in electronic products has been on the rise and is even being used as a substitute for the more expensive GaN transistors in LED devices [71].

Naturally, ZnO is capable of withstanding high energy radiation [72-74] due to its strong ionic properties [72], enabling it to be resistant to radiation damage compared to

other common semiconductor materials such as Si, GaN, CdS and GaAs [72, 75]. As the advancement in nanotechnology continues, the use of ZnO nanoparticles in sunscreen products has proven to be safer (with lower toxicity) than conventional UV-blocking sunscreens when applied to the skin [53, 76, 77]. The high thermal resistance of ZnO provides an alternative to SiC materials commonly used as a high temperature sensing material [78, 79]. This allows ZnO to have even wider potential applications in the military, aeronautical, medical and industrial markets, where these factors are crucial [65].

ZnO owes its importance as a flat panel display material to its ability to maintain high optical transparency. This niche feature is especially useful for transparent transistors, electrodes and solar cells [65]. Currently, the major impediment of ZnO for a wider range of applications in electronics is directly associated with the difficulty in achieving *p*-type doping in the material. This has consequently led to a significant amount of research focused on the development of *p*-type conductivity in ZnO materials, as mentioned in a number of articles and reviews [53, 80-82].

For gas monitoring, the success of ZnO based gas sensors is due to the high sensitivity as a thin film. Using ZnO based nanostructures, they show more improvements [83-85], operating at lower temperatures and consuming less electricity compared to traditional thin film sensors [37, 39, 86].

Despite a long history of ZnO studies and the recent studies of nanostructures in gas sensing, some fundamental properties remain unclear. For instance, one question relates to the effect of surface defects on the gas-sensor reaction [65].

In addition to having a wide band gap and large exciton binding energy, there are other properties that make ZnO the preferred material over other metal oxides. One major advantage for ZnO is the fact that it can be grown in an abundant number of nanostructure morphologies, include nanorods [62, 87, 88], nanowires [54, 87, 89], nanobelts [89-91],

nanorings [92], nanohelices [93], nanosprings [94], nanosheets [95], nanocombs [96], nanoflowers [97], and multipods [98-100], to name a few. Descriptions encompassing the discovery, growth methods, properties, potential applications and recent advances of these nanostructures can be found in the following review papers [67, 68, 71, 89, 90, 101-103].

1.3.2 ZnO Growth and Characterisation Techniques

ZnO crystals can be grown by employing the following methods: physical vapour deposition [104], electrodeposition [105], thermal evaporation [91], chemical-vapour transport [106], seeded vapour-phase growth [107], hydrothermal growth [108, 109], and chemical vapour deposition (although this method is mostly used in growing epitaxial layers) [110, 111]. Epitaxial layers of ZnO can be produced via molecular beam epitaxy [112, 113], pulsed laser deposition [114-116], metal-organic chemical vapour deposition [117, 118], and hydride [119] or chloride [120] vapour phase deposition. Characterisation methods are now routine procedures that are part of most studies on ZnO. For brevity, the characterisation techniques of metal oxide samples can be found in the following reports ([121-125] and references therein). Based on these current growth techniques, the extremely versatile ZnO can be fabricated into various nano-sized structures with different morphologies by varying the temperature, pressure and reactant types (see for example Refs. [68, 102]).

1.3.3 Crystal Structures of ZnO

ZnO crystallises in three forms: zincblende, wurtzite, and rocksalt crystals [65]. The two common crystal structures of ZnO are the wurtzite and zincblende structures, whereas the rocksalt structure can be formed at high pressures at about 10 GPa [126]. The hexagonal

wurtzite structure is the most stable structure at room temperature, and is characterised by polar and non-polar surfaces, with the most stable surfaces being the {0001}, {$10\bar{1}0$} and 2 {$\bar{1}\bar{1}0$} facets. Here, the four index Miller notation {*hkil*} denotes the set of all planes that are equivalent to (*hkil*) by the symmetry of the lattice. The surface plane is denoted by the (*hkil*) notation. The (0001) polar surface is either Zn or O terminated, whereas the non-polar ($10\bar{1}0$) and ($2\bar{1}\bar{1}0$) surfaces can be described by having equal amounts of Zn and O atoms (see Figure **1.1**). Unlike polar surfaces of other materials, where they are reported to be meta-stable [127], the ZnO (0001) and ($000\bar{1}$) polar surfaces are stable without exhibiting surface reconstructions [128, 129]. Properties of these surfaces, that are physically and chemically different than the non-polar surfaces [130], are also known to contribute to the piezoelectric effect [101]. Under normal atmospheric conditions, the overall surface of ZnO nanostructures have been reported to comprise up to 80% of non-polar surfaces, namely the ($10\bar{1}0$) and ($2\bar{1}\bar{1}0$) surfaces, with the polar surfaces, (0001) and ($000\bar{1}$), accounting for the remaining 20% of the total surfaces [131].

Hence, the ($10\bar{1}0$) and ($2\bar{1}\bar{1}0$) crystal facets of ZnO are important because they constitute the majority of the surface area of ZnO nanostructures [89, 132]. ZnO nanostructures containing ($10\bar{1}0$) rich surfaces include nanocrystallites [133], nanowires [134, 135] and nanorods [136], whereas the ($2\bar{1}\bar{1}0$) surface can be found dominating in nanoplatelets [137], nanocombs [138], nanobelts [96] and nanowires [65, 139]. The difference between ZnO nanowires and nanorods is that nanorods contain hexagonal cross-sections and nanowires may have non-hexagonal cross-sections [22].

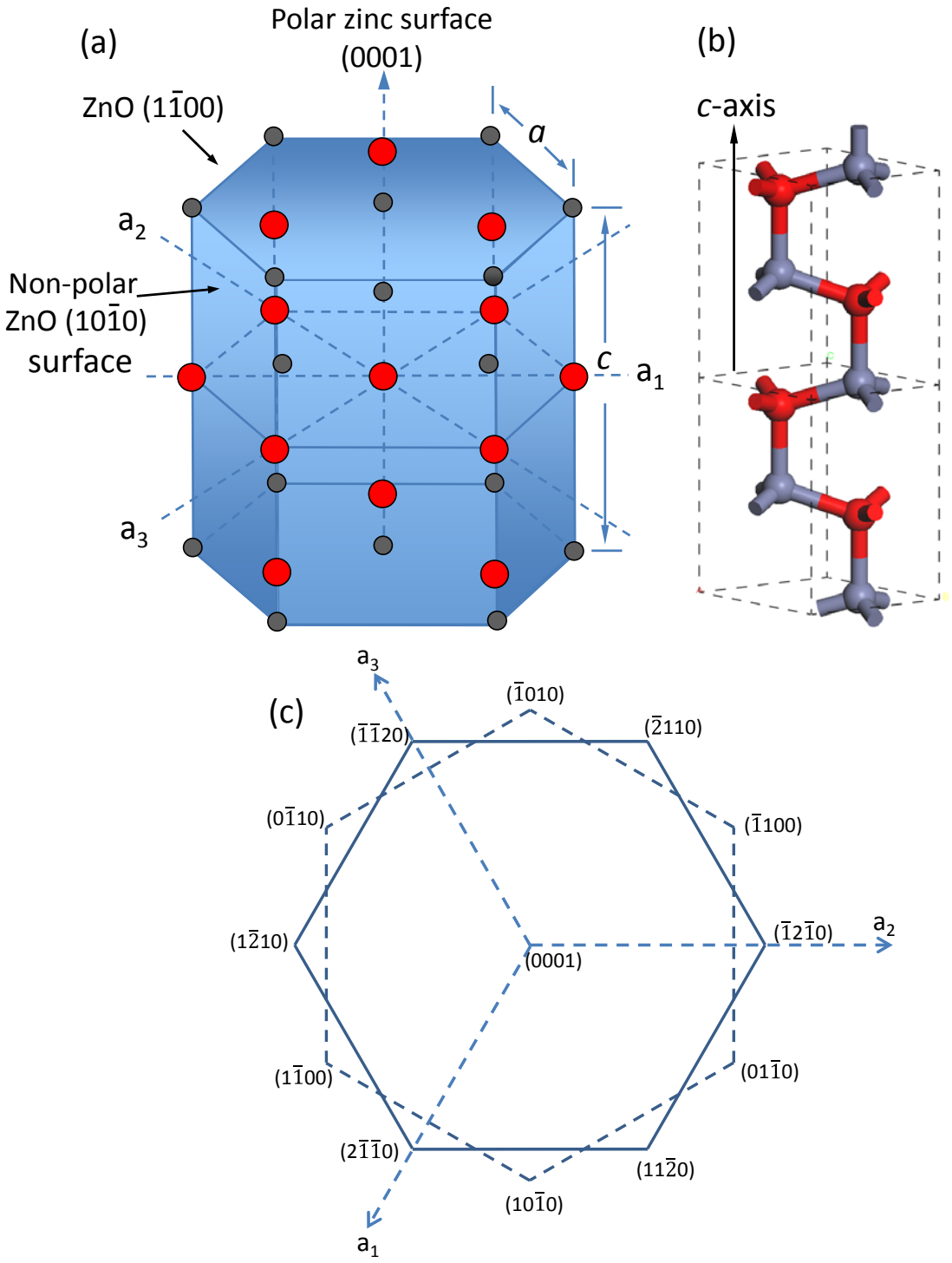

Figure 1.1 Hexagonal ZnO, showing the a) wurtzite ZnO crystal structure; b) bulk unit cell of ZnO showing tetrahedral coordination of Zn and O atoms; and c) various commonly studied surfaces of ZnO, *i.e.* the $(2\bar{1}\bar{1}0)$ surface is represented by the dotted line, whereas the $(10\bar{1}0)$ surface is represented by the solid line. The Zn atoms are represented by grey circles; the O atoms are represented by red circles.

1.3.4 Impurities and Defects in ZnO

In reality, ZnO surfaces do not exist in their perfect crystalline structure; they are commonly found with structural defects or contaminated with foreign particles [65]. The presence of surface defects in ZnO materials, however, can be used as an advantage in sensing applications, as an improved sensing performance can be achieved [140, 141].

Among the defects that can form on ZnO surfaces, oxygen vacancies have the lowest formation energy [142]. A low formation energy implies a high equilibrium concentration of the defect; a high formation energy indicates that defects are unlikely to form [65].

Investigation of the effect of surface V_O on gas-surface reactions could contribute to the development of more efficient gas sensors with high reusability. It has already been shown that oxygen vacancies on the ZnO($10\bar{1}0$) surface can be healed by promoting dissociative adsorption of gas molecules at the defect site, via the adsorption of molecular oxygen (O_2) [143, 144] or nitrogen dioxide [20, 132, 145]. Due to the lack of studies in this particular area, the relationship between surface defects and overall sensing performance is yet to be thoroughly investigated.

1.4 Current Challenges in ZnO Materials and Device Applications

Current ZnO gas sensing studies primarily focus on the synthesis and characterisation of the sensing material, and the sensitivity and response time toward common gases. Much less theoretical research on the sensing mechanism has been carried out. Here is where computational simulations can be used to determine the effect of surface facets and structural properties on the nanostructured sensor reactions to help assist in improving the efficiency of gas sensors.

1.5 Gas Monitoring

Health and safety issues caused by toxic, hazardous, pollutant and greenhouse gases have long been affecting human activities and the environment. The production of these gases, however, is sometimes inevitable. For instance, the gases emitted by livestock and soil account for a large portion of greenhouse gas emissions annually [146]. The volume of these gases released is great, yet the concentrations are variable, such that any meaningful monitoring can be impractical or impossible. In general, pollutant gases include greenhouse gases and volatile organic compounds (VOCs). Some of these pollutants are highly toxic (carbon monoxide) or explosive (methane), while others may cause irritation in humans or animals, *e.g*. paint coatings, new furniture or vehicles. Examples of greenhouse gases are H_2O, CO_2, CH_4, O_3, N_2O, and chlorofluorocarbons (CFCs) [147]. While greenhouse gases are important in maintaining the earth's temperature, so that the planet is habitable, high concentrations of greenhouse gases are undesirable and can cause a rapid heat distribution to the earth's surface.

Under the Kyoto Protocol, these greenhouse gases (amongst others) must be reported to the United Nations Framework Convention for Climate Change (UNFCCC) each year by each treaty party. On top of that, developed countries are also required to provide information on the indirect greenhouse gases, namely carbon monoxide (CO), nitrogen oxides (NO_X), and non-methane VOCs such as ethanol (CH_3CH_2OH) [148]. Efficient gas sensing in our environment allows us to assess how far emission reduction targets are being met at the domestic, company or global level. The gases studied in this work are nitrous oxide (N_2O), ethanol (CH_3CH_2OH), and hydrogen (H_2). The source and detection of these gases are described in the following sections. Importantly, the sensing mechanism these gases is not currently well understood.

1.5.1 Nitrous Oxide

Nitrous oxide exists as a non-flammable and colourless gas under room conditions [149]. Some of the main characteristics of this greenhouse gas is that it has an atmospheric lifetime of 120 years [150] and a global warming potential of 310 times higher than that of CO_2 [148]. The rise in the global atmospheric concentration of N_2O can be traced back to the *Industrial Revolution* [151], where its global concentration has risen as the world has become increasingly industrialised [151-153].

The N_2O concentration in the atmosphere is approximately 320 ppb (as measured in 2010) [441]. Changes in the atmospheric concentration of this gas have attracted considerable concern, mainly due to the role of N_2O in regulating ozone levels, contributing to the greenhouse effect and formation of acid-rain [152]. Additionally, N_2O is used extensively in dentistry and surgical operations as an anaesthetic gas [154-156]. It has been reported that N_2O contamination in the operating room is very common, being caused by poor management of waste anaesthetic gas [157]. Due to the euphoric effect caused by N_2O via inhalation, the residual gas poses risks to the personnel working in operating rooms over a prolonged period of time [158]. Lesser known, though, is that it also produces NO and NO_2 indirectly through the oxidation processes of N_2O [159] by reacting with high-energy oxygen atoms that contribute to the ozone depletion [147, 160-162]. The NO molecule that is produced is rapidly oxidised in air to NO_2, which is a major air pollutant and toxic gas with a sharp odour. Although the emission of N_2O resulting from human-related activities is well known (through deforestation, fertilisers and combustion of fossil fuels), the gas is also released to the atmosphere through a series of natural processes, such as microbial activities in soil and water [152].

1.5.2 Ethanol Vapour

The concentration of indoor volatile organic compounds (VOCs) is ten times higher than the outdoor concentration. VOCs may cause both short and long term health effects arising from inhalation of irritant gases and vapours. Even small amounts of ethanol can irritate the nose and throat, causing coughing and difficulty in breathing. For this reason, VOCs in the air pose a real threat to those who suffer from asthma and other respiratory problems. The current occupational (airborne) exposure limit for the United Kingdom, the United States and Australia to ethanol is 1,000 ppm over an 8-hour work shift, which is equivalent to ingestion of 10g of ethanol (approximately a glass of alcoholic beverage) [163]. The interest in ethanol detection is also motivated by its wide application in medicine [164, 165], food and beverages [166, 167], as well as the food packaging industry [168, 169].

1.5.3 Hydrogen Gas

To reduce the overall release of greenhouse gases caused by human activities, there is growing interest in developing alternative fuels that may improve energy efficiency while reducing pollution. Examples of alternative ‘clean’ fuels are hydrogen and ethanol. In order to develop these technologies the demand for more efficient sensing materials has increased. Hydrogen, as an alternative fuel, eliminates the emission of carbon dioxide from vehicles, while increasing those of water vapour.

1.6 Research Objectives

The adsorption interaction of different gases on ZnO surfaces is investigated in this thesis. Specifically, the objectives of this dissertation are as follows:

- To adsorb different gases, including nitrous oxide and ethanol on different ZnO surfaces using DFT calculations.
- To obtain a set of stable structures of different gases adsorbed on the ZnO $(10\bar{1}0)$ and $(2\bar{1}\bar{1}0)$ surfaces and their associated structural and electronic properties.
- To investigate using DFT calculations, the influence of surface morphology, molecular configuration, surface defects, and gas coverages, on the gas-surface interaction.
- To experimentally characterise the presence of hydrogen (H_2) in ZnO nanopowder samples, using Scanning Electron Microscopy (SEM), Transmission Electron Microscopy (TEM), X-ray Diffraction (XRD), Diffuse Reflectance Infrared Fourier Tansform (DRIFT), Attenuated Total Reflectance (ATR), Fourier Transform Infrared (FTIR) and Raman spectroscopy.
- Where possible correlate the theoretical simulations with the measured device characteristics to better understand the principles of the gas sensing mechanism.

1.7 Thesis Outline

The main goal of this dissertation is to provide further understanding of the adsorption interaction of a number of gases with ZnO surfaces using a theoretical and experimental approach.

In Chapter 1, an introduction to the gases and materials used for gas sensing applications is given.

Chapter 2 provides the theoretical background of DFT calculations, as well as a variety of first principles approaches used at different levels of chemical accuracies for electronic structure calculations.

Chapter 3 addresses the computational methods and parameters employed in the simulations. Here, properties of bulk ZnO and the $(10\bar{1}0)$ and $(2\bar{1}\bar{1}0)$ surfaces are described, as well as the set-up of the gas-surface models.

Using DFT calculations, the adsorption of different gases on the ZnO $(10\bar{1}0)$ and $(2\bar{1}\bar{1}0)$ surfaces is presented in chapters 4-6. Chapter 4 covers the adsorption of N_2O on the ZnO $(10\bar{1}0)$ and $(2\bar{1}\bar{1}0)$ surfaces, and describes why ZnO is particularly suitable for the monitoring/detection of this gas. Chapters 5 and 6 report the adsorption of ethanol on the ZnO $(10\bar{1}0)$ and $(2\bar{1}\bar{1}0)$ surfaces, respectively, including the role of surface defects on the overall adsorption.

Chapter 7 reports the synthesis and experimental characterisation of ZnO nanomaterials for gas sensing of hydrogen (H_2).

In the final chapter, the author summarises the major findings and provides some links between the simulated adsorption results and the experimental characterisation outcomes.

Chapter 2

Electronic Structure Calculations: Theory and Algorithms

2.1 Introduction: The First Principles Approach

The first principles (*ab-initio*) methods employ a quantum mechanical approach for determining the physical properties of many-body systems by utilising a set of ions, according to their atomic number. This group of methods has been refined over the years and is now capable of describing systems ranging from a few molecules to thousands of atoms [170], made possible by the exponential growth and availability of computational resources, and improved algorithms. The advantage of first principles calculations is that they are capable to provide microscopic properties that may not be available from other techniques. First principles methods have been employed to accurately describe the structural and electronic properties of: molecules [171], solids [172], surfaces (including defects) [173-176], nanomaterials [177], as well as large-scale nanostructures [170]. This chapter will describe the theoretical foundation of the first principles methods, as well as their capabilities and limitations.

The only inputs required for first principles methods are the physical constants used to solve the Schrödinger equation. The ground state energy structure can then be calculated to represent the physical structure of a system. This is a computationally demanding task and approximations are used. However, those approximations are of the algorithmic nature and contain no adjustable physical parameters [178]. The two main groups of first principles methods are wave function based methods and density functional theory (DFT) based methods.

2.2 The Born-Oppenheimer Approximation

Max Born and J. Robert Oppenheimer assumed the mass of the nuclei and the electrons to be different [180], where a nucleus is approximately 1836 times heavier than an electron [181]. Under this assumption, a separation exists between the electronic and nuclear motion time scales, as the electrons relax very rapidly into the instantaneous ground state configuration. This assumption allows the electronic ground state to be determined first, followed by the nuclear motion. Thus, the approach of treating the nuclei adiabatically (fixed) and separating the electrons and the nuclear motion in the many body wave function is known as the Born-Oppenheimer (BO) approximation [182]. This approximation solves the Schrödinger's equation in fewer steps (TISE), as motion implies time-dependence.

In quantum mechanics, the information required to describe a system is contained in the system's wave function (Ψ). The simplest representation of the BO approximation can be described in terms of the wave function Ψ:

$$\Psi_{Tot}(R,r) = \sum_{i=1}^{\infty} \Psi_{ni}(R)\Psi_{i}(R,r) \qquad \textbf{(2.1)}$$

where the total wave function is the sum of the electronic wave function and the nuclear wave function (*R* denotes the nuclear positions and *r* the electronic coordinates). The electronic energy consists of the kinetic and potential energy of the moving electrons, where nuclear repulsion is only added to the electronic energy when the nuclear position is changed. Due to the possibility that a number of meta-stable arrangements of the nuclei may exist under the BO approximation, a solution such as energy minimisation is required to determine the ground state configuration(s) [178].

2.2.1 Statement of the Problem

Realistically, the size of the systems of interest ranges from atoms and molecules to solids. Assuming the Born-Oppenheimer approximation, one must solve the problem of determining the electronic ground state of the Hamiltonian (for a fixed position of the nuclei) in quantum chemistry. Therefore, a description of different approximation methods for finding the ground state will be the subject of the following sections.

2.3 The Wave Function Methods

The wave function can be solved by using the nonrelativistic time-independent Schrödinger's equation (TISE):

$$\left\{-\frac{\hbar^2}{2m}\nabla^2 + V_{ext}\right\}\Psi(r) = E\Psi(r) \qquad \textbf{(2.2)}$$

This is a simplification of the time-dependent Schrödinger equation, where $\hbar$ is represented by Planck's constant; the electron mass, *m*; the external potential, V_{ext}, and the Laplacian for the kinetic energy operator, ∇^2. A single particle (*e.g.* an electron) is considered in this theory, where the electron motion in space (*r*) is characterised by the

wave function Ψ, and the groundstate energy (E) is independent of time, hence the time-independent Schrödinger equation.

Possible solutions to the Schrödinger equation are often required to have certain conditions such as normalisation, orthogonality and orthonormality. These are described below:

1) For the probability of finding a particle over all space, if integrating the square of an electronic wave function yields the value of 1, then the particle must exist somewhere in space:

$$\int \Psi^* \Psi d\tau = 1 \qquad \textbf{(2.3a)}$$

Wave functions that satisfy this rule are normalised. The term $d\tau$ simply indicates that the integration is over all space.

2) Also, it is usual to require the solutions to Schrödinger's equation to be orthogonal, *i.e.* the two wave functions Ψ_m and Ψ_n belong to different energies ($E_m \neq E_n$):

$$\int \Psi_m^* \Psi_n d\tau = 0 \qquad where\, m \neq n \qquad \textbf{(2.3b)}$$

3) Orthonormality is a term coined to describe different wave functions that satisfy both the above normalisation and orthogonality rules:

$$\int \Psi_m^* \Psi_n d\tau = \delta_{mn} \qquad \textbf{(2.3c)}$$

where the Kronecker delta (δ_{mn}) equals to 1 if *m*=*n*, and zero otherwise.

Equation (2.2) can be reduced to $H\Psi = E\Psi$, where H is the Hamiltonian operator:

$$\hat{H} = -\frac{\hbar^2}{2m}\nabla^2 + V_{ext} \qquad \textbf{(2.4)}$$

It contains all the terms that contribute to the energy of a system. This two-part Hamiltonian contains the kinetic energy operator as the first part, whereas V_{ext} represents the external potential (independent of time).

About four decades after the formulation of Schrödinger's equation, the ground state energy was proved to be a unique functional of the electron density by Pierre Hohenberg and Walter Kohn (Hohenberg-Kohn theorem), which serves as the basis of density functional theory (DFT) [179]. The theorem states that the electron density that minimises the energy of the overall functional is the true electron density, corresponding to the full solution of the Schrödinger equation. In the context of first principles, the term "true" can be used interchangeably with "exact" (*i.e.* true energy), unless stated otherwise. The theory behind DFT will be discussed further in Section **2.7**.

2.4 The Hartree Approximation

The oldest and the simplest method of evaluating the electronic wave function is the Hartree approximation, developed by Hartree [183]. The Hartree approximation states that the total electronic wave function (Ψ) of a single-particle system is the product of N single-particle orbitals. When this constraint is satisfied, the total electronic wave function (Ψ) is unchanged (symmetric), and the product is called the Hartree Product:

$$\Psi(\hat{r}_1, \hat{r}_2, ..., \hat{r}_N) = \chi_1(\hat{r}_1)\chi_2(\hat{r}_2)...\chi_N(\hat{r}_N) \quad \textbf{(2.5)}$$

The single-particle wave functions, including electron spin (see page 24), are denoted by χ (however, the notation ψ is also commonly found in the literature, which can be confusing if not used correctly) to distinguish them from the N-particle (total) wave function Ψ, whereas the capital letter N represents the number of electrons. The drawback of this approach is that Pauli's exclusion principle is not taken into account, therefore, the

electrons are considered as occupying single-particle orbitals in this system. Most importantly, this method fails to satisfy the antisymmetry principle for spin orbitals that requires the electrons to be indistinguishable, which will be discussed in the following section.

2.5 The Hartree-Fock Method

The Hartree-Fock (HF) method utilises *self-consistent field* (SCF) technique [184] to solve the electronic Schrödinger equation for many-electron systems under the Born-Oppenheimer approximation. It was developed after the lack of antisymmetry in the electron wave function was noticed later by Fock [185] and Slater [186]. The antisymmetry principle was met by implementing a linear combination of the Hartree products, often found described in the form of Slater's determinant. The solution ensured that the set of N-particle wave function must either remain unchanged (symmetric) or change sign (antisymmetric) when any pair of the electron coordinates are exchanged.

It is important to introduce the variational principle (before introducing the Slater determinant), as the starting point for the Hartree-Fock approach is to construct a *variational*[*] wave function. The variational theorem states that any inexact/approximate orthonormal wave function has energy larger than the true ground state. Consider E_0 as the lowest energy E_n (ground state energy), the energy of an arbitrary state Ψ can be expressed as:

[*] To solve the equation for many-body systems, it is necessary for the variation principle to be applied, as the stationary Schrödinger equation (2.2) can only be applied to a restricted amount of system [181].

$$\begin{aligned}\left\langle \Psi \middle| \hat{H} \middle| \Psi \right\rangle &= \sum_{m,n} C_m^* C_n E_n \delta_{mn} \\ &= \sum_n \left| C_n \right|^2 E_n \geq \sum_n \left| C_n \right|^2 E_0 = E_0\end{aligned} \tag{2.6}$$

Here, the eigenstates of the Hamiltonian operator (Ψ) are chosen to be orthonormal, *i.e.* $\langle \Psi | \Psi \rangle = \delta_{mn}$, where the expansion coefficients *C* are the subsets of the Hilbert space; *m* and *n* denote two basis vectors [181]. The equation above states that any wavefunction in the Hilbert space has an energy E_n larger than that of the ground state. Since the Hartree-Fock theory states that the energy calculated from an approximation of the true wave function will always be greater than the true energy E_0, it can be safely assumed that the most accurate wave function will yield the closest calculated energy to the E_0 value (but not below the true energy).

Here, the wave functions from (**2.5**) can be re-written in the form of a Slater determinant, Ψ_{HF}. The antisymmetric many-body wave function that contains a set of orthonormal single-electron states (N spin-orbitals) can be described as:

$$\Psi_{HF} = \frac{1}{\sqrt{N!}} \begin{vmatrix} \chi_1(\hat{r}_1) & \chi_2(\hat{r}_1) & \cdots & \chi_N(\hat{r}_1) \\ \chi_1(\hat{r}_2) & \chi_2(\hat{r}_2) & \cdots & \chi_N(\hat{r}_2) \\ \vdots & \vdots & & \vdots \\ \chi_1(\hat{r}_N) & \chi_2(\hat{r}_N) & \cdots & \chi_N(\hat{r}_N) \end{vmatrix} \tag{2.7}$$

where χ is the one-electron wave functions. The use of determinantal wave functions ensures that the Pauli exclusion principle (antisymmetry) is satisfied, that no two electrons may occupy the same orbital state. For orthonormal spin orbitals, only the identical wave functions from the determinant will be non-zero when integrated over all space. For the one-electron orbitals to be not only normalised, but also mutually orthogonal, the orthonormality constraint is imposed:

$$\left\langle \chi_i \middle| \chi_j \right\rangle = \delta_{ij} \qquad i, j = 1, \ldots, N. \tag{2.8}$$

Before moving to the next step, the electron spin that will be incorporated to solve the Schrödinger equation in this section is explained. The spin states for an electron can be characterised by the quantum number *s*, where the angular momentum (m_s) on the *z* axis (±1/2), is commonly referred to as the "up spin" or "down spin". A general spin orbital (χ_i) of equation (2.5) may be described by the spin functions ("α" for spin up and "β" for spin down). Spin functions, depending on the m_s, can have the values of either 0 or 1. They can be defined as $\alpha(+1/2) = 1$, $\alpha(-1/2) = 0$, $\beta(+1/2) = 0$ and $\beta(-1/2) = 1$. These general spin orbitals can be used to describe the *General Hartree-Fock* (GHF) formalism.

Subsequently, the Hamiltonian for a many-body system can be reduced with simplified notations:

$$\hat{\mathrm{H}} = \left(-\frac{1}{2}\sum_{i=1}^{N} \nabla_i^2 - \frac{1}{r_{1A}} - \frac{1}{r_{1B}} \ldots + \frac{1}{r_{12}} + \frac{1}{r_{13}} + \ldots \right) \tag{2.9}$$

where the nuclei are labelled as A, B, C, etc., and the electrons are labelled 1, 2, 3, etc. A more detailed derivation of the non-relativistic Hamiltonian can be found in the literature, for example, in the review by Echenique and Alonso [181]. The Hamiltonian consists of the kinetic energy for each electron plus the potential energy operator due to the Coulomb attraction between the electrons and nuclei, and also the Coulomb repulsion between the electrons [182].

Together with the Hamiltonian and the determinantal wave function, as described in (**2.7**) and (**2.9**), the energy of the many-body system can be calculated using (**2.6**), in the following form:

$$E_{HF} = \left\langle \Psi_{HF} \middle| \hat{H} \middle| \Psi_{HF} \right\rangle = \sum_i H_i + \frac{1}{2} \sum_{i,j} \left(J_{ij} - K_{ij} \right) \quad \textbf{(2.10)}$$

Equation (**2.10**) includes the three types of interactions (H_i , J_{ij} , and K_{ij}) that contribute to the total electronic energy of the system. They can be expressed in the following equations:

$$H_i = \int d\tau_1 \chi_i(1) \left(-\frac{1}{2} \nabla^2 + V_{ext} \right) \chi_i(1) \quad \textbf{(2.11a)}$$

$$J_{ij} = \iint d\tau_1 d\tau_2 \chi_i(1) \chi_j(2) \left(\frac{1}{r_{12}} \right) \chi_i(1) \chi_j(2) \quad \textbf{(2.11b)}$$

$$K_{ij} = \iint d\tau_1 d\tau_2 \chi_i(1) \chi_j(2) \left(\frac{1}{r_{12}} \right) \chi_i(2) \chi_j(1) \quad \textbf{(2.11c)}$$

where H_i has been defined together with the *two-electron* integrals, J_{ij} and K_{ij}. The numerical values "1" and "2" are used to represent an integral with a single-electron and two-electrons, respectively. The *one-electron* integrals H_i are a one-particle part (that only operates on the *i*th coordinates) of the total Hamiltonian in (**2.9**), since it only operates on either of *i* or *j*. It is associated with the kinetic and potential energy of the electron moving within the field of the nuclei. The two-electron integral (J_{ij}) is often associated with the Coulomb interaction between electrons in spin orbitals (*i* and *j*), *i.e.* the electrostatic repulsion between pairs of electrons. The third contribution (K_{ij}) to the total energy is the exchange interaction.

The advantage of this approach (GHF) is that additional constraints can be added to the single-electron orbitals to obtain different variants of Hartree-Fock theory. In general, there are three types of restrictions that affect the spin part of the one-electron orbitals (χ_i); the unrestricted HF theory, restricted HF theory (closed-shell system), and the

restricted open-shell HF theory [181]. Specifically, the *general* and *restricted* HF methods will be discussed in this chapter.

2.5.1 Hartree-Fock Energy for a Closed-shell System

The *restricted* Hartree-Fock method, which can also be referred to as a *closed-shell* system, is a more common method of approximation than the *general* Hartree-Fock. As mentioned before, this method utilises a set of restricted electron orbitals, by treating the number of "spin-up" and "spin-down" electrons to be equal, and therefore, can only be used with systems containing an even number of electrons. For a *closed-shell* system containing N electrons and N/2 orbitals, the orbitals can be described by the spatial orbital ψ_i: ψ_α and ψ_β (each spatial wavefunction occurs twice: once multiplied by α and once by β). For a molecular spin orbital (χ_i) containing only one electron, the energy contribution can be represented by H_i^{core}. Therefore, the $2H_i^{core}$ term represents two electrons in the orbitals χ_i. The energy contribution can be represented by $2H_i^{core}$ and N/2 orbitals in the following form:

$$\sum_i^{N/2} 2H_i^{core} \tag{2.12}$$

where the energy calculation for a *closed-shell* system can be represented by the three types of interactions that contribute to the total energy:

$$E_{HF} = 2\sum_i^{N/2} H_i^{core} + \frac{1}{2}\sum_{i,j}^{N/2}\left(2J_{ij} - K_{ij}\right) \tag{2.13}$$

This approach reduces the size of the search space, as a consequence of reduced N/2 functions compared to the GHF method (N). Also, this method benefits from restrictions that lower the computational cost at the expense of a reduction in accuracy [181].

2.5.2 The Hartree-Fock Equations

As the Hartree-Fock energy functional in (**2.10**) is derived, it is desirable to have the equation optimised under the orthonormality constraint (**2.8**). The Hartree-Fock equations are derived by requiring the functional to be orthonormal, as well as the functional derivative to be zero, *i.e.* $\delta E/\delta\psi = 0$. Therefore, a most accurate wave function (minimum) is obtained when the first derivative of the energy (δE) is zero. For this reason, this process is called energy minimisation. The notation S_{ij} is used to describe the *overlap integral* between two orbitals (*i* and *j*) under the orthonormal condition:

$$S_{ij} = \int \chi_i \chi_j d\tau = \delta_{ij} \qquad (\delta_{ij} \text{ is the Kronecker delta}) \tag{2.14}$$

This type of constrained energy minimisation can be achieved by introducing Lagrange multipliers (λ_{ij}) to impose normalisation:

$$\delta E + \delta \sum_i \sum_j \lambda_{ij} S_{ij} = 0 \tag{2.15}$$

However, because the multiplier λ_{ij} is actually related to the molecular orbital energies* [187], the multipliers can be written in eigenvalues as $-2\varepsilon_{ij}$, and the equation now becomes:

* Orbitals energies are represented by eigenvalues ε_i as described by Koopmans' theorem [187]

$$\delta E - 2\delta \sum_i \sum_j \varepsilon_{ij} S_{ij} = 0 \tag{2.16}$$

The Hartree-Fock energy can be expressed in a way similar to (**2.11**), in the form of three operators:

$$\hat{H}^{core}(1) = -\frac{1}{2}\nabla^2 - \sum_{A=1}^{M} \frac{Z_A}{r_{1A}} \tag{2.17a}$$

$$\hat{J}_j(1) = \int d\tau_2 \chi_j(2) \frac{1}{r_{12}} \chi_j(2) \tag{2.17b}$$

$$\hat{K}_j(1)\chi_i(1) = \left[\int d\tau_2 \chi_j(2) \frac{1}{r_{12}} \chi_i(2) \right] \chi_j(1) \tag{2.17c}$$

The first operator $\hat{H}^{core}(1)$ is the one-electron core Hamiltonian operator that corresponds to the motion of an electron in the field of fixed nuclei, where Z_A indicates the atomic number, and r_{1A} corresponds to the i^{th} coordinate of the electron. The second operator $\hat{J}_j(1)$ is the Coulomb operator, where the Coulomb integrals are the expectant values of spin-orbitals with the operator. The exchange operator $\hat{K}_j(1)$ (the third operator) is a non-local operator, as it is dependent on the value of the spin orbital χ_i, *i.e.* the value of the function in all space is needed in order to calculate the expectant values of the exchange integrals.

In brevity, the operators that contribute to the Hartree-Fock energy for the electron in χ_i can be expressed as a non-linear integro-differential equation:

$$\left[\hat{H}^{core}(1) + \sum_{j\neq 1}^{N} \hat{J}_j(1) - \sum_{j\neq 1}^{N} \hat{K}_j(1) \right] \chi_i(1) = \sum_j \varepsilon_{ij} \chi_j(1) \tag{2.18}$$

Next, the Hartree-Fock equations can be further reduced by introducing a *Fock operator*:

$$\hat{f}_i \chi_i = \sum_j \varepsilon_{ij} \chi_j \tag{2.19}$$

where $\hat{f}_i$ is the Fock operator. The Fock operator is a one-electron Hamiltonian in the polyelectronic system. Using the self-consistently constructed Fock operator, the Hartree-Fock equation can be written as a function of one-electron orbitals. This leads to the derivation of the Fock operator for GHF and RHF formalisms, written as:

$$\hat{f}_i^{\,GHF}(1) = \hat{H}^{core}(1) + \sum_{j=1}^{N} \left\{ \hat{J}_j(1) - \hat{K}_j(1) \right\} \tag{2.20}$$

$$\hat{f}^{\,RHF}{}_i(1) = \hat{H}^{core}(1) + \sum_{j=1}^{N/2} \left\{ 2\hat{J}_j(1) - \hat{K}_j(1) \right\} \tag{2.21}$$

The N-coupled and N/2-coupled equations of the GHF and RHF operators in (**2.20**) and (**2.21**), respectively, can then be simplified to a standard eigenvalue representation:

$$\hat{f}_i \chi_i = \varepsilon_i \chi_i \qquad i = 1,..., N. \tag{2.22}$$

We recall that the electrons are assumed to move within the field of stationary nuclei in describing the time-independent equations. First, a set of trial solutions χ_i to the Hartree-Fock eigenvalue equations are obtained. A typical iterative procedure begins by proposing an initial guess for the set of N spin-orbitals χ_i^0. A Fock operator $\hat{f}_i$ is then imposed on the Hartree-Fock equation, then solving a set of *N* equations in (**2.22**) as one simple eigenvalue problem. Subsequently, the following set of solutions (χ_i^1) that correspond to the *N* lowest eigenvalues (ε_i^1) are selected to obtain the new Fock operator $\hat{f}_i \chi_i^1$. This process is repeated until the n^{th} set of solutions (χ_i^n) yields a difference from the $(n-1)^{\text{th}}$ set (χ_i^{n-1}) by less than a value, which is reasonably small. When this criterion is met, a system is said

to be converged and the solution orbitals are *self-consistent*. Therefore, this type of iterative process is also known as *self-consistent field* (SCF) calculation.

2.5.3 Linear Combination of Atomic Orbitals: The Roothaan-Hall Approach

It is widely accepted that it is impossible to compute a general function as it is (complete basis sets tend to have an infinite number of functions), and therefore, the problem must be discretised in some way. Unfortunately, the direct solution to the HF equations in the form of the Slater determinant is not practical for most solid-based systems [188]. Also, solving the RHF equations numerically using finite-difference methods (*numerical Hartree-Fock* method) on a discrete grid is only feasible for very small molecules [189].

To deal with larger systems, Roothaan and Hall independently proposed in 1951, that discretisation must be performed in the Hilbert space of the one-electron orbitals [190, 191]. The term “discretisation” is used to describe the truncation of the one-electron Hilbert space using a finite *basis set*. Although the Hilbert space is infinite in actuality, any function in it can be approximated by a finite *linear combination of atomic orbitals* (LCAO). This method expresses each molecular orbital in K amount of atomic orbitals (basis functions). A set of these functions is called a basis set. A molecular orbitals can then be written as:

$$\chi_i = \sum_{\nu=1}^{K} c_{\nu i}\phi_\nu \qquad \textbf{(2.23)}$$

where χ_i is the spatial molecular orbital, and $c_{\nu i}$ is a coefficient. The one-electron orbitals ϕ_ν are regarded as basis functions and correspond to one of the K atomic orbitals. The basis functions will be represented by the letters ν, μ, λ, and σ. There are a total of K molecular orbitals (finite) that can be derived from the K basis functions, although not all

orbitals would necessarily be occupied by electrons. The result (calculated up to several significant values) of the above equation leads to the identification of the *Hartree-Fock limit*, where the energy of the system can no longer be reduced any further by the imposition of additional basis functions.

The lowest energy wave function (*i.e.* $\partial E = 0$) for a given set of coefficients c_{vi} can be written as:

$$\frac{\partial E}{\partial c_{vi}} = 0 \tag{2.24}$$

Subsequently, by introducing the linear combination in (**2.23**) to the Hartree-Fock equations in (**2.22**), we obtain

$$\hat{f}_i(1)\sum_{v=1}^{K} c_{v1}\phi_v(1) = \varepsilon_i \sum_{v=1}^{K} c_{v1}\phi_v(1) \tag{2.25}$$

Multiplying each side of equation (**2.25**) with $\phi_\mu(1)$ (which is also a basis function) and integrating the one-electron function on (1) gives:

$$\sum_{v=1}^{K} c_{v1}\int dv_1\, \hat{f}_i(1)\phi_v(1)\phi_\mu(1) = \varepsilon_i \sum_{v=1}^{K} c_{v1}\int dv_1 \phi_v(1)\phi_\mu(1) \tag{2.26}$$

The equation above can be simplified by introducing the *Fock matrix* on the left side of the equation and an *overlap matrix* on the right side of the equation. A more elaborate derivation of the matrices can be found in the Roothaan-Hall equations [190, 191], and also in the literature [181, 182]. In short, the Fock matrix can be represented as:

$$F_{\mu v} = \int dv_1\, \hat{f}_i(1)\phi_v(1)\phi_\mu(1) = \left\langle \phi_\mu \middle| \hat{f}[\chi] \middle| \phi_v \right\rangle \tag{2.27}$$

and the overlap matrix can be written as:

$$S_{\mu\nu} = \int dv_1 \phi_\nu(1)\phi_\mu(1) = \left\langle \phi_\mu \middle| \phi_\nu \right\rangle \quad \textbf{(2.28)}$$

Note that in this case, the overlap between the basis functions "μ" and "ν" is not required to be mutually orthogonal, *i.e.* not necessarily zero. The two matrices above can then be represented as (**F**= $F_{\mu\nu}$) and (**S**= $S_{\mu\nu}$). Next, if the coefficients of $c_{\nu i}$ and the orbital energies ε_i can also be expressed as matrix equations, they can then be represented as (**C**= $\sum_{\nu=1}^{K} c_{\nu 1}$) and (**E**= ε_i) [182]. Thus, the Roothaan-Hall equation (**2.26**) can be expressed in the matrix form:

$$\mathbf{FC=SCE} \quad \textbf{(2.29)}$$

In fact, computational implementation of the Hartree-Fock theory was not feasible until this formalism became available. The procedure for solving the Roothaan-Hall equations in matrix form (iteratively) is essentially the same as that mentioned in the Hartree-Fock equations (Section **2.6.2**). The iterative steps are available in the following literature [181, 182].

2.5.4 Introduction to Basis Sets

A basis set refers to a set of one-particle functions used to define molecular orbitals, where one electron has one atomic orbital. There are two main types of basis functions in the HF formalism, where their strengths and limitations will be described in this section. Basis sets are an important component of the Hartree-Fock method, which is a precursor to density functional theory, and as such will be briefly mentioned here.

Importantly, only the non-relativistic *hydrogen-like atom* can be described exactly at the HF level. A hydrogen-like system contains a nucleus and only one electron, (*e.g.* H,

He^{+}, Li^{2+}). Acceptable hydrogen-like molecular orbitals are those where the orbital exponent takes into account the screening effect by inner-shell electrons. Hence, it is a good practice to choose functions that are centred at the atomic nuclei, and also partially resemble the exact solutions for the hydrogen-like atoms.

The first type of basis set involved the *Slater-type orbitals* (STO), proposed by Slater [192] and Zener [193]. Slater-type orbitals have the functional form as:

$$\phi_{\mu}^{STO} = R_n(r)\,Y_{lm}(\theta,\ \varphi) \tag{2.30}$$

The function $Y_{lm}(\theta,\ \varphi)$ is the *real spherical harmonics*, and the integers *l* and *m* are considered as quantum numbers. The radial function $R_n(r)$ can be written as:

$$R_n(r) = \frac{(2\alpha)^{n+1/2}}{\sqrt{(2n)!}}\, r^{n-1} \exp(-\alpha r) \qquad n = 1,2,3,\ldots \tag{2.31}$$

where α is an adjustable parameter. Within the set of all possible STOs, every hydrogen-like energy eigenfunction can be formed as a linear combination, constituting a complete basis set. This is important because it shows that the Hartree-Fock limit can be reached by increasing the K value (linear combination of K functions). Despite the theoretical quality of an STO, for which it expands the molecular orbitals that make up the N-particle solution to the Hartree-Fock equations, it presents significant limitations in calculating the properties of large molecules. In a large system, STO becomes inapplicable in the SCF calculations from calculating the orbitals of four-centre integrals (*e.g.* $<\nu\mu|1/r_{12}|\lambda\sigma>$) [194, 195]. For instance, equation (**2.27**) that involves only two-centred basis functions (μ and ν) can be expressed as $<\nu\mu|1/r_{12}|\nu\mu>$ and is solvable. Therefore, STO only scales well with the generalised eigenvalue problem in equation (**2.29**), with two-centre integrals, up to three-centre integrals (*e.g.* $<\nu\mu|1/r_{12}|\lambda\mu>$) [194, 195]. As the Slater type orbitals are

not good for molecular orbital calculations (on different atoms), it is common to replace the Slater orbitals with Gaussian type orbitals (GTO).

Gaussian-type orbitals can be written in the form of:

$$\phi_{\mu}^{GTO} = x^{a} y^{b} z^{c} \exp(-\alpha r^{2}) \tag{2.32}$$

where *x*, *y* and *z* consist of the Euclidean coordinates of the electron and the nucleus, and the letters *a*, *b* and *c* are the orbital quantum numbers (which take values from 0 to ∞), which can take values from 0 to ∞ [181]. It was roughly around the same period when Roothaan and Hall proposed the discretisation of the one-electron orbitals, Boys showed that all the integrals appearing in the SCF theory can be calculated if the function (ϕ_{v}) in equation (**2.23**) can be described in the form of equation (**2.32**) [196]. This approach, also known as the *Cartesian* GTO (cGTO), makes possible the use of much larger number of functions to have the ϕ_{v} expanded, by expressing the product of two Gaussians as a single Gaussian [182, 195]. The physical properties of these Gaussian-type orbitals are not as precise as the STO, as STOs are known to have better short- and long-range behaviour than that of GTOs [181]. However, the enormous computational advantage overshadows this, which has resulted in the universal acceptance of GTO in SCF calculations.

To overcome the poor physical properties of the cGTOs mentioned above, the linear combination of the basis functions (K) in cGTO can be employed, which leads to the *uncontracted* Gaussian method, also known as *primitive* GTO (pGTO). Each linear combination can be written as:

$$\phi_{\mu} = \sum_{i=1}^{L} d_{i\mu} \phi_{i}(\alpha_{i\mu}) \tag{2.33}$$

L is the number of functions in the expansion, where $d_{i\mu}$ is the coefficient of the pGTO function ϕ_i, which has an exponent $\alpha_{i\mu}$. This method also requires a significant amount of computational power; however, the number of numerical integrals can be reduced by contracting the basis sets [182].

The method of combining a single basis function with a number of primitive Gaussian functions, *minimal basis set*, was developed by Pople and co-workers [197], where one basis function is selected for every atomic orbital that is required to describe the free atom[*]. The term STO-*n*G can be used to indicate all minimal basis sets in which *n* Gaussian functions are used to represent each orbital. Examples of STO-*n*G basis sets are: STO-3G, STO-4G, STO-6G and STO-3G* (polarised version of STO-3G). The drawback of this method is that a minimal basis set contains only one contraction per atomic orbital, where the functions cannot expand or contract in size in accordance with the molecular environment [182].

Pople and co-workers, again, implemented improvements on the minimal basis sets using the *split-valence* approach, where the core shells and valence shells are different (*i.e.* the hydrogen atom has a 1s valence shell, whereas the first row atoms have 2s and 2p shells as valence and the 1s as core shells). Some of the examples of split-valence basis sets[†] are: 3-21G, 4-21G, 4-31G, etc. Split-valence basis sets, including some minimal basis sets, can be augmented with diffuse functions for calculations involving charged species, especially anions [198-200]. This is due to the nature of charged species having extended charge density (a 'tail') in space, where there is a need to study the tails of the density distribution to account for relevant chemical interactions in the system. Subsequently,

[*] Examples for the minimal basis set is the 1s orbital for hydrogen, whereas for carbon, the minimal basis set consists of a 1s orbital, a 2s orbital and the full set of three 2p orbitals. The minimal basis set for a molecule, for example methane, consists of four 1s orbitals (one per hydrogen atom), and the set of five (1s, 2s and 2p) orbitals described for carbon. Therefore, the minimal basis set consists of nine basis functions.

[†] In general, these basis sets can be further calibrated to include: polarisation for heavy atoms (non-hydrogen), polarisation on hydrogen and helium, diffuse functions, etc.

Pople's contribution to the development of basis sets, as well as reducing the computational cost, resulted in the award of a Nobel Prize in chemistry.

2.6 Post-Hartree-Fock Methods

Post Hartree-Fock methods were developed with the aim to improve the Hartree-Fock or the self-consistent field theories, where the correlation effect is often neglected. The term post Hartree-Fock implies a single determinant starting point [201], where functionals at this level utilise the unoccupied orbitals and eigenvalues [202]. Like its predecessor, the quality of a post Hartree-Fock method depends on the level of theory and the size of the basis set [195]. There are different categories of post Hartree-Fock methods: the configuration interaction (CI) methods [203], quadratic configuration interaction (QCI) [204], many-body perturbation theory (MBPT) [205], also known as MP [201]), and the coupled-cluster theory (CC) [206, 207]. To date, post Hartree-Fock methods are known to be an affordable yet accurate approach to electron correlation [208].

The post Hartree-Fock methods will be described briefly in this section. The CI optimisation method is based on the variational principle, where the trial wave function is written in a linear combination of determinants, hence the name *configuration*. The extended version of the CI (Quadratic CI) that corrects the size-consistency is based on the CI theory. The second method is based on the Møller-Plesset perturbation theory, often referred to as MP*n* where *n* is the order of the perturbation[*] (MP2, MP3, MP4 and beyond). While the perturbation theory adds all types of corrections to a given order *n*, the third method, Coupled cluster (CC) attempts to include all corrections of a given type to infinite order.

[*] The zeroth-order wave function is the Hartree-Fock determinant, whereas the zeroth-energy is the exact Hartree-Fock energy.

Another type of post Hartree-Fock method, called the composite method, employs a high level of theory but smaller basis sets. This is in contrast to the majority of calculations with lower level of theory but larger basis sets. Some of the composite methods are the Gaussian-type (G2, G3 and G4) and complete basis set (CBS) methods [195].

Almost all post Hartree-Fock methods share a combination of poor scaling with the system size and a strong dependence on basis sets, thus limiting their application to small systems in practice. However, a reduced error and improved geometrical accuracy can be obtained by the introduction of empirical parameters [209].

2.7 Density Functional Theory

There are numerous first principles approaches in calculating the electronic properties of materials at different levels of sophistication. However, choosing the most appropriate first principles method for a particular application, for instance transition metal oxides, can be challenging. It was shown in the previous sections that the Hartree-Fock method provides a good approximation for systems where the exchange effect is emphasised, neglecting the importance of the correlation effect. Density functional theory is an approach beyond the Hartree-Fock formalism to include correlation effects in a material, with increased accuracy at a similar computational cost. It is used for a wide range of materials to produce a ground state property of a system, giving accurate results to within a few percent of experimental data [172, 210]. An intuitive way of describing this theory is that the number of electrons, the nuclei positions and nuclear charges in a system can be determined by the electron density [195]. Specifically, the integral of the density defines the number of electrons; the cusps in the density define the position of the nuclei; the heights of the cusps define the corresponding nuclear charges. The main advantage of DFT is perhaps best

exemplified by comparing it with the Hartree-Fock wave function approach as described in the previous sections.

Wave function approach:

- The wave function scales as N^4 for an N-electron system containing 4N variables for each electron, three spatial and one spin coordinate.
- Complexity of wave function increases exponentially with the increase of N-electrons.

Density functional approach:

- The electron density is the square of the wave function, where each spin density depends on three spatial *x*-, *y*-, and *z*-coordinates of the individual electron. Hence, it can be said to scale three-dimensionally as N^3.
- The electron density is independent of the system size, having the same amount of variables.

2.7.1 Hohenberg-Kohn Theorem

One of the most important breakthroughs in quantum mechanics occurred in 1964, when Hohenberg and Kohn made significant contributions in predicting the electronic ground state of many-body systems, long after the approximate model developed by Thomas [211] and Fermi [212] in the late 1920s. It is important to know that the foundation of the DFT formalism rests on the two theorems proved by Hohenberg and Kohn, as well as the derivation of a set of equations formulated by Kohn and Sham later in 1965 [213].

Consider an electron in a time-independent external potential (with exchange and correlation effect included); the Hamiltonian for this system consists of three contributions, *i.e.* kinetic energy, electron-electron interaction and the electron-ion interaction. The first Hohenberg-Kohn theorem states that the ground state energy of the system, described by Schrödinger's equation, is a unique functional of the electron density $\rho(r)$. The energy functional can be written as:

$$E[\rho(r)] = \int V_{ext}(r)\rho(r)dr + F[\rho(r)] \qquad \textbf{(2.34)}$$

where the first term describes the interaction of electrons with an external potential $V_{ext}(r)$. The second term, the Hohenberg-Kohn functional $F[\rho(r)]$, is the sum of the kinetic energy of the electrons and contribution from interelectronic interactions. However, the precise form of this functional was unknown in this postulation, until it was approximated by Kohn and Sham [213].

The second Hohenberg-Kohn theorem proved that the ground state electron density and energy can be obtained using the variational principle, via the minimisation of $E[\rho(r)]$. As usual, the exact ground state wave function is given by $\Psi_0(\hat{r}_1, \hat{r}_2, ..., \hat{r}_N)$, corresponding to the ground state density $\rho_0(r)$. The ground state wave function must produce not only the ground state density, but also minimise the energy. Any electron density other than the ground state density will have energy higher than the ground state energy. A constraint is imposed on the electron density such that the number of electrons (N) is fixed. To minimise the energy $E[\rho(r)]$, a Lagrangian multiplier $(-\mu)$ is introduced to the minimisation scheme

$$\frac{\delta}{\delta\rho(r)}\left[E\rho(r) - \mu\int \rho(r)dr\right] = 0 \qquad \textbf{(2.35)}$$

which can be reduced to the DFT equivalent of the Schrödinger equation, under the constraint of the fixed external potential

$$\left(\frac{\delta E[\rho(r)]}{\delta \rho(r)}\right)_{V_{ext}} = \mu \tag{2.36}$$

where the Lagrange multiplier is now a chemical potential that corresponds to the electronegativity.

2.7.2 Kohn-Sham Theorem

The success of modern DFT is based on the Kohn-Sham equations that were formulated based on the difficulty in determining the unknown energy functional $F[\rho(r)]$. Kohn and Sham showed that finding the correct electron density can be achieved in a way that involves solving a set of equations, in which each equation involves only one electron. Here, the density of an N-particle system can be described as

$$\rho(r) = \sum_{i=1}^{N} |\phi_i(r)|^2 \tag{2.37}$$

where the equation is the sum of square moduli of the one-electron orthonormal orbitals set $\phi_i(r)$. By replacing a many-body problem with a set of self-consistent equations for a single electron, the Kohn-Sham model of the density functional theory can take on the energy contribution form, similar to that of the Hartree-Fock method. The Kohn-Sham equation can be written as

$$F[\rho(r)] = E_{KE}[\rho(r)] + E_H[\rho(r)] + E_{XC}[\rho(r)] \tag{2.38}$$

where F[ρ(r)] is the sum of the following energy functions: kinetic energy $E_{KE}[\rho(r)]$, Coulombic electron-electron contribution, also known as the Hartree electrostatic energy $E_H[\rho(r)]$, and the exchange-correlation functional energies $E_{XC}[\rho(r)]$ [182, 213].

The key to the Kohn-Sham theory is to obtain the one-particle Schrödinger equation in a fictitious system, *i.e.* the kinetic energy $E_{KE}[\rho(r)]$ of the system is calculated under the assumption of *non-interacting* electrons, where the density of the electrons remains the same as the real system. The Kohn-Sham energy of an N-electron system is then derived from the equation above (**2.38**), where the total energy equates to the sum of the three contributions and an external potential (pseudopotential energy), *i.e.* the difference between the real kinetic energy of the system and $E_{KE}[\rho(r)]$

$$E_{KS}[\rho(r)] = E_{KE}[\rho(r)] + E_H[\rho(r)] + E_{XC}[\rho(r)] - \sum_{A=1}^{M} \int \frac{Z_A}{|r - R_A|} \rho(r) dr \qquad \textbf{(2.39)}$$

The fourth term is the electrostatic potential that describes the contributions from both the nuclei (R_A) and electrons (r), written in the form appropriate to the interaction with M number of nuclei, where Z_A is the nuclear charge. Next, by applying the electron density expression in (**2.37**) to the equation above, the one-particle Schrödinger equation for N-orbitals lowest in energy can be written in an eigenvalue representation

$$\left\{ -\frac{\nabla_1^2}{2} + v(r_1) \right\} \phi_i(r_1) = \varepsilon_i \phi_i(r_1) \qquad \textbf{(2.40)}$$

where the first term is the kinetic energy of the non-interacting electrons. The one-electron potential $v(r_1)$ is also known as the Kohn-Sham potential, containing all the contributions from the electron-nuclear interaction, electron-electron interaction, and the exchange and correlation potential. On the right side of equation, ε_i are the orbital energies.

The lowest energy can be calculated self-consistently by using equation (**2.40**) with an initial guess of electron density. Consequently, the solved equation yields a set of Kohn-Sham orbitals, where they are used to derive an improved density for the following iteration. This process is repeated until the density and exchange-correlation energy have satisfied the convergence criteria [182].

2.7.3 Kohn-Sham Approximations: Exchange-Correlation Functionals

To more accurately describe a many-body system, we recall that the electron exchange contribution and the electron correlation contribution (Section **2.8**) are required. The main difference between the Hartree-Fock and Kohn-Sham theories is that the former treats just the electron exchange contribution; Hartree-Fock neglects the electron correlation contribution. In the Kohn-Sham theorem, both the exchange and correlation terms are treated reasonably well but not precisely. In other words, the unavoidable approximations of the DFT method concern only the exchange-correlation energy, which is one of the key ingredients to accurate DFT calculations. Several methods of approximating the exchange-correlation energy of a system will be introduced in this section.

Approximation methods for the exchange-correlation can be illustrated by the biblical Jacob's ladder (see Figure **2.1**). Jacob's ladder of approximations starts from the Hartree formalism (without exchange-correlation), where each step up to the next rung consists of functionals based on the previous rung, where the level of constraints and accuracy are iteratively increased, as well as the computational cost.

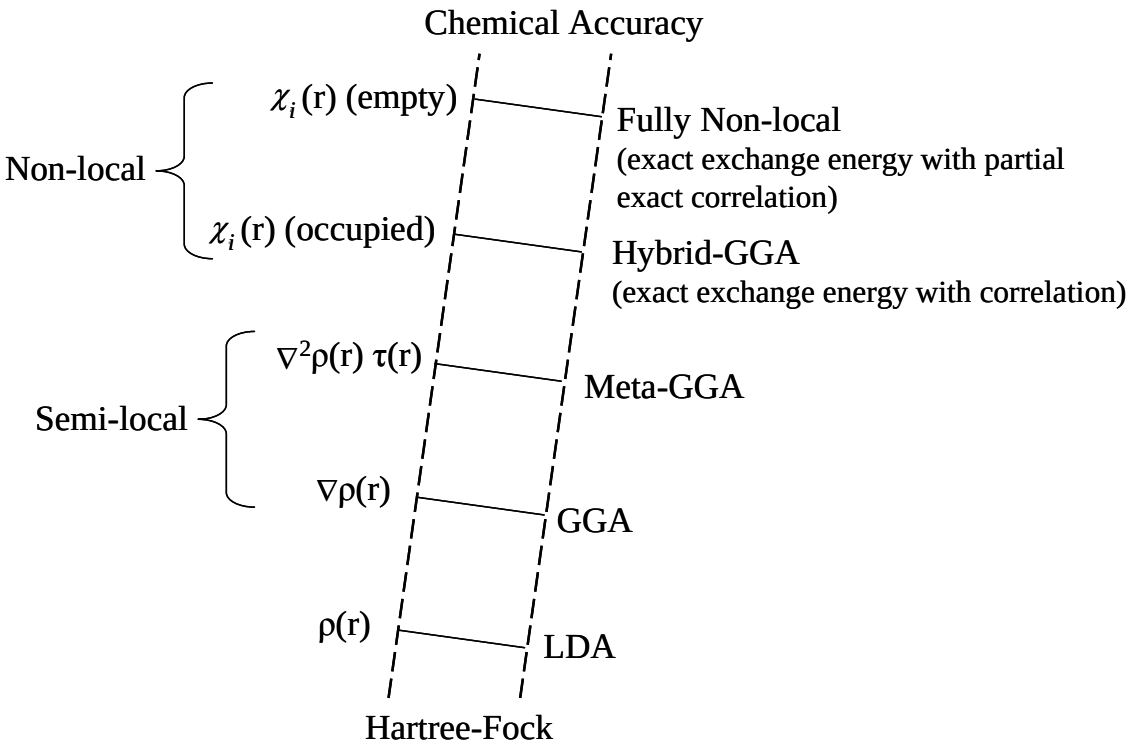

Figure 2.1 Jacob's ladder of density functional approximations for the exchange-correlation energy.

2.7.3.1 Local Density Approximation (LDA)

Local density approximation (LDA) is the simplest way of describing the exchange-correlation energy of a system based on a uniform electron gas model [179, 213]. The assumption states that the total exchange-correlation energy of a non-uniform electron density can be approximated as a sum of contributions characterised by a uniform electron density $\left(\varepsilon_{XC}^{\text{hom}}\rho(r)\right)$. In other words, the electron density is constant throughout all space. The total exchange-correlation energy can be written as

$$E_{XC}^{LDA}[\rho(r)] = \int \left(\varepsilon_{XC}^{\text{hom}}\rho(r)\right)\rho(r)dr \qquad \textbf{(2.41)}$$

To treat magnetic fields, the local spin density approximation (LSDA) was introduced, where the spin-polarisation of a material is taken into account by having a spin-up and a spin-down electron density [214].

LDA-based Kohn-Sham equations can be described as entry-level DFT, and are often regarded as the lowest rung of the approximations ladder. Examples of the commonly used LDA functionals that incorporate the correlation energy of a homogeneous (uniform) electron gas calculated by Ceperley and Alder [215] include the Perdew and Zunger functional [216], and the functional by Vosko *et al.* [217]. In general, this approximation method (LDA or LSDA) describes accurately the bulk properties of metals, where the electron density in this type of system varies slowly. However, most molecular structures are spatially inhomogeneous and the electron density varies rapidly in reality. This causes an underestimation of the exchange energy by ~10%, for which the error itself is larger than the total correlation energy. Furthermore, electron correlation and bond strengths are often overestimated. The resulting accuracy in this approximation method is therefore comparable to that of Hartree-Fock method, and because of the drawbacks, the LDA approximation is often not suitable for chemical applications. In general, LDA is known to underestimate the atomic ground state energies, whereas in the case of binding energies, hydrogen bond calculations are often overestimated [172, 202, 210].

2.7.3.2 Generalised Gradient Approximation (GGA)

The generalised gradient approximation (GGA) is an improvement over LDA which takes into account not only the density-dependent exchange and correlation energies, but also the exchange and correlation, which is dependent on the gradient of the density, $\nabla\rho(r)$ [210]. An improvement upon this was proposed by Hohenberg, Kohn and Sham [179, 213], however the GGA exchange-correlation energy discussed in this section is the collective work by Langreth and Mehl [218], and Perdew [219] and Becke [220]. The general form of GGA can be expressed as

$$E_{XC}^{GGA}[\rho(r)] = \int \varepsilon_{XC}^{GGA}(\rho(r), \nabla\rho(r))\rho(r)dr \quad \textbf{(2.42)}$$

Unlike LDA which contains no empirical data, the exchange-correlation functionals of the GGA form may include empirical information [221-224]. Many different GGA-based functionals have been developed since the late 1980s with specific applications and advantages, with further information on these functionals being well documented and reviewed in the literature [225, 226]. Similar to LDA, the exchange-correlation energy of GGA may also include the spin-polarisation of up and down electron spin densities (GGSA).

Only the general features and the more common functionals will be discussed here. For calculations involving solids, the non-empirical Perdew-Wang (PW91) [227] and Perdew-Burke-Ernzerhof (PBE) [228] functionals are two of the more commonly used GGA functionals, where the latter was developed based on the correct features of PW91. Another functional that is well-established is the Lee-Yang-Parr (LYP) functional, although not based on LDA [229]. The popular LYP correlation functional is derived from the properties of the exact HF orbital of helium atom [229, 230], in contrast to the uniform electron gas approach employed by the PW91 functional [227], showing that the energy of the ground state of a many-body system can be solved in the HF-like single consistent calculations at a lower computational cost [231].

It is generally accepted that the GGA methods perform better than LDAs [210, 222, 228, 232]. This is because GGA retains the correct features of LDA and includes another important feature, the gradient-corrected functional [228]. Furthermore, GGA was designed to include some inhomogeneity effects based on the LSDA model. GGA was tested against LDA in a series of calculations involving metals, where the GGA results compared favorably with the LDA values [178]. More importantly, the inclusion of gradient terms in GGA generally leads to a significant shortening of the overestimated

hydrogen bond in LDA calculations, as well as reduced hydrogen dissociation energy of the overestimated binding energy in LDA calculations [233-236]. As such, GGA methods account for hydrogen bonds much better than the LDA [178]. Compared to the LDA approach, errors produced in GGA-based calculations are reduced drastically, resulting in an improved accuracy of the total energy [171, 228] and structural energy differences [228, 237, 238].

One of the disadvantages of this approximation is that GGA-predicted bond lengths are not always superior to the corresponding results obtained with the LDA. This is because GGA is known to soften and expand bondings, but sometimes the effect does overcorrect the LSDA prediction [228]. It is well known that both LDA and GGA underestimate the band gap in semiconductors, *e.g.* ZnO [239], which is a bottleneck for band structure calculations. Also, it has been shown that the PW91 functional, in some cases, describes the electron density of a uniform electron gas less accurately than LSDA [240, 241]. Although the above limitations proved GGA can be a nuisance in accurate energy calculations, physical and chemical reactions are not just determined by the total energy, but also energy differences, dissociation energy, atomisation energy, hydrogen bonding, etc [178]. Therefore, it is important to consider the overall advantages and computational accuracy relative to the drawbacks in using an approximation functional for a specific application.

2.7.3.3 Meta-GGA

In LDA, only one electron density at **r** is needed (**2.41**), whereas in GGA both the electron density and its gradient are utilised (**2.42**). To increase the accuracy of the approximation method, meta-GGA can be employed, which includes the dependence on higher derivatives. This trend sees the move from the local LDA functional (one variable) to the

semi-local GGA functional (two variables), as well as the inclusion of empirical parameters as the level of theory increases. Based on GGA, the meta-GGA exchange-correlation functional includes an additional third-order gradient density $\nabla^2\rho(r)$ variable, and another local parameter, the kinetic energy density $\tau(r)$. At this level, the third rung semi-local meta-GGA is a step closer to becoming a fully non-local functional. The exchange-correlation energy of the meta-GGA can take on the following general form

$$E_{XC}^{mGGA}[\rho(r)] = \int \varepsilon_{XC}^{mGGA}\left(\rho(r), \nabla\rho(r), \nabla^2\rho(r), \tau(r)\right)\rho(r)dr \qquad \textbf{(2.43)}$$

where $\nabla^2\rho$ is a Laplacian of the electron density.

This method is less commonly used because it is computationally much more demanding than the GGA method, while the additional variable provides only a limited correction to the GGA calculation. Furthermore, it has been reported that this method shows no significant improvement over GGA for calculations involving bond lengths, and only moderate advance for vibrational frequencies, however, better atomisation energies are observed [178]. Hence, meta-GGA is often applied in conjunction with other methods, such as using the solutions obtained from a self-consistent GGA or Hartree-Fock calculation.

An example of meta-GGA functionals, such as the non-empirical Tao-Perdew-Staroverov-Scuseria (TPSS) developed by Perdew, Scuseria and co-authors, can be considered as the next improvement over the PBE functional [195, 242]. Interestingly, this functional does not depend on the Laplacian at all, $\varepsilon_{XC}^{TPSS} = \varepsilon_{XC}^{mGGA}\left(\rho(r), \nabla\rho(r), \tau(r)\right)$ [242, 243]. It has been shown that TPSS provides an improved description of hydrogen bonds [244] and reduces the error in lattice constants of solids compared to PBE-GGA [242]. Other meta-GGA functionals have originated from the concepts of Becke (B88C and B95) [245, 246] and co-workers (Becke-Roussel) [247].

2.7.3.4 Hybrid Functionals

Hybrid-GGA, also known as hyper-GGA, is placed at the fourth rung of the approximation ladder. Hybrid-GGA functional describes the exchange using a combination of functionals that must include the contribution from the exact (Hartree-Fock) exchange energy, and a mixture of GGA-type functionals. The role of the exact exchange, mainly the complete cancellation of the self-interaction, is described in the following article [248]. In general, hybrid functionals have been found to be a significant improvement over semilocal GGA type functionals as a result of some cancellations of errors [178, 243].

An example of the tremendously well-received hybrid-GGA functional is the B3LYP functional [249, 250]. The B3LYP exchange-correlation functional can be written as:

$$E_{XC}^{hybrid}[\chi_1,\chi_2,\ldots,\chi_N]=\alpha(E_X[\chi_1,\chi_2,\ldots,\chi_N]-E_X^{GGA}[\rho(r)])+E_{XC}^{GGA}[\rho(r)] \qquad \textbf{(2.44)}$$

where $E_X[\chi_1,\chi_2,\ldots,\chi_N]$ is the Hartree-Fock expression for the exchange energy. The term E_X^{GGA} is the Becke 88 exchange functional, and the Lee-Yang-Parr correlation functional is written in E_C^{GGA}. The constant α is a numerical parameter that can be chosen arbitrarily, *e.g.* $\alpha=0.5$ [243, 251]. Another hybrid-GGA method (PBE0) that includes the PBE exchange-correlation coupled with the exact exchange energy was found to compare well with the empirical hybrid B3LYP functional [252].

To date, there are more than ten hybrid functionals reported in the literature. A detailed description of different functionals can be found in the review article by Sousa and co-workers [210], which provides further understanding of the general performance and limitations on the functionals.

2.7.4 Dispersion and van der Waals Forces

It is generally accepted that the most popular approximate functionals (*i.e.* LDA and GGA) fail to accurately describe weak interactions. This is because the transition state in chemical interactions is often characterised by weakly interacting atoms and molecules. This type of interaction is known as the weak van der Waals (vdW) interaction, where the force between instantaneously induced dipoles can be described by the London dispersion force. With the increasing popularity of DFT in biological simulations where weak interactions play an important role, as shown by the critical role of vdW forces in the stabilisation of protein structures [253], there is a need to improve the description of vdW or dispersion interactions.

The consequence of using an approximate functional for both biological and industrial materials, as opposed to having the exact functional, is that the dispersion force is always miscalculated. The London dispersion force can be described by the asymptotic $1/R^6$ behaviour [202, 254, 255], where if the distance between two interacting systems increases ($R \rightarrow \infty$), there should be an attractive part of the energy that asymptotically decays as $1/R^6$. The Hellmann-Feynman theorem states that the origin of vdW long-range attractions can be attributed to the accumulation of electron density between two closed-shell systems [256]. It was also shown that vdW interactions can exist between two neutral systems without the overlap of electron densities [257].

Fortunately, the inability to describe the weak interactions can be overcome by applying some simple corrections, where the dispersion force can be treated with empirical [254, 255] and non-empirical methods [258-263]. In the C_6/R^6 correction method, the coefficients C_6 can be derived using experimental data (fitted with atomic polarisabilities) [254, 264, 265], or calculated using first principles methods [202]. The C_6 coefficients, however, can vary considerably depending on the chemical environment and atom pairs.

When the distance between two systems R is small and there is an overlap of electron densities, the R^{-6} dependance behaviour is no longer appropriate, thus, the vdW energy term should have a damping factor [255, 266]. Correctly assigning the coefficients in a bonding environment with an appropriate damping function still remain a challenge. The application of the C_6 coefficient is therefore known as the DFT-D method. More recent ideas have been proposed to capture the dispersion interaction [267-269], and multiple efficient implementations of the dispersion correction have since been developed [270-272].

2.8 Bloch's Theorem: Solving the Schrödinger Equation in Periodic System

In the previous section, it was shown how Kohn and Sham derived the single-particle Schrödinger equations. The next problem to solve is the single-particle Kohn-Sham equations for periodic systems such as crystalline solids. Although it was shown in the previous section that the electronic structure of a many-body system can be calculated using DFT, the large number of electrons* contained in a macroscopic crystalline structure translates to an extremely large basis set with too many wave functions, hence, the Schrödinger equation cannot be solved directly for such a system. To overcome this problem, the symmetry of periodic crystals can be exploited to reduce the system size significantly by assuming that the solid possesses an ideal crystalline structure. *Bloch's theorem* enables the Schrödinger equation for an infinite periodic solid to be solved by replacing the solid with a *unit cell* that is repeated throughout space using *periodic boundary conditions*. In this section, the method of treating periodic solids in unit cells with Bloch's theorem will be explained.

* A 1 cm^3 crystal solid contains some 10^{23} nuclei and 10^{24} electrons

Although this method facilitates calculations with perfect periodicity, in reality, solids contain imperfections such as stacking faults, defects (point, line, and surface), dopants, dangling bonds, interstitials, for example. Nevertheless, there are usually large regions of crystalline structures that possess the quality of a periodic structure. For this reason, the discussion in this section will be restricted to ideal systems without any imperfections.

In the context of the electronic structure of crystals with nuclei that are highly ordered in a periodic lattice, a lattice can be defined as an infinitely periodic arrangement of points in space. The crystal structure can be constructed by filling the space (*real space*) with unit cells without leaving gaps and overlapping. The content in a unit cell, *e.g*. atom, molecule, solid, etc., is called the *basis*. There are fourteen different basic unit cells that can be defined by three vectors, which are known as the *Bravais* lattices. The common lattices include *hexagonal* and cubic (*e.g. body-centered* and *face-centered*) cells. Examples of such unit cells with the symmetry of the Bravais lattices, as well as their structural properties can be found in the literature [273].

To model a periodic material, a primitive cell in real space with the minimum amount of atoms required to define a periodic material must be re-described in *reciprocal space* in a *reciprocal cell*. A reciprocal cell can be defined by three vectors $\mathbf{b}_1$, $\mathbf{b}_2$ and $\mathbf{b}_3$. They are derived from the Cartesian $\mathbf{a}_1$, $\mathbf{a}_2$ and $\mathbf{a}_3$ vectors of the unit cell that corresponds with the real space (see Figure **2.2**), where $\mathbf{b}_i \cdot \mathbf{a}_j = 2\pi\delta_{ij}$ (δ_{ij} is the Kronecker delta).

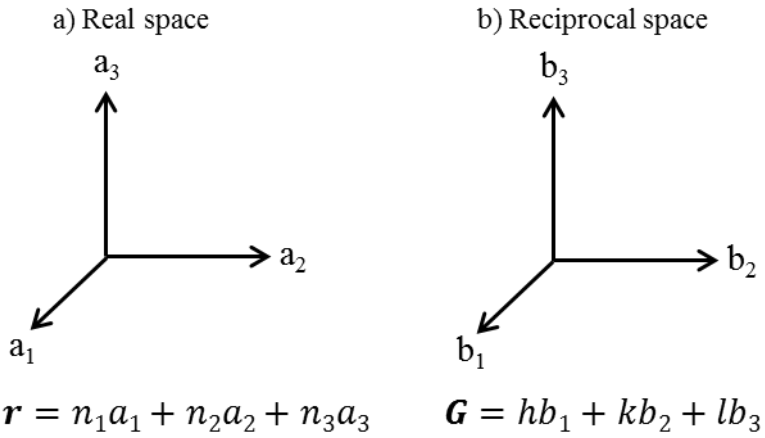

Figure 2.2 Schematic diagrams of a) real space and b) reciprocal space. The real space and reciprocal space vectors, **r** and **G**, respectively, are not necessarily in the same direction.

It is useful to know that larger lattice vectors in real space correspond to shorter lattice vectors in reciprocal space. In other words, the doubling of a cell size in real space halves the reciprocal cell. The equivalent of a primitive cell in reciprocal space is called the *first Brillouin zone* (FBZ), whereas a further reduced zone in the reciprocal space can be derived from the first BZ, called the irreducible Brillouin zone.

Just as a point in real space can be represented by a vector **r**, similarly, a point in reciprocal space (**k**-space) can be represented by a vector **k**, which plays an important role in simplifying the periodic wave function in a periodic structure. The cell volume can then be reduced to an integral corresponding to the **k**-space values in the BZ, where the FBZ is restricted to only one cell in the reciprocal lattice. This is necessary for calculating the wave function and energy for a solid as the Kohn-Sham equations are solved in reciprocal space by sampling of **k**-points in the BZ. The sampling of **k**-points is crucial for accurate ground state energy calculations because insufficient **k**-points results in poor energy calculations and excessive **k**-points (finer *mesh* size) results in costly computation. However, it is generally accepted that an increase in **k**-points produces more precise

results. In DFT calculations, the popular **k**-point sampling scheme of Monkhorst and Pack can be employed to represent the BZ [274].

The periodicity in ideal solids implies that the nuclei arrangement in each cell must be identical under the *Born-von Karman boundary condition*. The condition can be stated as

$$\psi(\mathbf{r}+\mathbf{R}) = \psi(\mathbf{r}) \tag{2.45}$$

i.e. the external potential on an electron in space **r** can be described as

$$V_{ext}(\mathbf{r}) = V_{ext}(\mathbf{r}+\mathbf{R}) \tag{2.46}$$

where **R** is a lattice vector that describes the size of the system. Bloch's theorem states that in a periodic system, solutions to the time-independent Schrödinger equation must be in the form of

$$\phi_{\mathbf{k}}(\mathbf{r}) = \exp(i\mathbf{k}\cdot\mathbf{r})u_{\mathbf{k}}(\mathbf{r}) \tag{2.47}$$

where ϕ is an arbitrary wave function that can be expanded as a *Fourier series*[*] over the reciprocal lattice vectors, and **k** is the crystal momentum that reflects the periodicity of the system. This allows the eigenfunctions to be restricted to within one unit cell. Alternatively, Bloch's theorem can be explained as a product of a wave-like part and a cell-periodic part. The wave-like part $\exp(i\mathbf{k}\cdot\mathbf{r})$ is defined as the plane wave functions, where calculations based on this term are referred to as plane-wave calculations. The cell-periodic part $u_{\mathbf{k}}(\mathbf{r})$, also known as the *Bloch orbital*, and can be written as a plane wave basis

[*] Computationally, the *fast Fourier transform* (FFT) algorithm is used to switch the complex Fourier series from reciprocal space to real space, or vice versa.

$$u_{\mathbf{k}}(\mathbf{r}) = \sum_{G} c_{i,\mathbf{G}} \exp[i\mathbf{G}\cdot\mathbf{r}] \tag{2.48}$$

where **G** are the reciprocal lattice vectors, such that $\mathbf{G}\cdot\mathbf{R} = 2\pi M$ where M is an integer number. A cell that is repeated periodically in space can be described by the Bloch orbital with the lattice vectors $\mathbf{a}_1$, $\mathbf{a}_2$ and $\mathbf{a}_3$. That is, $u_{\mathbf{k}}(\mathbf{r} + n_1\mathbf{a}_1 + n_2\mathbf{a}_2 + n_3\mathbf{a}_3) = u_{\mathbf{k}}(\mathbf{r})$ for any integers n_1, n_2 and n_3. For this reason, the term $u_{\mathbf{k}}(\mathbf{r})$ is a function that is strictly periodic in space within the lattice.

For a finite crystal, Bloch's theorem allows the full electronic structure to be solved in real space by considering one cell of the lattice for each **k,** and then applying boundary conditions to the unit cell, as dictated in the cell-periodic part in (**2.47**). Introduction of the periodic boundary conditions is equivalent to treating an infinite Bravais lattice, where each facet of the unit cell boundary has a bounded facet that is translated over the lattice vector **R** (see Figure **2.3**).

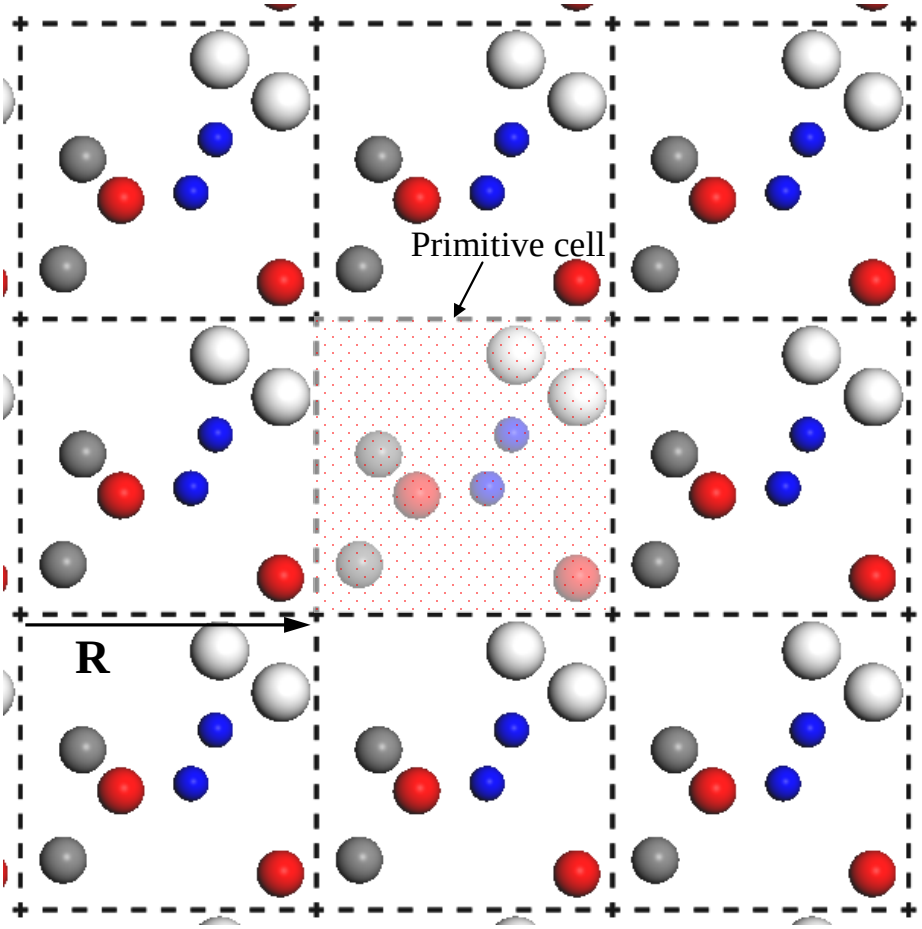

Figure 2.3 Illustration of periodic boundary conditions.

A *supercell* is an artificial cell constructed by replicating the crystal unit cell to a sufficiently large number of repetitions in all three directions. As the doubling of cell size halves the reciprocal cell, doubling of cell to construct a supercell translates to a doubled basis size and a halved Brillouin zone. In the supercell, a vacuum space in the *z*-direction is necessary in order to create a "slab" or surface structure along the (*x*,*y*) plane. Under periodic boundary conditions, the structure inside the supercell then becomes an infinite number of states as indexed by the vector **k**. The supercell structure is then calculated (relaxed) for convergence testing with respect to the vacuum spacer size and slab thickness. A well-considered supercell size not only minimise the computational effort, but also prevents interactions of the system with its neighbouring images. Similarly, this procedure can be employed to study impurities, grain boundaries, and surfaces including

defects. A defect surface structure is constructed by introducing the defect species by removing an atom at the topmost surface layer, for example.

Bloch's theorem enables the calculation of the energy band structure of a crystalline material via the *band theory* method. Let us consider a group of free atoms brought together to form a periodic solid. The electronic wave function in the solid can be expressed as a linear combination of atomic orbitals (LCAO). Assuming the atoms form a crystal structure on a lattice with lattice vector **R**, the Hamiltonian of the solid is obtained as the potential $V_{ext}(\mathbf{r})$ is periodic in the real lattice and can be expanded in a Fourier series. Therefore, the solutions to the Schrödinger equation can be expressed as

$$\hat{H}\phi_{\mathbf{k}}(\mathbf{r})=\mathrm{E}(\mathbf{r})\,\phi_{\mathbf{k}}(\mathbf{r}) \tag{2.49}$$

The consequence of this theorem is that the resultant energy spectra produced can be represented by their band structure [188]. This provides the electronic levels in crystal structures that are characterised by the Bloch vector **k** and a band index *n*. The way the energy of all states in a cell changes with **k** is called a *band structure*, where it is obtained by plotting the calculated orbital energy values against **k** within the first Brillouin zone. The total number of energy states within an energy interval (dE), plotted against the total energy, is known as the *density of states* (DOS).

2.9.1 The Fermi Surface, Metals, Semiconductors and Insulators

The calculated band structure and DOS of a solid show us whether the material under investigation is a metal, semiconductor or insulator by showing the *highest occupied molecular orbital* (HOMO) and *lowest unoccupied molecular orbital* (LUMO) near the *Fermi level*, *i.e.* conduction and valence bands. The energy of the highest occupied electronic state is called the *Fermi energy*, whereas the energy that separates the

conduction and valence bands is called *band gap*[*]. In general, band gaps larger than 3eV are considered as wide band gaps [251]. Besides electrical properties, the band structure also allows optical and even some magnetic properties of a solid to be determined.

A brief description of the difference between metal and semiconductor materials in quantum computing is explained here. In a metal the BZ can be separated into two regions, one unoccupied, and the other occupied by electrons, where the separation in between these two regions is called the *Fermi surface*. In contrast, the BZ is unoccupied by electrons in semiconducting materials, with only a small fraction of it occupied by the Fermi surface. The number of **k**-points required to accurately represent the wave function in metals is also much higher than that of semiconductors. This is because the bands in metals have more dispersion than semiconductors or insulators.

2.10 Plane-wave Methods and Pseudopotentials

To solve the KS equations (**2.40**), the cell-periodic wave function in Bloch's theorem needs to be expanded in a basis set, with the two common methods of representing this basis set in DFT calculations being the Gaussian and the plane wave basis sets, however, only the plane wave method (employed in this study) will be discussed in this section. As equation (**2.47**) can be constructed as a linear combination of localised or delocalised functions, these functions serve as the basis set. In the basis set containing periodic basis functions, only certain plane waves within a cutoff wave vector are included in the set. The convergence of DFT calculations with respect to the basis set size is therefore determined by varying the cutoff energy hence, calculated ground state energies must be compared with identical cutoff energy values.

[*] Standard DFT calculations often fail to describe accurately the electronic states near the Fermi energy, resulting in band gap underestimation.

Similar to molecular systems, the electrons in a solid can be separated into *core* and *valence electrons*. Core electrons are strongly localised around the nuclei in closed shells while the valence electrons take part in the bonding between atoms. Even though the core electrons contribute to most of the total energy in a system at about a thousand times more than the valence electrons, they are negligible in chemical bonding [275, 276]. As the core orbitals change very little (depending on the chemical bonding situation), majority of the computational effort is spent calculating the chemically uninteresting part of the basis functions. In contrast, the important chemical region, which is the valence electrons, plays an important role in determining the chemical and transport properties of a material.

The plane wave approach neglects the ionic core region, unlike Gaussian basis sets that include the core regions. This is because a significantly large number of plane waves would be required to describe the fast oscillations in the core region. The advantage of using plane waves over the Gaussian approach is that the plane waves are orthogonal and are independent of atomic positions. Most importantly, a plane wave basis set utilises the same basis set for molecules and solids, whereas the Gaussian method requires the basis sets to be different for molecules and solids.

The essence of the plane wave approach is that the Coulombic electron-nucleus interaction is replaced with pseudopotentials in the Kohn-Sham equations, *i.e*. the valence electrons are described via a set of pseudo-wave functions. Since the core states are chemically inert and chemical binding happens far away at the valence region, the pseudopotentials should have identical properties as the exact valence wave functions. The introduction of pseudopotentials results in two major outcomes. First, the total energy calculation becomes much more attainable than the all-electron calculation, which is an advantage in the especially costly *ab-initio* molecular dynamics (MD) calculations. Secondly, by having the true core-valence wave functions replaced by pseudopotentials, a

smaller basis set size is obtained via the removal of electrons within the ionic core region (*e.g*. 20 valence electrons are kept instead of 30 for zinc).

Despite the reduced plane wave basis set size, this approach still requires a large number of basis functions compared to other methods such as the localised basis sets in the Hartree-Fock approach (see **2.5.4**). This computational bottleneck can be overcome by employing the fast Fourier transform (FFT) method. As the wave functions can have a finite Fourier representation (described previously), FFT, enable the number of plane waves to be significantly reduced from N_{pw}^2 to a $N_{pw}\ln(N_{pw})$ scaling. The FFT algorithm transforms the electron density from reciprocal space to real space, or *vice versa*.

There are several variants of pseudopotentials such as the frozen-core approximation [277], norm-conserving pseudpotentials [278-281], projector augmented wave (PAW) [172, 282], fully non-local pseudopotentials and Vanderbilt ultrasoft peudpotentials (USPP) [279, 283].

The key advantage of the USPP approach is that the necessary energy cutoff for transition metals is reduced by a factor of 2-4, effectively reducing the basis set size[*] [212]. Instead of representing the full valence wave function by plane waves, only a small portion of the wave function is calculated; allowing the plane wave energy cutoff to be reduced substantially. Pseudopotentials that require high cutoff energies are said to be hard, while a more computationally efficient pseudopotentials with low cutoff energies are soft, hence the naming of the USPP approach.

The PAW method originally introduced by Blochl [282], was introduced to avoid some of the disadvantages in USPPs. It is generally accepted that a well-constructed USPPs and the PAW method produce results of identical accuracy and are in good agreement with full-electron calculations [251]. However, the PAW method gives more

[*] A typical energy cutoff of 200 eV corresponds to a basis set with ~20,000 plane wave functions [195]

reliable results than the former in calculations involving transition metals with strong magnetic moments [277].

2.11 Quantum Mechanics Calculation Packages

Because of the significant number of simulation packages available for first principle calculations, it is quite impossible and unnecessary to summarise all the codes and their distinctions. The codes given below are therefore not a complete listing and encompass only DFT based software, where they can be differentiated by the basis sets utilised.

Examples of the plane-wave scheme used in electronic structure calculation software include, but not limited to, VASP [211, 212, 279], CASTEP [275], ABINIT [284], QUANTUM-ESPRESSO [285] and CPMD [286] packages. Software programs such as WIEN2K [287] employ the computationally-demanding all-electron approach. In contrast, the programs DMOL3 [288], SIESTA [289], ONETEP [290] and CONQUEST ([291-293] and references therein) utilise the less costly numerical basis sets and linear-scaling algorithms. The Gaussian basis set is employed in GAMESS [294], CRYSTAL [295], and GAUSSIAN [296] simulation packages, whereas the approach of using transport basis sets in DFT calculations is adopted in the software packages SMEAGOL and WANNIER-TRANSPORT. While most of these computational packages would be suitable to examine the systems studied in this thesis, VASP was chosen to be consistent with our previous calculations of ZnO surfaces and their interactions with other gases.

Chapter 3

Computational Methodology and Surface Models

3.1 VASP: Introduction and General DFT Setup

All the calculations were performed within the framework of density functional theory (DFT) using the Vienna *ab-initio* simulation package (VASP) [211, 212, 279]. VASP is a program capable of performing quantum mechanical calculations using pseudopotentials with a plane wave basis set; concepts that have been explained in detail in Chapter 02 (Section **2.9**). The interaction between ions and electrons is described by either the projector-augmented wave (PAW) method or by Vanderbilt's ultrasoft pseudopotentials (USPP). VASP is used to perform a variety of *ab-initio* calculations such as static (single point) and relaxation (geometry optimisation).

As the computational set up may have multiple combinations of different parameters, the choice of an electronic structure method can have significant impact on the numerical accuracy, *i.e.* density functional, pseudopotentials, Fast Fourier Transform

(FFT) grid, **k**-point mesh, energy cutoff, to name just a few. Where not otherwise specified, our DFT calculations have been performed using the Vanderbilt US pseudopotentials [283]. The Generalised Gradient Approximation (GGA) with the functional of Perdew and Wang (PW91) was used [227]. Our calculations have also included *spin-polarisation*. In this study, a plane wave pseudopotential cutoff energy of 400 eV is adopted for the energy calculations. The **PREC**-tag in a VASP input file determines this energy cutoff and the density of the FFT mesh size of a system. For **PREC=ACCURATE**, the energy cutoff for the system represented here is set to a maximum value of 400 eV, where the wrap around errors are eliminated if the FFT meshes are sufficiently large [297]. The Monkhorst-Pack [274] **k**-point mesh sizes employed in this study will be presented later in Section **3.4.3**. The type of properties calculated using VASP of the adsorbate-substrate systems are described in this chapter.

3.2 Computational Methods

The energy of a system varies according to its structural configuration, which can be represented by different electronic states on the *potential energy surface* (PES) as shown in Figure **3.1**. They are minima, transition states and higher order saddle point structures.

Once the Kohn-Sham equations have been solved for a large number of nuclear geometries consisting of multiple electronic states, the PES is known. Mapping a complete PES for systems containing more than four atoms is virtually impossible; however, it is possible to obtain useful information from parts of a PES. For instance, by starting with different initial geometries it is possible to find multiple minimum energy arrangements of an adsorbate-substrate system that correspond to unique adsorption geometries.

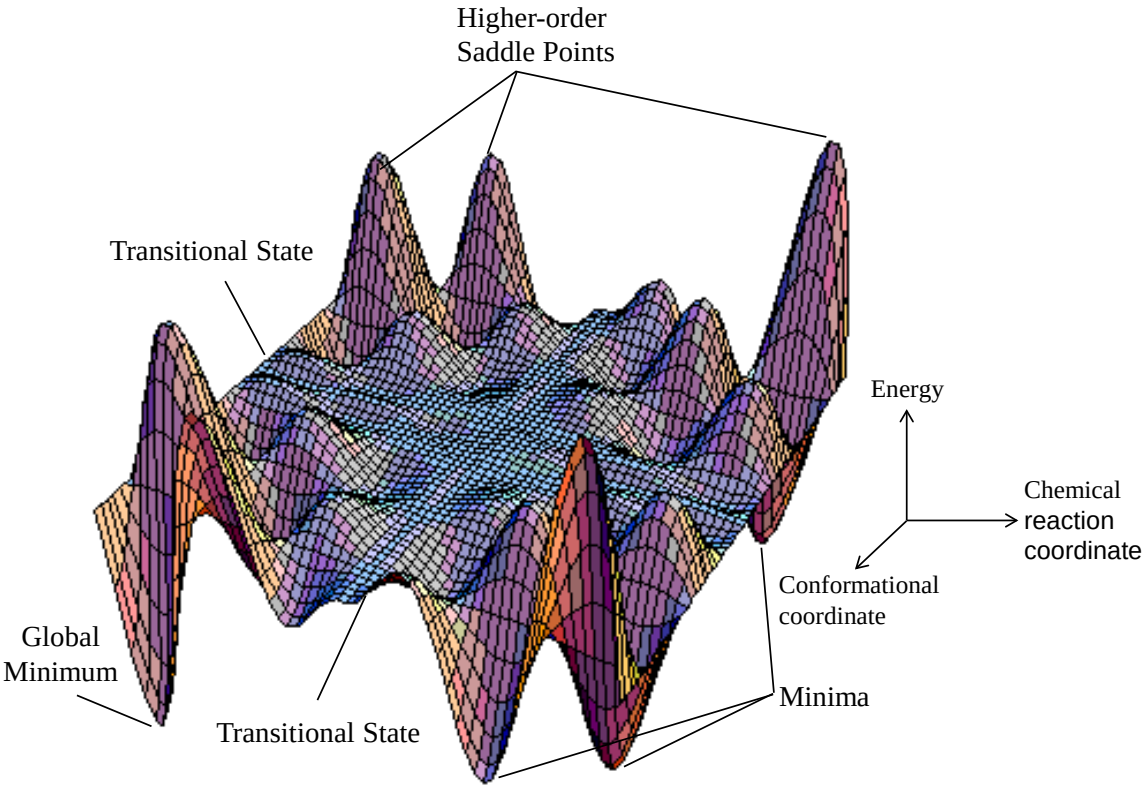

Figure 3.1 Schematic representation of a potential energy surface (PES) showing minima, transition states and higher-order saddle points.

3.2.1 Energy Minimisation

The DFT geometry optimisation method minimises the total energy of a system as a function of the ion configuration and the electron density. In this method, small adjustments are made to the location of ions to find the new position that is lower in energy than the previous one. This process is repeated (and the total energy recalculated) until a stationary point is found.

Commonly used electronic optimisation algorithms (defined by the **IALGO** tag in VASP) are the block-Davidson scheme [298, 299] and the residual minimisation - direct inversion in the iterative subspace scheme (RMM-DIIS) [300, 301]. Geometry optimisation schemes available in VASP include the quasi-Newton algorithm or the *conjugate gradient* method (**IBRION = 2**), of which the latter is employed in this study

and which uses energy-based optimisers to determine the minimum energy states [302]. In VASP the **POTIM** parameter specifies the size of the ionic relaxation trial steps in the geometry optimisation calculations, where a smaller value generally provides a more accurate relaxation. We use a **POTIM** step size of 0.1 Å.

3.3 Calculated Properties

Once the optimised stable structures are obtained, the position of atoms (*e.g.* bond distances and angles) of a system, as well as other electronic properties can be determined and examined. These are described in the following sub-sections.

3.3.1 Binding Energies

The *binding energy* (BE) for a geometrically optimised minimum energy structure can be calculated to determine the adsorption stability of an adsorbed species on a surface, including an estimation of the strength of the bonds formed between the adsorbate and the surface. For a system consisting of only one adsorbed molecule, the BE is calculated as follows:

$$BE = E_{(ads/subs)} - (E_{adsorbate} + E_{substrate}) \quad \textbf{(3.1)}$$

where $E_{ads/subS}$ is the total energy of the minimised adsorbate/ZnO system; $E_{adsorbate}$ is the total energy of the free molecule; and $E_{substrate}$ is the total energy of the relaxed ZnO surface.

For an optimised adsorbate/ZnO system consisting of two molecules, the binding energy per molecule can be determined by using two approaches. The first approach considers the binding energy of a molecule on the ZnO substrate which already has an

adsorbed species (referred to as sequential adsorption), and the second approach considers the binding energy of the two molecules adsorbed on to the ZnO substrate at the same time (referred to as co-adsorption). The BE for a sequential adsorption is calculated as:

$$BE_{seq-} = E_{ads1,2/sub} - (E_{ads2} + E_{ads1/sub}) \quad \textbf{(3.2)}$$

where $E_{ads1,2/sub}$ is the total energy of the geometry optimised system with two molecules; E_{ads2} is the total energy of the free molecule; and $E_{ads1/sub}$ is the total energy of the pre-adsorbed molecule on the ZnO surface. Next, the BE value for co-adsorption (per molecule) is calculated as follows:

$$BE_{co-} = \frac{E_{ads1,2/sub} - (E_{ads1} + E_{ads2} + E_{sub})}{2} \quad \textbf{(3.3)}$$

where $E_{ads1,2/sub}$ is the total energy of the geometry optimised system with two molecules; E_{ads1} and E_{ads2} are the total energy of the free molecules; and E_{sub} is the total energy of the relaxed ZnO surface.

3.3.2 Structural Geometry: Molecular and Surface Configurations

The formation of a bond between an adsorbate and surface can be inferred by the adsorption geometry (together with the calculated BE). The presence of additional bond(s), such as hydrogen bonds can also be determined. Specifically, the distance between the closest adsorbate and substrate atoms can give an indication whether the adsorbate is physisorbed or chemisorbed on the surface.

Surface reconstructions and relaxations caused by the adsorbate-substrate interaction can also be calculated for the systems studied. Surface reconstruction is the movement of surface atoms along the *x*- and *y*- directions (*i.e*. in the plane of the surface), whereas surface relaxation is defined as movement of the surface atoms in the direction

perpendicular to the surface plane (*i.e*. *z*-direction). Adsorbate-induced surface reconstruction and relaxations are calculated by measuring the change in the position of the substrate surface atoms with adsorbate present, relative to the relaxed clean surface atom positions.

3.3.3 Vibrational Frequencies

Vibrational frequency calculations using DFT methods not only provide information about the vibrational properties of the adsorbed system, but also determine the type of stationary point on the potential energy surface. The procedure for vibrational frequency calculations using VASP is based on diagonalisation of a finite difference construction of the Hessian (second derivative) matrix, where we use a displacement of 0.015 Å (as defined by the **POTIM** tag in VASP). In other words, the calculation is only valid when the first derivatives of the energy with respect to the atomic positions are zero [297, 303]. A stable structure is identified when there are no calculated *imaginary frequencies*, a metastable structure (transition state) contains one imaginary frequency and an unstable structure two or more imaginary frequencies. The changes in the magnitude of the calculated vibrational frequency values of an adsorbate-substrate system, relative to the isolated molecule, can be described as being *red* shifted (to a lower frequency) or *blue* shifted (to a higher frequency) [304]. The visualisation tool wxDragon is used to identify the different types (*e.g*. stretches, bends, twists, etc.) of vibrational modes calculated for the systems in this study [305].

3.3.4 Planar Averaged Charge Density Difference and Electron Localisation Functions

The ground state electron density of a material as determined by DFT, provides information about the charge distribution in a system. A planar averaged charge density calculation is useful for determining the redistribution of charge after adsorption, and specifically the magnitude of charge accumulation or depletion at a particular location in the material. Such information can provide an insight into the spatial charge redistribution and bonding between the gas species and the ZnO surface. The charge density difference is defined as the difference between the electron density of the adsorbed system and those of the relaxed clean surface and a free (isolated) adsorbate molecule. The colouring scheme used in the charge density difference plots (presented in later chapters) is as follows; “red” denotes charge accumulation, while “blue” indicates charge depletion.

The *electron localisation function* (ELF) in DFT calculations, formulated by Savin *et al*. [306], is a simplified representation of the electron density distribution that can be computed from the outer valence shell [307, 308]. An ELF plot is useful for showing the extent of electron localisation in the surrounding space of a reference electron, at a given point and with the same spin. The ELF has values that lie between 0 and 1 and describes the degree of localisation; 1 corresponds to perfect localisation, 0.5 corresponds to electron-gas-like pair probability, and ELF close to zero corresponds to delocalisation. The characterization of chemical bonds using ELF calculations is generally qualitative rather than quantitative, and an ELF plot can indicate the type of bonding between atoms as being covalent or ionic in nature [308]. Bonding electron pairs are represented by a region of high ELF along the bond path, whereas a low ELF value in between the core attractors (or atoms) represents non-bonding electron pairs [308].

The charge density and ELF in this study are calculated using VASP and are plotted using the VASP data viewer [309], by taking slices through the adsorbate and substrate along different directions.

3.3.5 Bader Analysis

There are numerous schemes proposed for determining the partial charges on atoms. The correct assignment of charges to individual atoms is important for calculating the transfer of charge in a system. Some common charge analysis methods include Mulliken [310], natural [311], Hirshfeld [312], Bader [313, 314], Merz-Kollman [315] and the ChelpG scheme [316]. The different charge analysis methods have their own benefits and drawbacks. The Mulliken population method, for example, is sensitive to the choice of basis set and may only produce acceptable results on certain materials [317]. The Bader analysis method, however, is preferred over other methods using DFT calculations because this analysis is based solely on the charge density [318]. Comparative studies of different charge analysis schemes have been conducted by the groups of Jacquemin [319] and Guerra [320].

In this study, the Bader charge analysis is employed to calculate the partial charges on the atoms within a system, and hence the transfer of charge between the adsorbate and surface. Bader charge analysis is a post-processing method that uses the calculated charge density to generate the net charge associated with each of the atoms in a system. By integrating the electronic density within the *Bader region* (where an atom's nucleus is located), and possibly taking into account the electronic charge in nearby regions that do not include a nucleus, the total charge on an atom can be calculated [318]. Because the analysis quantifies the charge on each atom, the distribution of the total electronic charge in a system can be estimated by summing over the corresponding individual charges.

We employ the procedure described by Henkelman *et al*. [318] to calculate the Bader charge of individual atoms in stable structures, relaxed clean surfaces, and isolated gas molecules studied in this thesis. Further information related to the description of the analysis parameters has been described by Henkelman and co-workers in Refs. [318, 321].

As mentioned above, the input for the Bader analysis is a charge density grid which gives the value of the electron density specified on a regular grid of points in space (the **CHGCAR** file in VASP). The spacing between the grid points should be fine enough for a sufficiently good approximation in the bonding region between atoms [318]. In the Bader algorithm, the accuracy of the charge values is dependent on the number of *grid points* used in the representation of electron density, which scales linearly with computational effort [318]. In general, an FFT mesh (see Chapter 2 Section **2.9**) with a finer grid is essential to obtain accurate total charge values, which is achieved by increasing the size of the NG(X,Y,Z)F grid within VASP.

We employed the PAW and GW potentials, in addition to the US pseudopotential (USPP), to validate our Bader charge calculations. This approach allows us to compare the Bader charge values of a system calculated using the three potentials with different grid sizes. Using each of the three potentials, we performed single-point calculations on stable structures with NG(X,Y,Z)F grid sizes of up to eight times the original mesh size. The USPP-calculated charge transfer values in this study were found to be identical to those calculated using the PAW and GW potentials, which validates the suitability of the USPP values and reduces the required computational effort. We also showed that finer mesh sizes were not required as the partial charge values were converged using the initial mesh size.

3.3.6 Work Function Changes

The work function describes the minimum amount of energy required to remove an electron from a surface. It can differ from one crystal plane to another, which means the work function of the $(10\bar{1}0)$ single crystal facet could be different to the $(2\bar{1}\bar{1}0)$ surface. Other factors influencing the work function change could be the adsorbate coverage, and the bonding configuration of the adsorbate on the surface. Work function calculations are a useful method for determining the direction of charge transfer after adsorption of a gas species on a ZnO surface. Experimental [322] and theoretical [323-325] methods can be employed to measure the work function of ZnO materials.

In this study, the work function is determined theoretically by using DFT calculations. The work function, ϕ, and work function change, $\Delta\phi$, were calculated for optimized minimum energy structures using the following equation:

$$\phi = E_{vac} - E_F \quad \textbf{(3.4)}$$

where E_{vac} is the electrostatic potential in the vacuum region of the supercell on the adsorbate side and E_F is the Fermi energy (*i.e.* the energy of the highest occupied quantum state in a system of *fermions* at absolute zero temperature). The workfunction change $\Delta\phi$ is calculated as follows:

$$\Delta\phi = \phi - \phi_c \quad \textbf{(3.5)}$$

where the ϕ_c is the workfunction of the clean ZnO surface.

3.3.7 Density of States

The total and partial density of states (DOS) of a system can be calculated by performing a static self-consistent calculation, which produces a **DOSCAR** file (in VASP). The total

DOS and partial DOS of an adsorbed system is often compared with that of a reference system (*e.g*. surface), to highlight the effect of the adsorbate on the electronic structure of the surface [297]. For the partial DOS calculation, the Wigner Seitz radius (**RWIGS**-tag as supplied by VASP) for each atomic species is specified, enabling the partial *spd*-orbital character of a DOS to be calculated. The band gap for a structure can be obtained by determining the difference in energy between the top of the valence band and the bottom of the conduction band in the DOS plot. It is well known that GGA based exchange-correlation functionals often underestimate the band gap in semiconductor materials, however, changes in the band gap can be useful for determining the effect of an adsorbate on the surface conductivity. Information on ZnO band gap underestimation and correction in GGA-based calculations can be found in articles published together by Lany and Zunger [326, 327].

An accurate DOS representation requires a fine **k**-point mesh size. This problem directly affects the calculated DOS patterns because an increased number of **k**-points are required to produce dense packing of data points in the Brillouin zone for a smoother interpolation line.

Our DOS are calculated by using the charge density profile (**CHGCAR** file in VASP) from the self-consistent (SC) calculation of a converged structure, to perform a non-SC calculation with high **k**-point density to produce the DOS (**DOSCAR** file in VASP). We tested and validated our DOS calculations by using different **k**-point mesh sizes, as well as using the band gap corrected GW algorithm. We calculated the total DOS and orbital resolved local DOS of the relaxed clean surfaces and the adsorbed structures. By comparing the DOS before and after adsorption, the effect the adsorbate has on the surface electronic structure can be determined. In addition, it can be determined whether the adsorbate increases or decreases the band gap which can be related to a change in conductivity after detection of the gas.

3.4. Modelling of ZnO with DFT

In this section, the procedure employed to represent the different ZnO nanostructure surfaces is presented. There are two theoretical approaches for simulating oxide surfaces [328]. The first approach is the cluster method, where a surface is represented by a group of atoms. The second, more popular method, uses two-dimensional slab models which are repeated under periodic boundary conditions (PBCs), and which is used in this study.

3.4.1 Bulk ZnO

As discussed in Chapter 1, wurtzite and zincblende are the common crystal structures of ZnO, while the rock-salt structure is rarely observed. Wurtzite ZnO can be represented by a hexagonal unit cell with two lattice parameters *a* and *c* (see Chapter 01 Figure **1.1**.). Within the unit cell, the structure comprises two interpenetrating hexagonal closed-packed (hcp) sublattices, each of which contains four atoms in a unit cell. Here, each atom of one kind is surrounded by four atoms of the other kind (*i.e.* tetrahedral coordination), in other words, each sublattice consists of one type of atom displaced from the other along the threefold *c*-axis by an amount $u = b/c$ (the internal parameter u is defined as the length of the bond parallel to the *c*-axis divided by the *c* lattice parameter). The u parameter has been defined as 0.375 for an ideal wurtzite structure [65]. However, as real wurtzite ZnO crystals tend to deviate from the ideal conformation, the u parameter may deviate from the ideal value, giving an increased value when the c/a ratio decreases.

The lattice parameters for wurtzite ZnO are commonly measured via x-ray diffraction (XRD) based methods experimentally and using first principles calculations theoretically [65]. The lattice parameters (a, b and c) of the wurtzite ZnO with an internal parameter (u), that have been reported previously and obtained experimentally and theoretically, are presented in Table **3.1**. From these studies, the a and c values range from

3.166 to 3.298 Å, and from 5.070 to 5.294 Å, respectively [329-331, 338]. The *c*/*a* ratio and the *u* parameter range from 1.572 to 1.617, and from 0.376 to 0.389, respectively [329, 332-334]. Our calculated lattice constants, using DFT [335], agree well with previously determined values. It has been noted that the presence of free charge, stress, temperature, impurities, oxygen vacancies and other point defects can be responsible for the increase of the lattice constants [65, 336] and may explain some of the small differences in the values obtained from theory and experiment.

Table 3.1 The lattice parameters calculated using DFT for wurtzite ZnO that are used in this study [335]. The values obtained from previous experimental and theoretical studies are also presented.

Ref	Year	Technique	Lattice Parameters		
			a	***c***	***u***
[337]	2013	QM (DFT-GGA)	3.276	5.278	-
		(DFT-PBESOL)	3.237	5.220	
[338]	2012	QM (DFT-GGA)[a]	3.2978	5.2843	0.3816
[330]	2012	QM (DFT-LDA+U)	3.166	5.070	0.380
[331]	2012	QM (DFT-GGA+U)	3.258	5.227	0.381
		(DFT-GGA)	3.295	5.294	0.381
[335]	**2010**	**QM (DFT-GGA)**	**3.268**	**5.233**	**0.3826**
[339]	2010	XRD-RSM[b]	3.254	5.206	-
[34]	2010	XRD	3.249	5.205	-
[340]	2009	QM (HF)	3.297	5.231	0.384
		(DFT-LDA)	3.200	5.125	0.382
		(DFT-PBE)	3.285	5.248	0.383
		(DFT-B3LYP)	3.285	5.261	0.382
		(DFT-PBE0)	3.263	5.195	0.383
[128]	2008	QM (DFT-B3LYP)	3.259	5.205	0.382
[139]	2008	QM (DFT-LDA)	3.20	5.16	-
[341]	2007	QM (DFT-GGA)	3.25	5.20	-
[342]	2006	QM (DFT-GGA)	3.1959	5.1585	-
[343]	2005	QM (DFT-GGA)	3.270	5.218	0.3822
		XRD	3.253	5.213[c]	0.3820
[344]	2003	QM (HF)	3.286	5.241	0.383
[345]	2003	QM (DFT)	3.270[c]	5.252[d]	0.383[d]
[333]	2003	QM (DFT-LDA)	3.193	5.163	0.3783
		(DFT-GGA)	3.282	5.291	0.3792

[346]	2002	MM	3.2518	5.1969	0.3806
[347]	2001	QM (HF) (B3LYP)	3.290 3.253	5.200 5.207	0.3858 0.3850
[348]	2000	QM (DFT-B3LYP)	3.249[d]	5.21[d]	0.383[d]
[332]	1999	QM (DFT-LDA)	3.175	5.121	0.376
[329]	1996	MM	3.2303	5.0767	0.389
[349]	1994	QM (HF)	3.290	5.241	0.386
[350]	1989	HRPD[e]	3.2501	5.2071	0.3817
[351]	1989	Neutron diffraction[f]	3.2417	5.1876	0.3819
[352]	1987	MM	3.250	5.207	-
[334]	1978	LEED	5.628	5.210	-

The lattice parameters obtained in this study are shown in **bold**.

[a] Available from the article's supporting information

[b] X-ray reciprocal space mapping (RSM)

[c] Calculated from strain-free wurtzite ZnO

[d] Calculated from other values given in paper (value not given directly)

[e] Neutron High Resolution Powder Diffractometer

[f] Measured at a temperature of 20 K

3.4.2 ZnO Non-polar Surfaces

For wurtzite ZnO, the non-polar $(10\bar{1}0)$ surface is the most stable surface and has been extensively studied (see for example [22]). Comparatively less attention has been focused on the non-polar $(2\bar{1}\bar{1}0)$ surface. The $(10\bar{1}0)$ and $(2\bar{1}\bar{1}0)$ surfaces are two of the most commonly found facets in ZnO nanostructures, where the later surface structure contains twice the number of Zn and O atoms per unit cell (Figures **3.2** and **3.3**).

3.4.3 Molecular and Surface Models with Periodic Boundary Conditions

In this section, the molecule and surface models employed in this work (using PBCs) are described.

The isolated gas molecules are modelled by placing an individual molecule in the middle of a 15 x 15 x 15 $Å^3$ cubic cell. A characteristic of insulators or semiconductors

(like ZnO) is that there is a gap at the Fermi level, where the bands above are empty, and bands below the gap are filled for all values of **k**. In this case, integrations over **k** handle these discontinuities by the broadening of energy-levels using the Gaussian function. The Gaussian smearing method (**ISMEAR-**tag) with a smearing width (**SIGMA-**tag) of 0.1 eV, and a cutoff energy of 400 eV were used. A single **k**-point (Γ point) was used for each of the isolated gas molecules

Both surfaces employed in this study corresponded to those cleaved from the bulk wurtzite structure of ZnO. It is important to choose the right number of surface layers and vacuum thickness, not only to ensure that the slab is sufficiently thick to contain bulk layers and to prevent interactions between adjacent slabs, but also to be computationally feasible. Our surfaces were modelled using eight-layered surface slabs with a vacuum spacer of ~15 Å (as shown in Figures **3.2** and **3.3**).

We used different sized supercells to represent different surface gas coverages. A supercell with vectors spanning m$\overrightarrow{a_1}$ and n$\overrightarrow{a_2}$ is named [mxn], in which the cell is represented by vector lengths of |m| and |n|, for instance, a [1x1] cell will have an apparent 1x1 periodicity. A larger surface cell, [1x2] cell, is a product of doubling of the [1x1] cell in the *y*-direction. In this study, [1x1], [1x2], and [2x2] supercells were used for both surfaces.

As the cell size increases, the doubling in real space of the supercells reduces the number of **k**-points (in the direction of the cell size increase) required to achieve convergence [251]. We tested the number of **k**-points for the $(10\bar{1}0)$ and $(2\bar{1}\bar{1}0)$ surface slabs and found that the total energy was converged to ~4 meV using a Monkhorst-Pack mesh of 7 x 7 x 1 and 5 x 5 x 1, respectively [335]. For the [1x2] cell, mesh sizes of 7 x 3 x 1 and 5 x 3 x 1 were used for the $(10\bar{1}0)$ and $(2\bar{1}\bar{1}0)$ surface slabs, respectively. For the [2x2] cell, a mesh size of 3 x 3 x 1 was used for both the $(10\bar{1}0)$ and $(2\bar{1}\bar{1}0)$ surface slabs.

For the stoichiometric and defect surface structures, the same **k**-point configuration was used.

The geometry optimisation and single point energy calculations were performed using the tetrahedron scheme (a method of dividing the Brillouin Zone into tetrahedra) [353], with a smearing width of 0.1 eV. For the geometry optimisation calculations, the bottom two layers were kept fixed, while the rest of the atomic positions were relaxed until the total energy was converged to 10^{-4} eV and the Hellmann-Feynman force on each relaxed atom was less than 0.02 eV/Å [335].

3.4.3.1 Stoichiometric Surfaces

For testing and evaluation of the slab thickness, in order to determine how many layers were required to converge the surface energy (SE), slabs of 8-42 layers (16-84 atoms) for the $(10\bar{1}0)$ surface and 4-20 layers (16-80 atoms) for the $(2\bar{1}\bar{1}0)$ surface were constructed. The bottom two layers were fixed for each surface during the geometry optimisation calculation, while the remaining surface atoms were allowed to relax in the *x*-, *y*- and *z*-directions. For both surfaces, eight ZnO layers were sufficient to describe the surfaces, as the bulk-like properties were reached after the fourth layer on both surfaces. Also, the increases from eight to a greater number of layers produced no significant changes in geometry of the topmost surface layers [335]. Comparison of our calculated SE values and the surface relaxation parameters with the literature are presented later in Section **3.5**. For the purpose of charge transfer calculations, the work function for the clean ZnO $(10\bar{1}0)$ and $(2\bar{1}\bar{1}0)$ surfaces were calculated to be 5.86 and 6.22 eV, respectively.

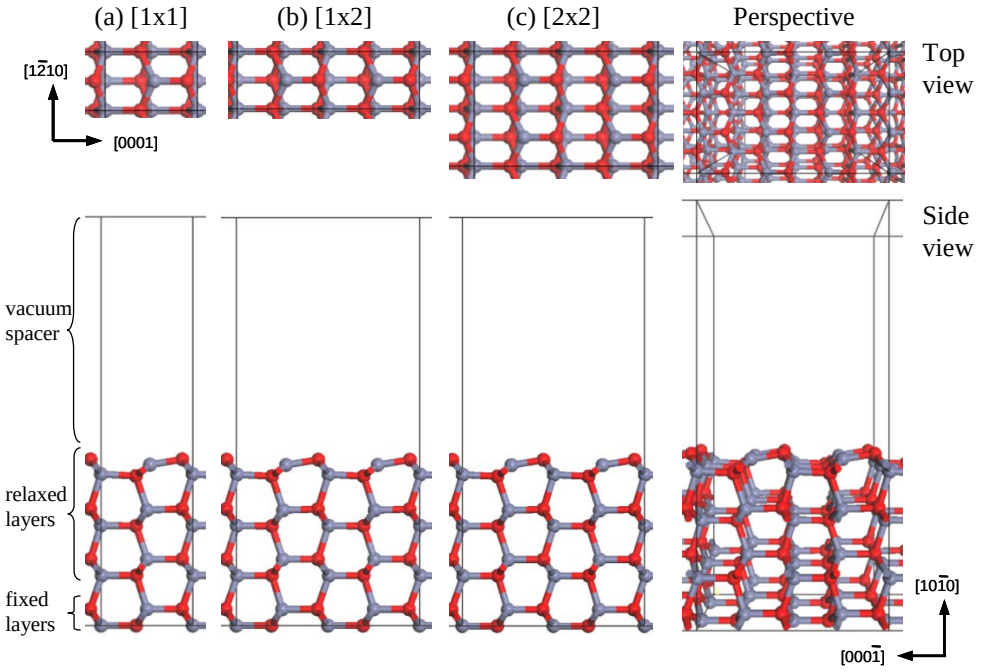

Figure 3.2 Top and side views of the relaxed ZnO(10$\bar{1}$0) surface models: (a) [1x1], (b) [1x2], (c) [2x2] supercells. A perspective view of the [2x2] surface is also shown (right). The grey spheres represent zinc atoms, and the red spheres represent oxygen atoms.

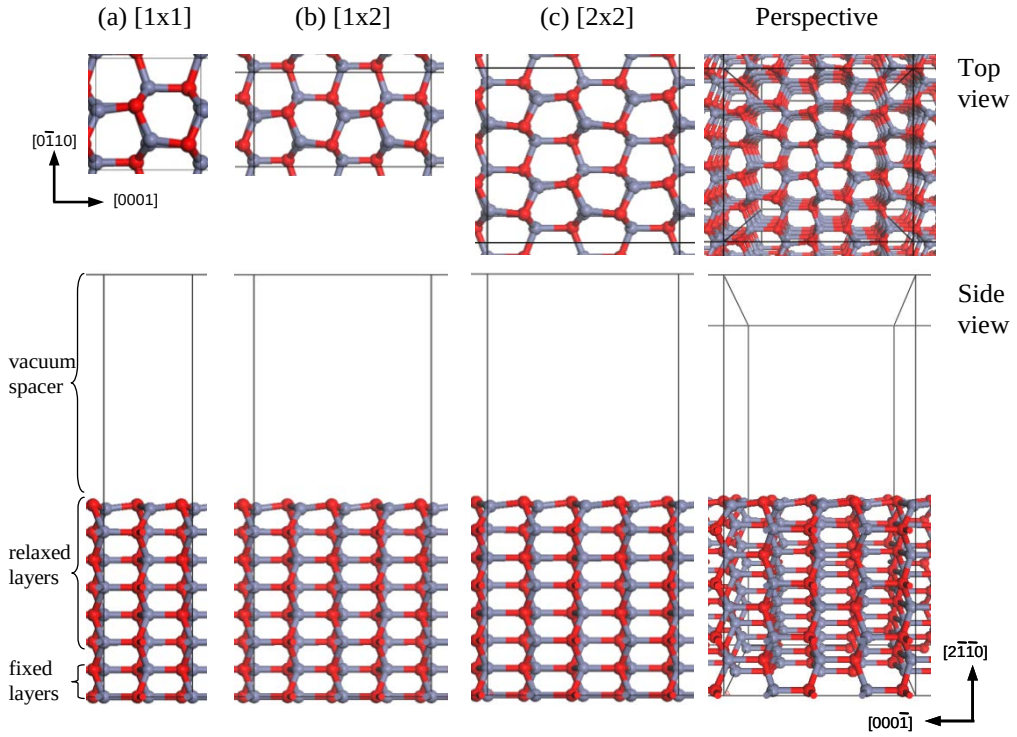

Figure 3.3 Top and side views of the relaxed ZnO(2$\bar{1}\bar{1}$0) surface models: (a) [1x1], (b) [1x2], (c) [2x2] supercells.

A diagram of the relaxed stoichiometric surfaces showing different calculated parameters is presented in Figure **3.4**. We present the geometric parameters that have been calculated for the two surfaces in Tables **3.2** and **3.3**, along with a summary of the values obtained from previous theoretical and experimental studies. The stoichiometrically balanced surfaces contain equal numbers of Zn and O atoms. The previous experimental studies of the two ZnO surfaces encompasses techniques such as low energy electron diffraction (LEED), X-ray diffraction (XRD), scanning tunnelling microscopy (STM), scanning tunnelling spectroscopy (STS), and low energy He^+ ion-scattering spectroscopy (LEIS). The theoretical studies have included quantum mechanical (QM) and molecular mechanics (MM) type calculations, using either periodic slab or cluster models.

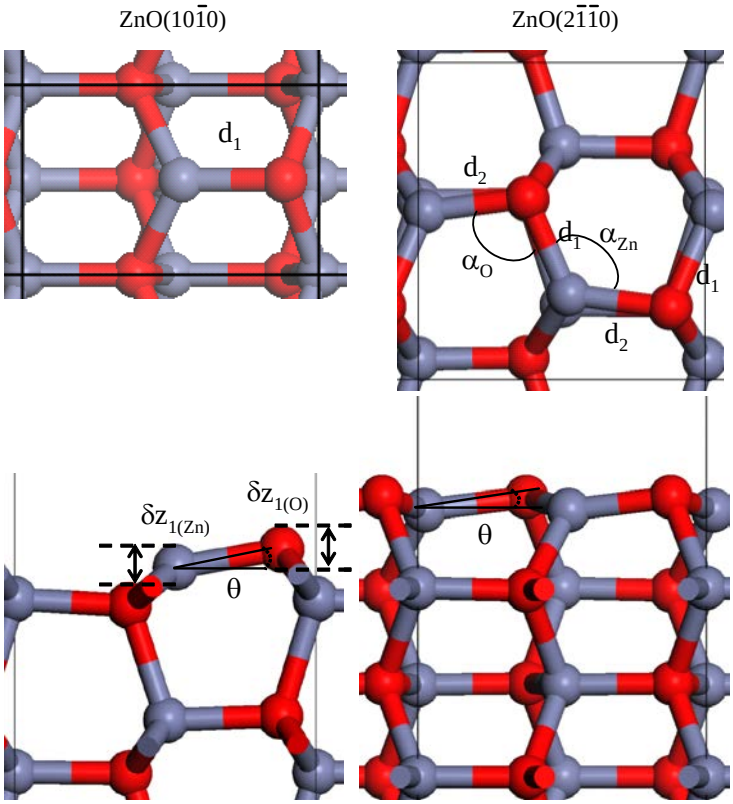

Figure 3.4 Parameters calculated for the relaxed ZnO (a) (10$\bar{1}$0) and (b) (2$\bar{1}\bar{1}$0) surfaces, showing top (above) and side (below) views.

3.4.3.2 Defect Surfaces

To create a surface containing oxygen vacancies (V_O), an oxygen atom was removed from the topmost surface layer of the supercell. These surfaces are referred to as ZnO($10\bar{1}0$)-V_O and ZnO($2\bar{1}\bar{1}0$)-V_O. By varying the supercell size ([1x1], [1x2] and [2x2]), the concentration of oxygen vacancies was varied from 100% to 25% for the ($10\bar{1}0$) surface, and from 50% to 12.5% for the ($2\bar{1}\bar{1}0$) surface. As with the stoichiometric surfaces, during geometry optimisation the bottom two surface layers were fixed. The relaxed ZnO ($10\bar{1}0$)-V_O and ($2\bar{1}\bar{1}0$)-V_O defect surfaces are presented in Figures **3.5** and **3.6**, respectively. We present the geometric parameters that have been calculated for the two surfaces in Tables **3.2** and **3.3**, along with a summary of the values obtained from previous theoretical and experimental studies.

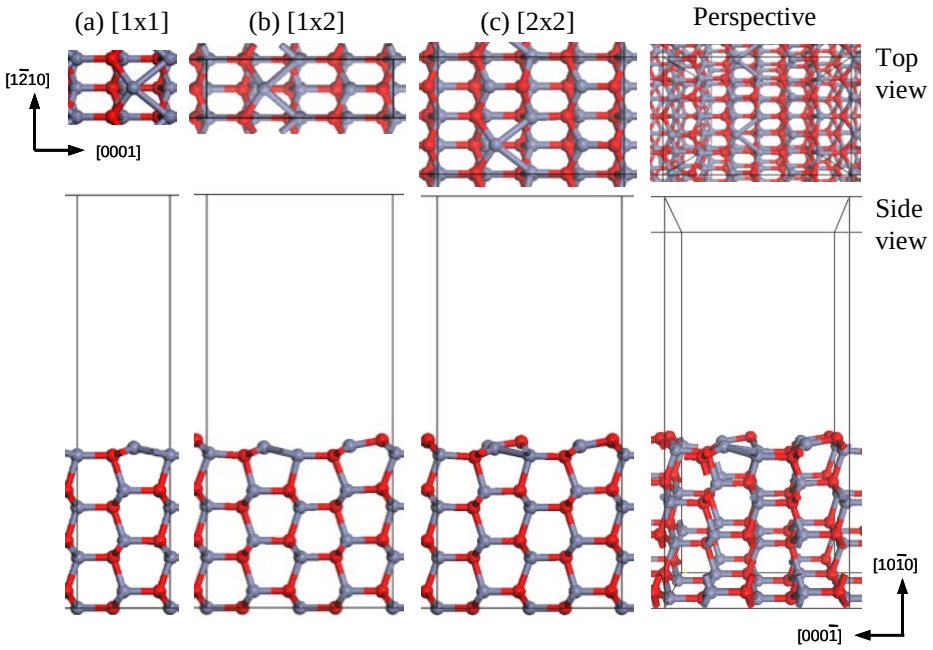

Figure 3.5 Top and side views of the relaxed ZnO($10\bar{1}0$)-V_O surface models, in orthographic and perspective representations: (a) [1x1], (b) [1x2], (c) [2x2] supercells.

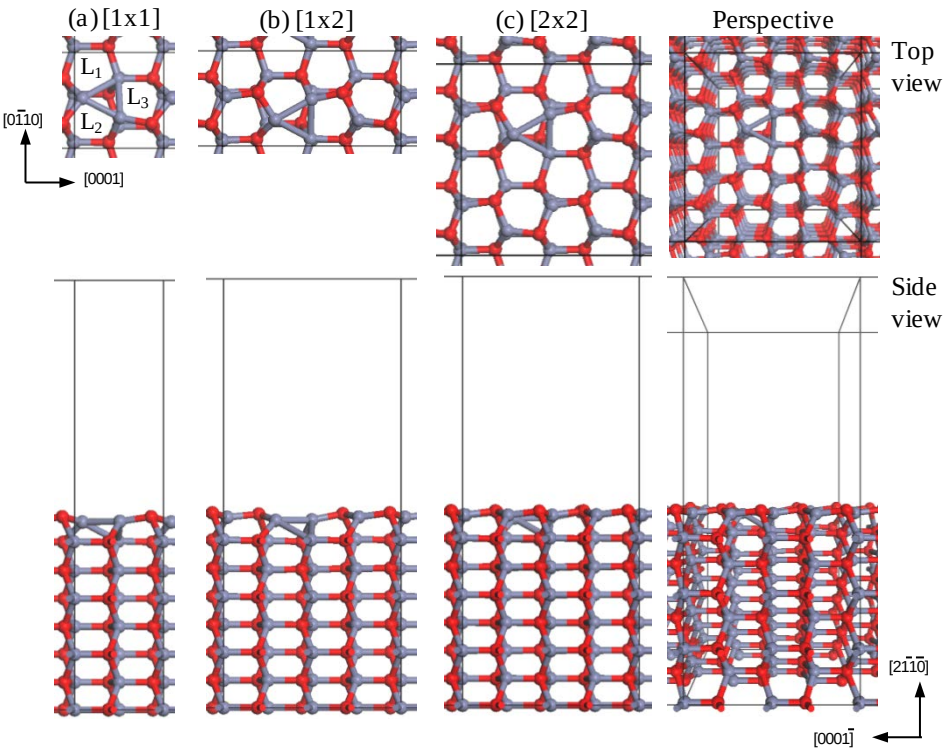

Figure 3.6 Top and side views of the relaxed ZnO($2\bar{1}\bar{1}0$)-V_O surface models, in orthographic and perspective representations: (a) [1x1], (b) [1x2], (c) [2x2] supercells.

3.5 Relaxed Clean ZnO ($10\bar{1}0$) and ($2\bar{1}\bar{1}0$) Surfaces

3.5.1 ZnO ($10\bar{1}0$) and ($2\bar{1}\bar{1}0$) Surface Energies

For the ($10\bar{1}0$) surface, the surface energy (SE) was found to be converged to at least 0.01 Jm^{-2} for a slab of 8 layers comprising 16 atoms, while for the ($2\bar{1}\bar{1}0$) surface the SE was also converged to at least 0.01 Jm^{-2} for an 8 layer slab comprising 32 atoms [335]. The relaxed surface energy values were 1.04 and 1.06 Jm^{-2} for the ($10\bar{1}0$) and ($2\bar{1}\bar{1}0$) surfaces, respectively, and are in general agreement with previous theoretical studies (see Tables **3.2** and **3.3**). The calculated SE values also agree with experiments which suggest that the ($10\bar{1}$ 0) surface is more stable than the ($2\bar{1}\bar{1}0$) surface. In particular, previous STM studies [354, 355] indicate that the ($2\bar{1}\bar{1}0$) surface contains a rougher morphology than the ($10\bar{1}0$)

surface, consistent with it being less stable. The SE values of our unrelaxed surfaces (1.20 and 1.19 Jm^{-2}, respectively) are as expected, higher than after relaxation.

Table 3.2 Calculated surface relaxation parameters and surface energy values for the ZnO($10\bar{1}0$) surface, obtained from experimental and theoretical studies.

Ref.	Yr.	Tech.	δ_{Z1} Zn (Å)	δ_{Z1} O (Å)	θ (°)	d (bulk) (Å)	Layers (atoms)	SE (unrelaxed) (Jm^{-2})
[356]	2013	GGA	-	-	10.2-10.6	1.846 1.849 1.852	12 16 20	-
[357]	2013	GGA	–0.129	–0.03	10.27	1.872	8	-
[337]	2013	GGA	–0.32	-	-	-	12	-
[338]	2012	GGA	–0.42	–0.08	10.4	1.883[a]	40 (80)	-
		HRTEM	–0.44 ±0.05	–0.07 ±0.07	9.4	1.893[a]	20exp	-
[331]	2012	GGA	–0.341	–0.003	10.3	~1.9(2.02)	12	0.833[b]
[335]	**2010**	**GGA**	**–0.21**	**0.1**	**9.56**	**1.864(2.001)**	**8**	**1.04(1.20)**
	2009	PBE0	–0.34 -	- 0.02 -	10.1 9.6		8 10	1.25 -
[341]	2007	GGA					8	1.025
[128]	2008	B3LYP	–0.21	0.002	-	1.861(1.979)	12	1.3
[358]	2007	HRTEM	[c]	[d]	-	-	-	-
[342]	2006	GGA	–0.33	–0.05	-	1.83(1.98)	12(24)	1.19
[343]	2005	GGA	-	-	9	1.849-1.859 (1.997-1.999)	8-24	1.6-2.4
[345]	2003	DFT	–0.285	–0.041	7.48	1.858(2.009)	6,8,10	-
[333]	2003	LDA	–0.36	–0.04	10.7	1.866	4-20 (8-40)	(1.15)
		GGA			10.1	1.862		(0.80)
[346]	2002	MM	–0.25	0.036	-	-	6	1.003
[347]	2001	HF	–0.147	–0.103	1.52	2.007	8[e]	1.86
		B3LYP	–0.171	–0.094	2.74	2.006		1.76
[348]	2000	B3LYP	–0.255	–0.083	5.20	1.905(1.998)	6[f](12)	-
[359]	2000	B3LYP	-	-	-	-	-	1.16
[360]	2000	XRD	–0.06 ± 0.02	–0.12 ± 0.06	–1.8 ± 2.3	1.9 ± 0.06	-	-
[332]	1999	LDA	–0.50	–0.13	-	[g]	9(18)	0.85 eV (1.22)
[361]	1998	LDA	-	-	7.35	1.844	4[f]	-
[329]	1996	MM	–0.22	–0.26	-	(1.948)	8	1.1

[362]	1994	LDA	–0.32	–0.2	3.6	1.83(1.99)	8	-
[349]	1994	HF	–0.23	–0.158	2.31	1.876(2.021)	4	0.72(0.92)
[352]	1987	MM	-	0.57[h]	-	-	8	-
[363]	1982	ARPES	–0.4 ± 0.05	-	-	-	-	-
[334]	1978	LEED	–0.45 ± 0.1	–0.05 ± 0.1	-	-	-	-
[364]	1977	LEED	–0.3 ± 0.1	–0.1 ± 0.05	-	-	-	-
[365]	1976	LEED	< 0.1	< 0.1	-	-	-	-
[366]	1976	LEED	–0.3	–0.1	-	-	-	-

References, Ref.; year, Yr.; techniques, Tech.; relaxation of Zn in *z*-direction, δ_{Z1} Zn; relaxation of O in *z*-direction, δ_{Z1} O; θ, and d, as shown in **Figure 3.4**; surface energy, SE.

[a] Values calculated based on a bulk value of 2.02 Å

[b] Contribution from the fixed bottom layers was subtracted

[c] –13% of $d_{(0110)}$.

[d] $-0.1d_{(0110)} + 0.1c$.

[e] Only relax in *x*-, *z*-directions.

[f] Full relaxation not allowed for all atoms.

[g] Bond contraction of 6%.

[h] Displacement of the top O layer relative to Zn.

List of acronyms:

GGA: DFT generalised gradient approximation

B3LYP: DFT Becke, three-parameter, Lee-Yang-Parr

HRTEM: high resolution transmission electron microscopy

LDA: DFT local density approximation

MM: molecular modelling

HF: Hartree Fock

XRD: X-ray diffraction

ARPES: angle-resolved photoelectron spectroscopy

LEED: low energy electron diffraction

Table 3.3 Calculated surface relaxation parameters and surface energy values for the ZnO($2\bar{1}\bar{1}0$) surface, obtained from experimental and theoretical studies.

Ref.	Yr.	Tech.	δ_{Z1} Zn (Å)	δ_{Z1} O (Å)	θ (°)	α_O	α_{Zn}	d_1 (bulk) (Å)	d_2 (bulk) (Å)	Layers (atoms)	SE (unrelaxed) (Jm^{-2})
[357]	2013	GGA	–0.085	–0.006	10.75	-	-	1.890	-	8	-
[331]	2012	GGA			7.7			~7%[a]	~7%[a]	12	0.881[b]
[335]	**2010**	**GGA**	**–0.14**	**0.10**	**7.45**	**105.2 (108)**	**119.7 (108)**	**1.901 (1.984)**	**1.882 (2.002)**	**8**	**1.06 (1.19)**
[128]	2008	B3LYP	–0.093	0.064	-	-	-	1.877 (1.979)	1.893	12	1.4
[139]	2008	LDA	-	-	-	100.3 92.4[c] (109.9)	117.1 118.0[c] (109.9)	1.857 1.881[c] (1.951)	1.843 1.853[c] (1.954)	12 - (48)	-
[341]	2007	GGA	-	-	-	-	-	-	-	8	1.122
[342]	2006	DFT	-	-	-	-	-	1.84	-	5 (20)	-
[343]	2005	GGA	-	-	8	-	-	-	-	4-16	1.8-2.0
[367]	2004	GGA	-	0.24	7.48	-	-	1.875[d]	1.886[d]	7(56)	-
[333]	2003	LDA	[e]	[e]	7.6	-	-	–5.8	-	4-8[f] (16-32)	(1.25)
		GGA			7.4			–6.4			(0.85)
[359]	2000	B3LYP	–0.03	0	-	-	-	-	-	4-7 (16-28)	2.05
[329]	1996	MM	–0.15	–0.17	-	-	-	(1.948)	-	8	1.2
[352]	1987	MM	-	0.54[g]	-	-	-	-	-	8	-
[364]	1977	LEED	0	0	-	-	-	-	-	-	-

References, Ref.; year, Yr.; techniques, Tech.; relaxation of Zn in *z*-direction, δ_{Z1} Zn; relaxation of O in *z*-direction, δ_{Z1} O; θ, α_O, α_{Zn}, d_1, d_2, as shown in **Figure 3.4**; surface energy, SE. Where it is not clear if d_1 or d_2 are presented, the value is listed as d_1.

[a] Bond lengths contraction of about 7% was reported

[b] Contribution from the fixed bottom layers was subtracted

[c] Measured from the optimised ZnO($2\bar{1}\bar{1}0$) nanowire outermost layer

[d] Measured against our measured bulk values of d_1 and d_2 of 1.984 and 2.002, respectively

[e] Atomic displacements are of same order of magnitude as the ZnO($2\bar{1}\bar{1}0$) surface

[f] Zn constrained in in-plane directions (results shown for converged 4-layer slab)

[g] Displacement of the top O layer relative of Zn

3.5.2 Geometry

The geometric parameters that have been calculated for the two surfaces are presented in Tables **3.2** and **3.3**, along with a summary of the values obtained from previous theoretical (including quantum mechanical (QM) and molecular mechanics (MM) methods) and experimental studies. It should be noted that while some surface geometry features have been described in previous studies, not all the same parameters are determined. In some studies different parameters to those shown in Figures **3.4** and **3.7** were calculated, however, as they give similar information we do not present them here. The previous experimental studies of the two ZnO surfaces have included techniques such as Low Energy Electron Diffraction (LEED), X-Ray Diffraction (XRD), Scanning Tunneling Microscopy (STM), Scanning Tunneling Spectroscopy (STS) and Low Energy He^+ Ion-scattering Spectroscopy (LEIS). The theoretical studies have included quantum mechanical (QM) and molecular mechanics (MM) type calculations, using either periodic slab or cluster models.

3.5.3 Geometrical Properties of ZnO $(10\bar{1}0)$ and $(10\bar{1}0)$-V_O

For the $(10\bar{1}0)$ surface, the atoms are arranged in rows comprising anion-cation dimers. Each surface atom is three-fold coordinated, bonding to one surface atom and two next layer atoms, all of the same atom type. Our results indicated that the surface Zn atom relaxes inwards by –0.21 Å, while the O atom expands by 0.1 Å, resulting in a buckling of the surface layer and tilting of the Zn-O bond by 9.56°. The ZnO bond length shortens by 0.14 Å to become 1.86 Å. For the defect surface in a [2x2] cell, the formation of an oxygen vacancy at the defect site can be characterised by two identical Zn-Zn bonds each measuring 2.55 Å. These changes are generally consistent with the majority of previous works which indicate a buckling of the surface atoms and shortening of the Zn-O surface

bond, though both Zn and O contract. The calculated values agree very well with the DFT study of Marana *et al*. [128], even though they used a larger surface slab. In contrast, the surface movements found by Jedrecy *et al.* [360], were considerably different to most previous results as they determined from grazing incidence XRD that the Zn atom only contracts by –0.06 ± 0.02 Å and the O atom by –0.12 ± 0.06 Å, indicating that Zn may sit higher on the surface. Due to their uncertainty in the O position, they were unable to provide the Zn-O distance or rotation angle with accuracy. They suggested that a better agreement with DFT calculations may be obtained by inclusion of GGA or fractional site occupancies; however, such recent studies (including our own) do not give better agreement with their results. The calculations of Nyberg *et al.* [329] also showed that O relaxed more than Zn, however, by only 0.04 Å. The magnitude of relaxation of both atoms, however, was greater than the XRD results and similar to the other studies. The early LEED studies were consistent with movements of the Zn and O surface atoms of <0.1 Å each [365] and up to 0.45±0.1 Å and -0.05±0.1 Å, although we note that the error bar is larger than the result itself [334, 364, 366].

For the defect $(10\bar{1}0)$ surface, the unpaired Zn surface atom further relaxed towards the bulk (as compared to the stoichiometric surface) by 0.13 to 0.16 Å, in agreement with previous calculations [134, 144, 368, 369], forming three Zn-Zn bonds with the two neighbouring Zn atoms of the second topmost layer. We have also observed a noticeable surface reconstruction, with the unpaired surface Zn atom moving towards the vacancy site (along the [0001] direction). For the [1x1] supercell, the Zn-Zn bonds were calculated to be 2.64, 2.64, and 3.27 Å. The Zn-Zn bond lengths in the [1x2] and [2x2] supercells, however, were calculated to be 2.55, 2.55, and 3.55 Å. The shorter Zn-Zn bonds in the larger cells show good agreement with the surface Zn-Zn bond lengths reported previously [134, 370], which tend to be highly metallic, as they are shorter than that of the hexagonal bulk Zn bonds (2.6 Å) [371].

3.5.4 Geometrical Properties of ZnO ($2\bar{1}\bar{1}0$) and ($2\bar{1}\bar{1}0$)-V_O

For the ($2\bar{1}\bar{1}0$) surface, the topmost surface atoms are again three-fold coordinated, however, each atom is bonded to two surface atoms and one next layer atom. Our calculations indicated that the surface Zn atom was found to contract by 0.14 Å, while the O atom expanded by 0.1 Å, resulting in a tilting of the Zn-O bond by 7.45°, and shortening to 1.90 Å. The O-Zn-O angle (α_{Zn}) increased from 108° to 119.7°, while the Zn-O-Zn angle (α_O) decreased from 108° to 105.2°.

For the defect surface, the formation of an oxygen vacancy at the [2x2] cell topmost layer can be characterised by three Zn-Zn bonds (L_1, L_2 and L_3) measuring 2.46, 2.62 and 2.61 Å, respectively. Our results are generally in agreement with previous studies, however, this surface has been far less studied than the ($10\bar{1}0$) surface. Our calculated parameters agree well with the DFT calculations by Marana *et al*. [128], however, they calculated a smaller contraction of the Zn atom of only –0.093 Å. The values of Wang *et al.* [139], agree very well with our calculations, however, they do not present values for $\delta z_{1(Zn)}$, $\delta z_{1(O)}$ and θ. Our results are consistent with those of Meyer and Marx [333], however, they only say that the atomic displacements of the surface atoms are of the same order of magnitude as the ($10\bar{1}0$) surface and do not give the exact values. The relaxation of the Zn atom in the calculations of Nyberg *et al.* [329] is almost the same as our value; however, they indicate that the O atom relaxes significantly more than found by us or any other study, and in fact slightly more than Zn. They mention that there are some lateral movements of the surface Zn and O atoms, but they do not give the tilting angle or rotation angles within the surface plane. The results of Wander *et al.* [348] indicate much smaller relaxations of the Zn and O atoms in the *z*-direction; however, their surface energy value is almost twice as large as other studies.

To date, the geometry of the ZnO($2\bar{1}\bar{1}0$) surface has only been characterised by a limited number of experimental techniques. The LEED experiments performed by Duke [364, 366] indicated that this surface is basically bulk terminated and does not reconstruct and surface deviations are smaller than 0.1 Å [365]. In our calculations, the smaller geometry changes after relaxation of the surface are in line with the smaller change in SE values after relaxation.

These relaxed surfaces are used in this thesis for the adsorption of different gas species, which are presented in the following chapters.

3.6 Adsorption of Molecules on ZnO Surfaces

The adsorption of gas molecules on the 8-layer ZnO surface models was examined for different adsorption sites and surface coverage. The calculated total energy for the relaxed gas and surface models are show in Table **3.4**. The molecule of interest (for example, ethanol) was placed on a relaxed surface (clean or V_O) ~3 Å above from the topmost layer, or on a relaxed surface which contains a pre-adsorbed molecule. Different adsorption sites can yield different adsorbed orientations depending on the type of molecules (and hence have different relative adsorption stability, provide an insight into the sensing performance of a gas sensor). Different orientations of the adsorbed molecule were also considered. Examples of the adsorption sites that are commonly found on both surfaces are shown in Figure **3.7**. The adsorbate may, however, reposition itself during geometry optimisation.

The interaction between adjacent adsorbate molecules can give rise to repulsive (or attractive) energies of interaction between the adsorbates, with a larger disparity in adsorption energy values between different supercell sizes (at very high coverage) [439]. The interaction energy was calculated as follows:

$$E_{int.} = E_{(2ethanol/ZnO)} - 2E_{(ethanol/ZnO)} \quad \textbf{(3.6)}$$

where $E_{(2ethanol/ZnO)}$ is the energy of two adsorbed molecules in a [1x2] cell and $E_{(ethanol/ZnO)}$ is the energy one ethanol adsorbed on ZnO in a [1x1] cell.

Table 3.4 Ultrasoft pseudopotential (USPP) calculated total energy values for the gas molecules and ZnO $(10\bar{1}0)$ and $(2\bar{1}\bar{1}0)$ surfaces (including V_O defect surfaces).

Material	**15 x 15 x 15 Å^3 cell (eV)**	**[1x1] cell (eV)**	**[1x2] cell (eV)**	**[2x2] cell (eV)**
N_2O	–21.30	-	-	-
Ethoxy	–41.36	-	-	-
Ethanol	–47.08	-	-	-
H_2O	–14.26	-	-	-
ZnO$(10\bar{1}0)$	-	–70.47	–140.86	–281.72
ZnO$(10\bar{1}0)$-V_O	-	–62.34	–132.82	–273.81
ZnO$(2\bar{1}\bar{1}0)$	-	–141.43	–282.78	–565.47
ZnO$(2\bar{1}\bar{1}0)$-V_O	-	–133.56	–274.98	–557.93

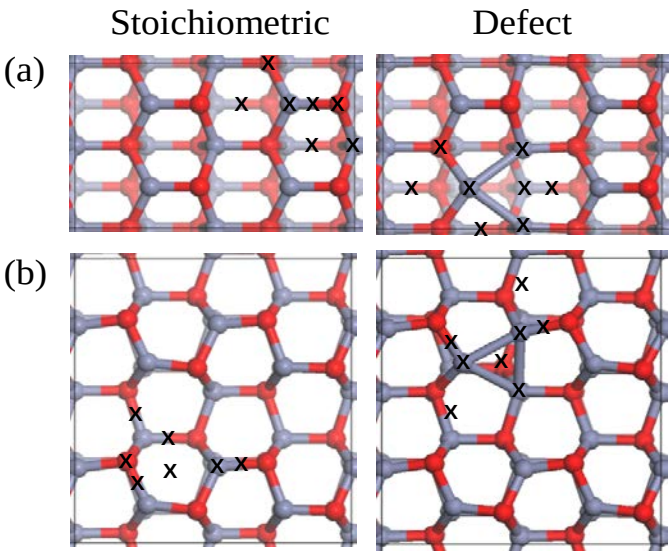

Figure 3.7 Top view of the surface models showing different adsorption sites (as indicated by "X") on the ZnO: (a) $(10\bar{1}0)$ and $(10\bar{1}0)$-V_O surfaces; (b) $(2\bar{1}\bar{1}0)$ and $(2\bar{1}\bar{1}0)$-V_O surfaces.

3.7 Surface Coverages

The surface coverages considered in this study are stated in terms of a fraction of monolayer (ML), in other words, the number of adsorbate molecules per surface unit cell (Figure **3.8**). One gas molecule in a ZnO($10\bar{1}0$)-[1x1] surface cell has a surface coverage of one monolayer (1 ML). Coverages of ½ ML and ¼ ML were modelled using [2x1] and [2x2] cells, respectively. To test for the formation of adsorbate superstructures, two molecules were adsorbed in a [2x1] cell which represents a single ML coverage.

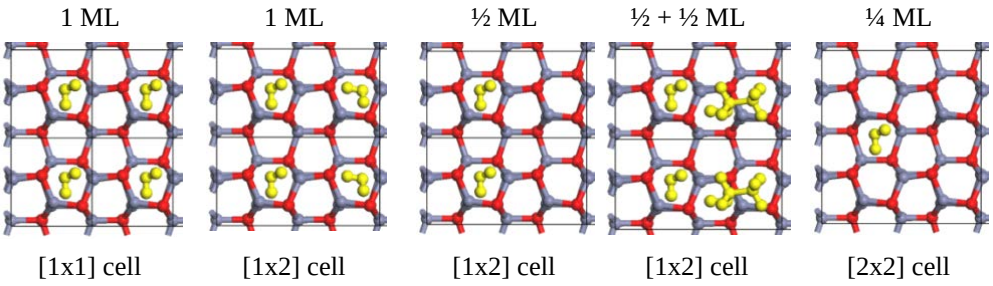

Figure 3.8 Top view of the relaxed stoichiometric ZnO($10\bar{1}0$) surface models showing adsorbate molecule(s) (in yellow) at different coverages.

3.8 Chapter Summary

In this chapter, the methods employed to model the gas molecules and surfaces have been described, together with the specific surface defects, gas coverages and adsorption sites that were examined.

For the ZnO surface models, the lattice parameters, slab thickness, vacuum thickness, **k**-point mesh size, cut off energy, and other parameters used in the DFT calculations were presented. An eight layer slab was used to model each surface, where the bottom two layers were fixed while relaxing all other atoms. Upon optimisation, the surface properties including work function and structural geometry were determined.

Previously reported experimental and theoretical findings of the ZnO $(10\bar{1}0)$ and $(2\bar{1}\bar{1}0)$ surface properties were also presented and compared. Overall, our data obtained for both surfaces are in line with the values reported in the literature. Our calculations showed that the topmost layer on the $(10\bar{1}0)$ and $(2\bar{1}\bar{1}0)$ surfaces became tilted after relaxation, as a result of the topmost Zn atom displacing inwards on the stoichiometric and defect surfaces. Noticeable surface reconstructions were found only at the defect site on both surfaces.

The surface unit cells used in this work ([1x1], [1x2] and [2x2] cells) enables different gas coverages (in terms of ML coverages), adsorption sites, as well as surface defect concentrations to be modelled.

For the adsorbate-surface calculations, a description of the properties that are presented in the following chapters was given, including: binding energy, work function, geometry, vibrational frequencies, charge density, electron localisation function, charge transfer, and density of states.

Chapter 4

N_2O Adsorption on ZnO $(10\bar{1}0)$ and $(2\bar{1}\bar{1}0)$ Surfaces

4.1 Background

Adsorption of the greenhouse pollutant gas nitrous oxide (N_2O) has been studied on surfaces of various materials, including TiO_2 [372-378], ZnO [45, 379-381], ZrO_2 [382], MgO [383], Cu_2O [384], GaN [159], Si [385], and a number of transition metals [386-395]. The gas molecule adsorbs not only in linear and bent molecular configurations [14], but also in dissociated configurations on defect-containing metal oxide surfaces. The decomposition of N_2O has been reported specifically on TiO_2 [376, 378], ZnO [381, 396], ZrO_2 [382], and Cu_2O [384] surfaces.

For metal oxide surfaces, Kanazawa and co-workers [380] tested 23 types of single oxides experimentally to determine which material gives the highest sensitivity to N_2O. The *n*-type oxides SnO_2, WO_3, In_2O_3 and ZnO were reported to have sensitivity values to 300 ppm N_2O of 1.66, 1.32, 1.21, and 1.05 at 450 °C. In the work by Quy *et al.* [45], a

quartz crystal microbalance gas sensor coated with ZnO nanorods was employed for the detection of various gases, including N_2O, NO_2, CO, CO_2, natural gas (CH_4), and liquefied petroleum gas (C_3H_8, C_4H_{10}). The thermal decomposition of N_2O over ZnO powder between 725 K and 825 K was investigated by Zemva *et al*. [379] using kinetic isotope methods. The activation energy was found to be 120 ± 4 kJ/mol [379]. The adsorption energies calculated for the adsorption of N_2O on the TiO_2 and ZnO surfaces reveal that the gas molecule physisorbs and chemisorbs on these surfaces [378, 396]. Using a DFT approach the possible decomposition of N_2O on the TiO_2(110) surface has been examined [373]. It was found that dissociation is not favourable on the stoichiometric surface; however, decomposition is possible with the presence of oxygen bridging vacancies [384]. A recent DFT study by Kaewruksa *et al*. [396] revealed the structural and electronic parameters of N_2O and other gases (including CO/N_2O coadsorption) on the graphene-like ZnO nanosheet; only one adsorption configuration of N_2O on the nanosheet was, however, reported.

Although extensive studies of N_2O on different materials have been reported in the literature, the adsorption mechanism of the gas molecule on single crystalline ZnO surfaces remains unclear. Moreover, theoretical studies performed on the adsorption of N_2O are limited and it appears to have only been studied on one particular ZnO nanomaterial [396]. In this chapter, the adsorption of N_2O on the ZnO $(10\bar{1}0)$ and $(2\bar{1}\bar{1}0)$ surfaces is examined using DFT calculations. The most stable adsorption structures, their binding energy, work function change, optimised adsorption geometry, vibrational frequencies, and charge density are presented. The outcomes of this chapter have been published in the journal of Materials Chemistry and Physics [335].

4.2 Results and Discussion

The relaxed clean ZnO $(10\bar{1}0)$ and $(2\bar{1}\bar{1}0)$ surfaces described in Chapter 3 are used as surface models for the adsorption of N_2O.

4.2.1 Binding Energy

N_2O was found to adsorb on both surfaces in multiple stable configurations. Table **4.1** shows the calculated BE values for these structures.

On $(10\bar{1}0)$, four minimum energy structures were found at the monolayer coverage. Although structure 1 has the strongest binding energy, the value of –0.11 eV indicates that the adsorption is very weak. The weakest adsorbate (structure 4) has a binding energy of only –0.02 eV, which indicates an extremely weak physisorption which is likely to be easily reversible and possibly represents a meta-stable structure.

Table 4.1 Calculated parameters for minimum energy structures of N_2O adsorbed on the ZnO $(10\bar{1}0)$ and $(2\bar{1}\bar{1}0)$ surfaces at one monolayer coverage.

Surf.	Struct.	BE (eV)	ΔΦ (eV)	N_2O-ZnO	d(ads-sub) (Å)	d⊥(ads-sub) (Å)	d(N-N-O) (Å)	∠ NNO	∠ NNO⊥
$(10\bar{1}0)$	**1**	–0.11	–0.58	NN**O**-**Zn**O	2.66	2.17	1.14, 1.21	178.7	27.8
	2	–0.06	–0.65	**N**NO-**Zn**O	2.53	2.27	1.14, 1.20	179.8	36.5
	3	–0.05	–0.06	NN**O**-**Zn**O	3.51	2.68	1.14, 1.20	179.3	27.3
	4	–0.02	–0.12	NN**O**-**Zn**O	3.63	3.13	1.14, 1.20	179.4	42.9
$(2\bar{1}\bar{1}0)$	**1**	–0.25	–0.76	**N**NO-**Zn**O	2.36	1.79	1.14 , 1.20	179.6	9.8
	2	–0.16	–0.76	**N**NO-**Zn**O	2.39	2.01	1.14 , 1.20	179.7	35.7
	3	–0.11	–0.31	N_2**O**-**Zn**O	2.67	2.39	1.14 , 1.20	179.6	31.4
	4	–0.11	–0.43	N_2**O**-**Zn**O	2.99	2.62	1.14 , 1.20	179.9	16.2
	5	–0.09	–0.32	N_2**O**-**Zn**O	2.77	2.52	1.14 , 1.20	179.8	22.7

Binding energy of N_2O/ZnO $(10\bar{1}0)$ or $(2\bar{1}\bar{1}0)$, **BE**; work function change, **ΔΦ**; in bold type, the specific atom on the adsorbate and substrate that are closest together, **(N_2O-ZnO)**; shortest distance between adsorbate and substrate, ***d*(ads-sub)**; perpendicular height of adsorbate above the top ZnO surface layer, ***d*⊥(ads-sub)**; N-N and N-O bond distances of N_2O after adsorption on the surface, ***d*(N-N-O)**; N_2O bond angle after adsorption on the surface, **∠NNO**; angle between the plane of the top surface layer and the molecule axis, **∠NNO⊥**.

For N_2O adsorbed on the ZnO$(2\bar{1}\bar{1}0)$ surface, five minimum energy structures were found, with the most stable having a binding energy of –0.25 eV. The binding energy of the other stable structures ranged from –0.16 to –0.09 eV. Again, these values indicate weak binding of N_2O on the surface, however, adsorption on this surface is stronger than on ZnO$(10\bar{1}0)$. These weak binding energies are consistent with a previous study by Kanazawa *et al.* [380] that examined the gas sensing response of N_2O adsorption on 23 different metal oxide surfaces and reported a relatively low surface sensitivity value for

ZnO, suggesting weak adsorbate-substrate interactions between N_2O and the metal oxide surfaces.

Weak binding energies of N_2O on the TiO_2 (110) and (101) surfaces were also observed. Binding energies of –0.12 and –0.18 eV were calculated for N_2O binding to the (110) surface via the O or N atom [373]. Similarly, weak binding energies of –0.13 and –0.17 eV were calculated for N_2O binding to the (101) surface [378]. Our previous studies of NO_x (x = 1,2) compounds adsorbing on the $(10\bar{1}0)$ and $(2\bar{1}\bar{1}0)$ surfaces also indicate weak binding with values of –0.31 and –0.25 eV for the adsorption of NO_2 and NO, respectively, on ZnO$(10\bar{1}0)$ (using the same computational method) [324, 325]. Additionally, the theoretical study of N_2O adsorption on the graphene-like ZnO nanosheet by Kaewruksa *et al*. [396] reported a BE value of –0.12 eV. Adsorption of N_2O, however, still appears to be generally weak. Although plane wave DFT methods have been used to investigate weak interactions of adsorbates on different ZnO surfaces [389, 397], the nature of the interaction of N_2O with ZnO surfaces is unclear. For this reason, the transfer of charge for the N_2O/ZnO $(10\bar{1}0)$ and $(2\bar{1}\bar{1}0)$ interactions have been calculated and will be discussed in Section **4.2.5**.

At the 1 ML N_2O coverage we are modelling, it could be expected there would be an interaction between adjacent molecules on the surface. We calculated the interaction energy (equation **3.6**) between adjacent molecules using the same computational parameters to be –0.01 and –0.02 eV for the $(10\bar{1}0)$ and $(2\bar{1}\bar{1}0)$ surfaces, respectively. These values correspond to approximately 11% and 9% of the BE values for the two surfaces. While not very high, such an interaction between the molecules likely reduces the interaction of the adsorbate with the surface, hence contributing to the weak BE values. One would expect that at lower coverages, where the N_2O-N_2O interaction is weaker the binding to the surface would be stronger.

4.2.2 Work Function Change

The calculated change in work function ($\Delta\Phi$) values of the minimum energy structures are shown in Table **4.1**. The most stable structure on the $(10\bar{1}0)$ surface showed a decrease in the work function value of 0.58 eV. The other 3 minimum energy structures also showed a decrease in work function values of 0.65, 0.06, and 0.12 eV, respectively. On the $(2\bar{1}\bar{1}0)$ surface, a negative work function change is also calculated with the most stable structure showing a decrease of 0.76 eV. The other minimum energy structures show decreases of between 0.31 to 0.76 eV. The decrease in work function after N_2O adsorption on both surfaces indicates that N_2O is behaving as an electropositive adsorbate, donating electrons to the surface. The magnitude of the $\Delta\Phi$ values tends to increase with increasing binding energy, corresponding with a greater charge transfer for the more stable structures. In addition, when N_2O bonds via the N atom to the surface, it causes a larger decrease in the work function, which indicates a larger donation of charge to the surface than when the O atom bonds to the surface, possibly due to the greater electronegativity of O than N.

The calculated work function changes, are however, in contrast to the experimental results obtained by Kanazawa *et al.* [380] which indicate that N_2O behaves as an electron accepting adsorbate on n-type oxides such as SnO_2, WO_3, In_2O_3 and ZnO, as exposure to the gas results in an increase in electrical resistance. However, the explanation offered for this resistance increase suggests it is the presence of both negatively charged adsorbed N_2O as well as negatively charged surface O species (resulting from N_2O decomposition) that give rise to the resistance increase. The amount of adsorbed O species from decomposition does vary with surface temperature and composition; however it is thought that the contribution of the adsorbed N_2O species to the resistance change is negligible. The decrease in work function values may warrant a more detailed experimental analysis to fully explain our calculations. It should be noted that a balance between a fast rate of

decomposition and a slow one is needed for an effective gas sensor material (although the adsorbate decomposition is not necessary for gas sensors). An intermediate rate of dissociation on the surface allows the N_2O to diffuse into the material before dissociation in order to maximise the surface area available for negatively charged O adsorption. Decomposition of N_2O is not observed in the 0K simulations; however including temperature effects may lead to dissociation of the molecule on the surface. Specifically, the presence of surface defects or impurities may also enhance the likelihood of dissociation, as was seen on the $Cu_2O(111)$ surface [384]. These factors are not within the scope of this study, however, but will be considered in future work.

4.2.3 Geometry

The optimized geometry of the minimum energy structures for N_2O adsorbed on the ZnO $(10\bar{1}0)$ and $(2\bar{1}\bar{1}0)$ surfaces are shown in Figures **4.1** and **4.2**, with the calculated structural parameters, including distances and angles, presented in Tables **4.1**, **4.2**, and **4.3**. As it is not always clear from the figures which atom on the adsorbate and substrate are closest together, this structural information has been included in Table **4.1**.

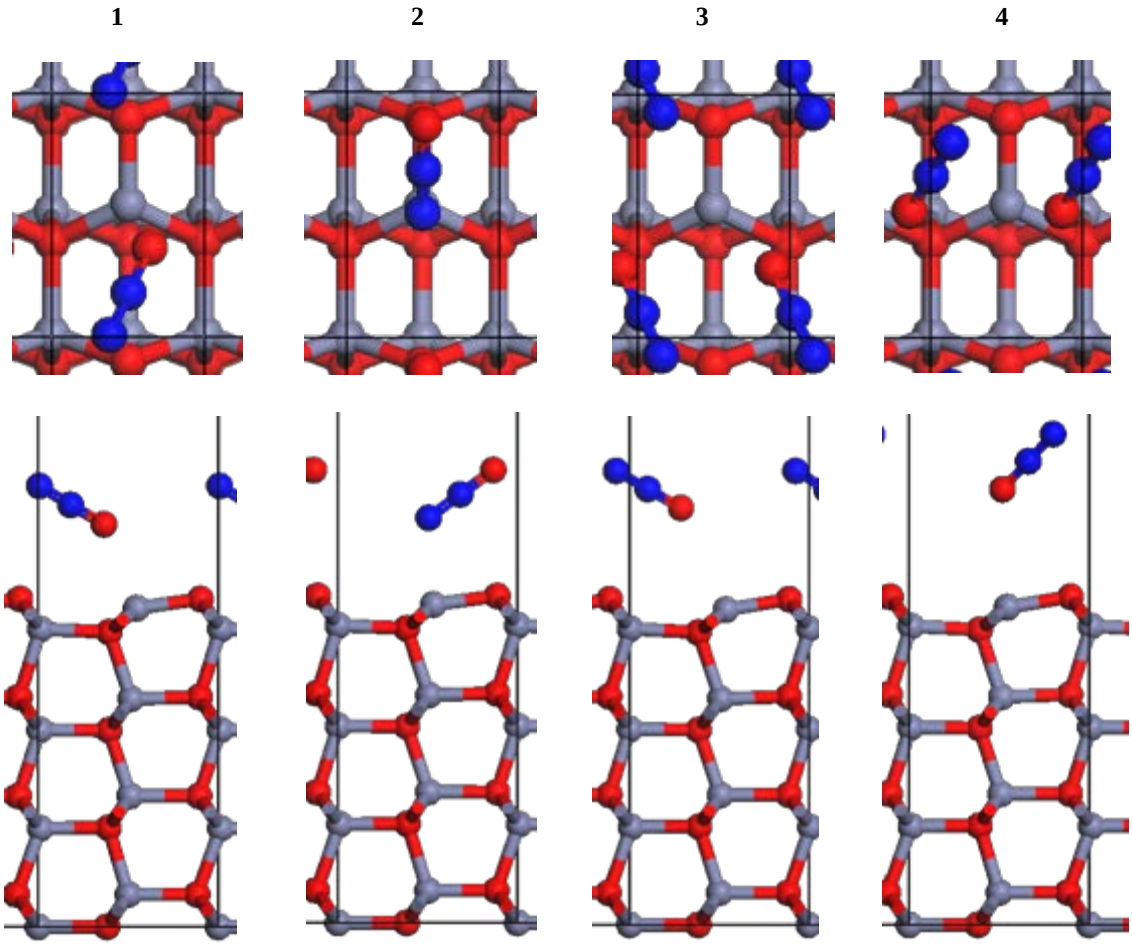

Figure 4.1 Top and side views (bottom) of the minimum energy structures of N_2O/ZnO$(10\bar{1}0)$.

On the $(10\bar{1}0)$ surface, N_2O generally prefers to adsorb to a surface Zn atom via the O atom on N_2O, as seen for structures 1, 3 and 4. For structure 2, N_2O also adsorbs to a surface Zn atom, but via the N atom instead. The shortest adsorbate-substrate distances calculated are 2.66, 2.53, 3.51 and 3.63 Å, respectively, while the perpendicular distance of N_2O above the surface is 2.17, 2.27, 2.68 and 3.13 Å, respectively. As can be seen the adsorbate-substrate bond lengths for structures 3 and 4 are quite large, indicating weaker interaction of N_2O with the surface, as reflected by the small BE values.

Following adsorption, the geometry of the N_2O molecule is little changed; the N-N bond length remains the same for all structures, the N-O bond length increases by no more than 0.8% and the N_2O bond angle only decreases by < 0.7% from its original linear

arrangement. The largest change in the N_2O geometry is observed for the most stable structure, which is not unexpected as there is a stronger interaction between the adsorbate and the substrate. However, overall, adsorption on the $(10\bar{1}0)$ surface has little, if any, effect on the geometry of the adsorbate molecule.

For all structures, N_2O prefers to adsorb to the surface in a tilted orientation relative to the surface plane. For structure 1, N_2O is tilted at an angle of 27.8° to the surface. For this structure, as well as structures 3, and 4, the N_2O molecule axis lies between 25° and 32° off the [0001] direction. For structure 2, the gas molecule axis (tilted at an angle of 36.5° on the surface) axis lies parallel to the Zn-O bond in the [0001] direction, as can be seen from the top view in Figure **4.1**.

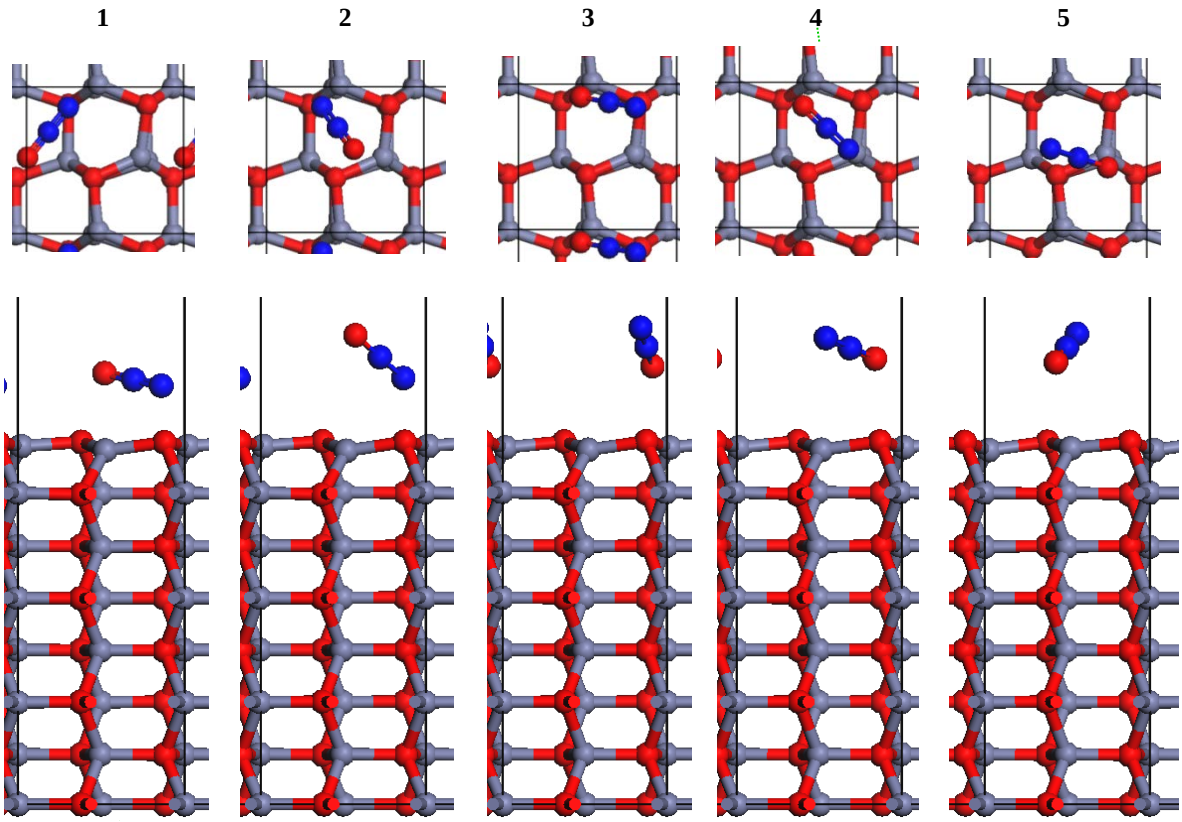

Figure 4.2 Top and side views of the minimum energy structures of $N_2O/ZnO(2\bar{1}\bar{1}0)$.

Of the five local minima found for adsorption of N_2O on ZnO$(2\bar{1}\bar{1}0)$, the two most stable structures showed N_2O bonding to a surface Zn atom via the N atom. For the other minima, N_2O also adsorbs on a surface Zn atom, but via the O atom. Such a preference was also seen on ZnO$(10\bar{1}0)$ and is similar to adsorption on other oxide surfaces such as $Cu_2O(111)$ where N_2O adsorbs to surface Cu atoms via the N atom [384].

In the most stable configuration on the $(2\bar{1}\bar{1}0)$ surface, N_2O adsorbs on the surface at a distance of 2.36 Å which is the shortest of all structures on either surface, and is consistent with the larger binding energy. Similarly, the N_2O molecule tends to sit closer to the surface, as measured by the perpendicular height above the topmost surface layer in the more stable configuration. Overall, the N_2O geometry is little changed upon adsorption, with a largest decrease in the bond angle of only ~ 0.2%, similar to the $(10\bar{1}0)$ surface. N_2O also adsorbs at an angle to the $(2\bar{1}\bar{1}0)$ surface, being closer to a parallel arrangement for the most stable structure, to possibly increase the interaction with the surface.

Adsorption of N_2O on both surfaces was found to cause some surface relaxations (movements in the *z*-directions) as well as an adsorbate-induced reconstruction (movements in the *x*-, *y*- directions) of the surface. A negative relaxation value indicates a contraction of the layer towards the bulk, while a positive value indicates an expansion. The movements were calculated relative to the relaxed stoichiometric surface geometry. These calculated values are shown in Table **4.2**.

Table 4.2 Magnitude of relaxation/reconstruction (Å) of the top three surface layers of the ZnO $(10\bar{1}0)$ and $(2\bar{1}\bar{1}0)$ surfaces after adsorption of N_2O.

Surf.	Struct.	Layer 1			Layer 2			Layer 3		
		δ_{x1}	δ_{y1}	δ_{z1}	δ_{x1}	δ_{y1}	δ_{z1}	δ_{x1}	δ_{y1}	δ_{z1}
$(10\bar{1}0)$	1	–0.02	**0.24**	**–0.16**	–0.02	0.07	**0.17**	–0.02	0.08	0.03
		–0.02	0.10	0.11	–0.02	0.07	0.09	–0.02	0.07	0.08
	2	–0.04	**0.17**	**–0.17**	–0.03	0.01	**0.16**	–0.03	0.03	0.03
		–0.03	0.03	0.08	–0.03	0.00	0.08	–0.03	0.01	0.07
	3	–0.03	**0.19**	**–0.19**	–0.03	0.01	**0.20**	–0.03	0.03	0.03
		–0.03	0.03	0.12	–0.03	0.00	0.09	–0.03	0.02	0.10
	4	0.02	**0.24**	**–0.19**	0.02	0.06	**0.20**	0.00	0.07	0.03
		0.02	0.08	0.12	0.02	0.05	0.10	0.00	0.06	0.10
$(2\bar{1}\bar{1}0)$	1	0.13	0.10	–0.05	0.00	–0.02	0.10	–0.01	–0.03	0.04
		–0.24	0.12	**–0.19**	–0.04	–0.02	0.08	–0.02	–0.02	0.00
		0.01	–0.01	0.07	0.01	–0.01	0.08	0.01	–0.01	0.04
		–0.07	–0.01	0.08	–0.04	–0.01	0.04	–0.03	–0.01	0.04
	2	**0.20**	0.07	–0.05	0.06	–0.06	0.11	0.04	–0.05	0.05
		–0.15	0.09	**–0.20**	0.03	–0.05	0.12	0.03	–0.04	0.01
		0.08	–0.05	0.09	0.07	–0.04	0.09	0.05	–0.04	0.06
		0.02	–0.04	0.10	0.04	–0.05	0.04	0.02	–0.03	0.05
	3	**0.18**	0.09	–0.09	0.02	–0.04	0.12	0.00	–0.03	0.04
		–0.20	0.10	**–0.17**	–0.02	–0.04	0.12	–0.01	–0.03	0.02
		0.04	–0.04	0.10	0.02	–0.03	0.08	0.00	0.00	–0.01
		–0.02	–0.03	0.10	–0.01	–0.03	0.06	0.00	–0.02	0.04
	4	**0.19**	0.07	–0.09	0.03	–0.07	0.12	0.01	–0.05	0.05
		–0.18	0.07	**–0.17**	–0.01	–0.06	0.12	0.00	–0.05	0.02
		0.04	–0.07	0.10	0.03	–0.05	0.09	0.02	–0.04	0.06
		–0.02	–0.06	0.10	–0.01	–0.06	0.05	–0.01	–0.04	0.06
	5	**0.19**	0.13	**–0.18**	0.01	–0.03	0.10	0.00	–0.03	0.01
		–0.19	0.11	–0.12	–0.03	–0.02	0.10	–0.01	–0.03	0.03
		0.02	–0.02	0.08	0.01	–0.02	0.05	0.01	–0.02	0.05
		–0.05	–0.01	0.09	–0.03	–0.02	0.07	–0.02	–0.02	0.05

The blue and yellow shaded values represent Zn and O atoms, respectively. Bold number indicates a displacement of ≥ 0.15 Å

For the ZnO$(10\bar{1}0)$ surface, none of the Zn or O atoms in the third layer displaced more than 0.10 Å after adsorption of N_2O, indicating that the interaction with this surface layer is very weak. While the reconstructions were also minor for the second layer atoms,

the relaxations were larger, with both Zn and O atoms moving outwards by up to 0.20 and 0.10 Å, respectively, leading to an expansion of this layer. In the first layer, the movements were more significant than the other layers, reflecting the stronger interaction of N_2O with these atoms. In contrast to layer 2, the Zn atoms relaxed downwards (by up to 0.19 Å), while the O atoms relaxed outwards (by up to 0.12 Å), emphasising the tilt of the Zn-O surface bond. Surface reconstructions were also calculated for this layer, with the Zn atoms moving in the *y*-direction by up to 0.24 Å, leading to a small stretching of the Zn-O bond (d_1 in Table **4.3**).

Table 4.3 Calculated structural parameters of the ZnO $(10\bar{1}0)$ and $(2\bar{1}\bar{1}0)$ surfaces after adsorption.

Surf.	Struct.	d_1 (Å)	d_2 (Å)	α_{Zn} (°)	α_O (°)
$(10\bar{1}0)$	**1**	1.88	-	-	-
	2	1.88	-	-	-
	3	1.87	-	-	-
	4	1.87	-	-	-
$(2\bar{1}\bar{1}0)$	**1**	1.89	1.90	119.3	100.2
	2	1.89	1.90	117.9	100.0
	3	1.89	1.90	119.0	100.9
	4	1.89	1.90	118.4	100.7
	5	1.89	1.91	118.3	102.6

Surface ZnO bond lengths at the topmost layer, d_1 and d_2; Surface ZnO bond angles at the topmost layer, α_{Zn} and α_O; as illustrated in Figure **3.7**

For the ZnO$(2\bar{1}\bar{1}0)$ surface, the relaxations and reconstructions for the third surface layer atoms were minor ($\leq \pm$ 0.06 Å), indicating little interaction of the adsorbate with this layer. Some larger displacements were seen for the second topmost layer atoms, however, they were generally smaller than for the $(10\bar{1}0)$ surface and all were < 0.12 Å. The most noticeable movements were seen in the top layer. Here, the Zn atoms relaxed towards the

surface while the O atoms moved outwards, resulting in a further tilting of the Zn-O bonds to yield a buckled surface with O atoms located higher on the surface, similar to the $(10\bar{1}0)$ surface. The Zn-O bond lengths (d_1 and d_2) and the in-plane angles (α_{Zn} and α_O), as shown in Table **4.3**, are also little changed upon adsorption, consistent with the weak interaction with the surface.

4.2.4 Vibrational Frequencies

The calculated vibrational frequency values for the minimum energy structures of N_2O adsorbed on both surfaces, as well as those obtained for the isolated N_2O molecule are shown in Table **4.4**.

Table 4.4 Calculated vibrational frequencies (cm^{-1}) of N_2O adsorbed on the ZnO $(10\bar{1}0)$ and $(2\bar{1}\bar{1}0)$ surfaces. The experimental values reported by Hussain *et al.* [399] are compared.

Surf.	Struct.	υ(N-N)	Δ*v*(N-N)	υ(N-O)	Δ*v*(N-O)	δ_{NNO}	$(\Delta\delta_{NNO})$
N_2O	**calc. (exp.)**	2271 (2224)	-	1293 (1285)	-	578 (589)	-
$(10\bar{1}0)$	1	2285	(14)	1282	(–11)	575	(–3)
	2	2291	(20)	1304	(11)	581	(3)
	3	2278	(7)	1291	(–2)	578	(0)
	4	2279	(8)	1293	(0)	581	(3)
$(2\bar{1}\bar{1}0)$	1	2289	(18)	1308	(15)	571	(–7)
	2	2283	(12)	1304	(11)	574	(–4)
	3	2272	(1)	1280	(–13)	581	(3)
	4	2267	(–4)	1287	(–6)	576	(–2)
	5	2271	(0)	1282	(–11)	574	(–4)

For all N_2O/ZnO$(10\bar{1}0)$ structures, the υ(N-N) band is shifted to a higher energy (blue shift) after the molecule adsorbs on the surface, while two υ(N-O) values decrease (red shift), while structure 2 shows an increase of 11cm^{-1}. The bending mode is little changed (< 3 cm^{-1}) after adsorption. On the $(2\bar{1}\bar{1}0)$ surface, the υ(N-N) band is also generally blue shifted, while the υ(N-O) values decrease by less than 13 cm^{-1}, except for structures 1 and 2 which increase by less than 15 cm^{-1}. Again, the bending mode is changed by no more than 7 cm^{-1}. Overall, the υ(N-N) band is shifted the most by adsorption on the surface. In addition, when N_2O adsorbs on the surface via the N atom, the υ(N-N) band is blue shifted more than when N_2O adsorbs via the O atoms. Likewise, the υ(N-O) band is blue shifted when the N atom adsorbs to the surface, and red shifted when the adsorption occurs via the O atom. All these changes are minor, consistent with the weak BE values.

Previous high resolution electron energy loss spectroscopy (HREELS) studies of N_2O adsorption on Pt(111) [389], W(110) [387], and Ru(0001) [387, 398] surfaces also indicated a blue shift in the υ(N-N) stretching band which increased from 2224 cm^{-1} in the gas phase to 2290 cm^{-1} or more upon adsorption. No change in the υ(N-O) band was found [387, 389, 398]. On a reduced or oxidized pressed powder ZnO sample [399], infrared studies showed that N_2O adsorption caused an increase in the υ(N-N) of 13 cm^{-1} and a decrease in the υ(N-O) of 30 cm^{-1}, inferring bonding through the O atom. Our results are in general agreement with this study; however, Hussain *et al.* [399] did not consider single crystalline faces and were unable to identify the actual binding sites with the techniques they applied. From our calculated vibrational frequencies, it seems that there is no big difference between the two bonding configurations of N_2O on the surface, nor does the type of crystal face appear to alter the resulting bands. The large number of local minima found for these surfaces also suggests that N_2O may be adsorbed in multiple adsorption sites, leading to a spectrum comprising mixed surface species.

4.2.5 Charge Density, Electron Localisation Function and Transfer of Charge

Charge density difference plots of the most stable structures for N_2O adsorbed on both surfaces are presented in Figures **4.3** and **4.4**. The charge density difference, $\Delta\rho$, is calculated according to the following equation:

$$\Delta\rho = \rho(N_2O/ZnO) - \rho(ZnO) - \rho(N_2O)$$

where $\rho(N_2O/ZnO)$, $\rho(ZnO)$, and $\rho(N_2O)$ are the charge density of the adsorption system, the isolated clean surface and the isolated N_2O molecule, respectively, all at their relative positions in the adsorption system.

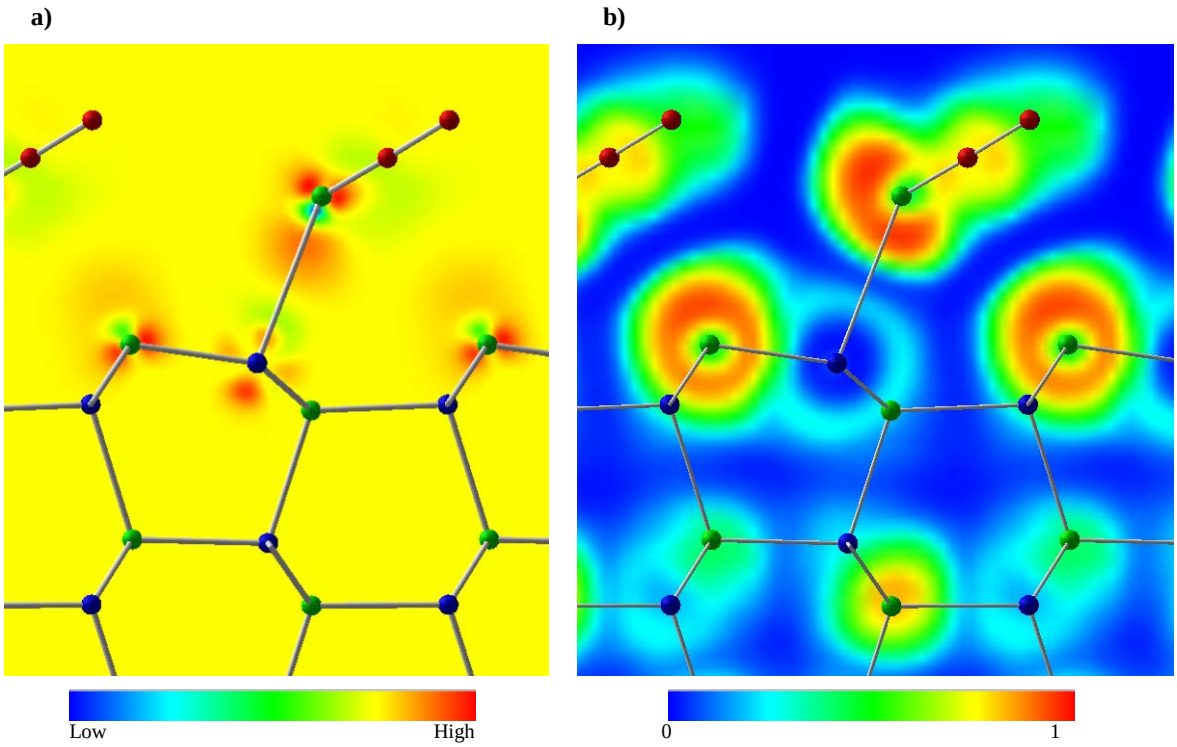

Figure 4.3 (a) Charge density difference and (b) electron localisation function slices of the most stable structure of $N_2O/ZnO(10\bar{1}0)$. Note the different colourings used here for the atoms (oxygen in green, nitrogen in red, and zinc in blue).

The slices are taken so that they lie in the plane that cuts the two atoms forming the shortest adsorbate-substrate distance (that is Zn-N for the $(10\bar{1}0)$ surface and Zn-O for the

$(2\bar{1}\bar{1}0)$ surface) as well as the adjacent surface O atom. It should be noted that the N_2O molecule lies out of the plane of the page so the slice does not cut the other adsorbate atoms.

On the $(10\bar{1}0)$ surface, some regions of charge accumulation and depletion can be seen after adsorption. A region of charge accumulation as well as depletion can be seen along the closest adsorbate-substrate atoms with the area of charge accumulation being located closer to the adsorbate atom, while the region of charge depletion is located closer to the substrate Zn atom. Going between these atoms, however, there is also a region of charge accumulation around the Zn atom and some depletion around the O atom. Such changes are only minor and consistent with the weak binding energies calculated for this structure.

The charge density changes located around the adjacent surface O atom indicate that the adsorbed N_2O interacts with this surface atom as well, and explains the relaxation of this atom after adsorption, as discussed in Section **4.2**. The regions of charge accumulation around this O atom tend to be directed along the ZnO bond, with a region of depletion being located perpendicular to this atom, pointing away from the surface. There is also a region of accumulation surrounding this atom which extends away from the surface region, but is weaker than the accumulation seen between the surface bonds.

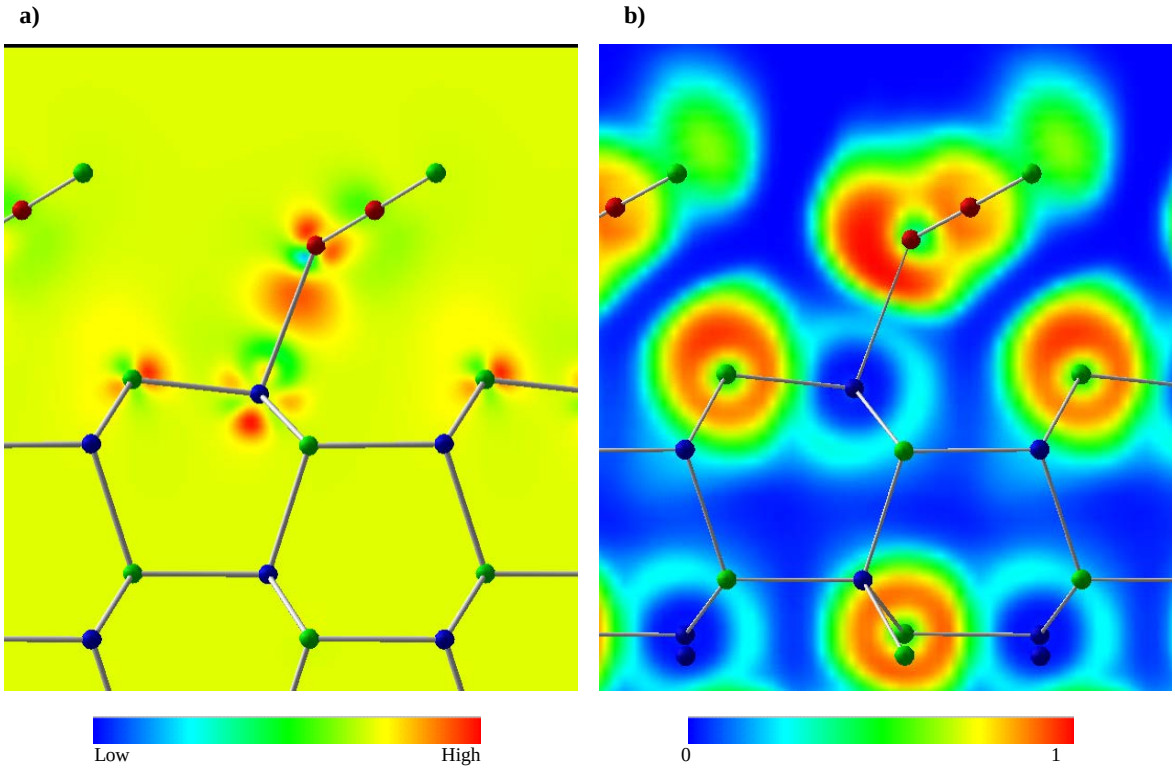

Figure 4.4 (a) Charge density difference and (b) electron localisation function slices of the most stable structure of N_2O/ZnO$(2\bar{1}\bar{1}0)$. Note the different colourings used here for the atoms (oxygen in green, nitrogen in red, and zinc in blue).

The charge density difference slice for the $(2\bar{1}\bar{1}0)$ surface is very similar to that of the $(10\bar{1}0)$ surface, even though it is the O atom that bonds to the surface instead of the N atom. Again, regions of charge accumulation and depletion seem to be located in similar regions on this surface, indicating the same type of interaction between the adsorbate and surface. The magnitude of the charge density changes, however, is larger on this surface, which explains the stronger binding energy of N_2O on this surface, also reflected by the shorter adsorbate-substrate distances. These changes on both surfaces reflect the polarization of the adsorbate electrons, which are attracted by the surface Zn cation. The larger reorganization is expected for the N-facing configurations due to the N-end of N_2O being more polarisable than the O-end.

Table 4.5 Bader charges of the most stable structures of N_2O adsorbed on the ZnO $(10\bar{1}0)$ and $(2\bar{1}\bar{1}0)$ surfaces; N_a= terminal N atom, N_b= middle N atom.

Atom	**N_2O**	**ZnO $(10\bar{1}0)$**	**N_2O/ZnO $(10\bar{1}0)$**	**Atom**	**ZnO$(2\bar{1}\bar{1}0)$**	**N_2O/ZnO $(2\bar{1}\bar{1}0)$**
N_a	0.20	-	0.24	N_a	-	0.19
N_b	0.13	-	0.12	N_b	-	0.11
O	–0.33	-	–0.38	O	-	–0.31
Zn1	**-**	**1.14**	**1.13**	**Zn1a, Zn1b**	**1.14, 1.14**	**1.13, 1.13**
Zn2	-	1.19	1.18	Zn2a, Zn2b	1.18, 1.18	1.19, 1.19
Zn3	-	1.19	1.19	Zn3a, Zn3b	1.19, 1.19	1.19, 1.19
Zn4	-	1.18	1.17	Zn4a, Zn4b	1.20, 1.20	1.19, 1.19
Zn5	-	1.20	1.18	Zn5a, Zn5b	1.19, 1.19	1.19, 1.19
Zn6	-	1.20	1.19	Zn6a, Zn6b	1.18, 1.18	1.18, 1.18
Zn7	-	1.18	1.19	Zn7a, Zn7b	1.18, 1.18	1.18, 1.18
Zn8	-	1.13	1.17	Zn8a, Zn8b	1.15, 1.15	1.18, 1.14
O1	**-**	**–1.14**	**–1.15**	**O1a, O1b**	**–1.14, –1.14**	**–1.15, –1.15**
O2	-	–1.18	–1.17	O2a, O2b	–1.18, –1.18	–1.18, –1.17
O3	-	–1.20	–1.18	O3a, O3b	–1.18, –1.18	–1.18, –1.19
O4	-	–1.18	–1.18	O4a, O4b	–1.20, –1.20	–1.19, –1.19
O5	-	–1.20	–1.18	O5a, O5b	–1.19, –1.19	–1.19, –1.19
O6	-	–1.19	–1.20	O6a, O6b	–1.19, –1.19	–1.19, –1.19
O7	-	–1.17	–1.19	O7a, O7b	–1.19, –1.19	–1.19, –1.18
O8	-	–1.15	–1.15	O8a, O8b	–1.13, –1.13	–1.15, –1.15

The Bader charges calculated for these systems are presented in Table **4.5**. For both surfaces, the charge on the atoms is little affected by the adsorbed N_2O. Likewise, the charges on the individual N_2O atoms are not significantly changed, however, on the $(10\bar{1}0)$ surface the N atom of N_2O redistributes charge to the adsorbate O atom while on the $(2\bar{1}\bar{1}0)$ surface, the redistribution of charge is in the opposite direction. These changes can be correlated to the arrangement of the adsorbed molecule on the surface, where the atom facing the surface gains charge. The calculated charge transfer, Δq, for each system (per molecule) is –0.01 *e* and –0.02 *e* for the $(10\bar{1}0)$ and $(2\bar{1}\bar{1}0)$ surfaces, respectively, indicating that N_2O behaves as a charge acceptor. Although we note that there is a discrepancy of the calculated work function change (Section **4.2.2**), the calculated Δq

values correspond with experimental findings that show the resistance of a ZnO powder sensor increases when exposed to N_2O gas [380]. This behaviour (*i.e.* electronegativity) is also in agreement with the charge transfer calculated for NO_2 adsorbed on a ZnO single walled nanotube using DFT [20, 135, 145]. The discrepancy with the calculated work function values warrants further investigation.

The electron localisation function (ELF) plots for N_2O adsorbed on these surfaces are also shown in Figures **4.3** and **4.4** and are taken through the same atoms as the charge density difference slices. The ELF can be particularly useful as high values (~ 0.8) can be interpreted as bonding and non-bonding electron pairs. On both surfaces an intermediate value (~ 0.65) of the ELF can be seen in the middle of the bond between the surface Zn and O atoms and is indicative of the covalent nature of the bonding in ZnO. The highest value of the ELF (~ 0.75) for both surfaces appears around the terminal O and N atoms of the N_2O molecule. This localisation becomes asymmetric on the atom that lies closest to the surface, with the region of highest localisation being oriented slightly away from the surface, indicating lone pairs on these atoms. The absence of high ELF values in between the N_2O and the surface reflects the lack of covalent bonding. Overall, the ELF is indicative of the weak binding energy values and small geometric changes seen after adsorption of N_2O on both surfaces. The charge difference therefore is generally confined to the admolecule and the closest surface atom, indicating that the major effect of adsorption is internal charge redistribution (with polarization of the adsorbate and the surface) rather than surface to adsorbate charge transfer.

It is to be expected that inclusion of defects or impurities will model more realistic surfaces, which may also show stronger interactions with the N_2O molecule. The calculations presented in this chapter provide a necessary reference for comparison with future studies which will examine gas adsorption on the defect surfaces.

4.3 Summary

N_2O adsorbs relatively weakly on the $(10\bar{1}0)$ and $(2\bar{1}\bar{1}0)$ surfaces, being more strongly bound to the $(2\bar{1}\bar{1}0)$ surface. Multiple surface species were found for both surfaces, with N_2O preferring to adsorb to surface Zn atoms. Adsorption via either the O or the N atom of N_2O was seen on both surfaces, being more stable on the $(10\bar{1}0)$ surface via O-facing configurations and on the $(2\bar{1}\bar{1}0)$ surface via N-facing configurations. The geometry of the N_2O molecule was little changed upon adsorption due to the weak interaction with the surface. It adsorbs in a tilted orientation on the surface, causing small surface relaxations and adsorbate-induced reconstructions. The interaction of N_2O with each surface mainly leads to charge polarization within the adsorbate molecule and the surface, resulting in a small transfer of charge from the surface to the adsorbate.

Chapter 5

Adsorption of Ethanol on the ZnO($10\bar{1}0$) Surface

5.1 Background

It is generally accepted that optimum gas sensing can be achieved at lower temperatures with nanostructure-based sensors, rather than thin film based sensors. Using ZnO nanostructure based sensors, a high sensitivity toward ethanol, with a quick response and recovery time has been demonstrated [47, 108, 400], with the increased response of the nanostructures to the gas, compared to the thin film, being attributed to their high surface area-to-volume ratio. While there are already theoretical [401] and experimental [402] studies that have investigated the interaction of ethanol with ZnO, the gas sensing mechanism for this system is still unclear. At elevated temperatures, ethanol dissociates to form acetaldehylde and adsorbed hydrogen species on ZnO surfaces. Kwak and Yong [402] used temperature-programmed desorption (TPD) experiments to determine the

desorption products from the reaction of ethanol with ZnO nanowires (having primarily ($10\bar{1}0$) crystal facets) at different temperatures and gas exposures. In their study they propose surface reactions for ethanol on the nanowires; the details of the specific surface reactions are however, not certain. The geometry of the adsorbed ethanol, the preferred adsorption sites and the associated electronic properties are also unknown. More recently, Yuan *et al*. [401] used DFT calculations to explore the gas-sensing mechanism of ethanol with the ZnO($10\bar{1}0$) surface at ¼ ML coverage. They showed that the ethanol O atom forms a bond to a surface Zn atom, with the distance between the ethanol hydroxyl H atom and a surface O atom indicating formation of a second interaction, namely a hydrogen bond. Their results also indicate that ethanol causes an increase in electronic conductivity after detection, in agreement with experiment. While these studies have provided important information to help understand the ethanol-ZnO interaction, a number of factors have not been determined, including the effect of different ethanol coverages and surface defects.

In this chapter, DFT calculations are used to examine adsorption of ethanol on one of the most common crystal faces found on the ZnO nanowires examined by Kwak and Yong [402] namely the ($10\bar{1}0$) facet. Some of the different factors that contribute to the sensing mechanism, such as the effect of gas coverage, the presence of surface oxygen vacancies and the possibility of the adsorbed ethanol forming superstructures are investigated. A better understanding of such factors in the gas-nanostructure sensing reactions will facilitate improvements in gas sensing device performance. The outcomes of this chapter resulted in the publication in the Journal of Physics: Condensed Matter [371].

5.2 Surface models

Three different sized supercell models were used in this study (see Chapter 3 Figure **3.3**), each containing eight layers with 16, 32 and 64 atoms for [1x1], [1x2] and [2x2] slabs of

ZnO($10\bar{1}0$), respectively. The defect surface, ($10\bar{1}0$)-V_O, was modelled by removing one of the topmost surface oxygen atoms (Figure **3.5**) to create an oxygen vacancy, V_O, yielding 3 defect concentrations of 100%, 50% and 25% for the [1x1], [2x1] and [2x2] supercells, respectively. Although these seem quite high, it enables us to explore different types of surface environments that may be present on the ZnO nanostructure surface for ethanol adsorption. The measured structural properties of the ($10\bar{1}0$) surface are shown in Figure **3.7**. Ethanol was initially positioned between 2.5 to 3 Å above the ZnO surface in different surface sites and initial orientations (see Figure **3.8a**). The [1x1], [1x2], and [2x2] supercells correspond to coverages of 1, ½ and ¼ monolayer (ML), respectively.

5.3 Results and Discussion

5.3.1 Binding Energy

The minimum energy structures for ethanol adsorbed on the ZnO($10\bar{1}0$) surface at 1, ½ and ¼ ML coverages are shown in Figure **5.1**, with the calculated binding energy (BE) values presented in Table **5.1**. Three minimum energy structures were found for each of the ethanol coverages examined. While Yuan *et al.* [401] suggested that more than one stable structure may exist at ¼ ML coverage, they only presented one structure. In this study, it is demonstrated that other stable structures do exist on the surface at this coverage.

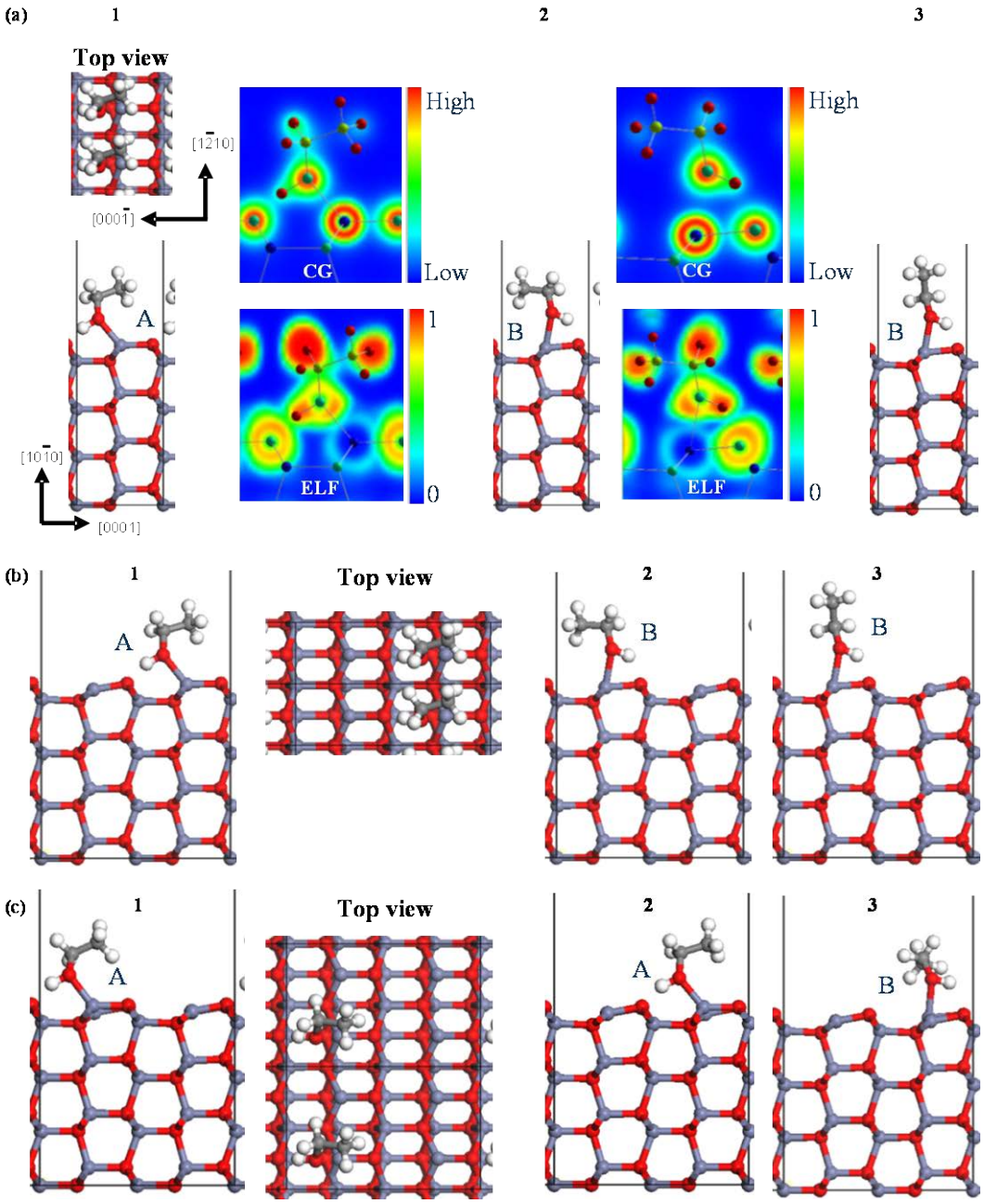

Figure 5.1 Minimum energy structures of ethanol/ZnO(10$\bar{1}$0) at: (a) 1, (b) ½ and (c) ¼ ML coverages. Charge density (CG) and electron localisation function (ELF) plots are shown for the 1 ML structures 1 and 2, which correspond to adsorption configurations Type A and B, respectively.

Table 5.1 Calculated binding energy and structural parameters for ethanol adsorbed on the ZnO($10\bar{1}0$) surface at the coverages indicated. Note that [1x1], [1x2] and [2 x 2] denote the size of the supercell used for the coverage intended.

Surf.	Struct.	Type	BE (eV)	d(O_{ads}-Zn_{sub}) (Å)	d⊥ (ads-sub) (Å)	d(O-H) (Å)	d(H_{ads}-O_{sub}) (Å)	∠O-H··O (°)	d_1 (Å)	θ (°)
Ethanol (exp)		-	-	-	-	0.97	-	-	-	-
Clean	1x1	-	-	-	-	-	-	-	1.86	9.5 9.3 9.4
1 ML [1x1]	1	A	–0.69	2.07	0.99	1.08	1.41	165.3	1.95	1.1
	2	B	–0.25	2.21	1.53	1.02	1.70	137.6	1.96	5.6
	3	B	–0.02	2.18	1.54	1.02	1.68	137.1	1.97	5.6
1 ML [1x2]	1_P	A A	–0.74 (–0.78)	2.07 2.07	1.03 1.03	1.08 1.08	1.42 1.42	165 165	1.95	1.1
	2_{AP}	A B	–0.41 (–0.11)	2.10 2.22	1.00 1.63	1.04 1.00	1.51 1.85	168 135	1.90 1.99	2.5 5.8
½ ML [1x2]	1	A	–0.71	2.08	1.09	1.04	1.54	161.0	1.90	1.5
	2	B	–0.35	2.18	1.61	1.01	1.77	133.3	1.96	4.3
	3	B	–0.09	2.15	1.57	1.01	1.72	134.7	1.97	4.3
¼ ML [2x2]	1	A	–1.08	2.06	1.17	1.04	1.57	159.7	1.90	0.5
	2	A	–1.06	2.04	1.11	1.04	1.54	158.6	1.89	0.6
	3	B	–0.68	2.14	1.76	1.00	1.94	125.0	1.95	5.0

Binding energy of ethanol adsorbed on the ZnO surfaces, **BE** (calculated sequential BEs for the superstructures are shown in brackets); distance between the O atom of ethanol and the closest Zn atom of ZnO, ***d*(O$_{ads}$-Zn$_{sub}$)**; perpendicular height of adsorbate above the top ZnO surface layer, ***d*⊥(ads-sub)**; the ethanol OH group bond length, ***d*(O-H)**; distance between hydrogen of the ethanol OH group and the surface oxygen atom, **d(H$_{ads}$-O$_{sub}$)**; bond angle of O-H···O between the OH group of ethanol and the surface oxygen atom (**∠O-H···O**); ZnO surface bond length, $\mathbf{d_1}$; Zn-O-Zn surface bond angle, **θ**.

At 1 ML coverage, the binding energy of structure 1 is −0.69 eV, which we classify as strongly physisorbed. The BE for structures 2 and 3 are weaker and consistent with physisorption. At ½ ML coverage, the BE values are stronger than at 1 ML, with the BE of structure 1 indicating it is chemisorbed (at −0.71 vs −0.69 eV), while structures 2 and 3 are physisorbed. At ¼ ML coverage, the BE of structures 1 and 2 are again stronger than at the higher coverages, indicating chemisorption, while we classify structure 3 as being strongly

physisorbed. The minimum energy structure found previously by Yuan *et al*. [401] at ¼ ML coverage was calculated to have a BE value of −1.18 eV, which compares well with our BE of −1.08 eV for the most stable structure we found at this coverage. The small difference between the two BE values may be attributed to the different computational approach employed, where Yuan *et al.* [401] used a numerical basis set and a smaller supercell with a slab comprising 4 layers (as opposed to our 8 layers).

Our results show that ethanol binds more strongly at the lower coverage indicating there may be an interaction between adjacent ethanol molecules at the higher coverage that reduces the interaction of ethanol with the surface. We calculated the interaction energy (equation **3.6**) between adjacent adsorbate molecules at 1 and ¼ ML coverages to be 73% and 9% (of the total BE), respectively, indicating that the cross interaction is very strong at the high coverage, while it is relatively minor at the lower coverage.

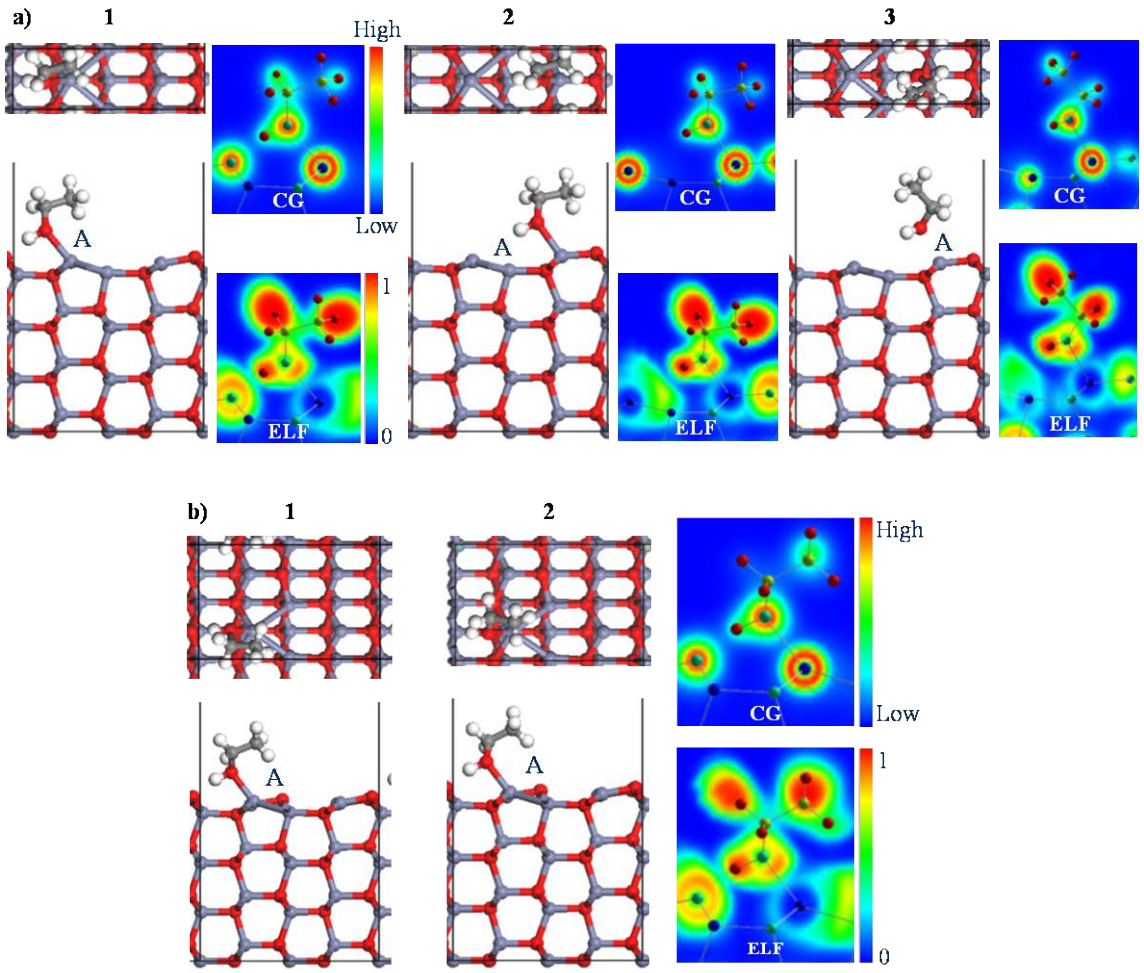

Figure 5.2 Minimum energy structures of ethanol/ZnO(10$\bar{1}$0)-V_O at: (a) ½ and (b) ¼ ML coverages. Charge density (CG) and electron localisation function (ELF) plots are shown for most structures.

On the defect surface, we found 3 minimum energy structures at ½ ML coverage and 2 structures at ¼ ML coverage (see Figure **5.2**, Table **5.2**). At 1 ML coverage we did not find any stable orientations of ethanol adsorbed on the surface, indicating that the presence of surface O atoms is essential to stabilise the binding. At ½ ML coverage, all three structures are more weakly adsorbed than on the stoichiometric surface (see Table **5.1**), with BE values of −0.43, −0.23, and −0.22 eV for structures 1, 2 and 3, respectively. Hence, ethanol may be considered strongly physisorbed in structure 1, and weakly physisorbed in structures 2 and 3. At ¼ ML coverage, the binding is stronger with ethanol being chemisorbed with a BE value of −0.85 eV for both structures; however, the binding

is still weaker than on the stoichiometric surface. Such a trend is in contrast to previous findings that surface oxygen vacancies enhance the binding strength and charge transfer and hence the sensor change in conductivity [132, 135, 145].

Table 5.2 Calculated binding energy and structural parameters for ethanol adsorbed on the ZnO($10\bar{1}0$)-V_O surface at the coverages indicated.

Surf.	Struct.	BE (eV)	d(O_{ads}-Zn_{sub}) (Å)	d⊥ (ads-sub) (Å)	d(O-H) (Å)	d(H_{ads}-O_{sub}) (Å)	∠O-H··O (°)
1 ML [1x1]	-	-	-	-	-	-	-
1ML [1x2]	1_P	–0.32	2.20	1.29	0.99	-	-
		–0.20	2.22	1.00	1.03	1.62	167.8
	2_{AP}	–0.28	2.23	1.56	1.00	1.75	138.2
		–0.13	2.23	0.97	1.02	1.67	173.1
½ ML [1x2]	1	–0.43	2.20	1.05	1.02	1.68	165.8
	2	–0.23	2.20	1.27	0.99	-	-
	3	–0.22	2.25	1.53	0.98	-	-
¼ ML [2x2]	1	–0.85	2.14	1.02	1.02	1.66	165.7
	2	–0.85	2.14	1.02	1.02	1.66	165.4

Binding energy of ethanol adsorbed on the ZnO surfaces, **BE**; distance between the O atom of ethanol and the closest Zn atom of ZnO, **d(O_{ads}-Zn_{sub})**; perpendicular height of adsorbate above the top ZnO surface layer, **d⊥(ads-sub)**; the ethanol OH bond length, **d(O-H)**; distance between hydrogen of the ethanol OH group and the surface oxygen atom, **d(H_{ads}-O_{sub})**; bond angle of O-H···O between the OH group of ethanol and the surface oxygen atom (**∠O-H···O**).

Overall, our calculated relatively weak binding energies are consistent with the observation by Kwak *et al.* [402] that molecular ethanol desorbs between 250–275 K from the nanowires, as the energy barrier for desorption of the physisorbed ethanol is likely to be overcome at this temperature. This is in contrast to Ref. [11] which proposes that ethanol dissociates on the surface, into chemisorbed ethoxy and hydrogen, which then subsequently recombined and desorbed in the molecular form at elevated temperatures.

However, we note that the work of Kwak and Yong [402] and Vohs *et al.* [403] examined the (0001)-terminated ZnO surface. Hence, the difference between our findings may be due to the different surface terminations examined.

In order to investigate the likelihood of dissociation of ethanol on the surface we performed a number of calculations involving of adsorbed ethoxy and H. The ethoxy is bound to a surface Zn atom and the H bound to an adjacent surface O atom at ¼ ML coverage on the stoichiometric surface. Our calculations show that the two species spontaneously recombine to form adsorbed ethanol (in the geometry of structure 1 at ¼ ML, in Figure **5.2**) indicating that dissociation of ethanol is not favourable in this case.

Next, we performed a calculation of adsorbed ethoxy and H on the defect (10$\bar{1}$0) surface containing an O vacancy, as it is suggested that these are strong adsorption sites for ethoxy [402]. We find the ethoxy adsorbs on the surface with its O atom sitting in the surface vacancy site, and the H atom adsorbing on a surface Zn atom (see Figure **5.3**). This structure is however, 0.36 eV higher in energy than the molecularly adsorbed structure 1, indicating that it is preferable for ethanol to adsorb molecularly.

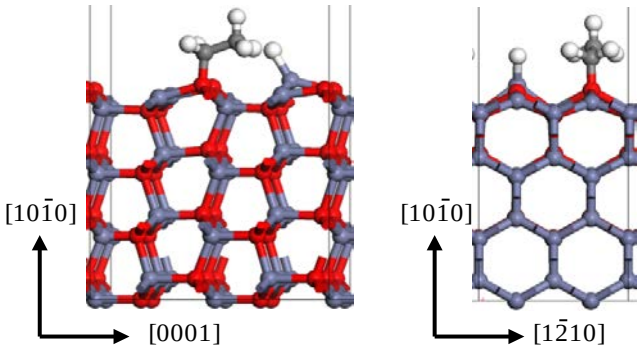

Figure 5.3 Side views of the adsorbed ethoxy species and atomic H on the ZnO(10$\bar{1}$0)-V_O surface at ¼ ML coverage.

Finally, we also modelled the same adsorption configuration but with the H atom adsorbed on a surface O atom which is energetically more favourable [27] than the Zn site; however, this binding was found to be unfavourable.

While there may be other arrangements of ethoxy and H on the surface, we believe our results indicate that ethanol prefers to adsorb associatively at low temperatures on the ($10\bar{1}0$) surface. Although the surface bound ethoxy and H were identified to be stable by our calculations and could lead to recombinative desorption after heating and contribute to the molecular desorption peak observed by Kwak and Yong [402], it is likely to be a small contribution relative to the molecularly adsorbed ethanol, consistent with the findings by Vohs *et al.* [403].

5.3.2 Geometry

As seen in Figure **5.1**, all the structures on the stoichiometric surface can be classified into two general geometric types, based on the relative orientation of the ethanol OH group to the surface atoms: the first where the OH group is positioned above the second layer surface atoms (orientation A); and the second, where the OH group is positioned above the topmost surface layer atoms (orientation B). Structures 1 (1 ML, ½ ML and ¼ ML) and structure 2 (¼ ML) correspond to geometry A, while the remaining structures correspond to geometry B. This geometric distinction correlates with the binding energy values, where structures in orientation A are more strongly bound or chemisorbed on the surface, indicating this orientation is favourable, while structures in orientation B are less stable.

Table 5.3 Calculated properties for ethanol adsorbed on the ZnO($10\bar{1}0$) surface at the coverages indicated.

Surf.	Struct.	Type	∠O-H··O (°)	∠Zn··O-C (°)	Δq (*e*)	∠C-C-O (°)	∠C-O-H (°)	d(C-O) (Å)
Ethanol	ethanol[a]		-	-	-	107.8	108.7	1.44
1 ML [1x1]	1	A	165.3	133.5	–0.01	111.7	112.0	1.43
	2	B	137.6	136.3	–0.01	110.6	113.3	1.44
	3	B	137.1	132.5	0.00	118.2	113.6	1.44
½ ML [1x2]	1	A	161.0	131.4	0.02	110.9	112.6	1.44
	2	B	133.3	137.0	0.02	110.5	113.3	1.44
	3	B	134.7	132.5	0.01	118.0	113.0	1.45
¼ ML [2x2]	1	A	159.7	121.7	0.01	109.3	112.8	1.45
	2	A	158.6	131.4	0.01	109.7	114.2	1.44
	3	B	125.0	131.2	0.00	113.3	112.8	1.45

Free molecule, **ethanol[a]**; bond angle of O-H···O between the OH group of ethanol and the surface oxygen atom **(∠O-H···O)**; bond angle of Zn···O-C between the surface Zn atom and the carbon and oxygen atoms of ethanol **(∠Zn···O-C)**; overall transfer of charge, **Δq**; bond angle of carbon-carbon-oxygen in ethanol, **<C-C-O**; bond angle of carbon-oxygen-hydrogen in ethanol, **<C-O-H**; carbon-oxygen bond length, **d(C-O)**.

Table 5.4 Calculated parameters for ethanol adsorbed on the ZnO($10\bar{1}0$)-V_O surface at the coverages indicated.

Surf.	Struct.	d(H···O) (Å)	∠O-H··O (°)	∠Zn··O-C (°)	δL_1, δL_2, δL_3 (Å)	Δq (*e*)	∠C-C-O (°)	∠C-O-H (°)	d(C-O) (Å)
Ethanol	ethanol[a]	-	-	-	-	-	107.8	108.7	1.44
½ ML [1x2]	1	1.68	165.8	133.5	0.09, 0.08, 0	0.00	110.5	110.3	1.44
	2	-	-	133.7	0.03, 0.05, 0	–0.02	110.2	110.8	1.45
	3	-	-	117.6	0.06, -0.01, 0	0.02	111.7	108.9	1.45
¼ ML [2x2]	1	1.66	165.7	125.7	0.08, 0.08, –0.15	0.02	109.8	109.6	1.45
	2	1.66	165.4	124.7	0.08, 0.08, –0.15	0.02	109.4	110.4	1.44

Free molecule, **ethanol[a]**; distance between hydrogen of the ethanol OH group and the surface oxygen atom, ***d*(H···O)**; bond angle of O-H···O between the OH group of ethanol and the surface oxygen atom, **(∠O-H···O)**; bond angle of Zn···O-C between the surface Zn atom and the carbon and oxygen atoms of ethanol, **(∠ Zn··O-C)**; oxygen deficient site Zn-Zn bond lengths changes, **δL_1, δL_2, δL_3**; overall transfer of charge,

Δq; bond angle of C-C-O in ethanol, **(∠C-C-O)**; bond angle of C-O-H in ethanol, **(∠C-O-H)**; C-O bond length, ***d*(C-O)**.

From Table **5.1** it can be seen there is a distinct difference between a number of the calculated distances and angles for these two adsorption geometries. For both orientations there appear to be two types of interactions between the ethanol and the surface; the first between the ethanol O atom and the topmost surface Zn atom; and the second between the ethanol hydroxyl H atom and the topmost surface O atom. The structure found by Yuan *et al.* [401] has geometry of type A, showing 2 interactions with the surface, however, our calculations identified other stable structures and geometries. For structures of type A, the distance from the ethanol O atom to the closest surface Zn atom, d(O_{ads}-Zn_{sub}), is between 2.04–2.07 Å, which is only <3.5% longer than the bulk Zn-O bond distance (~2.00 Å), indicating ethanol is chemisorbed. For orientation B, the d(O_{ads}-Zn_{sub}) distances are between 2.14–2.21 Å, which are at least 7% longer than in bulk ZnO, indicating a weaker interaction more typical for a physisorbed structure.

For the second type of ethanol-surface interaction, the distance between the ethanol hydroxyl H atom and the topmost surface O atom, d(H_{ads}-O_{sub}) is between 1.41–1.57 Å for structures with geometry A, while for structures with geometry B, this distance in between 1.68–1.94 Å. Together with the calculated bond angles between the ethanol OH group and the surface O atom (∠O-H…O) of between ~159°–165° for geometry A and between ~125°–138° for geometry B, this indicates formation of a hydrogen bond between ethanol and the surface. This is consistent with the increase of the ethanol OH bond length for all structures, and suggests a weakening of this bond due to the interaction with the surface. Since the presence of a H-bond generally correlates with linearity of the O-H...O bond angle (up to a value of 180°), this could be expected to hold also on the ZnO surface. Hence, the greater degree of linearity of the ∠O-H...O bond angle and the shorter H_{ads}-O_{sub}

bond length for structures in geometry A might suggest a stronger H-bond, which is consistent with the calculations by Cooke *et al.* [342] who found a short, strong hydrogen bond (with an H_{ads}-O_{sub} distance of 1.53 Å) for water adsorption on the ($10\bar{1}0$) surface. Charge density and electron localisation function (ELF) plots of structures 1 and 2 at the monolayer coverage are taken through the plane intersecting the OH bond of ethanol and the surface Zn atom it bonds to (see Figure **5.1**). Note that the slices do not intercept all of the atoms in the ethanol molecule, hence only the OH atoms of ethanol and the surface Zn atom should be considered when looking at these plots. The bond formed between the ethanol O atom and the surface Zn atom and the H-bond can be seen in the charge density plots, and in the ELF plots of structure 1 and structure 2 which represent geometries A and B, respectively. The charge density distribution between these atoms is similar to that between the surface Zn-O atoms which indicates the bonding type is similar. For both geometries A and B, the region of delocalised electrons (shown in green) between the ethanol hydroxyl H atom and the surface O atom confirms the H-bond interaction, and is more pronounced for geometry A where the H-bond is stronger. Hence, the formation of a secondary interaction with the surface, namely an H-bond, results in the increased stability of structures with geometry type A.

There is also a clear distinction between the calculated values for the perpendicular height of the ethanol above the surface ($d\perp_{(ads\text{-}sub)}$) for geometries A and B (as seen in Tables **5.1** and **5.2**) where this distance is <1.17 Å for geometry A and >1.53 Å for geometry B. The shorter H_{ads}-O_{sub} distance and more linear O-H…O bond angle of structure 1 (at 1 ML) compared to the other structures correspond to the shorter perpendicular height of ethanol above the surface, as well as the larger increase in the OH bond length. While this suggests a stronger H-bond, the disparity in the BE values (ethanol adsorbs more strongly at the ½ and ¼ ML coverages in geometry A) can be explained by

the interaction energy values discussed in **5.3.1**, which showed that the adsorbate-adsorbate interaction is very high at 1 ML coverage.

On the defect surface (see Figure **5.2**) at ½ ML coverage, the primary interaction between the adsorbate and the surface is also between the ethanol O atom and the surface Zn atom, as was found for the stoichiometric surface. For structure 1, the ethanol is oriented in geometry A, as on the stoichiometric surface, so that the ethanol also forms an H-bond with the surface. Due to the surface reconstruction on the defect surface, the O_{ads}-Zn_{sub} distance is ~6% longer than on the stoichiometric surface, which results in the weaker binding. For structures, 2 and 3, the ethanol is oriented so that the H atom of the ethanol sits above the defect site and hence is not able to form an H-bond to a surface O atom, suggesting a weaker interaction. The larger perpendicular height of the molecule above the surface and shorter OH bond for these structures are also consistent with the lack of an H-bond. At ¼ ML coverage, both structures adsorb with geometry A, forming an H-bond to the surface. Similar to the structures at the higher coverage, the longer adsorbate-substrate distance constitutes a weaker binding.

Adsorption of ethanol on the stoichiometric surface causes some minor adsorbate-induced relaxation (see Table **5.6**). While the surface O atom relaxes by <0.14 Å, the movement of the topmost surface Zn atom is greater (shown as $\delta Z_{1(Zn)}$) with the Zn atom moving upwards or away from the surface. The magnitude of this movement is greater for the more strongly bound structures adsorbed in orientation A. This relaxation results in a reduction of the tilt of the surface bond that is seen on the relaxed clean surface, being larger in magnitude for structures adsorbed in orientation A than B. These changes result in the ethanol O atom adsorbing very close to where the next surface O atom would be located, which may also explain the greater stability. The surface Zn-O bond distance (d_1) is found to increase for all structures (see Table **5.1**), with the increase being generally smaller in magnitude for the structures in orientation A, which may be related to the

greater relaxation of the surface Zn atom. It may also be related to a reduction of the surface Zn-O-Zn bond angle (θ) in all structures, more so when ethanol adsorbs in orientation A.

Table 5.6 Surface induced relaxations and reconstructions for ethanol adsorbed on the ZnO (10$\bar{1}$0) and (10$\bar{1}$0)-V_O surfaces at the coverages indicated.

Sur.	Str.	Layer$_1$						Layer$_2$					
		Zn$_1$			O$_1$			Zn$_2$			O$_2$		
		δx	δy	δz	δx	δy	δz	δx	δy	δz	δx	δy	δz
(10$\bar{1}$0) 1 ML	1A	0.09	–0.16	**0.30**	0.10	–0.04	0.03	0.10	–0.03	–0.10	0.09	0.00	0.01
	2B	0.03	–0.16	0.13	0.04	–0.04	0.01	0.04	–0.06	–0.03	0.04	–0.04	–0.01
	3B	–0.04	–0.06	0.10	–0.04	0.06	–0.02	–0.04	0.04	–0.06	–0.03	0.05	–0.04
(10$\bar{1}$0) ½ ML	1A	0.09	0.05	–0.02	0.10	0.07	0.01	0.09	0.00	0.01	0.09	0.06	0.01
		0.09	–0.02	**0.27**	0.09	0.04	0.01	0.10	0.11	–0.11	0.09	0.08	–0.02
	2B	0.02	–0.10	**0.18**	0.03	0.02	0.02	0.03	0.01	–0.01	0.03	0.01	0.01
		0.03	0.00	–0.06	0.03	–0.01	0.00	0.03	–0.03	–0.02	0.03	–0.01	–0.04
	3B	–0.04	–0.10	0.14	–0.03	0.02	–0.02	–0.03	0.02	–0.02	–0.03	0.02	–0.02
		–0.03	0.02	–0.05	–0.03	0.01	–0.01	–0.03	–0.01	–0.05	–0.03	0.01	–0.03
(10$\bar{1}$0) ¼ ML	1A	0.01	0.11	–0.06	0.01	0.11	–0.03	0.00	0.13	–0.05	0.02	0.12	–0.01
		0.01	0.02	**0.31**	0.01	0.08	0.00	–0.01	0.07	–0.01	–0.01	0.10	0.00
		0.01	0.08	–0.04	0.01	0.08	–0.01	0.02	0.12	–0.04	0.02	0.10	–0.01
		0.00	0.12	0.01	0.01	0.14	0.05	0.02	0.07	–0.02	0.00	0.11	–0.01
	2A	–0.01	0.03	–0.04	0.00	0.03	–0.01	0.00	0.02	0.00	0.00	0.05	–0.01
		–0.01	0.05	–0.01	0.00	0.07	0.04	0.01	0.07	–0.05	–0.01	0.06	–0.03
		–0.01	0.04	–0.04	–0.01	0.05	0.00	–0.02	0.02	0.00	0.01	0.06	0.00
		0.00	–0.03	**0.32**	–0.01	0.03	0.01	–0.01	0.08	–0.04	–0.01	0.04	–0.01
	3B	–0.01	–0.02	**0.16**	–0.01	0.09	0.01	–0.01	0.09	–0.01	–0.01	0.08	–0.02
		–0.02	0.09	–0.02	–0.01	0.08	0.01	–0.02	0.09	–0.01	–0.01	0.08	0.00
		–0.01	0.08	–0.03	–0.01	0.09	0.00	–0.02	0.07	–0.01	–0.01	0.08	–0.01
		–0.01	0.09	–0.03	–0.01	0.08	0.02	–0.01	0.07	–0.01	–0.01	0.08	–0.01
(10$\bar{1}$0)-Vo ½ ML	1A	0.03	–0.06	**0.23**	-	-	-	0.04	0.08	–0.14	0.03	0.05	–0.07
		0.03	0.09	0.03	0.04	0.13	0.04	0.02	0.00	0.08	0.03	0.10	0.04
	2B	0.01	0.02	0.01	-	-	-	0.01	–0.02	–0.01	0.01	0.03	0.01
		–0.03	–0.05	**0.20**	0.01	0.00	0.01	0.02	0.05	–0.05	–0.03	0.03	–0.04
	3B	0.02	0.03	–0.01	-	-	-	0.01	0.01	–0.01	0.03	0.04	0.00
		–0.03	–0.02	**0.16**	0.01	0.03	0.02	3.24	0.06	–0.04	3.25	0.05	–0.03
(10$\bar{1}$0)-Vo ¼ ML	1A	0.02	0.06	–0.05	-	-	-	0.04	0.02	–0.07	–6.49	0.01	–0.03
		0.01	–0.12	**0.26**	0.00	0.06	–0.02	–0.05	0.01	–0.07	–0.01	0.00	–0.04
		0.01	–0.05	–0.03	–0.01	–0.04	–0.01	–0.07	–0.02	0.03	6.51	0.02	0.01
		0.01	0.08	0.02	0.00	0.11	0.03	0.08	–0.02	0.03	0.05	0.02	0.01
	2A	–0.01	0.08	–0.06	-	-	-	0.05	0.03	–0.07	0.02	0.02	–0.04
		0.01	–0.10	**0.25**	0.00	0.08	–0.03	–0.04	0.04	–0.08	–0.03	0.03	–0.04
		0.01	–0.03	–0.03	0.00	–0.02	–0.02	–0.07	0.00	0.03	6.51	0.04	0.01
		0.01	0.10	0.02	0.00	0.13	0.03	0.08	0.00	0.03	0.05	0.03	0.01

Surface, Sur.; Structure, Str.; Significant atomic displacements in the z-direction are highlighted in red.

At temperatures above ~517 K, Kwak *et al.* [402] showed that ethylene desorbed from the surface. They proposed that it forms as a result of bond scission of the C-O bond and a C-H bond of the methyl group (through β-hydride elimination) of adsorbed ethoxy. Our calculations show that bond scission of adsorbed ethoxy can be facilitated by its adsorption geometry. In Figure **5.3**, it can be seen that the O atom of ethoxy fills the vacancy site, bonding to the surrounding surface Zn atoms. In this site, the ethoxy sits closer to the surface, with the methyl H atoms being located 2.63 Å from the closest surface atom, as compared to 3.37 Å for the molecularly adsorbed species. Hence, it may be facile for the ethoxy to tilt towards the surface, allowing scission of the O-Zn bond, followed by β-hydride elimination. We also suggest that the stronger binding of the chemisorbed molecular ethanol, determined from our calculations, may also allow it to remain bonded to the surface until it may dissociate into adsorbed ethoxy and then further to the ethylene at a higher temperature.

5.3.3 Vibrational Frequencies

The calculated vibrational frequencies for the adsorbed ethanol on the ($10\bar{1}0$) and ($10\bar{1}0$)-V_O surfaces are shown in Tables **5.7** and **5.8**, respectively. The following vibrational modes have been identified: stretching mode for the O-H, C-C and C-O bonds; asymmetric and symmetric stretching modes for the C-H bond in CH_3 and CH_2 groups; asymmetric and symmetric stretching modes for the bonds in C-C-O; bending, wagging, twisting and rocking modes for the CH_2 group; bending mode for the C-O-H and C-C-O bond angles. The corresponding vibrational frequencies for the free molecule are also shown (and are within 3% agreement with the experimental value [404]).

Table 5.7 Calculated vibrational frequencies (cm^{-1}) for ethanol adsorbed on the ZnO(10$\bar{1}$0) surface at the coverages indicated.

Site (cm^{-1})	ethanol	1 ML			½ ML			¼ ML		
		1A	2B	3B	1A	2B	3B	1A	2A	3B
υ(O-H)	3784	1899	3019	2993	2605	3171	3088	2631	2576	3380
υ(C-H_3)a	3067 3065	3316 3085	3123 3094	3087 3065	3119 3084	3127 3095	3092 3066	3062 3052	3062 3057	3050 3035
υ(C-H_3)s	2992	3011	3009	3009	3008	3013	3011	2980	2985	2971
υ(C-H_2)a	2956	3062	3086	3145	3070	3086	3151	3001	2992	3065
υ(C-H_2)s	2929	2942	2944	3029	2954	2961	3041	2957	2961	2986
β(C-H_2)	1476	1478	1473	1461	1483	1475	1459	1479	1479	1467
β(C-O-H)	1225	1517	1318	1296	1469	1272	1289	1450	1453	1246
υ(C-C)	1393	1363	1355	1349	1365	1357	1350	1372	1370	1364
ω(C-H_2)	1393	1342	1391	1387	1340	1388	1384	1324	1329	1351
τ(C-H_2)	1256	1288	1286	1361	1288	1296	1365	1261	1263	1319
ρ(C-H_2)	1137 797	- 779	1120 772	1139 -	1126 771	1117 768	1136 778	1142 801	1140 797	- 802
υ(C-O)	1064	1092	-	1080	-	-	1073	-	-	-
υ(C-C-O)a	1004	1060	1051	1050	1055	1039	1047	1043	1051	1025
τ(O-H)	295	1144	846	874	985	795	830	1014	991	746
υ(C-C-O)s	- 870	- 875	1088 893	- 842	1088 872	1081 876	- 850	1085 871	1088 872	- 856
β(C-C-O)	406	474	441	486	469	441	491	469	475	416

Vibrational frequencies for free ethanol molecule calculated in this study, **ethanol**.

Calculated vibrational modes: υ = stretching; β = bending; ω = wagging; τ = twisting; ρ = in-plane rocking

For all structures, the magnitude of the OH stretching frequency decreases when ethanol adsorbs on the surface. The largest decrease is calculated for the structures with geometry A, while for the more weakly bound or physisorbed structures with geometry B, the decrease in the OH frequency is smaller. For the structures with orientation B, the decrease of this frequency is between 11–21%, while for the chemisorbed species in orientation A, it is between 30–50%. Hence, the decrease in magnitude of the OH stretching mode is greater when the OH group lies above the second layer of the ZnO surface atoms as opposed to above the top layer. This decrease confirms the formation of a hydrogen bond, as suggested by the adsorption geometry and ELF charge density plots.

Table 5.8 Calculated vibrational frequencies (cm^{-1}) for ethanol adsorbed on the ZnO ($10\bar{1}0$)-V_O surface at the coverages indicated.

Site (cm^{-1})	ethanol	½ ML			¼ ML	
		1A	2B	3B	1A	2A
υ(O-H)	3784	2967	3457	3598	2869	2860
υ(C-H_3)a	3067 3065	3118 3084	3126 3091	3115 3086	3066 3054	3067 3058
υ(C-H_3)s	2992	3009	3010	3010	2983	2986
υ(C-H_2)a	2956	3068	3078	3078	2995	2997
υ(C-H_2)s	2929	2941	2968	3052	2953	2951
β(C-H_2)	1476	1484	1476	1493	1478	1475
β(C-O-H)	1225	1459	1262	1234	1466	1458
υ(C-C)	1393	1356	1390	1371	1366	1363
ω(C-H_2)	1393	1334	1361	1355	1330	1326
τ(C-H_2)	1256	1285	1292	1317	1234	1261
ρ(C-H_2)	1137 797	1127 772	1117 771	1110 763	1142 796	1140 793
υ(C-O)	1064	-	-	1013	-	-
υ(C-C-O)a	1004	1053	1031	1038	1043	1039
τ(O-H)	295	846	513	539	943	944
υ(C-C-O)s	- 870	1083 886	1065 863	- 857	1078 865	1076 866
β(C-C-O)	406	455	399	441	458	449

Vibrational frequencies for free ethanol molecule calculated in this study, **ethanol**.

υ = stretching; β = bending; ω = wagging; τ = twisting; ρ = in-plane rocking

On the defect surface, the trend is similar, with the decrease in the OH stretching mode being >22% for structure 1 (½ ML and ¼ ML) and structure 2 (¼ ML), where ethanol adsorbs in geometry A. For the other structures, the decrease in the magnitude of this frequency is <9%, consistent with the fact that no H-bond is formed for these structures.

Hence, the magnitude of the OH stretching frequency could be used as an indication of the binding strength of the ethanol to the surface as well as assist in distinguishing different adsorption geometries. To the best of our knowledge the

experimental vibrational frequencies of ethanol adsorbed on the ($10\bar{1}0$) surface have not been reported. The study by Yuan *et al.* [401] did not present calculated frequency data for their minimum energy structure of ethanol/ZnO($10\bar{1}0$)-¼ML. The values presented here may be useful for characterising the adsorbed geometry and binding strength of ethanol in future experimental studies.

5.3.4 Density of States

To further investigate the electronic properties of the gas-surface interaction, the density of states (DOS) have been calculated for the most stable structures of ethanol adsorbed on the relaxed ($10\bar{1}0$) stoichiometric and defect surfaces (see Figure **5.4**). The total density of states for the clean relaxed stoichiometric and defect surfaces are shown for comparison (Figure **5.4a**,**b**). The orbital resolved local DOS are also shown to indicate the contribution of ethanol (Figure **5.4c**,**d**) or ZnO (Figure **5.4e**,**f**) to the total DOS.

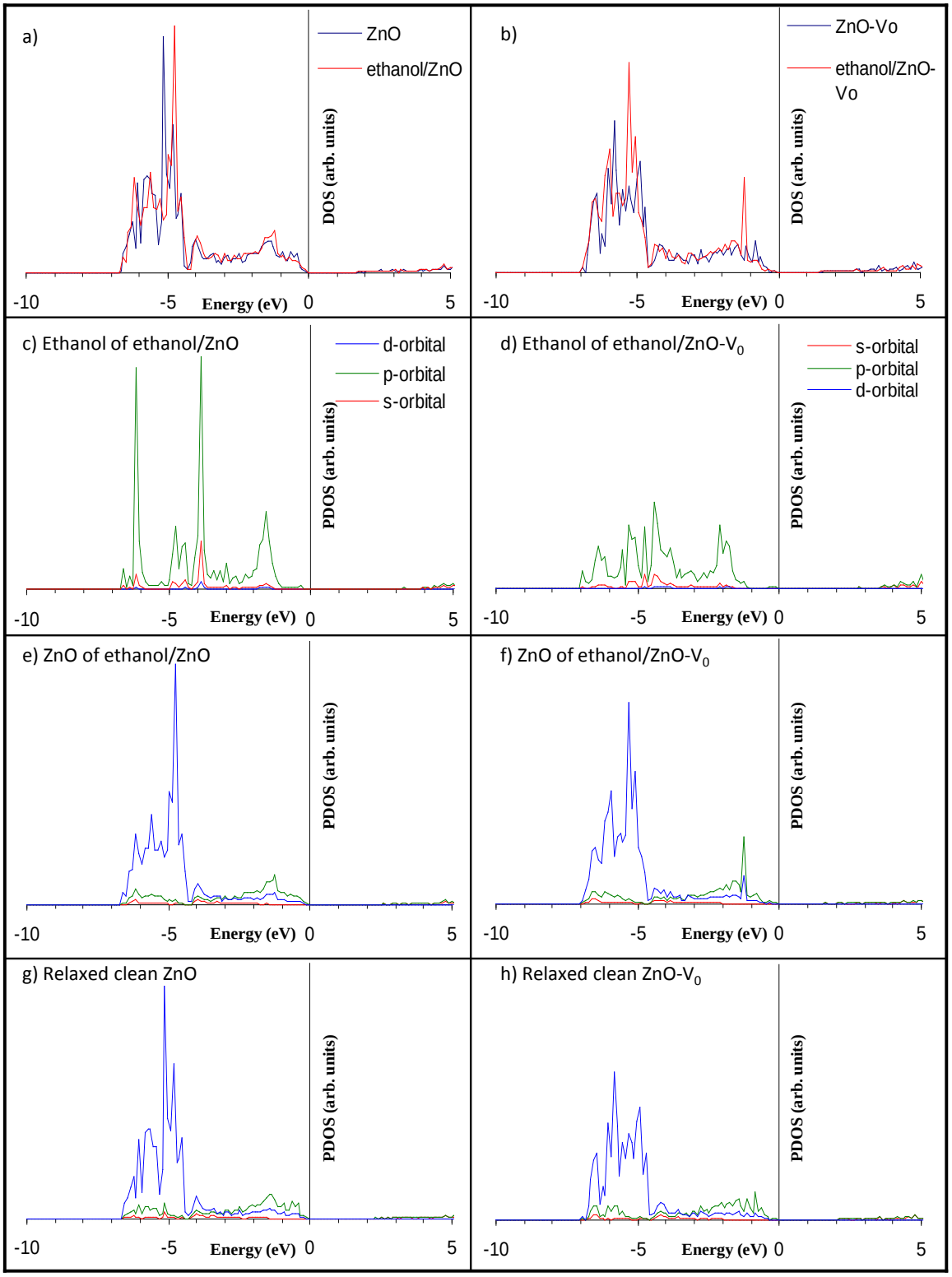

Figure 5.4 Total density of states (DOS) of clean and ethanol-adsorbed ZnO(10$\bar{1}$0) (a) stoichiometric and (b) defect surface. For the ethanol/ZnO and ethanol/ZnO-V_O systems, the orbital resolved local DOS of the (c), (d) ethanol and (e), (f) ZnO atoms on the respective surfaces are presented. Orbital resolved local DOS of the relaxed [2x2]-sized clean (g) stoichiometric and (h) defect surfaces. The zero of energy (E_F) is aligned to the highest occupied level.

The main change due to the interaction of ethanol with the surfaces is the decrease in intensity of the ZnO *d*-orbital states at −5.1 eV and −5.8 eV on the stoichiometric and defect surface, respectively, along with an increase in states at −4.7 eV and −5.3 eV, respectively (see Figure **5e,f**). There is also an increase in states on both surfaces in the region just below the Fermi level (E_F) to ~1.2 eV below E_F, which are primarily due to Zn *p*- and to a lesser extent *d*- orbitals. The contribution of ethanol to the total DOS is less on the defect surface than on the stoichiometric surface, consistent with the weaker interaction. On the stoichiometric surface we calculated no change to the band gap (any change is within our calculation accuracy), however, the calculated charge transfer of 0.03 *e* from ethanol to the surface is consistent with the findings of Yuan *et al.* [401]. On the defect surface, the same trend is seen, where ethanol donates charge to the surface (0.02 *e*) resulting in a decrease in the band gap by ~0.07 eV. Hence, despite the weakened H-bond interaction on the defect surface for this adsorbate orientation, we still observe the ability of ethanol to donate electrons to the surface, which results in an increase in conductivity. This is in agreement with an experimental study [405] that confirms ethanol acts as a reducing gas, donating electrons to the surface, causing an increase in conductivity.

5.3.5 Orientational Effects on Structure and Stability of Ethanol Monolayer on ZnO($10\bar{1}0$)

We have considered the possibility that ethanol molecules may adsorb in different orientations to each other, forming superstructures on the stoichiometric and defect surfaces. Such structures have been seen for other systems, such as water which forms a highly ordered superstructure on defect-free surfaces of ZnO, in which every second water molecule is dissociated [406]. We investigate the possibility of ethanol superstructure formation by modelling two molecules within a [1x2] supercell, which corresponds to 1

ML coverage. We consider two different relative orientations of the ethanol molecules; the first structure corresponds to two molecules aligned in a parallel arrangement (where the $Zn_{sub}...O_{ads}$ bonds are parallel and the methyl groups face the same direction); the second structure corresponds to an anti-parallel arrangement (where the $Zn_{sub}...O_{ads}$ bonds are anti-parallel and the methyl groups face each other). For the parallel structure, the initial orientation of each ethanol molecule was identical to that for structure 1 (1 ML). For the anti-parallel structure, the initial orientation of one of the ethanol molecules was the same as structure 1 (1 ML), while for the other molecule, it was the same as that of structure 2 (1 ML). For the defect surface the same two models were considered, with one of the surface O atoms removed to create the defect surface. We then performed a geometry optimisation of each structure, and calculated a BE value for co-adsorption of the two ethanol molecules as well as a BE value for adsorption of ethanol on the surface with a pre-adsorbed ethanol at ½ ML coverage (sequential adsorption). The optimised structures are shown in Figure **5.5** with the calculated properties in Tables **5.1** and **5.2**.

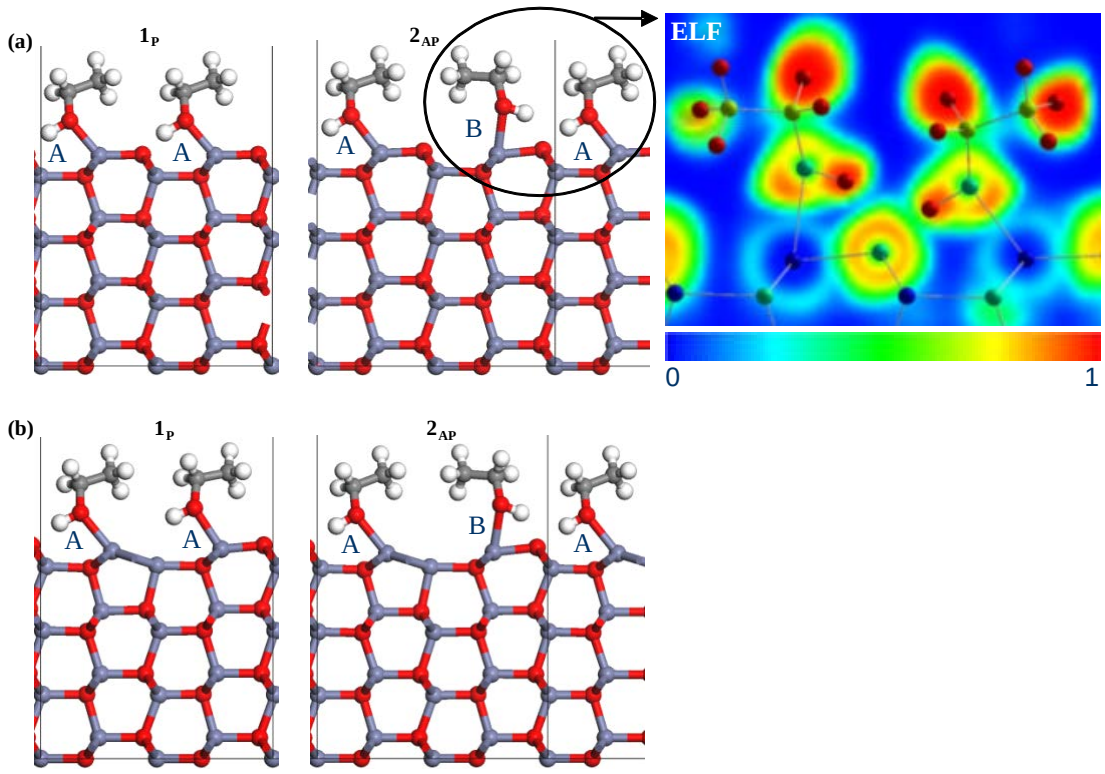

Figure 5.5 Minimum energy structures of ethanol adsorbed on the ZnO (a) (10$\bar{1}$0) and (b) (10$\bar{1}$0)-V_O surfaces at 1 ML coverage in parallel and antiparallel alignments. Electron localisation function (ELF) plot is shown for the anti-parallel arrangement of ethanol molecules on ZnO(10$\bar{1}$0).

5.3.5.1 Stoichiometric Surface

The BE values (Table **5.1**) for the parallel (structure 1_P) and anti-parallel (structure 1_{AP}) structures with ethanol co-adsorbed simultaneously are –0.74 eV/molecule (consistent with the [1x1]-1 ML calculation) and –0.41 eV/molecule, respectively. These values indicate that the preferred orientation of ethanol molecules at 1 ML coverage is the parallel arrangement. For sequential adsorption, the BE values for the second molecule are −0.78 eV and −0.11 eV, respectively, again indicating that the adsorbate molecules prefer to be adsorbed in the same orientation on the surface (parallel to each other). It also shows that once ½ ML coverage of ethanol is adsorbed it is unfavourable to adsorb further ethanol molecules in an anti-parallel arrangement.

Considering the geometry of the parallel arrangement, the ethanol molecules remain adsorbed in the same orientation as each other, with both molecules adsorbed in geometry A. The calculated bond lengths and angles are identical (see Table **5.1**) and only differ by <4% compared to the geometry of ethanol structure 1 ([1x1]-1 ML). For the anti-parallel arrangement, the ethanol molecules also remain in their initial orientation, with one molecule adsorbed in geometry A and the other in geometry B. The adsorption geometry indicates one molecule is chemisorbed while the other is physisorbed, consistent with the A and B geometries. The weaker binding for the anti-parallel arrangement can be explained by the adsorption geometry. Specifically, for the parallel arrangement each surface O atom is involved in an H-bond; however for the anti-parallel arrangement both ethanol molecules are H-bonded to the same surface O atom, leading to the weaker interaction and hence stability of this arrangement. The red shifts of the OH stretching mode, calculated but not presented in Table 5.7, support the formation of hydrogen bonds at the parallel (1948 and 1924 cm^{-1}) and anti-parallel (2467 and 3384 cm^{-1}) configurations of the ethanol molecules. From the ELF plot of this structure (Figure **5.5**), the two H-bond interactions can be seen, showing that one is stronger than the other due to the higher degree of electron localisation between the surface O atom and the ethanol hydroxyl H atom (*i.e.* some electron delocalisation at the H-bond region in geometry B can be seen). Hence, the ethanol prefers to adsorb so as to maximise the number and strength of the hydrogen bonds formed with the surface.

5.3.5.2 Defect Surface

The BE values for the parallel (structure 1_P) and anti-parallel (structure 2_{AP}) orientations on the defect surface are −0.32 eV/molecule and −0.28 eV/molecule, respectively. Hence, the slightly preferable orientation is for the ethanol molecules to be aligned in the same

direction, as we also showed for the stoichiometric surface. These values are significantly weaker than the corresponding values on the stoichiometric surface. For the parallel arrangement, the adsorption configuration of the two ethanol molecules is not the same as on the stoichiometric surface, which results in the weaker binding. Specifically, only one ethanol molecule forms an H-bond to the surface, due to the lack of available surface O atoms, which is in contrast to the stoichiometric surface where both ethanol molecules formed H-bonds to the surface, resulting in stronger binding. Again, the difference in the OH stretching mode associated with each molecule can be used to distinguish the presence or absence of the H-bond, where the molecule (shown to the left of the surface, Figure **5.5a**) has a smaller frequency value of 2717 cm^{-1}, while the molecule on the right (Figure **5.5a**) has a larger value of 3431 cm^{-1}, reflecting the absence of the H-bond. For the anti-parallel arrangement, one molecule is adsorbed in geometry A while the other is in geometry B; however the absence of one of the surface O atoms prevents the molecules from adsorbing as close to the surface, resulting in weaker binding. The calculated OH stretching frequencies for ethanol molecules (3207 and 2964 cm^{-1}) correspond to ∠O-H···O angles of 138° and 173°. Hence, on the oxygen deficient surface ethanol forms fewer H-bonds which results in weaker binding.

5.4 Summary

The adsorption of ethanol on the stoichiometric and oxygen deficient ZnO(10$\bar{1}$0) nanowire surface at ¼, ½ and 1 ML coverages has been analysed using density functional theory calculations. We have shown that ethanol adsorbs in multiple stable sites at all coverages investigated, with the binding being stronger at lower coverages presumably due to the weaker interaction between adjacent ethanol molecules. After adsorption, there were minor

surface reconstructions, indicating that the adsorption of ethanol would not cause major structural changes to the surface and affect the stability of the sensing device.

We have identified two adsorption geometries which are defined by the orientation of the OH bond of the ethanol molecule relative to the topmost surface atoms. For the first geometry, the OH bond lies over the second topmost surface Zn and O atoms, while for the second geometry, it lies over the topmost surface Zn and O atoms. The first geometry is more stable, representing chemisorption, while the second geometry corresponds to physisorption. For both geometries, ethanol forms two types of interactions with the surface; one being between the ethanol O atom and a surface Zn atom; and the other being a hydrogen bond between the ethanol hydroxyl H atom and a surface O atom. Our calculations show that the difference in the OH stretching frequency of these two adsorption configurations could be used to distinguish the two types of adsorption experimentally. Importantly, on the oxygen deficient surface, we show that the presence of surface defects does not strengthen the surface-ethanol binding interaction, in contrast to the other adsorbates on ZnO surfaces. We have demonstrated that the reason for the weaker binding is that the secondary adsorbate stabilising interaction — a hydrogen bond — is weaker or cannot be formed on an oxygen deficient surface.

Our results indicate that multiple ethanol molecules prefer to be adsorbed in the same geometry, parallel to each other on the surface, in contrast to aligning in an antiparallel orientation or superstructure, as this maximises the hydrogen bond formation and hence binding strength. While the adsorption of the ethanol dissociation products, ethoxy and H, at low temperatures is less stable than molecular adsorption, we have shown that on the defect surface, the ethoxy will adsorb so that the O atom of the adsorbate fills the O vacancy site. The lower stability of the dissociated products indicates that the ethanol detected experimentally desorbs from the surface below room temperature is likely to be

from molecularly adsorbed species rather than from the re-association of adsorbed ethoxy and H.

Overall, the adsorption behaviour of ethanol described here provides a better understanding of the gas-surface interaction and clarifies some of the uncertainties that existed previously.

Chapter 6

Adsorption of Ethanol on the ZnO($2\bar{1}\bar{1}0$) Surface

6.1 Background

To date, there is very little information about the ($2\bar{1}\bar{1}0$) surface sensing properties. The adsorption of ethanol on the ($2\bar{1}\bar{1}0$) surface has not been theoretically studied and the sensing mechanism is not fully understood.

Our previous study (presented in Chapter 5) and that by Yuan *et al*. [401] of ethanol adsorption on the ZnO($10\bar{1}0$) stoichiometric and oxygen deficient (V_o) surfaces, revealed that the ethanol O atom forms a bond to the surface Zn atom, and the hydroxyl H atom forms a hydrogen bond with the surface O atom [371, 401]. In this chapter we examine the adsorption of ethanol on the ($2\bar{1}\bar{1}0$) stoichiometric and oxygen deficient (Vo) surfaces using DFT calculations, since the nanostructures comprising this morphology have been shown to enhance their sensing ability for ethanol [407]. In order to understand and optimise the sensing performance of this surface and compare it to the ($10\bar{1}0$) surface we

analysed the ethanol binding energy values, adsorption geometry and electronic properties and discussed them in relation to the available experimental observations of the ZnO sensing performance.

6.2 Surface Models

Similar to the ($10\bar{1}0$) surface approach, three different sized supercells were used in this study, each containing eight layers with 32, 64 and 128 atoms for [1x1], [1x2] and [2x2] slabs of ZnO($2\bar{1}\bar{1}0$), respectively. The ($2\bar{1}\bar{1}0$)-V_O surface (see Figure **3.6**) was modelled by removing one of the topmost surface oxygen atoms to create V_O concentrations of 50%, 25% and 12.5% for the [1x1], [1x2] and [2x2] supercells, respectively. The calculated structural properties of the ($2\bar{1}\bar{1}0$) and ($2\bar{1}\bar{1}0$)-V_O surfaces are shown in Figure **3.7**. Ethanol was initially positioned between 2.5 to 3 Å above the ZnO surface at different sites and orientations. The [1x1], [1x2], and [2x2] supercells correspond to coverages of 1, ½ and ¼ ML, respectively.

6.3 Results and Discussion

6.3.1 Binding Energy

The binding energies of ethanol adsorbed on the ZnO($2\bar{1}\bar{1}0$) stoichiometric and oxygen-deficient surfaces at different coverages, are presented in Tables **6.1** and **6.2**. Multiple minimum energy structures were found on all surfaces.

Table 6.1 Calculated binding energy and structural parameters for ethanol adsorbed on the ZnO($2\bar{1}\bar{1}0$) surface at the coverages indicated.

Surf.	Struct.	BE (eV)	d(O_{ads}-Zn_{sub}) (Å)	d⊥(ads-sub) (Å)	d(O-H) (Å)	∠O-H··O (°)	$\delta z_{1(Zn)}$ (Å)	$\delta z_{1(O)}$ (Å)	d_1 (Å)	d_2 (Å)	θ (º)
Ethanol (exp)		-	-	-	0.97	-	-	-	-	-	-
ZnO	1x1	-	-	-	-	-	-	-	1.90	1.88	10.3 10.5 10.4
1 ML [1x1]	1	–0.95	2.10	0.87	1.04	171.6	0.20	–0.06	2.00	1.93	0.7
	2	–0.89	2.09	0.95	1.04	164.2	0.21	0.00	1.95	1.95	2.5
	3	–0.09	-	2.53	0.97	-	–0.02	–0.03	1.90	1.89	10.2
1 ML [1x2]	1_P	–1.01 (–0.96)	2.10 2.10	0.87 0.87	1.04 1.04	172 172	0.20 0.20	- -	2.00 2.00	1.92 1.92	0.8 0.8
	2_{AP}	–0.96 (–0.86)	2.10 2.09	0.85 1.00	1.04 1.04	173 163	0.23 0.17	- -	2.00 1.96	1.96 1.92	0.5 3.3
½ ML [1x2]	1	–1.06	2.08	0.88	1.03	171.6	0.22	–0.05	2.00	1.93	1.2
	2	–1.05	2.07	0.88	1.03	168.7	0.22	–0.04	2.00	1.92	0.9
	3	–0.98	2.09	1.00	1.03	161.4	0.23	0.01	1.96	1.92	2.2
	4	–0.98	2.06	1.17	1.01	149.4	0.20	–0.01	1.96	1.91	4.4
¼ ML [2x2]	1	–1.13	2.07	0.92	1.02	169.8	0.23	–0.04	1.95	1.93	1.1
	2	–1.12	2.08	1.01	1.02	166.5	0.22	–0.04	1.95	1.93	1.1
	3	–1.08	2.06	0.93	1.03	160.8	0.24	–0.01	1.96	1.92	2.5

Binding energy, **BE**; binding energy of the sequential adsorption for the superstructures are shown in brackets; distance between the O atom of ethanol and the closest Zn atom of ZnO, **d(O_{ads}-Zn_{sub})**; perpendicular height of adsorbate above the top ZnO surface layer, **d⊥(ads-sub)**; the ethanol OH bond length, **d(O-H)**; bond angle of O-H···O between the OH group of ethanol and the surface oxygen atom (**∠O-H···O**); relaxation of the topmost Zn and O atoms along the z-direction, **$\delta z1_{(Zn)}$**, **$\delta z1_{(O)}$**; ZnO surface bond lengths, **d_1** and **d_2**; Zn-O-Zn surface bond angle, **θ**; parallel and anti-parallel arrangements of ethanol molecules in the [1x2] supercell are denoted by 1_P and 2_{AP}, respectively.

On the stoichiometric ($2\bar{1}\bar{1}0$) surface, the most stable structures at 1, ½ and ¼ ML coverages had BE values of –0.95, –1.06 and –1.13 eV, respectively, indicating that ethanol adsorbs more strongly at lower coverages. At 1 ML coverage, structures 2 and 3 had BE values of –0.89 and –0.09 eV, respectively, indicating chemisorption for the former and weak physisorption for the latter structure. At ½ ML coverage, structures 2, 3 and 4 had BE values of –1.05, –0.98 and –0.98 eV, respectively, indicating that ethanol is chemisorbed on

the surface. Similarly, ethanol was found to be chemisorbed on the surface at the ¼ ML coverage with BE values between –1.13 and –1.08 eV. The increased BE values at lower coverages implies a stronger adsorption interaction due to less significant cross-adsorbate interactions. Generally, in comparison with the ($10\bar{1}0$) surface (see Tables **5.1** and **5.2**), ethanol adsorbs more strongly on the ($2\bar{1}\bar{1}0$) surface with higher BE values calculated for all coverages investigated.

Table 6.2 Calculated binding energy and structural parameters for ethanol adsorbed on the ZnO($2\bar{1}\bar{1}0$)-V_O surface at the coverages indicated.

Surf.	Struct.	BE (eV)	d(O-H) (Å)	∠O-H··O (°)	$\delta z_{1(Zn)}$ (Å)	δL_1, δL_2, δL_3 (Å)
1 ML [1x1]	1	–0.70	1.03	162	0.18	–0.13, 0.08, 0.13
1 ML [1x2]	1_P	–0.92 (–0.91)	1.03 1.03	174 173	0.23 0.21	0.11, 0.12, 0.00
	2_{AP}	–0.86 (–0.92)	1.03 1.02	172 168	0.21 0.18	0.10, 0.13, –0.06
½ ML [1x2]	1	–0.93	1.02	174	0.24	0.06, 0.07, –0.05
	2	–0.91	1.03	172	0.27	0.00, 0.03, 0.00
	3	–0.76	1.03	157	0.22	0.06, –0.12, 0.15
	4	–0.72	1.01	165	0.23	0.08, 0.10, –0.07
¼ ML [2x2]	1	–1.00	1.02	168	0.24	0.01, 0.01, –0.01
	2	–0.99	1.02	172	0.21	0.05, 0.05, –0.05
	3	–0.87	1.02	150	0.21	0.06, –0.10, 0.10
	4	–0.75	1.01	160	0.26	0.08, 0.12, –0.07
	5	–0.43	0.98	-	0.16	0.05, 0.05, –0.05

Binding energy, **BE**; binding energy of the sequential adsorption for the superstructures are shown in brackets; the ethanol OH bond length, **d(O-H)**; bond angle of O-H···O between the OH group of ethanol and the surface oxygen atom **(∠O-H···O)**; relaxation of the topmost Zn atom along the z-direction, $\delta z1_{(Zn)}$; oxygen deficient site Zn-Zn bond lengths changes, δL_1, δL_2, δL_3; parallel and anti-parallel arrangements of ethanol molecules in the [1x2] supercell are denoted by 1_P and 2_{AP}, respectively.

For the ($2\bar{1}\bar{1}0$)-V_O surface, only one stable structure with a BE value of –0.70 eV was found at 1 ML coverage. However, at ½ ML coverage four chemisorbed structures were found. At ¼ ML coverage, five stable structures were found, of which four were

chemisorbed and one physisorbed. Again, ethanol adsorbs on the ($2\bar{1}\bar{1}0$)-V_O surface more favourably at a lower coverage, as evidenced by the increased number of minima and general increased binding strength at the lower coverages (Table **6.2**). However, in comparison with the stoichiometric surface, ethanol was found to adsorb on a V_O site with much lower binding energy. These findings indicate that ethanol behaves differently to other gases when comparing its adsorption on the stoichiometric and defect surfaces. For example, the adsorption of molecular NO_2 on the ($2\bar{1}\bar{1}0$)-V_O surface was found to be stronger due to the presence of an oxygen vacancy site, generating a BE almost three times higher than for adsorption on a stoichiometric ($2\bar{1}\bar{1}0$) surface at the same coverage [132].

Overall, the BE values of ethanol adsorbed at the three different coverages examined indicate a stronger interaction with the ($2\bar{1}\bar{1}0$)-V_O surface compared to the ($10\bar{1}0$)-V_O surface (Table **5.2**), with more unique minimum energy structures being found at lower coverages on the former surface. Also, the interaction of ethanol with the defect ($10\bar{1}0$) and ($2\bar{1}\bar{1}0$) surfaces was found to be 12–26% and 21–39% weaker than with the stoichiometric surfaces, respectively (see Tables **5.1, 5.2, 6.1**, and **6.2**). This finding is particularly useful in identifying the relative adsorption stability of ethanol on ZnO surfaces at different molecular concentrations.

6.3.2 Geometry

The optimised geometries of ethanol adsorbed on the ($2\bar{1}\bar{1}0$) and ($2\bar{1}\bar{1}0$)-V_O surfaces are shown in Figures **6.1** and **6.2**; the structural parameters of the adsorbed configurations are summarised in Tables (**6.1**, **6.3**) and (**6.2**, **6.4**), respectively. The structures are presented in descending order of stability. In general, two types of adsorption configuration were found where the ethanol OH group aligns either along the [0001] or [$0\bar{1}10$] directions on both the

(2$\bar{1}\bar{1}$0) and (2$\bar{1}\bar{1}$0)-V_O surfaces.

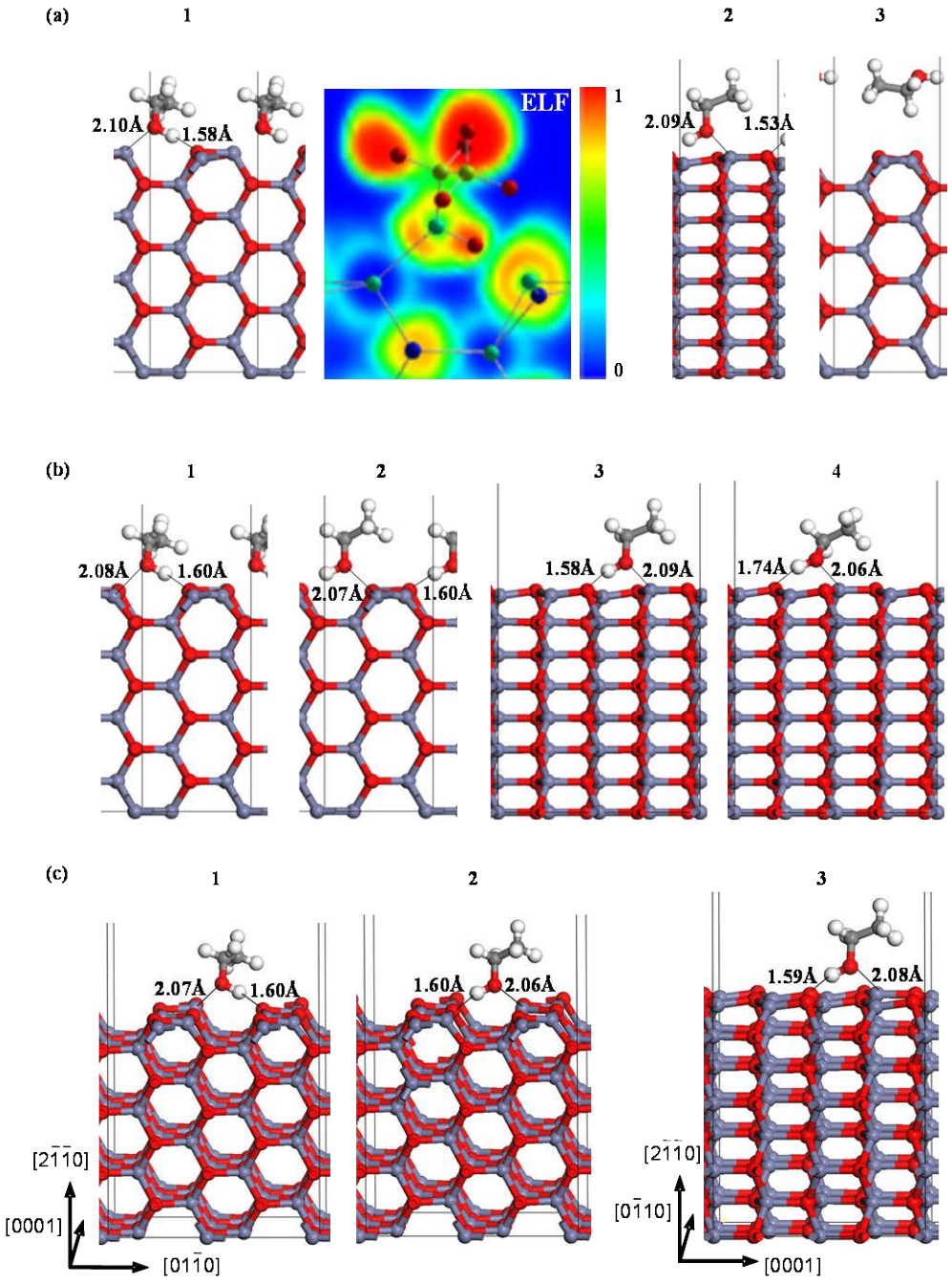

Figure 6.1 Minimum energy structures of ethanol adsorbed on the stoichiometric ZnO(2$\bar{1}\bar{1}$0) surface at: (a) 1 ML, (b) ½ ML and (c) ¼ ML coverages. The relaxed structures in c) are shown in perspective view for clearer visualisation of the surface atoms involved in the adsorption. Electron localisation function (ELF) plots are shown for the 1 ML structure 1.

Table 6.3 Calculated structural parameters for ethanol adsorbed on the ZnO($2\bar{1}\bar{1}0$) surface at the coverages indicated.

Surf.	Struct.	d(H_{ads}-O_{sub}) (Å)	∠Zn··O-C (°)	d⊥(ads-sub) (Å)	d(O_{ads}-Zn_{sub}) (Å)	∠C-C-O (°)	∠C-O-H (°)	d(C-O) (Å)	Δq (*e*)
Ethanol free molecule		-	-	-	-	107.8	108.7	1.44	-
1ML [1x1]	1	1.58	123.4	0.87	2.10	112.9	110.4	1.44	0.03
	2	1.53	122.8	0.95	2.09	110.1	110.5	1.44	0.03
	3	2.77	-	2.53	-	108.0	108.6	1.44	0.04
½ ML [1x2]	1	1.60	123.2	0.88	2.08	112.7	110.3	1.44	0.02
	2	1.60	122.3	0.88	2.07	109.2	112.5	1.44	0.02
	3	1.58	120.9	1.00	2.09	109.5	110.9	1.45	0.03
	4	1.74	125.6	1.17	2.06	107.8	116.1	1.45	0.03
¼ ML [2x2]	1	1.60	123.4	0.92	2.07	112.7	110.5	1.45	0.03
	2	1.59	122.6	1.01	2.08	109.1	112.7	1.45	0.03
	3	1.60	120.4	0.93	2.06	109.4	110.7	1.45	0.04

Distance between hydrogen of the ethanol OH group and the surface oxygen atom, **d(H_{ads}-O_{sub})**; bond angle of Zn···O-C between the oxygen and carbon atoms of ethanol and the surface zinc atom (**∠Zn···O-C**); perpendicular height of adsorbate above the top ZnO surface layer, **d⊥(ads-sub)**; distance between the O atom of ethanol and the closest Zn atom of ZnO, **d(O_{ads}-Zn_{sub})**; bond angle of C-C-O in ethanol (**∠C-C-O**); bond angle of C-O-H in ethanol (**∠C-O-H**); C-O bond length **d(C-O)**; overall transfer of charge, **Δq**.

At 1 ML coverage, ethanol adsorbs on the ($2\bar{1}\bar{1}0$) surface with the alcohol O atom at a distance from the surface Zn atom, of 2.10 and 2.09 Å, for structures 1 and 2, respectively. Compared to the bulk Zn-O bond distance of ~2.00 Å, the only slightly longer distance, d(O_{ads}-Zn_{sub}), suggests that ethanol adsorbs strongly on the surface. In addition to this interaction, the H atom of the ethanol OH group interacts with a surface O atom, whereby both the H(ethanol) to O(surface) distance, d(H_{ads}-O_{sub}), and O-H···O angles for the adsorbed structures indicate the formation of a surface hydrogen bond that leads to an increased stability. The electron localisation function (ELF) plot for structure 1 (Figure **6.1a**) confirms the formation of a hydrogen bond. We note two possible orientations of the bond, *e.g.* lying along the [$0\bar{1}10$] direction for structure 1 and along the [0001] direction

for structure 2. The former orientation may be slightly more stable due to the location of the second layer atoms that help stabilise the adsorption as they are closer to the adsorbed OH group.

For structure 3, the adsorbate molecule is located further from the surface with the alcohol OH group oriented away from the surface; hence the lack of a hydrogen bond between the adsorbate and substrate, which is consistent with the weak BE value.

At ½ ML coverage, the O-H···O bond angles and distances again indicate the formation of a hydrogen bond that stabilises structures 1, 2 and 3. Despite the similar strength of adsorption and structural parameters for structures 1 and 2, we note that the difference between these structures is due to the direction of the C-C bond, which for structure 2 is oriented along the [$0\bar{1}10$] direction. The changes to the ethanol geometry after adsorption are similar to those observed at the higher coverage as well as on the ($10\bar{1}$ 0) surface, indicating a similar interaction. At ¼ ML coverage, structures 1, 2 and 3 resemble their counterparts at ½ ML coverage, showing similar distances and angles and hence type of bonding. The most stable structures at each coverage exhibit O-H···O angles between 170–172° for the ($2\bar{1}\bar{1}0$) surface, compared to 160–165° for the ($10\bar{1}0$) surface (Table **5.1**). The more linear ∠O-H··O values for the structures on the ($2\bar{1}\bar{1}0$) surface suggest a stronger H-bond which may explain the greater adsorption strength of these structures compared to those on the ($10\bar{1}0$) surface.

At all coverages, surface relaxation of the stoichiometric ($2\bar{1}\bar{1}0$) surface due to the adsorption of ethanol (while small on both surfaces) is less significant in comparison with the stoichiometric ($10\bar{1}0$) surface (Table **5.6**). For both surfaces investigated, the adsorbate-induced surface relaxations were observed mainly at the top layer of ZnO surfaces where the ethanol adsorbs (see Table **6.1**). On the clean ($2\bar{1}\bar{1}0$) surface the topmost Zn-O bond length (1.88 Å) is similar to that on the ($10\bar{1}0$) surface (1.83 Å). Specifically, there is <0.01

Å change in the surface Zn-O bond lengths (Table **6.1**, d_1 and d_2 values) after adsorption on the (2$\bar{1}\bar{1}$0) surface, compared to <0.13 Å on the (10$\bar{1}$0) surface. The topmost Zn atom relaxes upwards by ~0.20 Å (Table **6.1**, $d_{Z1(Zn)}$) or 0.30 Å on the (2$\bar{1}\bar{1}$0) and (10$\bar{1}$0) surfaces, respectively. On both surfaces, these changes remove the tilt (Table **6.1**, θ) of the topmost Zn-O bond.

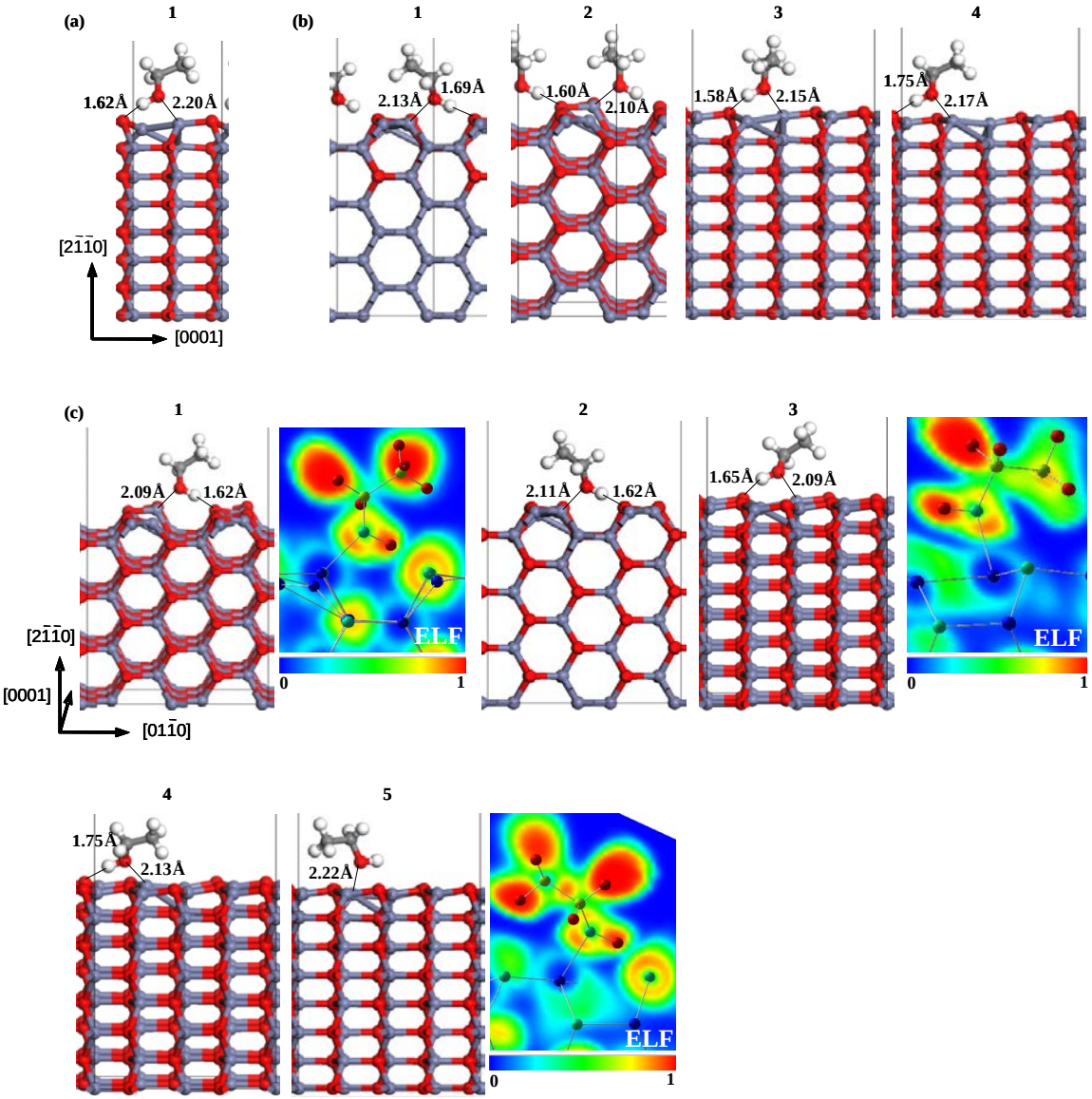

Figure 6.2 Minimum energy structures of ethanol adsorbed on the oxygen deficient ZnO(2$\bar{1}\bar{1}$0) surface at: (a) 1 ML, (b) ½ ML and (c) ¼ ML coverages. Selected ELF plots are also shown.

Table 6.4 Calculated structural parameters for ethanol adsorbed on the ZnO($2\bar{1}\bar{1}0$)-V_O surface at the coverages indicated.

Surf. ($2\bar{1}\bar{1}0$)-Vo	Struct.	BE (eV)	d(H_{ads}-O_{sub}) (Å)	∠Zn··O-C (°)	d⊥(ads-sub) (Å)	∠C-C-O (°)	∠C-O-H (°)	d(C-O) (Å)	Δq (*e*)
Ethanol free molecule		-	-	-	-	107.8	108.7	1.44	-
1 ML [1x1]	1	–0.70	1.62	118.9	1.03	110.1	108.3	1.45	–0.01
½ ML [1x2]	1	–0.93	1.69	114.1	0.82	109.1	110.5	1.45	0.01
	2	–0.91	1.60	129.9	0.84	111.6	111.7	1.44	0.00
	3	–0.76	1.58	126.1	1.01	113.6	112.4	1.45	0.01
	4	–0.72	1.75	-	-	-	-	-	-
¼ ML [2x2]	1	–1.00	1.62	115.7	0.96	111.9	120.1	1.45	0.03
	2	–0.99	1.62	122.8	0.83	109.2	110.5	1.45	0.02
	3	–0.87	1.65	128.2	1.11	108.5	115.0	1.45	0.03
	4	–0.75	1.75	136.7	1.00	109.5	111.9	1.45	-
	5	–0.43	-	97.1	1.59	108.8	109.6	1.47	0.02

Binding energy of ethanol adsorbed on the ZnO surfaces, **BE**; distance between hydrogen of the ethanol OH group and the surface oxygen atom, **d(H_{ads}-O_{sub})**; bond angle of Zn···O-C between the oxygen and carbon atoms of ethanol and the surface zinc atom (**∠Zn···O-C**); perpendicular height of adsorbate above the top ZnO surface layer, **d⊥(ads-sub)**; bond angle of C-C-O in ethanol (**∠C-C-O**); bond angle of C-O-H in ethanol (**∠C-O-H**); C-O bond length **d(C-O)**; overall transfer of charge, **Δq**.

On the defect surface at 1 ML coverage, one minimum energy structure was found, which indicates that adsorption of ethanol on the ($2\bar{1}\bar{1}0$)-V_O surface is more favourable than on the ($10\bar{1}0$)-V_O surface (Table **5.2**), where no stable structures were found at this coverage. Interestingly, the adsorbed ethanol geometry is similar to the most stable structures found on the ($10\bar{1}0$)-V_O surface at ½ and ¼ ML coverages (Figure **5.2**). As stated before, ethanol adsorbs less favorably on the defect surface compared to the stoichiometric surface, as indicated by the BE value.

At ½ ML coverage, ethanol is found to adsorb in multiple configurations on the defect surface, and more strongly than at 1 ML. Again, ethanol adsorbs more strongly when its OH group is oriented along the [$0\bar{1}10$] direction (structures 1 and 2), than along

the [0001] direction (structures 3 and 4). The difference between structures 1 and 2 is that in structure 1 ethanol adsorbs on a surface defect site Zn atom, whereas in structure 2, ethanol adsorbs on a stoichiometric site next to the oxygen vacancy. While the $d(H_{ads}\text{-}O_{sub})$ distance between ethanol and surface for structure 1 is longer compared with structure 2, the slightly higher BE value for structure 1 can be attributed to the lower perpendicular height of the adsorbate above the topmost ZnO surface layer. Structure 1 shows similar structural parameters to the most stable ethanol structure on the $(10\bar{1}0)$-V_O surface at ½ ML coverage, but the binding energy is significantly stronger (Table **5.2**). The almost linear O-H···O angle of 174° of the hydrogen bond between the ethanol and the surface on $(2\bar{1}\bar{1}0)$-V_O correlates with the greater stability than on the $(10\bar{1}0)$ surface. Compared to structures 1 and 2, the O-H···O angle for structure 3 is less linear (157°), consistent with a weaker BE. The large distance (1.75 Å) between the hydrogen atom of the ethanol OH group in structure 4 and the surface oxygen atom (Table **6.4**) explains why it has the weakest BE value at this coverage. Thus, the orientation of the ethanol OH group along the [0001] direction and the larger distance between the ethanol OH group and closest surface oxygen atom may explain why the adsorption of ethanol is weaker on the defect surface compared to that on the stoichiometric surface.

At ¼ ML, there are five unique minimum energy configurations indicating that the adsorption of ethanol is more favourable on the $(2\bar{1}\bar{1}0)$-V_O surface compared to the $(10\bar{1}0)$-V_O surface where only two unique structures were identified (Table **5.2**). Again, the ethanol OH group was aligned along the $[000\bar{1}]$ direction for the most stable structures.

The weaker adsorption of ethanol on the $(2\bar{1}\bar{1}0)$ surface at 1 and ½ ML coverages, compared to at ¼ ML, is due to the separation between the adsorbed molecules. The shortest distance between two neighboring ethanol molecules, measured along the $[0\bar{1}10]$ direction, is 5.66 Å at both 1 and ½ ML coverages, whereas it is 11.32 Å at ¼ ML

coverage. Hence, there is a greater interaction between adjacent molecules at the higher coverages that reduces the interaction with the surface. In general, the adsorption configuration of ethanol on the ($2\bar{1}\bar{1}0$) and ($2\bar{1}\bar{1}0$)-V_O surfaces can be described by the relative orientation of the alcohol OH group to the surface which is either along the [0001] or the [$0\bar{1}10$] directions. Ethanol is found to adsorb favourably above the second topmost ZnO layer atoms to allow shorter distances between the alcohol OH group and the surface zinc and oxygen atoms, as well as a lower height of the adsorbate above the ZnO surface. This is in contrast to that of the ($10\bar{1}0$) and ($10\bar{1}0$)-V_O surfaces, where ethanol can adsorb either above the first, or the second topmost surface layer atoms.

On the ($2\bar{1}\bar{1}0$)-V_O surface the oxygen vacancy site can be characterised by three Zn-Zn bonds (see L_1, L_2 and L_3 in Chapter 03 Figure **3.4**) corresponding to lengths of 2.46, 2.62 and 2.61 Å, respectively. The calculated Zn-Zn bond lengths are in good agreement with the values reported by Breedon *et al*. [132]. The orientation of the ethanol OH group above the oxygen vacancy site affects the elongation or contraction of the surface Zn-Zn bonds, with the largest lengthening of this bond being 0.15 Å and the largest contraction being 0.13 Å (Table **6.2**).

Overall, stronger BE values were calculated for adsorption of ethanol on the ($2\bar{1}\bar{1}0$) stoichiometric and defect surfaces at 1, ½ and ¼ ML coverages compared to the ethanol/ZnO($10\bar{1}0$) stoichiometric and defect surfaces (Tables **5.1** and **5.2**). This can be related to the increased surface area of the ($2\bar{1}\bar{1}0$) surface, as well as the higher oxygen content on the surface. The surface area for the ($2\bar{1}\bar{1}0$) surface is ~88% larger than that of the ($10\bar{1}0$) surface, thus resulting in less interaction between ethanol molecules in the adjacent periodic cells. In contrast to some other gases, in the case of ethanol, the V_O site of ($2\bar{1}\bar{1}0$) does not act as a reactive adsorption site since it disables the formation of the additional hydrogen bond and makes the adsorption weaker.

6.3.3 Vibrational frequencies

The ethanol vibrational frequency modes calculated after adsorption on the ($2\bar{1}\bar{1}0$) and ($2\bar{1}\bar{1}0$)-V_O surfaces are presented in Tables **6.5** and **6.6**, respectively. The calculated vibrational frequency modes of the free molecule, shown in Table **6.5**, are in good agreement with the experimental [404] and theoretical values [408] as discussed in Chapter 5. The vibrational frequency modes identified previously are also described in this chapter (Section **5.3.3**).

Table 6.5 Calculated vibrational frequencies for ethanol adsorbed on the ZnO($2\bar{1}\bar{1}0$) surface at 1, ½ and ¼ ML. All frequencies are in wave numbers (cm^{-1}).

Frequency (cm^{-1})	**Free ethanol**	**ZnO(2110) 1 ML**			**ZnO(2110) ½ ML**				**ZnO(2110) ¼ ML**		
		1	**2**	**3**	**1**	**2**	**3**	**4**	**1**	**2**	**3**
υ(O-H)	3784	2570	2462	3768	2660	2664	2740	3137	2791	2801	2760
υ($C-H_3$)a	3067 3065	3057 3034	3061 3056	3069 3050	3060 3045	3072 3055	3066 3053	3060 3052	3061 3047	3071 3054	3072 3057
υ($C-H_3$)s	2992	2959	2985	2981	2970	2985	2982	2980	2971	2987	2986
υ($C-H_2$)a	2956	3012	2982	2974	3022	3003	2990	3012	3026	3008	2999
υ($C-H_2$)s	2929	2963	2947	2891	2971	2965	2956	2968	2976	2968	2962
β($C-H_2$)	1476	1457	1468	1469	1456	1474	1471	1480	1456	1473	1472
β(C-O-H)	1225	1499	1495	1226	1491	1468	1463	1282	1468	1455	1459
υ(C-C)	1393	1360	1365	1390	1355	1363	1367	1364	1355	1366	1367
ω($C-H_2$)	1393	1343	1340	1226	1342	1342	1329	1400	1343	1336	1327
τ($C-H_2$)	1256	1272	1263	1254	1271	1270	1263	1261	1271	1268	1264
ρ($C-H_2$)	1137 797	1134 793	1139 800	1141 809	1133 792	1142 798	1140 797	1146 814	1134 793	1141 800	1141 798
υ(C-O)	1064	-	1069	1066	-	-	-	-	-	-	-
υ(C-C-O)a	1004	1037	1041	1011	1033	1043	1044	1023	1030	1038	1038
τ(O-H)	295	996	1098	300	972	948	1005	829	950	925	1004
υ(C-C-O)s	- 870	1088 869	- 869	- 878	1085 862	1082 872	1084 866	- 866	- 860	1081 871	- 864
β(C-C-O)	406	431	463	415	426	455	454	464	420	459	453

υ = stretching; β = bending; ω = wagging; τ = twisting; ρ = in-plane rocking.

Table 6.6 Calculated vibrational frequencies for ethanol adsorbed on the ZnO($2\bar{1}\bar{1}0$)-V_O surface at 1, ½ and ¼ ML. All frequencies are in wave numbers (cm^{-1}).

Frequency (cm^{-1})	**Free ethanol**	**ZnO (2110)-V_O 1 ML**	**ZnO(2110)-V_O ½ ML**				**ZnO(2110)-V_O ¼ ML**				
		1	**1**	**2**	**3**	**4**	**1**	**2**	**3**	**4**	**5**
υ(O-H)	3784	2678	2847	2655	2712	3089	2818	2819	2957	3124	3710
υ(C-H_3)a	3067 3065	3060 3056	3068 3057	3064 3056	3061 3050	3068 3052	3066 3057	3063 3055	3061 3060	3068 3058	3067 3062
υ(C-H_3)s	2992	2985	2988	2983	2978	2981	2986	2983	2984	2989	2986
υ(C-H_2)a	2956	2982	3002	3017	3025	3003	3028	3008	3010	3011	3016
υ(C-H_2)s	2929	2932	2964	2981	2982	2964	2979	2969	2974	2965	2977
β(C-H_2)	1476	1467	1477	1464	1462	1468	1482	1477	1482	1458	1475
β(C-O-H)	1225	1481	1467	1487	1423	1440	1452	1472	1304	1442	1219
υ(C-C)	1393	1366	1363	1366	1366	1362	1366	1366	1361	1355	1389
ω(C-H_2)	1393	1334	1342	1350	1347	1319	1348	1339	1408	1326	1366
τ(C-H_2)	1256	1263	1268	1275	1272	1263	1269	1267	1269	1270	1265
ρ(C-H_2)	1137 797	1137 798	1144 805	1132 780	1121 780	1140 798	1136 785	1145 804	1144 809	1136 784	1137 811
υ(C-O)	1064	-	-	-	-	-	-	-	-	-	-
υ(C-C-O)a	1004	1048	1033	1036	1029	1034	1030	1034	1023	1042	1010
τ(O-H)	295	1024	899	905	1006	911	964	925	890	801	392
υ(C-C-O)s	- 870	- 863	1078 864	1080 870	1082 858	1072 862	1079 855	1080 867	1079 861	1077 870	1041 841
β(C-C-O)	406	440	454	415	429	442	481	459	464	459	448

υ = stretching; β = bending; ω = wagging; τ = twisting; ρ = in-plane rocking

Our calculated OH stretch of the free molecule is in good agreement with the experimental (3658 cm^{-1}) and theoretical (3779 cm^{-1}) values reported by Barnes *et al*. [404] and Durig *et al.* [408], respectively. For the ($2\bar{1}\bar{1}0$) surface, the OH stretching frequency is significantly reduced after ethanol adsorption. This observation is consistent with experimental results reported previously, that show a red shift in the OH stretching mode is typically associated with an increase in the hydrogen bond strength [304]. The OH stretching frequency values calculated in this study are slightly higher than those for ethanol/ZnO($10\bar{1}0$) (Table **5.7**), which can be attributed to the small differences in the OH bond lengths and C-O-H bond angles after adsorption on the two surfaces. Nevertheless,

the shifts in the frequencies displayed similar trends to the ($10\bar{1}0$) surface, as evidenced by the blue shift of the C-O-H bending mode as well as the OH twist modes. The exception is for structure 3 at 1 ML (Table **6.5**), where ethanol is adsorbed far from the surface and is only weakly bound. It is not surprising the frequencies for this structure are hardly changed from those of the free molecule.

For the ($2\bar{1}\bar{1}0$)-V_O surface, the calculated vibrational frequency shifts again are similar to those observed for the ethanol/ZnO($10\bar{1}0$)-V_O systems, where the OH stretching frequency is significantly reduced after ethanol adsorption. Compared to the stoichiometric ($2\bar{1}\bar{1}0$) surface, the magnitude of the OH red shifts are smaller, consistent with a weaker interaction. To the best of our knowledge, detailed vibrational frequencies of ethanol adsorbed on the ($2\bar{1}\bar{1}0$) and ($2\bar{1}\bar{1}0$)-V_O surfaces have not been reported. The frequency values presented in this study may be useful for characterising the adsorbed geometry of ethanol experimentally in future studies.

6.3.4 Density of States

The total density of states (DOS) for the relaxed ($2\bar{1}\bar{1}0$) and ($2\bar{1}\bar{1}0$)-V_O surfaces, including the ethanol-adsorbed systems at ¼ ML coverage have been calculated in order to determine how the band gap changes after adsorption (Figure **6.3a**,**b**). While DFT typically underestimates the size of the band gap in semiconductor materials, a comparison of the change in band gap size is useful. It was previously shown that the DOS is directly influenced by the number of surface atoms nearest to the adsorption site (Section **5.3.4**).

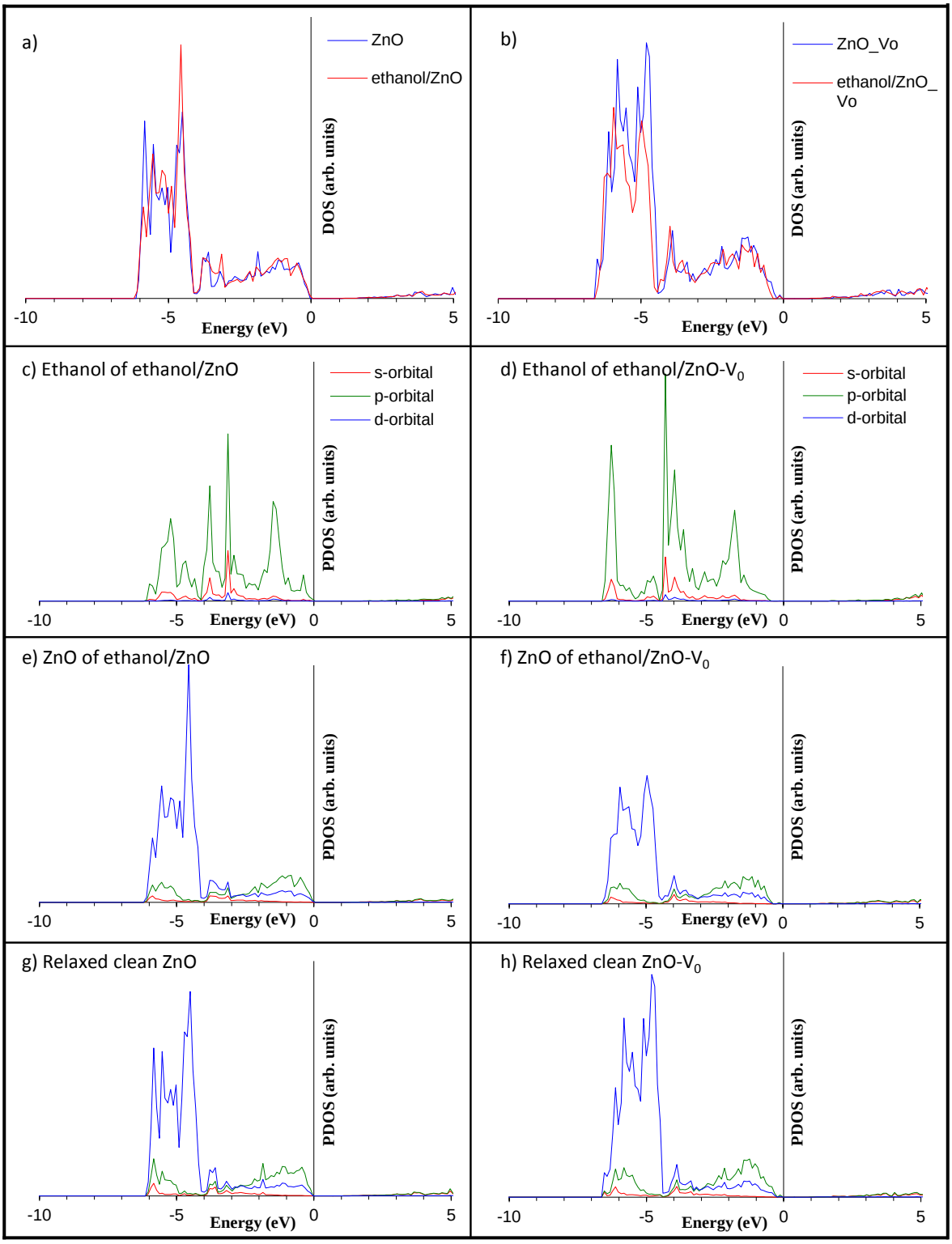

Figure 6.3 Total density of states (DOS) of clean and ethanol-adsorbed ZnO($2\bar{1}\bar{1}0$) (a) stoichiometric and (b) defect surface. For the ethanol/ZnO and ethanol/ZnO-V_O systems, the orbital resolved local DOS of the (c), (d) ethanol and (e), (f) ZnO atoms on the respective surfaces are presented. Orbital resolved local DOS of the relaxed [2x2]-sized clean (g) stoichiometric and (h) defect surfaces. The zero of energy (E_F) is aligned to the highest occupied level.

It has been previously shown that the presence of oxygen vacancies on the surface lead to a band gap narrowing [409]. In our calculations, the introduction of a V_O on the ZnO($2\bar{1}\bar{1}0$) surface indeed caused a band gap narrowing compared to the stoichiometric surface, as was also found for the ZnO($10\bar{1}0$) surface (see Section **5.3.4**). Specifically, the band gap for the clean ($2\bar{1}\bar{1}0$) and ($2\bar{1}\bar{1}0$)-V_O surfaces in a [2x2] cell was calculated to be 1.02 and 0.92 eV, respectively.

After adsorption of ethanol on the stoichiometric and defect surfaces at ¼ ML coverage, the most stable structures showed a band gap narrowing of 0.03 and 0.15 eV, respectively. These changes to the band gap after adsorption of ethanol are in good agreement with experiments that report an increase in conductivity after detection of ethanol, indicating a donation of electrons from ethanol to ZnO, resulting in an increased surface electron concentration [405]. The magnitude of the charge transfer for the most stable structures at ¼ ML coverage on the stoichiometric and defect surfaces was found to be 0.03 and 0.02 *e*, respectively, indicating that ethanol donates charge to the surface. A similar transfer of charge was reported for the chemisorption of ethanol on MgO(100) [410] and ZnO($10\bar{1}0$) [401] surfaces. A charge transfer of 0.03 and 0.02 *e* was also calculated for ethanol adsorbed on the ZnO ($10\bar{1}0$) and ($10\bar{1}0$)-V_O surfaces, respectively (see Chapter 5).

As a comparison, the charge-accepting NO_2 molecule was found to adsorb on the ($2\bar{1}\bar{1}0$)-V_O surface with a charge transfer value of 1.25 *e*, suggesting a significant decrease in the ZnO surface conductivity after adsorption [132]. While the adsorbate-induced charge transfer is less for ethanol (as compared to NO_2) on the ($2\bar{1}\bar{1}0$)-V_O surface, this can be ascribed to the smaller structural changes that ethanol undergoes on the surface. In contrast, the NO_2-induced ($2\bar{1}\bar{1}0$)-V_O surface reconstruction was found to be significant, with large increase in the Zn-Zn bond lengths for all the adsorbed NO_2 molecule structures

[132]. This transfer of charge to the ZnO surfaces confirms ethanol as a reducing gas leading to an increase in conductivity, which is consistent with experimental findings [405].

6.3.5 Orientational Effects on Monolayer Adsorption Stability

To investigate the possibility of hydrogen bonds forming between neighboring ethanol molecules and the effects of ethanol orientation on the surface, two ethanol molecules in different adsorption configurations were placed in a [1x2] supercell to form a superstructure. Parallel (1_P) and anti-parallel (2_{AP}) arrangements of the ethanol molecules within the supercell were examined on both surfaces. The BE values and structural parameters of the optimised superstructures are shown in Tables **6.1** and **6.2**, with the optimized geometries shown in Figure **6.4**.

We adopted two approaches to calculating the BE values for the optimised superstructures: (1) co-adsorption of the two molecules; (2) sequential adsorption of two ethanol molecules on the surface. The latter model had a pre-adsorbed ethanol on the surface at ½ ML coverage before an extra molecule was added. The binding energy (BE) values for the two molecules adsorbed on the ($2\bar{1}\bar{1}0$) superstructures were calculated by employing equations **3.2** and **3.3** (see Chapter 3 Section **3.3.1**). The two ethanol molecules ($ethanol_{01}$ and $ethanol_{02}$) can be treated as equivalent interacting molecules in the co-adsorption BE calculation. For the sequential adsorption calculation, $ethanol_{01}$ is the pre-adsorbed ethanol molecule on the surface. The BE value for the sequential adsorption was evaluated by subtracting the total energy of an isolated ethanol molecule and the pre-adsorbed ethanol at ½ ML coverage from the total energy of the optimised superstructure (see equation **3.2**).

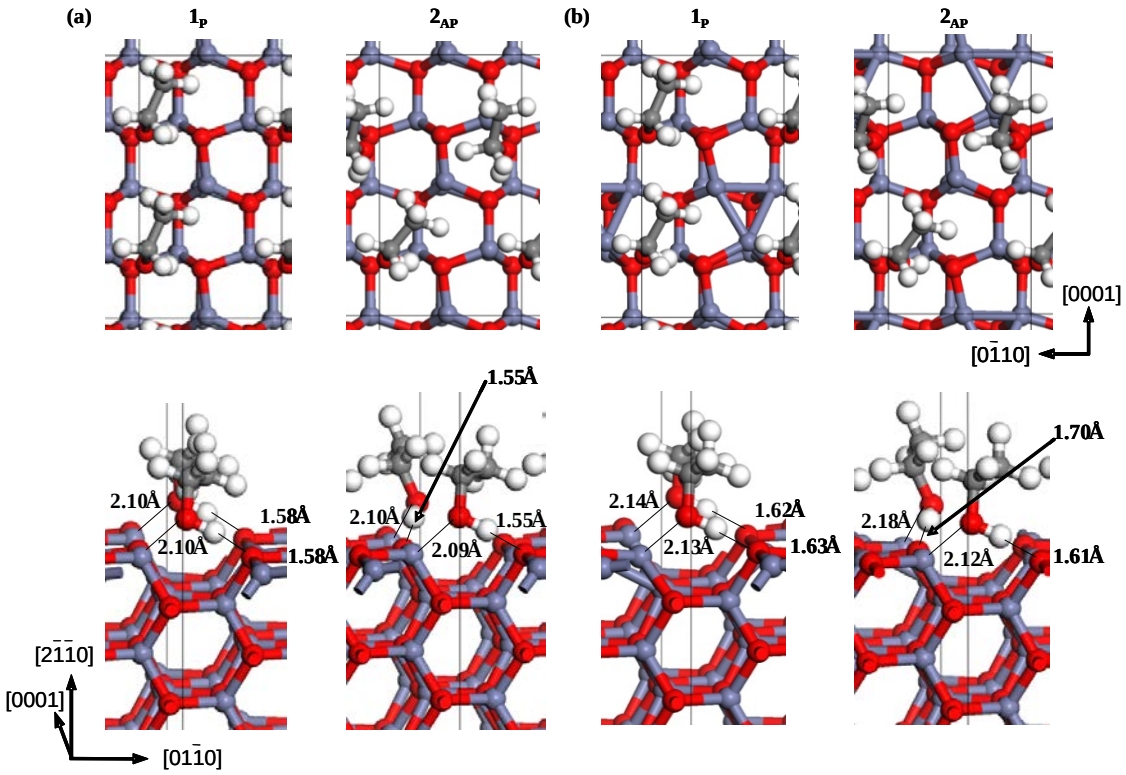

Figure 6.4 Top and side views of the converged superstructures of ethanol adsorbed on: (a) ZnO(2$\bar{1}\bar{1}$0) and (b) ZnO(2$\bar{1}\bar{1}$0)-V_O at 1 ML coverage.

Stable superstructures of ethanol molecules in parallel and anti-parallel configurations can exist on both the stoichiometric and defect surfaces. The calculated BE values for ethanol adsorption, whether simultaneously or sequentially (see Tables **6.1** and **6.2**), can be indicative of the adsorption preference of the gas molecules on these surfaces. For the stoichiometric surface, the calculated BE values indicated that a parallel arrangement of ethanol molecules is more likely to be formed via co-adsorption (–1.01 eV) than via sequential adsorption (–0.96 eV), whereas on the defect surface, co- (-0.92 eV) or sequential (–0.91 eV) adsorption is of almost equal stability. Hence, for all superstructures studied, the calculated BE values indicated that co-adsorption is favourable over sequential adsorption, except on the defect surface in the anti-parallel arrangement.

The shift to a lower vibrational frequency of the OH stretching mode supports the

formation of hydrogen bonds in the parallel (2590 and 2574 cm^{-1}) and anti-parallel (2479 and 2541 cm^{-1}) configurations. The change in the calculated O-H stretching frequency again serves as a good indication of the adsorption strength.

6.4 Summary

ZnO materials that contain surface oxygen vacancies play a pivotal role in the conductometric gas sensing efficiency of nanosensors, where the sensing performance of different ZnO-V_O surfaces varies depending on the V_O concentration. This chapter provided an insight into the relationship between the binding energy, charge transfer and band gap changes and the structural properties of the adsorption interactions (such as the type of surface, surface area-to-volume ratio, coverage, surface oxygen vacancy, and the adsorbate molecule content), where they have been shown to affect the overall sensing performance of a semiconducting gas sensor. We found that ethanol adsorption is more favourable on the stoichiometric ($2\bar{1}\bar{1}0$) surface, compared to the more stable ($10\bar{1}0$) surface, most likely due to the larger surface area and the higher density of surface oxygen atoms available. While multiple stable configurations of adsorbed ethanol were found on the stoichiometric and defect sites at all coverages investigated, ethanol adsorbs most strongly on the ($2\bar{1}\bar{1}0$) surface at ¼ ML coverage due to the reduced interactions between adjacent molecules on the surface. Besides the primary O_{ads}-Zn_{sub} interaction, ethanol adsorption was further stabilised by the formation of a hydrogen bond with a surface oxygen atom, which is particularly strong when the ethanol OH group is aligned along the [$0\bar{1}10$] direction. Minor surface relaxations did not cause significant structural changes, and are smaller in comparison with those observed on the ($10\bar{1}0$) and ($10\bar{1}0$)-V_O surfaces. Hence, ZnO nanostructures with ($2\bar{1}\bar{1}0$) crystal facets may show less structural changes when used for ethanol sensing. Similar to the ($10\bar{1}0$) surface, the presence of oxygen

vacancies did not enhance the binding energy of the ($2\bar{1}\bar{1}0$) surface towards ethanol, although the reduction in the binding strength caused by the ($2\bar{1}\bar{1}0$)-V_O surface was not as severe as that on the ($10\bar{1}0$)-V_O surface. The adsorption of ethanol superstructures on both the ($2\bar{1}\bar{1}0$) stoichiometric and oxygen deficient surfaces showed that it is more likely for ethanol to form a highly uniform arrangement where the molecules are similarly (parallel) oriented on the surface. No difference was found between the simultaneous or sequential adsorption of ethanol on the ($2\bar{1}\bar{1}0$) and ($2\bar{1}\bar{1}0$)-V_O surfaces unlike on the ($10\bar{1}0$) and ($10\bar{1}$ 0)-V_O surfaces.

The adsorption interaction of ethanol on ZnO can be suggested to involve charge transfer from ethanol to the surface after adsorption that is associated with the calculated band gap narrowing, corresponding to an increase of the substrate conductivity. The favourable adsorption of ethanol at a variety of concentrations (or coverages) explains why ZnO nanostructures comprising the ($2\bar{1}\bar{1}0$) surface morphology can be highly efficient for gas sensing applications in line with experimental observations.

Chapter 7

Experimental Study of Gas Interaction in ZnO Nanomaterials

7.1 Background

This chapter is devoted to the experiments that we conducted in order to elucidate the interaction of different gas molecules with ZnO nanoparticles. From the theoretical point of view, the use of *ab-initio* density functional theory (DFT) method for gas sensing studies provided us with structural and electronic properties of ZnO based nanostructures at the atomic scale. Here, we employ multiple characterisation techniques to study the interaction of different gases with ZnO nanoparticles, where theoretical and experimental results are compared where appropriate. The outcomes of this chapter have been published in the Journal of Nanotechnology [28].

As was established in previous chapters, the gases and vapour species we have investigated based on DFT calculations include ethanol (CH_3CH_2OH) and nitrous oxide (N_2O). The focus of this chapter is only on the interaction of ZnO nanostructures with a

small molecule, namely the hydrogen (H_2) gas. Larger molecules, such as CH_3CH_2OH and N_2O will be considered in future work.

There are several reports on the interaction study of H_2 with ZnO. Lavrov *et al.* [411] identified two shallow donors of hydrogen (H_2) using Raman spectroscopy, as bond-centered hydrogen (H_{BC}) and hydrogen bound within the oxygen vacancy (H_O). H_{BC} was found to be unstable at annealing temperatures above 190 °C. However, the H_O donor was found to be stable at temperatures up to 500 °C. It was also believed that these H shallow donors (typically found in hydrothermally grown ZnO samples) are undetected in the sample using IR spectroscopy, even though they have sufficient thermal stability to remain in ZnO for a month or longer at room temperature [412, 413]. Two OH local vibrational modes (3326 and 3611 cm^{-1}) were identified directly using IR absorption spectroscopy when ZnO was annealed in H_2 gas at ambient temperature [412, 414]. Nonetheless, these two IR absorption lines are strongly dependent on the source of the ZnO material; therefore, shifted IR spectral lines are expected for different ZnO nanostructures. In order to completely remove hydrogen from ZnO, an annealing temperature of at least 500–700 °C is necessary, depending on the ZnO source material [412, 415, 416]. Atomic hydrogen present in ZnO can be reactive enough to reduce the Zn-polar surface of the ZnO(0001) material into metallic Zn clusters, yet can be almost inert on the O-polar ZnO($000\bar{1}$) surface [417]. When annealed at higher temperatures, the number of interstitials (Zn_i) accumulating on the ZnO surfaces increases, leading to an abundant number of oxygen vacancies (V_O) in the oxide material. Zn_i, in this instance, act as a shallow donor on the surface [368].

The effects of hydrogen on ZnO, with different morphologies and stoichiometry, have also been investigated using different methods [415, 418, 419]. However, conclusive experimental studies of the interaction of hydrogen with ZnO nanostructures are far fewer in number. It has been suggested that hydrogen is much more susceptible to being trapped

between, or adsorbed onto ZnO nanoparticles, due to the increased surface area and larger amount of interstitial spacing between individual nanostructures, as opposed to microstructures [27]. Using DFT calculations, it has been demonstrated that hydrogen can be molecularly and dissociatively adsorbed between closely spaced ZnO nanorods, which provided an explanation as to why the nanostructures perform better in gas sensing applications [27]. It has been shown that the behaviour of macroscopic hexagonal ZnO prisms [411] was quite different to that of ZnO nanoparticles in studying a particular gas reaction. Additionally, there are different views on what the optimum temperature should be for the gas-ZnO interaction [43], as well as what dopants and concentrations are best [46, 420]. However, understanding the detailed properties of H interacting with ZnO nanostructures obtained from different sources also remains limited.

To date, there have been very few, if any, reports on the *in-situ* analysis of the gas-surface interaction using Raman spectroscopy, which are also confirmed by other characterization techniques such as x-ray diffraction (XRD) and Fourier transform infrared (FTIR) spectroscopy. IR absorption studies of hydrogen in ZnO at a high temperature have been performed, but IR absorption data at a lower temperature has not been reported [421]. It has been suggested that the direct IR measurement of H-related shallow donors in ZnO is hardly possible [421]. In several investigations, there have been reports on the existence of IR absorption lines, and Raman and photoconductivity signals that are being detected but they have not been clearly assigned to hydrogen-related defects, as indicated in the publications of Lavrov [411, 422].

Very few experimental investigations reported real time monitoring of the interaction of hydrogen with ZnO surfaces. For ZnO powders, in particular, Windisch *et al*. [423] suggest that further testing is needed in order to make direct comparisons between XRD and Raman spectra results in order to determine the presence of hydrogen. Also, the work by Du and Biswas [424] advise that there appears to be a hidden hydrogen reservoir

in ZnO that is invisible to IR spectroscopy, which can be associated with an interstitial H_2 species [424].

In light of the aforementioned uncertainties, we conduct *in situ* Raman spectroscopy, and *ex situ* XRD and IR spectroscopy characterisation experiments to investigate H_2-ZnO interactions within ZnO nanopowders of various dimensions. The primary focus of this study is to determine the effect of H_2 on the IR, Raman spectra and XRD peak positions and relative intensities obtained from the H_2 exposed ZnO nanopowders and analysing the results.

7.2 Characterisation Equipment and Methods

Two different sizes of ZnO nanopowders used in this study (Samples A and B) were sourced from Sigma Aldrich (< 50 nm particle size) and CRM (China Rare Metal Material Co.), respectively, both with 99.99% purity. The polycrystalline powders were drop cast deposited onto quartz substrates after being dispersed in ethanol solution, and then heat treated (80 °C) on a hot plate to remove the volatile compound.

The morphology of the samples was characterised by scanning electron microscopy (SEM) and transmission electron microscopy (TEM). SEM was performed using a FEI Nova NanoSEM operating at 15kV in immersion mode. ZnO powders were deposited onto silicon substrates to prevent electron charging, using the same procedure as the deposition of ZnO on quartz substrates. TEM was performed using a JEOL 2010 TEM equipped with a LaB_6 filament operating at 200 kV. TEM samples were prepared by dropping the nanoparticles on a copper grid (Lacey GSCu300FL).

The customised Raman spectrometer for this *in-situ* study consists of a sample chamber (Linkham HFS91-PB4) that has a quartz glass cover to allow the penetration of

the Raman system laser. It was equipped with a built-in sample heater and thermostat. The chamber outlet connects to a mass flow controller, regulating the flow of gas at 200 standard cubic centimetre per minute (sccm). *In situ* Raman spectroscopy was carried out with the sample chamber positioned under a standard Olympus microscope (Olympus objective lens Mplan 10× or SLMplan 50×) equipped with a 532 nm green laser (Shanghai Dream SD2-532-050T). The Raman spectra were collected and analysed using Spectrasuite 2009 software.

The crystal structure of the ZnO nanoparticles was studied by XRD using a Bruker D8 ADVANCE diffractometer fitted with a scintillation counter detector, using graphite-monochromated Cu Kα (lambda = 1.5406 Å) radiation. Data were collected at room temperature with a scan range of 2θ = 5–70°, a step size of 0.02°, and a count time of 2 seconds per step.

Diffuse reflectance infrared Fourier transform (DRIFT) spectroscopy was employed to study the ZnO surface vibrational frequency using a Perkin Elmer Spotlight 400 device. The samples were then mixed with potassium bromide (KBr powder), which is transparent to the incident IR radiation, and pressed into pellets for the IR absorbance analysis. The KBr powder must be of spectroscopy grade and spectroscopically dry [425]. As a result, the powder was heated at 100 °C for a few minutes to remove residual water.

7.3 Procedures

The ZnO samples (samples A and B) were annealed before being exposed to target gases. Sample A consist of ZnO grains in the order of less than 50 nm and sample B consist of grains in the order of several hundreds of nm. The ZnO samples were annealed at 300 °C, using a ramping rate of 20 °C per minute. It is suggested that such an annealing

temperature can only eliminate ~ 80% of the interstitial hydrogen from the ZnO interstitial site (H_i^+), leaving the more thermally stable hydrogen in the defect site (shallow donor, H_O^+) in ZnO [412]. Nevertheless, the majority of the H donors were removed from the surface, as will be shown later in the characterisation results.

In situ Raman spectrum measurements were carried out when the ZnO samples were exposed to the following gas mixtures: N_2, 3% H_2 in N_2 balance (*i.e.* 97% N_2), and zero air. Zero grade air contains ~23% purified oxygen, with the remaining being nitrogen, and 1 ppm total hydrocarbon (THC). N_2 gas served as an inert gas carrier for the H_2, while zero air replenished the O-atom lost during the H_2/ZnO interaction. In the experiment, the ZnO samples were placed in the chamber at room temperature and a Raman spectrum was taken as a background comparison. Following that, Raman spectra were taken throughout three different durations (30 minutes for N_2, 10 minutes 3% H_2 in N_2 balance, and 20 minutes in zero air). The measurements were conducted at 300 °C.

For the XRD measurements, the two ZnO nanopowder samples were exposed to 3% H_2 in N_2 balance for 30 mins at 300 °C. After that, one sample was examined immediately, while the other was stored in atmospheric condition for 5 days at room temperature before being examined.

For the FTIR measurements, the two ZnO nanopowder samples were annealed at 300°C for 30 minutes, one in zero air and the other in 3% H_2 in N_2 balance. These samples were then mixed with IR grade potassium bromide (KBr powder) and pressed into pellets for the IR absorbance analysis. A DRIFT experiment was carried out to study the change in frequency of the ZnO local vibrational modes induced by the presence of H_2 using the FTIR spectrometer (Perkin Elmer Spotlight 400).

7.4 Results

Here, we present and discuss the characterisation experiments conducted to assess the effect of H_2 gas exposure on ZnO nanopowder samples, that lead to the identification of the resulting gas-surface interactions.

7.4.1 Scanning Electron Microscopy

SEM images of the two different types of ZnO nanopowders are shown in Figure **7.1**.

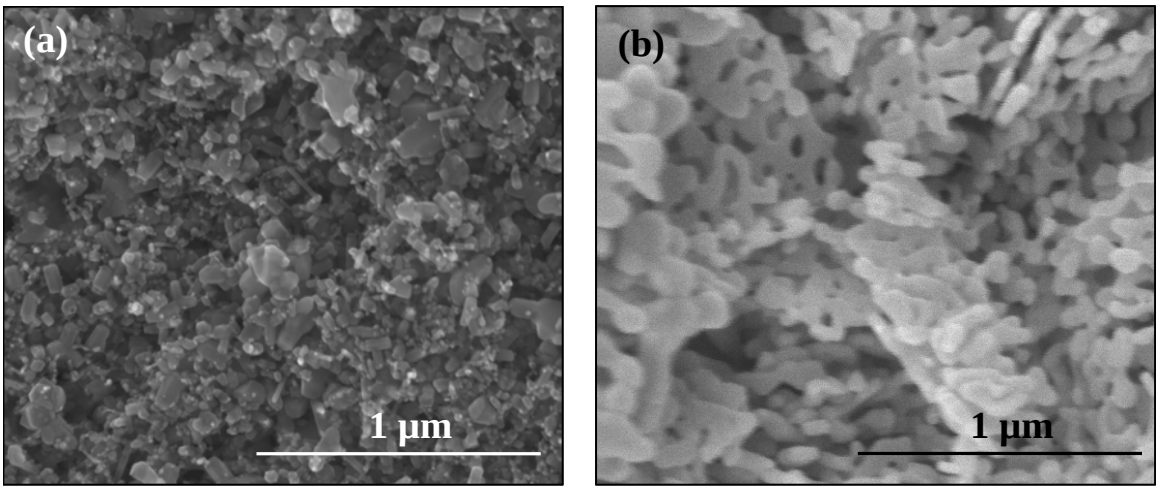

Figure 7.1 SEM micrographs of the prepared ZnO nanopowder samples obtained from (a) Sigma Aldrich (sample A) and (b) CRM (sample B).

As can be seen there is clear distinction between the two types of nanopowders in terms of their structural dimensions and homogeneity. The grain sizes of the annealed ZnO nanopowder samples from CRM (sample B) are much larger and different than those of Sigma Aldrich (sample A). For sample A (Figure **7.1(a)**), ZnO nanograins of varying sizes were identified on the substrate, being typically as small as 10 nm to as large as several tens of nm in length. However, the average grain size was overall less than 50 nm. The dimensions of the annealed ZnO nanopowder sourced from sample B were found to be of the order of several hundreds of nm.

7.4.2 Transmission Electron Microscopy

TEM images for samples A and B are shown in Figure **7.2**. ZnO nanoparticles with varying grain sizes are evident in Figure **7.2(a)**, whereas it is apparent that sample B is composed of larger particles with spherical morphology as shown in Figure **7.2(b)**, which is in good agreement with the SEM images obtained.

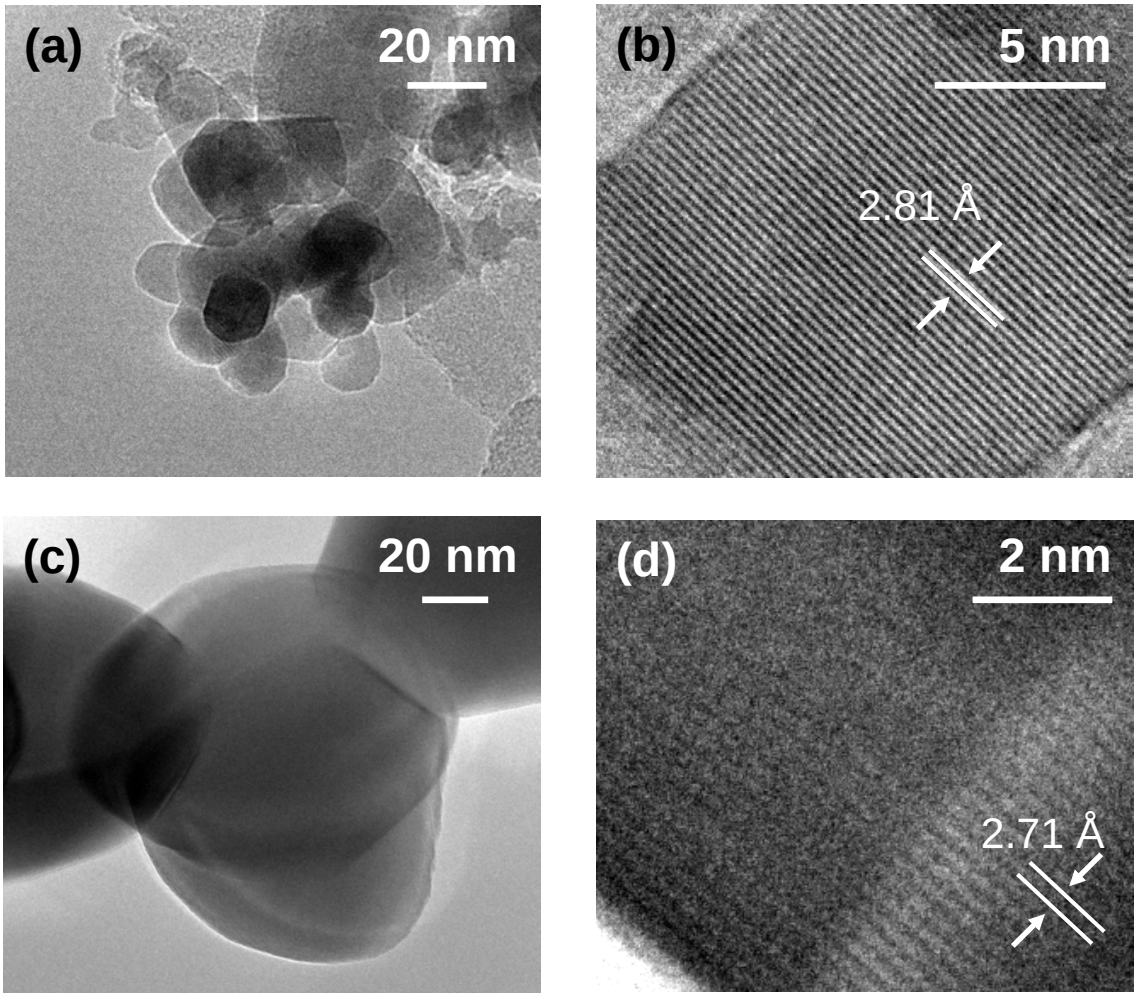

Figure 7.2 TEM micrographs of the non-annealed samples A (a) and B (c). Higher resolution images (b) and (d) are seen showing the atomic structures and lattice spacings of the ZnO samples A and B, respectively.

It can be seen that the nanoparticles are crystalline with lattice spacings of 2.81 and 2.71 Å for samples A and B, respectively. The lattice spacing in sample A can be

correlated to the $(10\bar{1}0)$ planes in the ZnO crystal structure, whereas the calculated lattice spacing in sample B may be identified as the (0002) lattice plane of the ZnO nanopowder [426].

7.4.3 Raman Spectroscopy

Raman spectroscopy was conducted during the exposure of both samples to a selected mixture of gases. Raman spectroscopy was utilized as it can be the best tool to reveal any surface interactions with the target gas due to its sensitivity to the type of functional groups that can be formed as a result of such interactions. In our apparatus, the customised gas chamber could allow *in situ* observations of the surface reaction of hydrogen with both ZnO nanopowder samples in real time.

The Raman spectra of sample A exposed to N_2, 3% H_2 in N_2 and zero air at 300 °C are shown in Figure **7.3**; the Raman spectra of sample B for the same conditions are shown in Figure **7.4**. The phonon modes, observed in this study, have been previously reported in Raman spectra [428, 431]. The identified Raman band modes are the E_2(high) at 435 cm^{-1}, A_1 longitudinal optical (LO) at 543 cm^{-1}, E_1 longitudinal optical (LO) at 566 cm^{-1}, and a secondary A_1 longitudinal optical (2LO) at 1105 cm^{-1} [427]. A_1 and E_1 are the polar modes, and are both Raman and infrared active [429]. Another low frequency feature involving bands associated with the difference between the E_2(high) and E_2(low) modes was also identified at 333 cm^{-1} [423]. Conversely, the E_2 modes, E_2(high) and E_2(low), are non-polar and are Raman active only [429]. There exists a peak at 979 cm^{-1} that has been assigned as A_1(LO)+E_2(high) mode, which is known to correspond to the vibrational mode caused by the two phonon combination [427].

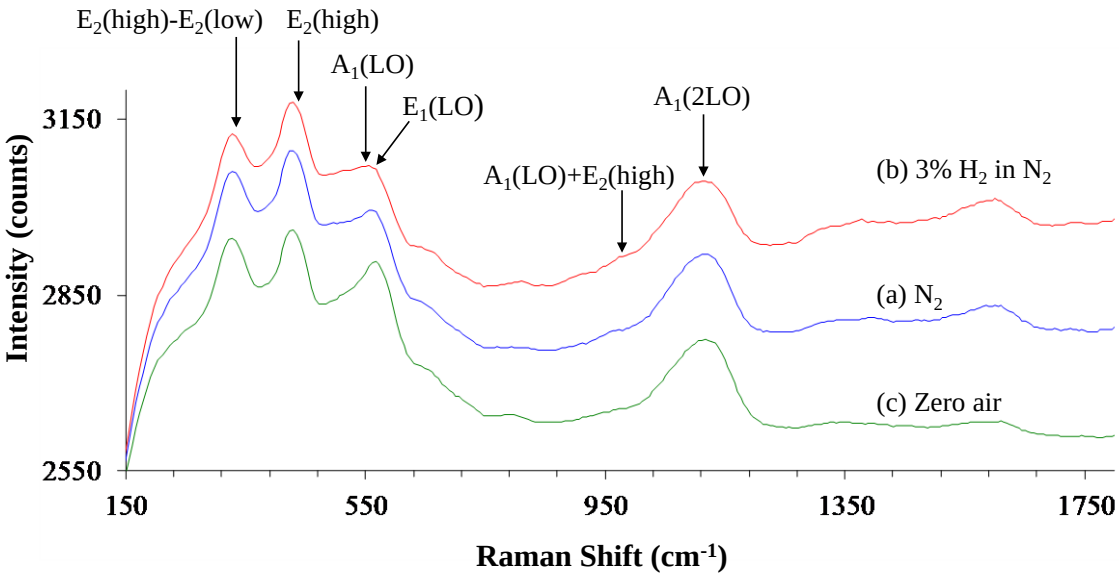

Figure 7.3 Raman spectra of sample A annealed at 300 °C sequentially in (a) N_2, (b) 3% H_2 in N_2, and (c) zero air.

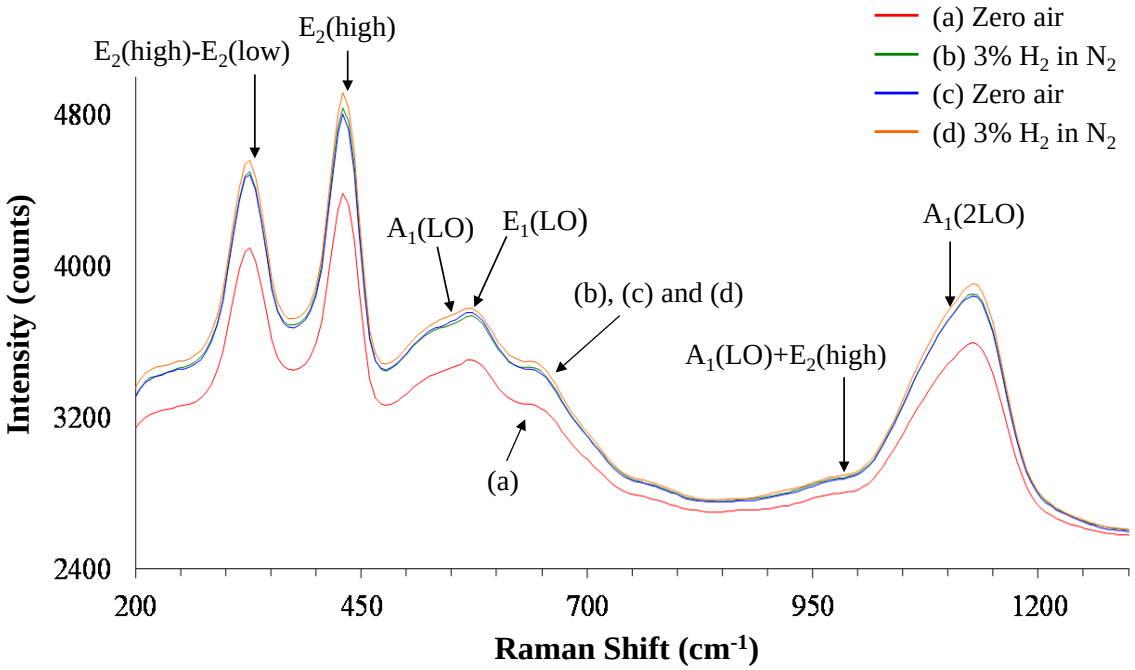

Figure 7.4 Raman spectra of sample B annealed and recorded at 300 °C sequentially in (a) zero air, (b) 3% H_2 in N_2, (c) zero air and (d) 3% H_2 in N_2.

The most intense mode identified in the Raman spectra of the ZnO nanopowder samples is in good agreement with previously reported values, and corresponds to the oxygen vibration mode E_2(high) of ZnO [428, 429]. A strong peak at the E_2(high) mode correlates to the oxygen vibration in the ZnO crystal lattice, and hence good crystallinity [427, 429]. Conversely, the relatively weak signal mode at E_2(high) suggests poor crystallinity of the ZnO nanostructures. The relative interaction of this band [427], thus indicated poorer crystallinity of sample A (smaller sized ZnO nanopowder), with a higher degree of crystallinity for sample B.

The A_1(LO) and the E_1(LO) modes at 543 and 566 cm^{-1} wavenumbers, respectively, are fairly close to each other and would be unresolved. The very weak A_1(LO) mode has been reported [423, 430, 431] but rarely assigned a band mode in the literature [423]. The present band at 566 cm^{-1} is thus considered to be predominant (E_1(LO)). A detailed relationship between the A_1(LO) and E_1(LO) modes however has been reported by Cusco *et al.*, where the E_1(LO) mode is more strongly affected by impurity and/or defect than the A_1(LO) mode [431]. The intensity of the E_1(LO) mode is correlated with surface defects such as oxygen vacancy or Zn interstitials in the nanopowder. Thus, the E_1(LO) mode which is present in the obtained spectra, indicates the presence of defects in the ZnO samples [430].

For the interaction of hydrogen with sample B (larger sized ZnO nanopowder), a similar pattern of Raman signals was identified. Two measurements (each in zero air and 3% H_2 in N_2) were carried out and depict the similar trend of gas/ZnO interaction and repeatability. The relatively sharper E_2(high) peak indicates a more homogeneous distribution of the nanopowder grain size and dimension. Comparing the relative ratio of the A_1(LO) and E_1(LO) modes to the E_2(high) mode, where the later peak is much more dominant, it can be implied that the ZnO nanopowder sample contains lesser amount of surface defects.

For sample A, the intensity of the Raman peak at 483 cm^{-1} increased more significantly after exposure to 3% H_2 in a balance of N_2 gas, relative to the other two exposures (Figure **7.3**). The intensity of this particular band has been observed to be dependent to the presence of H_2 [423]. While Windisch *et al.* reported an additional peak at ~570 cm^{-1}, and regarded it as an anomalous mode arising from oxygen vacancies in ZnO powders, Wang *et al.* assigned this peak to the E_1-LO mode of oxygen deficiency in ZnO nanowires [423, 432]. Xu *et al*. have also reported a strong intensity of the E_1(LO) band with a sharp peak at 556 cm^{-1}, indicating their thin film was severely oxygen deficient [433].

In all these studies, none of the authors have identified a band that could be correlated with the presence of hydrogen (and the formation of hydroxyl groups) on the ZnO surface. The formation of surface hydroxyls has been reported, however, mostly by FTIR or photoluminescence methods [434, 435]. We thus suggest that the H-sensitive peak at 483 cm^{-1} can be associated with OH formation. To the best of our knowledge, the identification of a Raman peak correlated with a surface hydroxyl species has not been presented previously. We therefore conducted complementary XRD and FTIR characterization of the ZnO samples after the exposure to H_2 to find any correlation of the 483 cm^{-1} band with the formation of surface hydroxyl groups on the ZnO nanopowder surfaces.

A similar procedure for H_2 exposure was applied to ZnO nanopowder sample B. No change of peak was observed in this experiment. It seems that the high crystallinity and grain size of nanopowder sample B is an important factor to inhibit the H_2 gas interaction with ZnO.

7.4.4 X-ray Diffraction

A series of XRD measurements were carried out to identify the presence of surface hydroxyl groups in the ZnO samples. The XRD patterns of sample A before annealing, after annealing, and after exposure to H_2, are shown in Figure **7.5 (a)** and **(b)**. Figure **7.6** shows the XRD patterns of samples A and B annealed at 300 °C. Similarly, the XRD patterns of sample B, before and after exposure to H_2 can be found in Figure **7.7**.

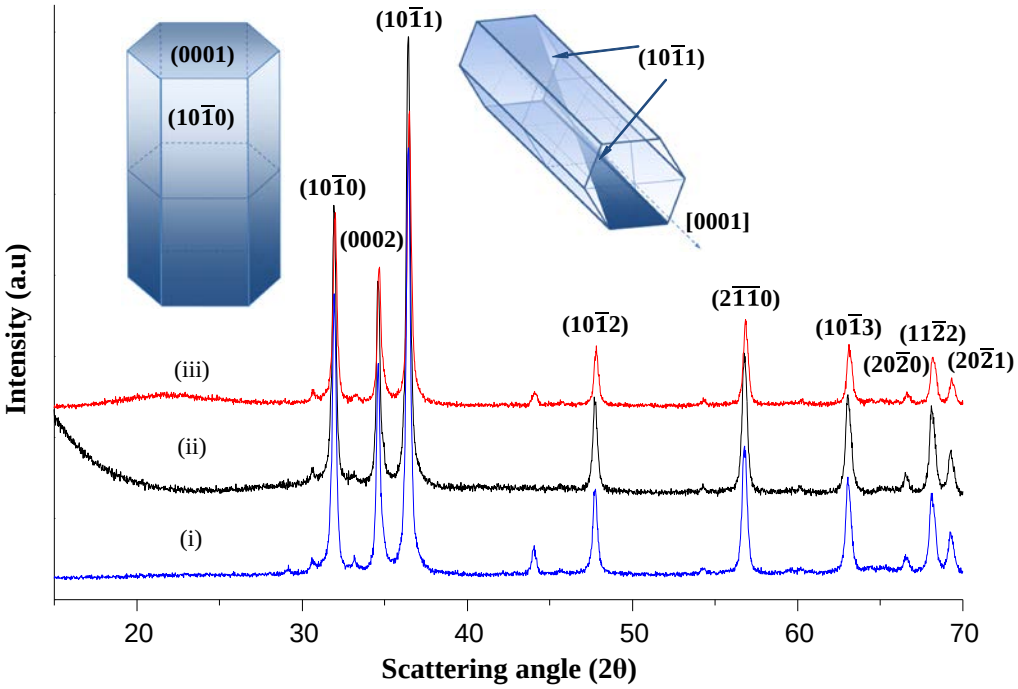

Figure 7.5(a) XRD patterns of sample A: (i) before annealing (hydrated), (ii) annealed at 300 °C in atmosphere and (iii) taken immediately after annealing (300 °C) with 3% H_2 in N_2 balance.

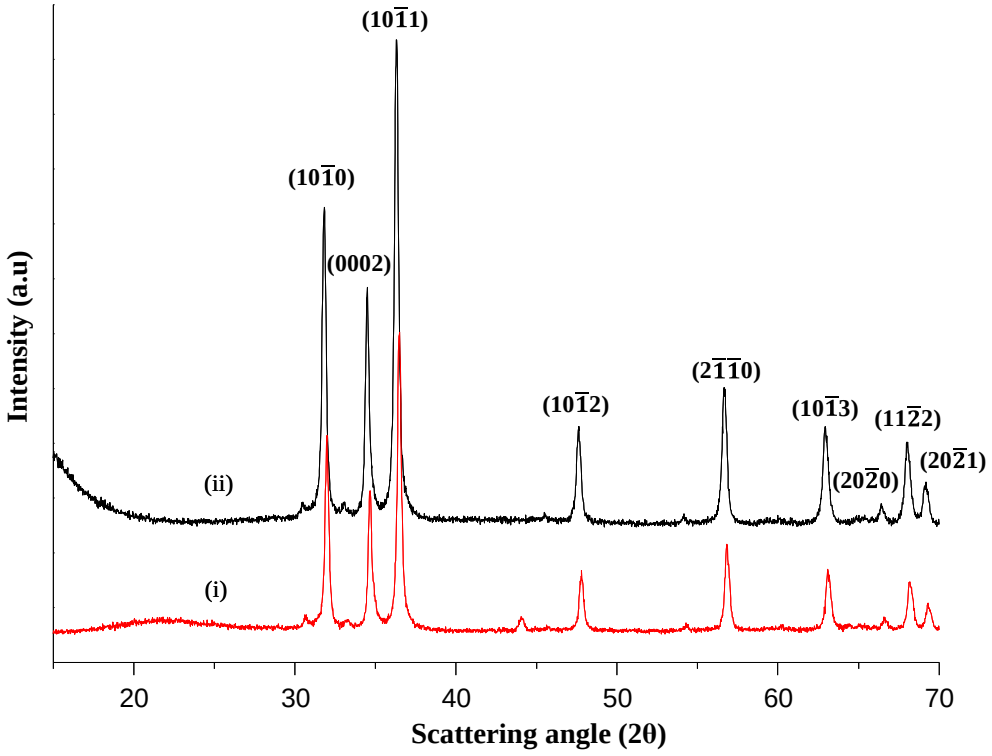

Figure 7.5(b) XRD patterns of sample A annealed at 300 °C with 3% H_2 in N_2 balance: (i) XRD measurement performed immediately after the annealing and (ii) XRD measurement performed five days after the annealing.

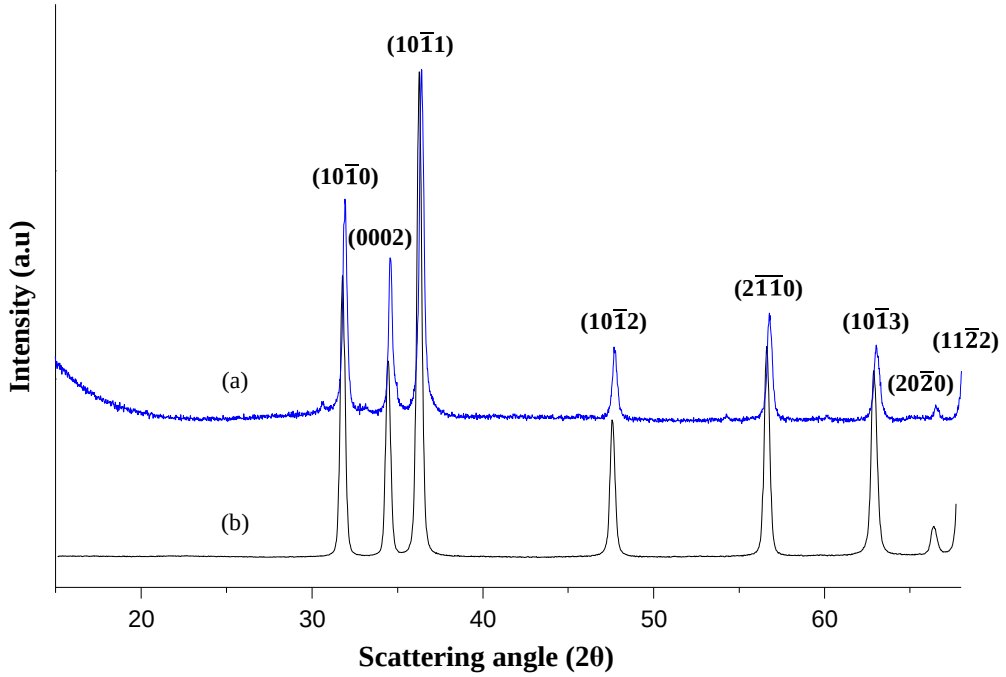

Figure 7.6 XRD patterns of: (a) sample A and (b) sample B, both annealed at 300 °C in atmosphere.

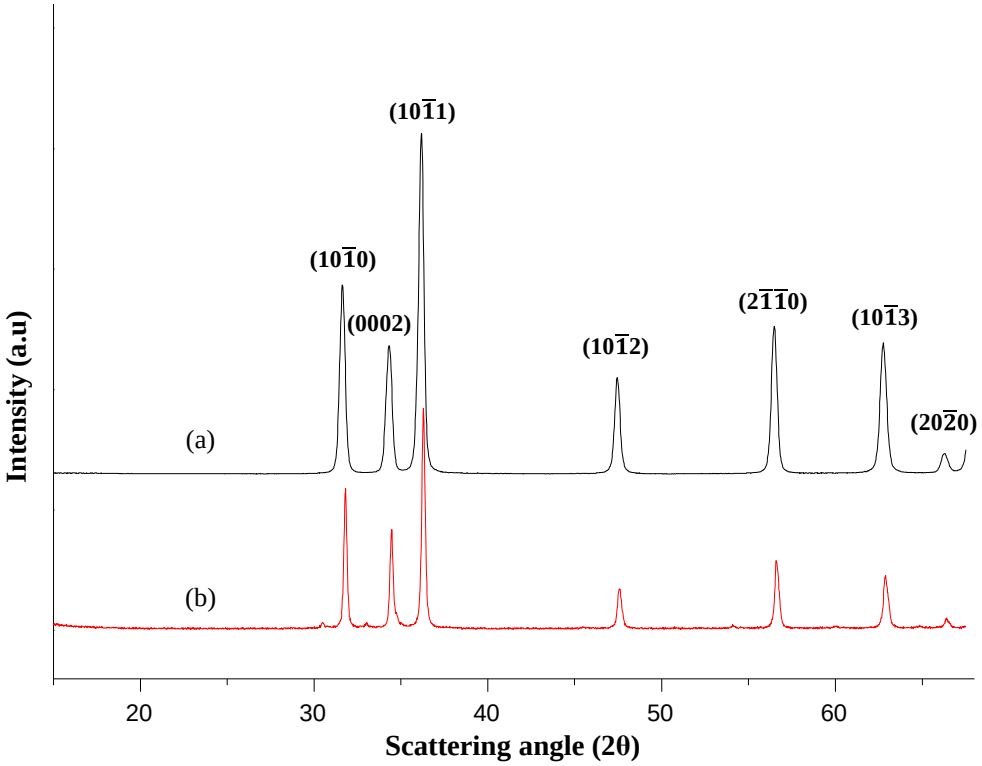

Figure 7.7 XRD patterns of sample B: (a) annealed at 300 °C and (b) annealed with 3% H_2 in N_2 balance.

From the XRD data (Figures **7.5.(a)** and **7.7**), a decrease in most of the peaks can be seen when samples A and B were exposed to H_2 as compared to the annealed samples. For both samples the strongest reflection was attributed to the $(10\bar{1}1)$ and $(10\bar{1}0)$ planes, where the highest peak corresponds to the semi-polar $(10\bar{1}1)$ planes, and the second highest peak corresponds to the non-polar $(10\bar{1}0)$ plane. The peak intensity at $(10\bar{1}1)$ corresponds to the crystallinity of ZnO; a high intensity indicates poor crystallinity, and a lower peak intensity corresponds to a higher degree of crystallinity [440]. The $(10\bar{1}0)$ and $(2\bar{1}\bar{1}0)$ peaks that correlate to the non-polar facets suggest that both our samples are comprised of hexagonal wurtzite nanostructures to a considerable degree [436, 437]. Next, the diffraction intensity ratio ($I_{(0002)}/I_{(10\bar{1}0)}$) of the (0002) polar plane to the $(10\bar{1}0)$ plane was calculated to be ~0.735 for both samples A and B. The diffraction intensity ratio ($I_{(0002)}/I_{(10\bar{1}0)}$) is the ratio that describes the portion of polar to non-polar surfaces. Here, the low ratio indicates a larger portion of the non-polar planes as opposed to the polar planes, *i.e.* a greater proportion of non-polar terminated ZnO surface facets exist in our nanopowder samples. Furthermore, sample B is shown to be more crystalline as indicated by the greater intensity of the $(10\bar{1}1)$ peak in the XRD pattern (Figure. **7.6**). The same discussion that was presented for the XRD patterns in Figures **7.5** is also similarly applicable for the Figure **7.6** XRD patterns. Basically the crystal phases and the peak intensity ratios are quite alike.

Both ZnO samples were exposed to H_2 gas in N_2 balance for 30 minutes, with the XRD plots being taken immediately after. While no extra peak was identified for the larger grain size sample (sample B), an additional peak at 44° was found for sample A (Figure **7.5.(a)**). This peak can also be seen in the non-annealed ZnO nanopowder (hydrated) sample that was dried before being exposed to H_2. This XRD study also shows that the

adsorption stability of H_2 on ZnO surfaces is directly related to the particle size and crystallinity of the ZnO material.

An XRD of sample A, taken after several days of storage under atmospheric condition, showed no peak at 44° (Figure **7.5.(b)**). The XRD plot showed that the critical loss of the adsorbed species from the surface of the ZnO samples that were stored in a room temperature environment is possible within days. To support our result, Lavrov *et al*. [412] have also observed that hydrogen leaves bulk ZnO after a period of a month or more [413].

7.4.5 Infrared Spectroscopy

The IR absorption spectra of both samples were examined. Again, the coarse powder (sample B) did not show any changes after H_2 exposure compared to the finer grained (sample A) which did demonstrate a change in the spectrum. Figure **7.8** shows the effect of introducing H_2 gas to the ZnO sample at 300 °C, where the increase in the absorbance at 1618 cm^{-1} is associated with the emergence of surface bound hydroxyl groups. An infrared study by Kleinwechter *et al.* [435] suggested that the IR peak at 1618 cm^{-1} can be specifically correlated to hydroxyl groups, most likely present on the particle surface. Previous high resolution electron energy loss spectroscopy (HREELS) study of hydrogen-induced metallicity on ZnO($10\bar{1}0$) [438] also indicated the formation of surface hydroxyl groups (but not Zn-H species), as only an OH (but no Zn-H) vibration was found in the HREELS data.

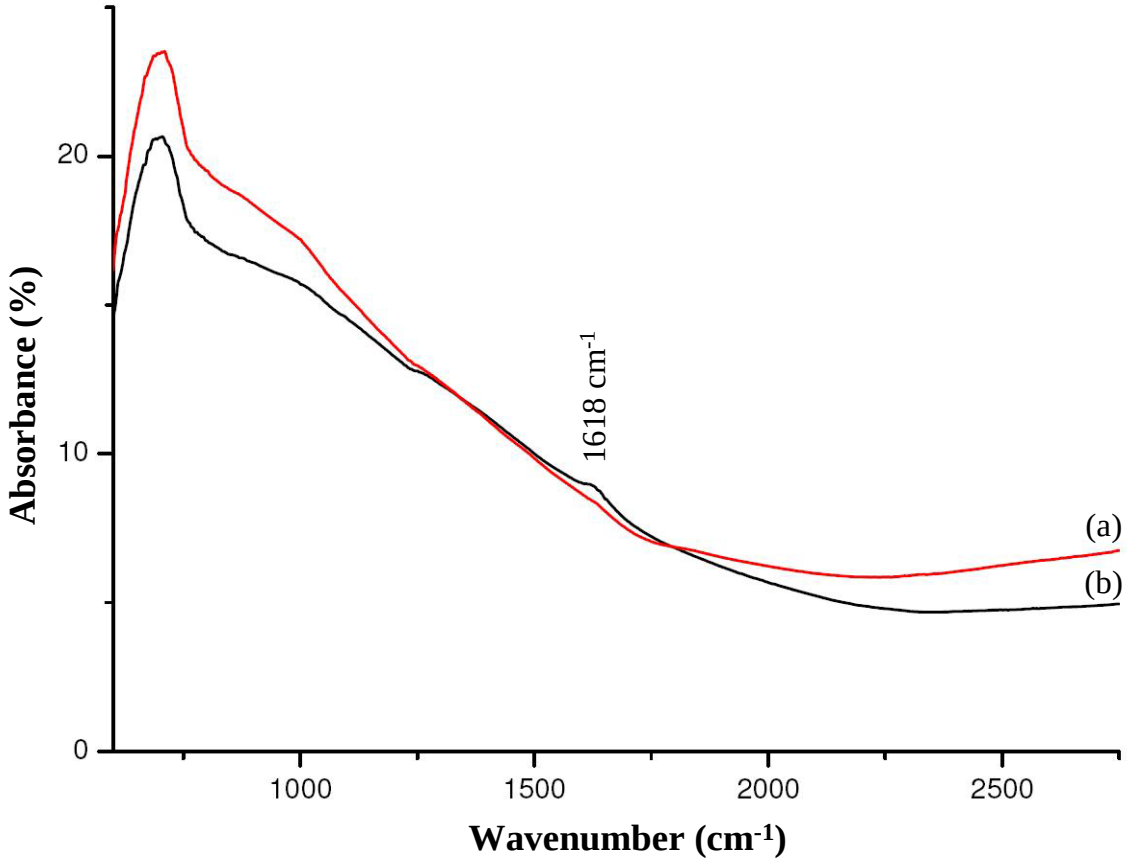

Figure 7.8 Infrared spectra of sample A recorded immediately after (a) annealing with zero air at 300 °C for 30 mins, and (b) annealing with 3% H_2 in N_2 balance at 300 °C for 30 mins.

7.5 Discussion

In this work, we demonstrated how H_2 gas can interact with ZnO nanopowders. Out of the two types of ZnO nanopowders that were studied, those with smaller grain dimensions and lower crystallinity could more efficiently interact with H_2 gas molecules. While previously the change in the Raman spectra of such an interaction has been mostly associated with ZnO interstitials and oxygen vacancies, the author strongly believes that surface bound hydroxyl groups are formed during the interaction and that the change in the Raman peak at 483 cm^{-1} can be strongly correlated with this change.

The results also correspond with some of the DFT calculations that show the adsorption of atomic H onto ZnO [139, 438] forms two possible arrangements; one where the H atoms adsorbed to surface Zn and O atoms; the other (corresponding to higher temperatures) where the H atoms adsorb to only surface O atoms. For both $(2\bar{1}\bar{1}0)$ and $(10\bar{1}0)$ structures corresponding to the references [139, 438], respectively, a hydroxyl species is formed. The interaction of H_2 with the $(2\bar{1}\bar{1}0)$ surface has also been investigated using DFT, and atomic hydrogen was found to chemisorb to the surface [139]. Hydrogen was found to preferably adsorb to the O site on the ZnO $(10\bar{1}0)$ and $(2\bar{1}\bar{1}0)$ surfaces [27, 139, 438], again indicating that the formation of a surface hydroxyl group is favourable. The effect of surface oxygen concentration on the $(2\bar{1}\bar{1}0)$ surface was also studied [139], where adsorption of hydrogen on the O-rich surface was found to cause the surface to become metallic, whereas adsorption on the stoichiometric surface retained the semiconducting nature of the material. In that study, two types of energetically stable adsorptions were found. The first, where H atoms adsorbed on both Zn and O sites (ZnO-2H), and the second where H atoms adsorbed on the O atom of the $(2\bar{1}\bar{1}0)$ surface (ZnO-H), where the ZnO-H type adsorption was identified as partial hydrogen adsorption.

7.6 Summary

This study has demonstrated, tentatively via infrared absorption, the presence of surface hydroxyl groups in small-sized ZnO grain nanopowder (~30 nm) samples at elevated temperatures. The complementary methods, Raman spectroscopy and XRD experiments, both suggest that the interaction of H_2 with the ZnO nanopowders leads to the adsorption of hydrogen, although more strongly in small sized powders. Collectively, these experiments indicate the importance of the size and crystallinity of the ZnO grains for their

interaction with hydrogen. The presence of hydrogen was not observed for highly crystalline ZnO nanopowders with larger grain sizes, while for the smaller grain sized powders, clear peak shifts confirm the presence of hydrogen. The presence of hydrogen on ZnO surfaces was found to be more prevalent on the non-polar surfaces, as supported by changes in the XRD patterns.

The experiments suggest that ZnO nanopowder can be used to detect the presence of hydrogen at low concentrations, if the crystallinity and the grain size of the ZnO sample are reduced. The relatively low intensity of the E_2(high) Raman peak can possibly be used as a good indicator of the material's suitability. Tentatively, the existence of surface hydroxyls reported in this work and the effect of ZnO grain size established a benchmark for the identification of surface bound hydrogen in ZnO nanopowders. This work can be associated with our previous DFT studies on ethanol that is hydrogen terminated, as both ethanol as well as hydrogen were found to have similar adsorption features on the $(10\bar{1}0)$ surface, *i.e*. reducing gas H atom bounds to a surface O atom.

Chapter 8

Conclusions

8.1 Summary

In this dissertation, density functional theory (DFT) and some experimental techniques have been employed to study the structural properties of adsorbate molecules on ZnO surfaces. The influence of gas type, surface facet, adsorption site, oxygen vacancy, gas coverage, and grain size on the adsorption interaction of ZnO nanostructures have been investigated.

The adsorption of nitrous oxide (N_2O) on the stoichiometric ZnO $(10\bar{1}0)$ and $(2\bar{1}\bar{1}0)$ surfaces at 1 ML coverage was computed using the DFT-GGA method. It was found that N_2O adsorbs relatively weakly (physisorbs) on both surfaces, being more strongly bound to the $(2\bar{1}\bar{1}0)$ surface. Adsorption via either the O or the N atom of N_2O was seen on both surfaces, though it is more stable on the $(10\bar{1}0)$ surface when adsorbed via the O-atom and on the $(2\bar{1}\bar{1}0)$ surface via the N-atom. Due to the weak interaction with the surface, N_2O causes small surface relaxations and adsorbate-induced reconstructions. The

interaction of N_2O with each surface mainly leads to charge polarization within the adsorbate molecule and the surface, but results in only a small transfer of charge from the surface to the adsorbate.

Likewise, the adsorption of ethanol (CH_3CH_2OH) on the stoichiometric and oxygen deficient $(10\bar{1}0)$ and $(2\bar{1}\bar{1}0)$ surfaces at ¼, ½ and 1 ML coverages was computed using the DFT-GGA method. We found that ethanol also adsorbs in multiple stable orientations, with the adsorption being stronger than that of N_2O, as possibly because it can form two bonds to the surface. One bond is between the ethanol O atom and a surface Zn atom, and the other is a hydrogen bond between the ethanol hydroxyl H atom and a surface O atom. For the defect surface, the binding is weaker, possibly because the additional hydrogen bond cannot be formed due to the reduced number of surface oxygen atoms. The formation of the hydrogen bond with a surface oxygen atom can be identified by a *red shift* of the ethanol OH stretching mode.

Overall, ethanol adsorbs more strongly on the $(2\bar{1}\bar{1}0)$ surface, compared to the $(10\bar{1}0)$ surface, with the binding being stronger at lower coverages due to the weaker interaction between adjacent ethanol molecules. The adsorption stability of ethanol on the different oxygen deficient surfaces varies depending on the oxygen vacancy (V_O) concentration. Although ethanol adsorbs in multiple stable sites at the lower coverages, the presence of surface defects does not strengthen the surface-ethanol binding interaction, in contrast to the other adsorbates on these surfaces. For instance, ethoxy (from the dissociation of ethanol) adsorbs strongly on the $(10\bar{1}0)$-V_O surface at ¼ ML coverage, with its O atom filling the vacancy site and the dissociated H atom adsorbing on an adjacent O atom.

Adsorption of ethanol on the $(2\bar{1}\bar{1}0)$ surface caused less structural changes compared to the $(10\bar{1}0)$ and $(10\bar{1}0)$-V_O surfaces. Overall, the changes are minor, indicating

that the adsorption of ethanol by ZnO would not cause major structural changes to the surface and affect its stability as a sensing device. We found that it is more likely for ethanol to form a highly uniform arrangement on the stoichiometric and V_O surfaces as this maximises the hydrogen bond formation and hence binding strength. In contrast to N_2O, there is a transfer of charge from ethanol to the surface after adsorption, whereas N_2O behaves as a charge acceptor; ethanol is a charge donor.

The differences in adsorption properties between the different gases (utilising the stoichiometry-dependence and the dynamics of the surface size) could help in understanding the selectivity and sensing performance of ZnO gas sensors. Both gases could be adsorbed on stoichiometric and defect $(10\bar{1}0)$ and $(2\bar{1}\bar{1}0)$ surfaces, corresponding with the semiconducting behaviour of ZnO in both reducing and oxidising environments. In our case, the stoichiometric surfaces showed a greater response to the reducing gas than the surfaces with oxygen vacancies. The ZnO surface with the higher oxygen content, namely the stoichiometric $(2\bar{1}\bar{1}0)$ surface, had stronger adsorbate-substrate interactions, suggesting that a greater sensitivity could likely be induced by oxidising or reducing gases.

Overall, our findings indicate that ZnO is a good candidate for N_2O and ethanol adsorption, in line with experimental observations, as the molecules can adsorb at different locations on the surface and at different gas coverages.

Experimentally, we have proposed, via IR spectroscopy, the identification of surface hydroxyl groups in small-sized ZnO grain nanopowder samples at elevated temperatures, through their interaction with hydrogen. The Raman and XRD characterisation techniques may provide additional/complementary information to further support the identification of adsorbate species present in the ZnO nanopowder samples. Importantly, our experiments demonstrate the influence of ZnO grain size and crystallinity on their interaction with hydrogen. The presence of hydrogen was not observed for highly

crystalline ZnO nanopowders with larger grain sizes, while for the smaller grain sized powders, Raman peak shifts confirm the presence of hydrogen. The presence of hydrogen on ZnO surfaces was found to be more prevalent on the non-polar surfaces, as supported by changes in the XRD patterns. Compared to our adsorption calculations, we propose that while ethanol and hydrogen are both reducing gases, hydrogen can only adsorb stably to surface O atoms, whereas ethanol can adsorb to both Zn and O atoms on the non-polar surfaces.

The experiments suggest that if the crystallinity and the grain size of the ZnO nanopowder sample are reduced, the presence of hydrogen at low concentrations could be detected. Furthermore, the relative intensity of the Raman signals may be used as a good indicator of the gas sensitivity of ZnO. The presence of hydrogen adsorbates and the effect of ZnO grain size established a benchmark for the identification of hydrogen in ZnO nanopowders.

8.2 Future Work

This study has raised important issues that require continued investigation and should be addressed in future research. Firstly, this dissertation is almost exclusively based on *ab-initio* DFT calculations, which are limited by the underestimation of the calculated band gap of semiconductors. The use of other theoretical approaches and analyses, such as *ab-initio* molecular dynamics and reaction pathway analysis, will further elucidate the ZnO sensing mechanism at elevated temperatures, and specifically the intermediate or transition state structures that are formed during the gas-surface reaction.

Further research is required to shed light on the effect of preadsorbed surface species on the adsorption of nitrous oxide, ethanol and hydrogen on ZnO surfaces. The

effect of preadsorbed oxygen or water species needs to be investigated both theoretically and experimentally in order to determine their effect on the sensing mechanism.

The modelling of true nanostructures of ZnO that will determine the effect of nanostructure morphology on the gas interaction also needs to be considered. A number of these factors are already being considered in the group of Dr. Spencer, amongst others.

The use of a combination of *in-situ* and *ex-situ* experimental techniques for the characterisation of metal oxide nanostructures will provide broad results for our understanding of the nanostructure gas sensing performance. Different types of annealed ZnO nanostructures could be used for the detection of other target gases. In addition, doping of ZnO may improve and optimise the gas sensitivity of ZnO nanostructures.

References

[1] Azad A M, Akbar S A, Mhaisalkar S G, Birkefeld L D and Goto K S 1992 Solid-State Gas Sensors - a Review *J. Electrochem. Soc.* **139** 3690-3704

[2] Yamazoe N, Sakai G and Shimanoe K 2003 Oxide semiconductor gas sensors *Catal. Surv. Asia* **7** 63-75

[3] Franke M E, Koplin T J and Simon U 2006 Metal and metal oxide nanoparticles in chemiresistors: Does the nanoscale matter? *Small* **2** 36-50

[4] Solis J L, Seeton G E, Li Y F and Kish L B 2005 Fluctuation-enhanced multiple gas sensing by commercial Taguchi sensors *IEEE Sens. J.* **5** 1338-1345

[5] Lantto V, Romppainen P and Leppavuori S 1988 A study of the temperature-dependence of the barrier energy in porous tin oxide *Sens. Actuators* **14** 149-163

[6] Werle P, Slemr F, Maurer K, Kormann R, Mucke R and Janker B 2002 Near- and mid-infrared laser-optical sensors for gas analysis *Opt. Lasers Eng.* **37** 101-114

[7] Stetter J R, Jurs P C and Rose S L 1986 Detection of hazardous gases and vapors: Pattern recognition analysis of data from an electrochemical sensor array *Anal. Chem.* **58** 860-866

[8] Fergus J W 2007 Materials for high temperature electrochemical NO_x gas sensors *Sens. Actuator B: Chem.* **121** 652-663

[9] Han C H, Hong D W, Han S D, Gwak J and Singh K C 2007 Catalytic combustion type hydrogen gas sensor using TiO_2 and UV-LED *Sens. Actuator B: Chem.* **125** 224-228

[10] Wagner C 1950 The mechanism of the decomposition of nitrous oxide on zinc oxide as catalyst *J. Chem. Phys.* **18** 69-71

[11] Hauffe K and Engell H J 1952 Zum Mechanismus der Chemisorption vom Standpunkt der Fehlordnungstheorie *Zeitschrift Fur Elektrochemie* **56** 366-373

[12] Seiyama T, Kato A, Fujiishi K and Nagatani M 1962 A new detector for gaseous components using semiconductive thin films *Anal. Chem.* **34** 1502-1503

[13] Neri G, Bonavita A, Rizzo G and Galvagno S 2004 Low temperature sol-gel synthesis and humidity sensing properties of $Cr_{2-X}Ti_XO_3$ *J. Eur. Ceram. Soc.* **24** 1435-1438

[14] Barsan N, Koziej D and Weimar U 2007 Metal oxide-based gas sensor research: How to? *Sens. Actuator B: Chem.* **121** 18-35

[15] Watson J 1984 The tin oxide gas sensor and its applications *Sens. Actuators* **5** 29-42

[16] Patil D R, Patil L A and Amalnerkar D P 2007 Ethanol gas sensing properties of Al_2O_3-doped ZnO thick film resistors *Bull. Mater. Sci.* **30** 553-559

[17] Al-Hardan N H, Abdullah M J, Abdul Aziz A, Ahmad H and Low L Y 2010 ZnO thin films for VOC sensing applications *Vacuum* **85** 101-106

[18] Shi L B and Yuan H K 2011 A study on the magnetic properties of carbon-doped $(11\bar{2}0)$ ZnO thin films *J. Magn. Magn. Mater.* **323** 857-863

[19] Mitra P, Chatterjee A P and Maiti H S 1998 ZnO thin film sensor *Mater. Lett.* **35** 33-38

[20] An W, Wu X J and Zeng X C 2008 Adsorption of O_2, H_2, CO, NH_3, and NO_2 on ZnO nanotube: A density functional theory study *J. Phys. Chem. C* **112** 5747-5755

[21] Sadek A Z, Wlodarski W, Li Y, Yu W, Li X, Yu X and Kalantar-Zadeh K 2007 A ZnO nanorod based layered ZnO/64° YX $LiNbO_3$ SAW hydrogen gas sensor *Thin Solid Films* **515** 8705-8708

[22] Spencer M J S 2012 Gas sensing applications of 1D-nanostructured zinc oxide: Insights from density functional theory calculations *Prog. Mater. Sci.* **57** 437-486

[23] Comini E, Faglia G, Sberveglieri G, Pan Z W and Wang Z L 2002 Stable and highly sensitive gas sensors based on semiconducting oxide nanobelts *Appl. Phys. Lett.* **81** 1869-1871

[24] Pan Z W, Dai Z R and Wang Z L 2001 Nanobelts of semiconducting oxides *Science* **291** 1947-1949

[25] Comini E, Baratto C, Concina I, Faglia G, Falasconi M, Ferroni M, Galstyan V, Gobbi E, Ponzoni A, Vomiero A, Zappa D, Sberveglieri V and Sberveglieri G 2013 Metal oxide nanoscience and nanotechnology for chemical sensors *Sens. Actuator B: Chem.* **179** 3-20

[26] Sadek A Z, Choopun S, Wlodarski W, Ippolito S J and Kalantar-zadeh K 2007 Characterization of ZnO nanobelt-based gas sensor for H_2, NO_2, and hydrocarbon sensing *IEEE Sens. J.* **7** 919-924

[27] Spencer M J S, Yarovsky I, Wlodarski W and Kalantar-Zadeh K 2011 Interaction of hydrogen with zinc oxide nanorods: why the spacing is important *Nanotechnology* **22** 135704 (6pp)

[28] Wong K W J, Field M R, Ou J Z, Latham K, Spencer M J S, Yarovsky I and Kalantar-zadeh K 2012 Interaction of hydrogen with ZnO nanopowders-evidence of hydroxyl group formation *Nanotechnology* **23** 015705(7pp)

[29] Zheng H D, Ou J Z, Strano M S, Kaner R B, Mitchell A and Kalantar-Zadeh K 2011 Nanostructured Tungsten Oxide - Properties, Synthesis, and Applications *Adv. Funct. Mater.* **21** 2175-2196

[30] Ou J Z, Ahmad M Z, Latham K, Kalantar-zadeh K, Sberveglieri G and Wlodarski W 2011 Synthesis of the nanostructured WO_3 via anodization at elevated temperature for H_2 sensing applications *Eurosensors XXV*, (*edited by Kaltsas G and Tsamis C*) (Amsterdam: Elsevier Science Bv) **25** 247-251

[31] Ou J Z, Yaacob M H, Campbell J L, Breedon M, Kalantar-zadeh K and Wlodarski W 2012 H_2 sensing performance of optical fiber coated with nano-platelet WO_3 film *Sens. Actuator B: Chem.* **166** 1-6

[32] Penza M, Sadek A Z, Aversa P, McCulloch D G, Wlodarski W and Kalantar-Zadeh K 2011 SAW Gas Sensors with Metal Oxides Nanoplatelets Layers *Sens. Lett.* **9** 920-924

[33] Penza M, Sadek A Z, Zheng H D, Aversa P, McCulloch D G, Kalantar-zadeh K and Wlodarski W 2011 SAW Gas Sensors with Titania Nanotubes Layers *Sens. Lett.* **9** 925-928

[34] Chen H Y, Wang L P, Bai J M, Hanson J C, Warren J B, Muckerman J T, Fujita E and Rodriguez J A 2010 *In-situ* XRD Studies of ZnO/GaN Mixtures at High Pressure and High Temperature: Synthesis of Zn-Rich $(Ga_{1-x}Zn_x)(N_{1-x}O_x)$ Photocatalysts *J. Phys. Chem. C* **114** 1809-1814

[35] Berna A Z, Trowell S, Cynkar W and Cozzolino D 2008 Comparison of metal oxide-based electronic nose end mess spectrometry-based electronic nose for the prediction of red wine spoilage *J. Agric. Food Chem.* **56** 3238-3244

[36] Cheng X, Li F and Zhao Y 2009 A DFT investigation on ZnO clusters and nanostructures *J. Mol. Struct. THEOCHEM* **894** 121-127

[37] Huang J and Wan Q 2009 Gas Sensors Based on Semiconducting Metal Oxide One-Dimensional Nanostructures *Sensors* **9** 9903-9924

[38] Strelcov E, Dmitriev S, Button B, Cothren J, Sysoev V and Kolmakov A 2008 Evidence of the self-heating effect on surface reactivity and gas sensing of metal oxide nanowire chemiresistors *Nanotechnology* **19** 355502 (5pp)

[39] Prades J D, Jimenez-Diaz R, Hernandez-Ramirez F, Barth S, Cirera A, Romano-Rodriguez A, Mathur S and Morante J R 2008 Ultralow power consumption gas

sensors based on self-heated individual nanowires *Appl. Phys. Lett.* **93** 123110 (3pp)

[40] Gong H, Hu J Q, Wang J H, Ong C H and Zhu F R 2006 Nano-crystalline Cu-doped ZnO thin film gas sensor for CO *Sens. Actuators B: Chem.* **115** 247-251

[41] Fouad O A, Glaspell G and El-Shall M S 2010 Structural, optical and gas sensing properties of ZnO, SnO_2 and ZTO nanostructures *Nano* **5** 185-194

[42] Xu J Q, Chen Y P, Chen D Y and Shen J N 2006 Hydrothermal synthesis and gas sensing characters of ZnO nanorods *Sens. Actuator B: Chem.* **113** 526-531

[43] Eriksson J, Khranovskyy V, Soderlind F, Kall P O, Yakimova R and Spetz A L 2009 ZnO nanoparticles or ZnO films: A comparison of the gas sensing capabilities *Sens. Actuator B: Chem.* **137** 94-102

[44] Meixner H and Lampe U 1996 Metal oxide sensors *Sens. Actuator B: Chem.* **33** 198-202

[45] Quy N V, Minh V A, Luan N V, Hung V N and Hieu N V 2011 Gas sensing properties at room temperature of a quartz crystal microbalance coated with ZnO nanorods *Sens. Actuator B: Chem.* **153** 188-193

[46] Rout C S, Raju A R, Govindaraj A and Rao C N R 2006 Hydrogen sensors based on ZnO nanoparticles *Solid State Commun.* **138** 136-138

[47] Rout C S, Krishna S H, Vivekchand S R C, Govindaraj A and Rao C N R 2006 Hydrogen and ethanol sensors based on ZnO nanorods, nanowires and nanotubes *Chem. Phys. Lett.* **418** 586-590

[48] Gründler P 2007 *Chemical Sensors: An Introduction for Scientists and Engineers* (Springer) (273pp)

[49] Zhao L, Choi M, Kim H S and Hong S H 2007 The effect of multiwalled carbon nanotube doping on the CO gas sensitivity of SnO_2-based nanomaterials *Nanotechnology* **18** 445501 (5pp)

[50] Kocemba I, Szafran S, Rynkowski J and Paryjczak T 2001 The properties of strongly pressed tin oxide-based gas sensors *Sens. Actuator B: Chem.* **79** 28-32

[51] Bochenkov V E and Sergeev G B 2010 *Metal Oxide Nanostructures and Their Applications, Vol. 3: Nanosensors, Nanodevices and Energy Applications (edited by Umar A and Hahn Y B)* (American Scientific Publisher) 31-52

[52] Hongsith N, Wongrat E, Kerdcharoen T and Choopun S 2010 Sensor response formula for sensor based on ZnO nanostructures *Sens. Actuator B: Chem.* **144** 67-72

[53] Moezzi A, McDonagh A M and Cortie M B 2012 Zinc oxide particles: Synthesis, properties and applications *Chem. Eng. J.* **185** 1-22

[54] Law M, Greene L E, Johnson J C, Saykally R and Yang P D 2005 Nanowire dye-sensitized solar cells *Nat. Mater.* **4** 455-459

[55] Rensmo H, *Keis* K, Lindstrom H, Sodergren S, Solbrand A, Hagfeldt A, Lindquist S E, Wang L N and Muhammed M 1997 High light-to-energy conversion efficiencies for solar cells based on nanostructured ZnO electrodes *J. Phys. Chem. B* **101** 2598-2601

[56] Keis K, Bauer C, Boschloo G, Hagfeldt A, Westermark K, Rensmo H and Siegbahn H 2002 Nanostructured ZnO electrodes for dye-sensitized solar cell applications *J. Photochem. Photobiol. A-Chem.* **148** 57-64

[57] Xu S, Qin Y, Xu C, Wei Y G, Yang R S and Wang Z L 2010 Self-powered nanowire devices *Nat. Nanotechnol.* **5** 366-373

[58] Wang X, Song J, Liu J and Wang Z L 2007 Direct-current nanogenerator driven by ultrasonic waves *Science* **316** 102-105

[59] Hoffman R L, Norris B J and Wager J F 2003 ZnO-based transparent thin-film transistors *Appl. Phys. Lett.* **82** 733-735

[60] Tsukazaki A, Ohtomo A, Onuma T, Ohtani M, Makino T, Sumiya M, Ohtani K, Chichibu S F, Fuke S, Segawa Y, Ohno H, Koinuma H and Kawasaki M 2005 Repeated temperature modulation epitaxy for *p*-type doping and light-emitting diode based on ZnO *Nat. Mater.* **4** 42-46

[61] Ohta H, Kawamura K, Orita M, Hirano M, Sarukura N and Hosono H 2000 Current injection emission from a transparent *p*-*n* junction composed of *p*-$SrCu_2O_2$/*n*-ZnO *Appl. Phys. Lett.* **77** 475-477

[62] Wang X D, Summers C J and Wang Z L 2004 Large scale hexagonal-patterned growth of aligned ZnO nanorods for nano-optoelectronics and nanosensor arrays *Nano Lett.* **4** 423-426

[63] Liu C, Yun F and Morkoc H 2005 Ferromagnetism of ZnO and GaN: A review *J. Mater. Sci.-Mater. Electron.* **16** 555-597

[64] Powell D A, Kalantar-zadeh K and Wlodarski W 2004 Numerical calculation of SAW sensitivity: application to ZnO/$LiTaO_3$ transducers *Sens. Actuator A: Phys.* **115** 456-461

[65] Ozgur U, Alivov Y I, Liu C, Teke A, Reshchikov M A, Dogan S, Avrutin V, Cho S J and Morkoc H 2005 A comprehensive review of ZnO materials and devices *J. Appl. Phys.* **98** 041301 (103pp)

[66] Wang R C, Liu C P, Huang J L and Chen S J 2005 ZnO hexagonal arrays of nanowires grown on nanorods *Appl. Phys. Lett.* **86** 251104 (3pp)

[67] Arya S K, Saha S, Ramirez-Vick J E, Gupta V, Bhansali S and Singh S P 2012 Recent advances in ZnO nanostructures and thin films for biosensor applications: Review *Anal. Chim. Acta* **737** 1-21

[68] Klingshirn C 2007 ZnO: Material, Physics and Applications *ChemPhysChem* **8** 782-803

[69] Li X H, Xing Y, Jiang Y H, Ding Y L and Li W L 2009 Antimicrobial activities of ZnO powder-coated PVC film to inactivate food pathogens *Int. J. Food Sci. Technol.* **44** 2161-2168

[70] Cushen M, Kerry J, Morris M, Cruz-Romero M and Cummins E 2012 Nanotechnologies in the food industry - Recent developments, risks and regulation *Trends Food Sci. Technol.* **24** 30-46

[71] Klingshirn C, Fallert J, Zhou H, Sartor J, Thiele C, Maier-Flaig F, Schneider D and Kalt H 2010 65 years of ZnO research - old and very recent results *Phys. Status Solidi B-Basic Solid State Phys.* **247** 1424-1447

[72] Look D C, Reynolds D C, Hemsky J W, Jones R L and Sizelove J R 1999 Production and annealing of electron irradiation damage in ZnO *Appl. Phys. Lett.* **75** 811-813

[73] Polyakov A Y, Smirnov N B, Govorkov A V, Kozhukhova E A, Vdovin V I, Ip K, Overberg M E, Heo Y W, Norton D P, Pearton S J, Zavada J M and Dravin V A 2003 Proton implantation effects on electrical and recombination properties of undoped ZnO *J. Appl. Phys.* **94** 2895-2900

[74] Kucheyev S O, Williams J S, Jagadish C, Zou J, Evans C, Nelson A J and Hamza A V 2003 Ion-beam-produced structural defects in ZnO *Phys. Rev. B* **67** 094115 (11pp)

[75] Look D C 2001 Recent advances in ZnO materials and devices *Mater. Sci. Eng., B-Solid* **80** 383-387

[76] Nohynek G J, Lademann J, Ribaud C and Roberts M S 2007 Grey goo on the skin? Nanotechnology, cosmetic and sunscreen safety *Crit. Rev. Toxicol.* **37** 251-277

[77] Burnett M E and Wang S Q 2011 Current sunscreen controversies: a critical review *Photodermatol. Photoimmunol. Photomed.* **27** 58-67

[78] Spetz A L, Tobias P, Baranzahi A, Martensson P and Lundstrom I 1999 Current status of silicon carbide based high-temperature gas sensors *IEEE Trans. Electron Devices* **46** 561-566
[79] Casady J B and Johnson R W 1996 Status of silicon carbide (SiC) as a wide-bandgap semiconductor for high-temperature applications: A review *Solid-State Electron.* **39** 1409-1422
[80] Look D C and Claftin B 2004 *p*-type doping and devices based on ZnO *Phys. Status Solidi B-Basic Solid State Phys.* **241** 624-630
[81] Cui J B 2012 Zinc oxide nanowires *Mater. Charact.* **64** 43-52
[82] Janotti A and Van de Walle C G 2009 Fundamentals of zinc oxide as a semiconductor *Rep. Prog. Phys.* **72** 126501 (29pp)
[83] Sberveglieri G 1995 Recent developments in semiconducting thin-film gas sensors *Sens. Actuator B: Chem.* **23** 103-109
[84] Guidi V, Carotta M C, Ferroni M, Martinelli G, Paglialonga L, Comini E and Sberveglieri G 1999 Preparation of nanosized titania thick and thin films as gas-sensors *Sens. Actuator B: Chem.* **57** 197-200
[85] Shimizu Y and Egashira M 1999 Basic aspects and challenges of semiconductor gas sensors *MRS Bull.* **24** 18-24
[86] Huang F C, Chen Y Y and Wu T T 2009 A room temperature surface acoustic wave hydrogen sensor with Pt coated ZnO nanorods *Nanotechnology* **20** 065501 (6pp)
[87] Vayssieres L 2003 Growth of arrayed nanorods and nanowires of ZnO from aqueous solutions *Adv. Mater.* **15** 464-466
[88] Breedon M, Rix C and Kalantar-Zadeh K 2009 Seeded growth of ZnO nanorods from NaOH solutions *Mater. Lett.* **63** 249-251
[89] Wang Z L 2003 Nanobelts, nanowires, and nanodiskettes of semiconducting oxides - From materials to nanodevices *Adv. Mater.* **15** 432-436
[90] Wang Z L 2004 Functional oxide nanobelts: Materials, properties and potential applications in nanosystems and biotechnology *Annu. Rev. Phys. Chem.* **55** 159-196
[91] Dai Z R, Pan Z W and Wang Z L 2003 Novel nanostructures of functional oxides synthesized by thermal evaporation *Adv. Funct. Mater.* **13** 9-24
[92] Hughes W L and Wang Z L 2004 Formation of piezoelectric single-crystal nanorings and nanobows *J. Am. Chem. Soc.* **126** 6703-6709
[93] Gao P X, Ding Y, Mai W J, Hughes W L, Lao C S and Wang Z L 2005 Conversion of zinc oxide nanobelts into superlattice-structured nanohelices *Science* **309** 1700-1704
[94] Gao P X and Wang Z L 2005 High-yield synthesis of single-crystal nanosprings of ZnO *Small* **1** 945-949
[95] Li J, Fan H and Jia X 2010 Multilayered ZnO Nanosheets with 3D Porous Architectures: Synthesis and Gas Sensing Application *J. Phys. Chem. C* **114** 14684-14691
[96] Pan Z W, Mahurin S M, Dai S and Lowndes D H 2005 Nanowire array gratings with ZnO combs *Nano Lett.* **5** 723-727
[97] Zhang H, Yang D, Ma X Y, Ji Y J, Xu J and Que D L 2004 Synthesis of flower-like ZnO nanostructures by an organic-free hydrothermal process *Nanotechnology* **15** 622-626
[98] Qiu Y and Yang S 2007 ZnO nanotetrapods: Controlled vapor-phase synthesis and application for humidity sensing *Adv. Funct. Mater.* **17** 1345-1352
[99] Wang J M and Gao L 2004 Synthesis of uniform rod-like, multi-pod-like ZnO whiskers and their photo luminescence properties *J. Cryst. Growth* **262** 290-294
[100] Chen Z, Shan Z W, Cao M S, Lu L and Mao S X 2004 Zinc oxide nanotetrapods *Nanotechnology* **15** 365-369

[101] Wang Z L 2009 Ten years' venturing in ZnO nanostructures: from discovery to scientific understanding and to technology applications *Chin. Sci. Bull.* **54** 4021-4034
[102] Wang Z L 2004 Zinc oxide nanostructures: growth, properties and applications *J. Phys. Condens. Matter* **16** R829-R858
[103] Klingshirn C 2007 ZnO: From basics towards applications *Phys. Status Solidi B-Basic Solid State Phys.* **244** 3027-3073
[104] Meng X Q, Zhao D X, Zhang J Y, Shen D Z, Lu Y M, Liu Y C and Fan X W 2005 Growth temperature controlled shape variety of ZnO nanowires *Chem. Phys. Lett.* **407** 91-94
[105] Xu L F, Guo Y, Liao Q, Zhang J P and Xu D S 2005 Morphological control of ZnO nanostructures by electrodeposition *J. Phys. Chem. B* **109** 13519-13522
[106] Galli G and Coker J E 1970 Epitaxial ZnO on sapphire *Appl. Phys. Lett.* **16** 439-441
[107] Shiloh M and Gutman J 1971 Growth of ZnO single crystals by chemical vapour transport *J. Cryst. Growth* **11** 105-109
[108] Zhang H, Wu J B, Zhai C X, Du N, Ma X Y and Yang D 2007 From ZnO nanorods to 3D hollow microhemispheres: solvothermal synthesis, photoluminescence and gas sensor properties *Nanotechnology* **18** 455604 (7pp)
[109] Croxall D F, Ward R C C, Wallace C A and Kell R C 1974 Hydrothermal growth and investigation of Li-doped zinc oxide crystals of high purity and perfection *J. Cryst. Growth* **22** 117-124
[110] Kern W and Heim R 1970 Chemical vapor deposition of silicate glasses for use with silicon devices .1. Deposition techniques *J. Electrochem. Soc.* **117** 562-568
[111] Kasuga M and Mochizuki M 1981 Orientation relationships of zinc oxide on sapphire in hetero-epitaxial chemical vapor deposition *J. Cryst. Growth* **54** 185-194
[112] Chen Y, Bagnall D M, Koh H J, Park K T, Hiraga K, Zhu Z and Yao T 1998 Plasma assisted molecular beam epitaxy of ZnO on *c*-plane sapphire: Growth and characterization *J. Appl. Phys.* **84** 3912-3918
[113] Fons P, Iwata K, Niki S, Yamada A and Matsubara K 1999 Growth of high-quality epitaxial ZnO films on alpha-Al_2O_3 *J. Cryst. Growth* **201** 627-632
[114] Vispute R D, Talyansky V, Trajanovic Z, Choopun S, Downes M, Sharma R P, Venkatesan T, Woods M C, Lareau R T, Jones K A and Iliadis A A 1997 High quality crystalline ZnO buffer layers on sapphire (001) by pulsed laser deposition for III-V nitrides *Appl. Phys. Lett.* **70** 2735-2737
[115] Narayan J, Dovidenko K, Sharma A K and Oktyabrsky S 1998 Defects and interfaces in epitaxial ZnO/α-Al_2O_3 and AlN/ZnO/α-Al_2O_3 heterostructures *J. Appl. Phys.* **84** 2597-2601
[116] Segawa Y, Ohtomo A, Kawasaki M, Koinuma H, Tang Z K, Yu P and Wong G K L 1997 Growth of ZnO thin film by laser MBE: Lasing of exciton at room temperature *Phys. Status Solidi B* **202** 669-672
[117] Liu Y Q and Zhou A R 2000 Vascular endothelial growth factor and nitric oxide *Sheng li ke xue jin zhan [Progress in physiology]* **31** 69-71
[118] Hahn B, Heindel G, Pschorr-Schoberer E and Gebhardt W 1998 MOCVD layer growth of ZnO using DMZn and tertiary butanol *Semicond. Sci. Technol.* **13** 788-791
[119] Kasuga M and Ogawa S 1983 Electronic properties of vapor-grown heteroepitaxial ZnO film on sapphire *Jpn. J. Appl. Phys., Part 1* **22** 794-798
[120] Takahashi N, Kaiya K, Nakamura T, Momose Y and Yamamoto H 1999 Growth of ZnO on sapphire (0001) by the vapor phase epitaxy using a chloride source *Jpn. J. Appl. Phys., Part 2* **38** L454-L456

[121] Zhang Y Y, Ram M K, Stefanakos E K and Goswami D Y 2012 Synthesis, Characterization, and Applications of ZnO Nanowires *J. Nanomater.* **22** 624520 (22pp)
[122] Rao C N R and Biswas K 2009 Characterization of Nanomaterials by Physical Methods *Annu. Rev. Anal. Chem.* **2** 435-462
[123] Chen S J, Liu Y C, Lu Y M, Zhang J Y, Shen D Z and Fan X W 2006 Photoluminescence and Raman behaviors of ZnO nanostructures with different morphologies *J. Cryst. Growth* **289** 55-58
[124] Comini E, Baratto C, Faglia G, Ferroni M, Vomiero A and Sberveglieri G 2009 Quasi-one dimensional metal oxide semiconductors: Preparation, characterization and application as chemical sensors *Prog. Mater. Sci.* **54** 1-67
[125] Zuo J A and Erbe A 2010 Optical and electronic properties of native zinc oxide films on polycrystalline Zn *Phys. Chem. Chem. Phys.* **12** 11467-11476
[126] Bates C H, Roy R and White W B 1962 New high-pressure polymorph of zinc oxide *Science* **137** 993-994
[127] Kuwabara R, Adachi H and Morimoto T 1988 Calculation of the electronic-structure of the polar ZnO($000\bar{1}$) surface by the DV-Xα cluster method *Surf. Sci.* **193** 271-286
[128] Marana N L, Longo V M, Longo E, Martins J B and Sambrano J R 2008 Electronic and structural properties of the ($10\bar{1}0$) and ($11\bar{2}0$) ZnO surfaces *J. Phys. Chem. A* **112** 8958-8963
[129] Wang Z L, Kong X Y, Ding Y, Gao P X, Hughes W L, Yang R S and Zhang Y 2004 Semiconducting and piezoelectric oxide nanostructures induced by polar surfaces *Adv. Funct. Mater.* **14** 943-956
[130] Coleman V A, Jagadish C, and Pearton S J 2006 *Zinc Oxide Bulk, Thin Films and Nanostructures*, (Oxford: Elsevier Science Ltd) 1-20
[131] Scarano D, Spoto G, Bordiga S, Zecchina A and Lamberti C 1992 Lateral interactions in Co adlayers on prismatic ZnO faces - A FTIR and HRTEM study *Surf. Sci.* **276** 281-298
[132] Breedon M, Spencer M J S and Yarovsky I 2010 Adsorption of NO_2 on Oxygen Deficient ZnO($2\bar{1}\bar{1}0$) for Gas Sensing Applications: A DFT Study *J. Phys. Chem. C* **114** 16603-16610
[133] Yang J H, Wang J, Li X Y, Lang J H, Liu F Z, Yang L L, Zhai H J, Gao M and Zhao X T 2012 Effect of polar and non-polar surfaces of ZnO nanostructures on photocatalytic properties *J. Alloy. Compd.* **528** 28-33
[134] Xu H, Fan W, Rosa A L, Zhang R Q and Frauenheim T 2009 Hydrogen and oxygen adsorption on ZnO nanowires: A first-principles study *Phys. Rev. B* **79** 073402 (4pp)
[135] Prades J D, Cirera A and Morante J R 2009 *Ab-initio* calculations of NO_2 and SO_2 chemisorption onto non-polar ZnO surfaces *Sens. Actuators, B* **142** 179-184
[136] Zhou Y, Wu W B, Hu G D, Wu H T and Cui S G 2008 Hydrothermal synthesis of ZnO nanorod arrays with the addition of polyethyleneimine *Mater. Res. Bull.* **43** 2113-2118
[137] Ye C H, Fang X S, Hao Y F, Teng X M and Zhang L D 2005 Zinc oxide nanostructures: Morphology derivation and evolution *J. Phys. Chem. B* **109** 19758-19765
[138] Hashimoto S and Yamaguchi A 1996 Growth morphology and mechanism of a hollow ZnO polycrystal *J. Am. Ceram. Soc.***79** 1121-1123
[139] Wang C C, Zhou G, Li J, Yan B H and Duan W H 2008 Hydrogen-induced metallization of zinc oxide ($2\bar{1}\bar{1}0$) surface and nanowires: The effect of curvature *Phys. Rev. B* **77** 245303 (7pp)

[140] Ahn M W, Park K S, Heo J H, Park J G, Kim D W, Choi K J, Lee J H and Hong S H 2008 Gas sensing properties of defect-controlled ZnO-nanowire gas sensor *Appl. Phys. Lett.* **93** 263103 (3pp)
[141] Liao L, Lu H B, Li J C, Liu C, Fu D J and Liu Y L 2007 The sensitivity of gas sensor based on single ZnO nanowire modulated by helium ion radiation *Appl. Phys. Lett.* **91** 173110 (3pp)
[142] Yan Y and Al-Jassim M M 2005 Structure and energetics of water adsorbed on the ZnO ($10\bar{1}0$) surface *Phys. Rev. B* **72** 235406 (6pp)
[143] Yang J, Shih Y R, Chen I C, Kuo C I and Huang Y S 2005 Characterization of infrared chemical sensors modified with ZnO nanowires for the detection of volatile organic compounds *Appl. Spectrosc.* **59** 1002-1008
[144] Moreira N H, Aradi B, da Rosa A L and Frauenheim T 2010 Native Defects in ZnO Nanowires: Atomic Relaxations, Relative Stability, and Defect Healing with Organic Acids *J. Phys. Chem. C* **114** 18860-18865
[145] Spencer M J S and Yarovsky I 2010 ZnO Nanostructures for Gas Sensing: Interaction of NO_2, NO, O, and N with the ZnO($10\bar{1}0$) Surface *J. Phys. Chem. C* **114** 10881-10893
[146] Hutsch B W, Wang X Z, Feng K, Yan F and Schubert S 1999 Nitrous oxide emission as affected by changes in soil water content and nitrogen fertilization *J. Plant Nutr. Soil Sci.* **162** 607-613
[147] Hansen J, Sato M, Ruedy R, Lacis A and Oinas V 2000 Global warming in the twenty-first century: An alternative scenario *Proceedings of the National Academy of Sciences of the United States of America* **97** 9875-9880
[148] Macfaul L 2004 *Verification Yearbook 2004: Monitoring greenhouse gases* (London: Verification Research, Training and Information Centre (VERTIC)) 145-169
[149] Trogler W C 1999 Physical properties and mechanisms of formation of nitrous oxide *Coord. Chem. Rev.* **187** 303-327
[150] Montzka S A and Fraser P J 2003 *Scientific Assessment of Ozone Depletion: 2002, Controlled Substances and Other Source Gases,* (Geneva: World Meteorological Organization) 1.1-1.83
[151] Badr O and Probert S D 1992 Nitrous-oxide in the Earth's atmosphere *Appl. Energy* **41** 177-200
[152] Badr O and Probert S D 1993 Environmental impacts of atmospheric nitrous-oxide *Appl. Energy* **44** 197-231
[153] Penner J E, Lister D H, Griggs D J, Dokken D J and McFarland M 1999 Summary for Policymakers: Aviation and the Global Atmosphere. In: *A Special Report of IPCC Working Groups I and III,* (San Jose, Costa Rica: Intergovermental Panel on Climate Change) 1-12
[154] Buring J E, Hennekens C H and Mayrent S L 1985 Health experiences of operating room personnel *Anesthesiology* **62** 325-330
[155] Borm P J A, Kant I J, Gouben G, Van Rijssen-Moll M and Henderson P T 1990 Monitoring of nitrous oxide in operating rooms: Identification of sources and estimation of occupational exposure *J. Occup. Med.* **32** 1112-1116
[156] Guirguis S S, Pelmear P L, Roy M L and Wong L 1990 Health effects associated with exposure to anaesthetic gases in Ontario hospital personnel *Brit. J. Ind. Med.* **47** 490-497
[157] Kanmura Y 1999 Causes of nitrous oxide contamination in operating rooms *Anesthesiology* **90** 693-696
[158] Sessler D I 1997 Risks of occupational exposure to waste-anesthetic gases *Acta Anaesthesiol. Scand., Suppl.* **41** 237-239

[159] Hu C L, Chen Y, Li J Q and Zhang Y F 2007 First-principles calculations of N_2O adsorption and decomposition on GaN (0001) surface *Chem. Phys. Lett.* **438** 213-217
[160] Artaxo P, Berntsen T, Betts R, Fahey D W, Haywood J, Lean J, Lowe D C, Myhre G, Nganga J, Prinn R, Raga G, Schulz M and Van Dorland R 2007 *Climate Change 2007: The Physical Science Basis* (*edited by Nakajima T and Ramanathan V*) (Cambridge University Press) 130-234
[161] Ravishankara A R, Daniel J S and Portmann R W 2009 Nitrous Oxide (N_2O): The Dominant Ozone-Depleting Substance Emitted in the 21st Century *Science* **326** 123-125
[162] Wuebbles D J 2009 Nitrous Oxide: No Laughing Matter *Science* **326** 56-57
[163] Bevan R J, Slack R J, Holmes P and Levy L S 2009 An assessment of potential cancer risk following occupational exposure to ethanol *J. Toxicol. Environ. Health B - Crit. Rev.* **12** 188-205
[164] Caravati E M and Anderson K T 2010 Breath Alcohol Analyzer Mistakes Methanol Poisoning for Alcohol Intoxication *Ann. Emerg. Med.* **55** 198-200
[165] Lindberg L and Grubb D 2012 Simultaneously recorded single-exhalation profiles of ethanol, water vapour and CO_2 in humans: impact of pharmacokinetic phases on ethanol airway exchange *J. Breath Res.* **6** 036001 (8pp)
[166] Daphne Phillips D, James P S, Ilsemarie T, Burke B and John W A 2000 Effect of ethanol vapor on growth and toxin production by *Clostridium Botulinum* in a high moisture bakery product *J. Food Saf.* **20** 111-125
[167] Kourkoutas Y, Bekatorou A, Banat I M, Marchant R and Koutinas A A 2004 Immobilization technologies and support materials suitable in alcohol beverages production: a review *Food Microbiol.* **21** 377-397
[168] Utama I M S, Wills R B H, Ben-Yehoshua S and Kuek C 2002 *In vitro* efficacy of plant volatiles for inhibiting the growth of fruit and vegetable decay microorganisms *J. Agric. Food Chem.* **50** 6371-6377
[169] Lanciotti R, Gianotti A, Patrignani F, Belletti N, Guerzoni M E and Gardini F 2004 Use of natural aroma compounds to improve shelf-life and safety of minimally processed fruits *Trends Food Sci. Technol.* **15** 201-208
[170] Agrawal R, Paci J T and Espinosa H D 2010 Large Scale Density Functional Theory Investigation of Failure Modes in ZnO Nanowires *Nano Lett.* **10** 3432-3438
[171] Perdew J P, Chevary J A, Vosko S H, Jackson K A, Pederson M R, Singh D J and Fiolhais C 1992 Atoms, molecules, solids, and surfaces: Applications of the generalized gradient approximation for exchange and correlation *Phys. Rev. B* **46** 6671-6687
[172] Hafner J 2008 *Ab-initio* simulations of materials using VASP: Density-functional theory and beyond *J. Comput. Chem.* **29** 2044-2078
[173] Oba F, Choi M, Togo A and Tanaka I 2011 Point defects in ZnO: an approach from first principles *Sci. Technol. Adv. Mater.* **12** 034302 (14pp)
[174] Janotti A and Van de Walle C G 2005 Oxygen vacancies in ZnO *Appl. Phys. Lett.* **87** 122102 (3pp)
[175] Erhart P, Albe K and Klein A 2006 First-principles study of intrinsic point defects in ZnO: Role of band structure, volume relaxation, and finite-size effects *Phys. Rev. B* **73** 205203 (9pp)
[176] Rangan S, Theisen J P, Bersch E and Bartynski R A 2010 Energy level alignment of catechol molecular orbitals on ZnO($11\bar{2}0$) and TiO_2(110) surfaces *Appl. Surf. Sci.* **256** 4829-4833

[177] Kang J, Zhang Y, Wen Y H, Zheng J C and Zhu Z Z 2010 First-principles study on the structural and electronic properties of ultrathin ZnO nanofilms *Phys. Lett. A* **374** 1054-1058
[178] Engel E and Dreizler R M 2011 *Density Functional Theory: An Advanced Course* (Heidelberg; New York: Springer) (536pp)
[179] Hohenberg P and Kohn W 1964 Inhomogeneous electron gas *Phys. Rev. B* **136** B864-B871
[180] Born M and Oppenheimer R 1927 Quantum theory of molecules *Ann. Phys. Berlin* **84** 0457-0484
[181] Echenique P and Alonso J L 2007 A mathematical and computational review of Hartree-Fock SCF methods in quantum chemistry *Mol. Phys.* **105** 3057-3098
[182] Leach A 2001 *Molecular Modelling: Principles and Applications* (Prentice Hall) (744pp)
[183] Hartree D R 1928 The wave mechanics of an atom with a non-Coulomb central field Part I theory and methods *Proc. Cambridge Philos. Soc.* **24** 89-110
[184] Slater J C 1951 A simplification of the Hartree-Fock method *Phys. Rev.* **81** 385-390
[185] Fock V 1930 Approximation method for the solution of the quantum mechanical multibody problems *Z. Phys.* **61** 126-148
[186] Slater J C 1930 Note on Hartree's method *Phys. Rev.* **35** 0210-0211
[187] Koopmans T 1934 The classification of wave functions and eigen-values to the single electrons of an atom *Physica* **1** 104-113
[188] Thijssen J M 2007 *Computational Physics* (Cambridge University Press, New York) (620pp)
[189] Kobus J 1997 *Advances in Quantum Chemistry, Vol. 28: Recent Advances in Computational Chemistry (edited by Lowdin P O, Sabin J R, Zerner M C, Karwowski J and Karelson M)* (Elsevier) 1-14
[190] Hall G G 1951 The molecular orbital theory of chemical valency. 8. A method of calculating ionization potentials *Proc. R. Soc. London Ser. A - Math. Phys. Sci.* **205** 541-552
[191] Roothaan C C J 1951 New developments in molecular orbital theory *Rev. Mod. Phys.* **23** 69-89
[192] Slater J C 1930 Atomic shielding constants *Phys. Rev.* **36** 0057-0064
[193] Zener C 1930 Analytic atomic wave functions *Phys. Rev.* **36** 0051-0056
[194] Pople J A 1999 Nobel Lecture: Quantum chemical models *Rev. Mod. Phys.* **71** 1267-1274
[195] Jensen F 2007 *Introduction to Computational Chemistry* (John Wiley & Sons) (429pp)
[196] Boys S F 1950 Electronic wave functions. 1. A general method of calculation for the stationary states of any molecular system *Proc. R. Soc. London Ser. A - Math. Phys. Sci.* **200** 542-554
[197] Hehre W J, Stewart R F and Pople J A 1969 Self-consistent molecular-orbital methods. I. Use of Gaussian expansions of Slater-type atomic orbitals *J. Chem. Phys.* **51** 2657-2664
[198] Frisch M J, Pople J A and Binkley J S 1984 Self-consistent molecular-orbital methods 25. Supplementary functions for Gaussian basis sets *J. Chem. Phys.* **80** 3265-3269
[199] Spitznagel G W, Clark T, Chandrasekhar J and Schleyer P V 1982 Stabilization of methyl anions by 1st row substituents - The superiority of diffuse function-augmented basis-sets for anion calculations. *J. Comput. Chem.* **3** 363-371
[200] Clark T, Chandrasekhar J, Spitznagel G W and Schleyer P V 1983 Efficient diffuse function-augmented basis sets for anion calculations. III. The 3-21+G basis set for first-row elements, Li-F *J. Comput. Chem.* **4** 294-301

[201] Bartlett R J and Stanton J F 1994 *Reviews in Computational Chemistry, Vol. 5 (edited by Lipkowitz K B and Boyd D B)* (New York: VCH Publishers) 65-169
[202] Cohen A J, Mori-Sanchez P and Yang W T 2011 Challenges for Density Functional Theory *Chem. Rev.* **112** 289-320
[203] Pople J A, Seeger R and Krishnan R 1977 Variational configuration interaction methods and comparison with perturbation theory *Int. J. Quantum Chem.* **12** S149-S163
[204] Pople J A, Headgordon M and Raghavachari K 1987 Quadratic configuration interaction. A general technique for determining electron correlation energies *J. Chem. Phys.* **87** 5968-5975
[205] Bartlett R J 1981 Many-body perturbation theory and coupled cluster theory for electron correlation in molecules *Annu. Rev. Phys. Chem.* **32** 359-401
[206] Bartlett R J 1989 Coupled-cluster approach to molecular structure and spectra - A step toward predictive quantum chemistry *J. Phys. Chem.* **93** 1697-1708
[207] Cizek J and Paldus J 1980 Coupled cluster approach *Phys. Scr.* **21** 251-254
[208] Pople J A, Binkley J S and Seeger R 1976 Theoretical models incorporating electron correlation *Int. J. Quantum Chem.* **10** S1-S19
[209] Řezáč J, Riley K E and Hobza P 2012 Evaluation of the performance of post-Hartree-Fock methods in terms of intermolecular distance in noncovalent complexes *J. Comput. Chem.* **33** 691-694
[210] Sousa S F, Fernandes P A and Ramos M J 2007 General performance of density functionals *J. Phys. Chem. A* **111** 10439-10452
[211] Kresse G and Furthmuller J 1996 Efficient iterative schemes for *ab-initio* total energy calculations using a plane-wave basis set *Phys. Rev. B* **54** 11169-11186
[212] Kresse G and Furthmüller J 1996 Efficiency of *ab-initio* total energy calculations for metals and semiconductors using a plane-wave basis set *Comput. Mater. Sci.* **6** 15-50
[213] Kohn W and Sham L J 1965 Self-consistent equations including exchange and correlation effects *Phys. Rev.* **140** A1133-A1138
[214] Barth U V and Hedin L 1972 A local exchange-correlation potential for spin polarized case: I *J. Phys. C: Solid State Phys.* **5** 1629-1642
[215] Ceperley D M and Alder B J 1980 Ground state of the electron gas by a stochastic method *Phys. Rev. Lett.* **45** 566-569
[216] Perdew J P and Zunger A 1981 Self-interaction correction to density functional approximations for many-electron systems *Phys. Rev. B* **23** 5048-5079
[217] Vosko S H, Wilk L and Nusair M 1980 Accurate spin-dependent electron liquid correlation energies for local spin-density calculations - A critical analysis *Can. J. Phys.* **58** 1200-1211
[218] Langreth D C and Mehl M J 1981 Easily implementable nonlocal exchange-correlation energy functional *Phys. Rev. Lett.* **47** 446-450
[219] Perdew J P 1986 Density functional approximation for the correlation energy of the inhomogeneous electron-gas *Phys. Rev. B* **33** 8822-8824
[220] Becke A D 1988 Density functional exchange energy approximation with correct asymptotic behavior *Phys. Rev. A* **38** 3098-3100
[221] Adamo C and Barone V 1998 Exchange functionals with improved long-range behavior and adiabatic connection methods without adjustable parameters: The mPW and mPW1PW models *J. Chem. Phys.* **108** 664-675
[222] Becke A D 1986 Density functional calculations of molecular bond energies *J. Chem. Phys.* **84** 4524-4529
[223] Gill P M W 1996 A new gradient-corrected exchange functional *Mol. Phys.* **89** 433-445

[224] Filatov M and Thiel W 1997 A new gradient-corrected exchange-correlation density functional *Mol. Phys.* **91** 847-859
[225] Grimme S 2006 Semiempirical GGA-type density functional constructed with a long-range dispersion correction *J. Comput. Chem.* **27** 1787-1799
[226] Zhao Y and Truhlar D G 2008 Density functionals with broad applicability in chemistry *Acc. Chem. Res.* **41** 157-167
[227] Perdew J P and Wang Y 1992 Accurate and simple analytic representation of the electron-gas correlation energy *Phys. Rev. B* **45** 13244-13249
[228] Perdew J P, Burke K and Ernzerhof M 1996 Generalized Gradient Approximation Made Simple *Phys. Rev. Lett.* **77** 3865-3868
[229] Lee C T, Yang W T and Parr R G 1988 Development of the Colle-Salvetti correlation energy formula into a functional of the electron density *Phys. Rev. B* **37** 785-789
[230] Colle R and Salvetti O 1975 Approximate calculation of correlation energy for closed shells *Theor. Chim. Acta* **37** 329-334
[231] Lee C and Sosa C 1994 Local density component of the Lee-Yang-Parr correlation energy functional *J. Chem. Phys.* **100** 9018-9024
[232] Capelle K 2006 A bird's-eye view of density-functional theory *Braz. J. Phys.* **36** 1318-1343
[233] Lee C Y, Vanderbilt D, Laasonen K, Car R and Parrinello M 1993 *Ab-initio* studies on the structural and dynamic properties of ice *Phys. Rev. B* **47** 4863-4872
[234] Barnett R N and Landman U 1993 Born-Oppenheimer molecular dynamics simulations of finite systems: Structure and dynamics of $(H_2O)_2$ *Phys. Rev. B* **48** 2081-2097
[235] Laasonen K, Sprik M, Parrinello M and Car R 1993 *Ab-initio* liquid water *J. Chem. Phys.* **99** 9080-9089
[236] Tsuzuki S and Luthi H P 2001 Interaction energies of van der Waals and hydrogen bonded systems calculated using density functional theory: Assessing the PW91 model *J. Chem. Phys.* **114** 3949-3957
[237] Hammer B, Jacobsen K W and Norskov J K 1993 Role of nonlocal exchange-correlation in activated adsorption *Phys. Rev. Lett.* **70** 3971-3974
[238] Hamann D R 1996 Generalized gradient theory for silica phase transitions *Phys. Rev. Lett.* **76** 660-663
[239] Tran F and Blaha P 2009 Accurate Band Gaps of Semiconductors and Insulators with a Semilocal Exchange-Correlation Potential *Phys. Rev. Lett.* **102** 226401 (4pp)
[240] Ortiz G 1992 Gradient-corrected pseudopotential calculations in semiconductors *Phys. Rev. B* **45** 11328-11331
[241] Bowen C, Sugiyama G and Alder B J 1994 Static dielectric response of the electron-gas *Phys. Rev. B* **50** 14838-14848
[242] Tao J M, Perdew J P, Staroverov V N and Scuseria G E 2003 Climbing the density functional ladder: Nonempirical meta-generalized gradient approximation designed for molecules and solids *Phys. Rev. Lett.* **91** 146401 (4pp)
[243] Wesolowski T A 2007 *Hohenberg-Kohn-Sham Density Functional Theory (edited by Sokalski W A)* (Springer Netherlands) 153-202
[244] Staroverov V N, Scuseria G E, Tao J M and Perdew J P 2003 Comparative assessment of a new nonempirical density functional: Molecules and hydrogen-bonded complexes *J. Chem. Phys.* **119** 12129-12137
[245] Becke A D 1988 Correlation-energy of an inhomogeneous electron gas: A coordinate-space model *J. Chem. Phys.* **88** 1053-1062
[246] Becke A D 1994 Thermochemical tests of a kinetic-energy dependent exchange-correlation approximation *Int. J. Quantum Chem.* **52** S625-S632

[247] Becke A D and Roussel M R 1989 Exchange holes in inhomogeneous systems - A coordinate-space model *Phys. Rev. A* **39** 3761-3767
[248] Becke A D 1993 Density-functional thermochemistry. III. The role of exact exchange *J. Chem. Phys.* **98** 5648-5652
[249] Stephens P J, Devlin F J, Chabalowski C F and Frisch M J 1994 *Ab-initio* calculation of vibrational absorption and circular-dichroism spectra using density-functional force-fields *J. Phys. Chem.* **98** 11623-11627
[250] Xu X, Zhang Q S, Muller R P and Goddard W A 2005 An extended hybrid density functional (X3LYP) with improved descriptions of nonbond interactions and thermodynamic properties of molecular systems *J. Chem. Phys.* **122** 014105 (14pp)
[251] Sholl D and Steckel J A 2009 *Density Functional Theory: A Practical Introduction* (Hoboken: John Wiley & Sons) (238pp)
[252] Ernzerhof M and Scuseria G E 1999 Assessment of the Perdew-Burke-Ernzerhof exchange-correlation functional *J. Chem. Phys.* **110** 5029-5036
[253] Liu H Y, Elstner M, Kaxiras E, Frauenheim T, Hermans J and Yang W T 2001 Quantum mechanics simulation of protein dynamics on long timescale *Proteins* **44** 484-489
[254] Elstner M, Hobza P, Frauenheim T, Suhai S and Kaxiras E 2001 Hydrogen bonding and stacking interactions of nucleic acid base pairs: A density functional theory based treatment *J. Chem. Phys.* **114** 5149-5155
[255] Wu Q and Yang W T 2002 Empirical correction to density functional theory for van der Waals interactions *J. Chem. Phys.* **116** 515-524
[256] Allen M J and Tozer D J 2002 Helium dimer dispersion forces and correlation potentials in density functional theory *J. Chem. Phys.* **117** 11113-11120
[257] Dobson J F, McLennan K, Rubio A, Wang J, Gould T, Le H M and Dinte B P 2001 Prediction of dispersion forces: Is there a problem? *Australian Journal of Chemistry* **54** 513-527
[258] Becke A D and Johnson E R 2006 Exchange-hole dipole moment and the dispersion interaction: High-order dispersion coefficients *J. Chem. Phys.* **124** 014104 (6pp)
[259] Becke A D and Johnson E R 2005 A density-functional model of the dispersion interaction *J. Chem. Phys.* **123** 154101 (9pp)
[260] Becke A D and Johnson E R 2005 Exchange-hole dipole moment and the ospersion interaction *J. Chem. Phys.* **122** 154104 (5pp)
[261] Becke A D, Arabi A A and Kannemann F O 2010 Nonempirical density-functional theory for van der Waals interactions *Can. J. Chem.* **88** 1057-1062
[262] Johnson E R and Becke A D 2006 A post-Hartree-Fock model of intermolecular interactions: Inclusion of higher-order corrections *J. Chem. Phys.* **124** 174104 (9pp)
[263] Johnson E R and Becke A D 2005 A post-Hartree-Fock model of intermolecular interactions *J. Chem. Phys.* **123** 024101 (7pp)
[264] Halgren T A 1992 The representation of van der Waals (vdW) interactions in molecular mechanics force fields: potential form, combination rules, and vdW parameters *J. Am. Chem. Soc.* **114** 7827-7843
[265] Miller K J 1990 Additivity methods in molecular polarizability *J. Am. Chem. Soc.* **112** 8533-8542
[266] Ahlrichs R, Penco R and Scoles G 1977 Intermolecular forces in simple systems *Chem. Phys.* **19** 119-130
[267] Dion M, Rydberg H, Schroder E, Langreth D C and Lundqvist B I 2004 Van der Waals density functional for general geometries *Phys. Rev. Lett.* **92** 246401 (4pp)
[268] von Lilienfeld O A, Tavernelli I, Rothlisberger U and Sebastiani D 2004 Optimization of effective atom centered potentials for London dispersion forces in density functional theory *Phys. Rev. Lett.* **93** 153004 (4pp)

[269] DiLabio G A 2008 Accurate treatment of van der Waals interactions using standard density functional theory methods with effective core-type potentials: Application to carbon-containing dimers *Chem. Phys. Lett.* **455** 348-353
[270] Roman-Perez G and Soler J M 2009 Efficient Implementation of a van der Waals Density Functional: Application to Double-Wall Carbon Nanotubes *Phys. Rev. Lett.* **103** 096102 (4pp)
[271] Vydrov O A and Van Voorhis T 2009 Nonlocal van der Waals Density Functional Made Simple *Phys. Rev. Lett.* **103** 063004 (4pp)
[272] Vydrov O A and Van Voorhis T 2010 Implementation and assessment of a simple nonlocal van der Waals density functional *J. Chem. Phys.* **132** 164113 (6pp)
[273] Elsayed M S A 2009 *The Bloch's Theorem* (McGill University) (35pp)
[274] Monkhorst H J and Pack J D 1976 Special points for Brillouin-zone integrations *Phys. Rev. B* **13** 5188-5192
[275] Walkosz W 2011 *Atomic Scale Characterisation and First-Principles Studies of Si_3N_4 Interfaces* (New York: Springer) (160pp)
[276] Payne M C, Teter M P, Allan D C, Arias T A and Joannopoulos J D 1992 Iterative minimization techniques for *ab-initio* total-energy calculations: molecular dynamics and conjugate gradients *Rev. Mod. Phys.* **64** 1045-1097
[277] Kresse G and Joubert D 1999 From ultrasoft pseudopotentials to the projector augmented-wave method *Phys. Rev. B* **59** 1758-1775
[278] Troullier N and Martins J L 1991 Efficient pseudopotentials for plane-wave calculations *Phys. Rev. B* **43** 1993-2006
[279] Kresse G and Hafner J 1994 Norm-conserving and ultrasoft pseudopotentials for first row and transition elements *J. Phys.-Condes. Matter* **6** 8245-8257
[280] Hamann D R, Schluter M and Chiang C 1979 Norm-conserving pseudopotentials *Phys. Rev. Lett.* **43** 1494-1497
[281] Bachelet G B, Hamann D R and Schluter M 1982 Pseudopotentials that work - From H to Pu *Phys. Rev. B* **26** 4199-4228
[282] Blochl P E 1994 Projector augmented-wave method *Phys. Rev. B* **50** 17953-17979
[283] Vanderbilt D 1990 Soft Self-Consistent Pseudopotentials in a Generalized Eigenvalue Formalism *Phys. Rev. B* **41** 7892-7895
[284] ABINIT [online] Available at: http://www.abinit.org/ [Accessed: 2 Nov 2013]
[285] Quantum-ESPRESSO [online] Available at: http://www.quantum-espresso.org/index/php. [Accessed: 2 Nov 2013]
[286] CPMD [online] Available at: http://www.cpmd.org/ [Accessed: 2 Nov 2013]
[287] WIEN2k [online] Available at: http://www.wien2k.at/ [Accessed: 2 Nov 2013]
[288] Delley B 2000 From molecules to solids with the $DMol^3$ approach *J. Chem.Phys.* **113** 7756-7764
[289] Soler J M, Artacho E, Gale J D, Garcia A, Junquera J, Ordejon P and Sanchez-portal D 2002 The SIESTA method for *ab initio* order-N materials simulation *J. Phys. Condens. Matter* **14** 2745-2779
[290] Skylaris C K, Haynes P D, Mostofi A A and Payne M C 2005 Introducing ONETEP: Linear-scaling density functional simulations on parallel computers *J. Chem. Phys*. **122** 084119
[291] Hernandez E and Gillan M J 1995 Self-consistent first-principles technique with linear scaling *Phys. Rev. B* **51** (15) 10157-10160
[292] Bowler D R, Bush I J and Gillan M K 2000 Practical methods for *ab initio* calculations on thousands of atoms *Int. J. Quant. Chem.* **77** (5) 831
[293] Bowler D R, Miyazaki T and Gillan M K 2002 Recent progress in linear scaling *ab initio* electronic structure techniques *J. Phys. Condens. Matt.* **14** (11) 2781
[294] Schmidt M W, Baldridge K K, Boatz J A, Elbert S T, Gordon M S, Jensen J H, Koseki S, Matsunaga N, Nguyen K A, Su S, Windus T L, Dupuis M and

Montgomery J A 1993 General atomic and molecular electronic structure system *J. Comput. Chem.* **14** 1347

[295] Orlando R, Piane M D, Bush I J, Ugliengo P, Ferrabone M and Dovesi R 2012 A new massively parallel version of CRYSTAL for large systems on high performance computing architectures *J. Comput. Chem.* 33 (28) 2276-2284

[296] Gaussian 09, Revision **D.01**, Frisch M J, Trucks G W, Schlegel H B, Scuseria G E, Robb M A, Cheeseman J R, Scalmani G, Barone V, Mennucci B, Petersson G A, Nakatsuji H, Caricato M, Li X, Hratchian H P, Izmaylov A F, Bloino J, Zheng G, Sonnenberg J L, Hada M, Ehara M, Toyota K, Fukuda R, Hasegawa J, Ishida M, Nakajima T, Honda Y, Kitao O, Nakai H, Vreven T, Montgomery J A Jr, Peralta J E, Ogliaro F, Bearpark M, Heyd J J, Brothers E, Kudin K N, Staroverov V N, Kobayashi R, Normand J, Raghavachari K, Rendell A, Burant J C, Iyengar S S, Tomasi J, Cossi M, Rega N, Millam N J, Klene M, Knox J E, Cross J B, Bakken V, Adamo C, Jaramillo J, Gomperts R, Stratmann R E, Yazyev O, Austin A J, Cammi R, Pomelli C, Ochterski J W, Martin R L, Morokuma K, Zakrzewski V G, Voth G A, Salvador P, Dannenberg J J, Dapprich S, Daniels A D, Farkas Ö, Foresman J B, Ortiz J V, Cioslowski J, Fox D J, Gaussian, Inc., Wallingford CT, 2009

[297] Kresse G, Marsman M and Furthmuller J 2009 *VASP the Guide* (University of Wien) (162pp)

[298] Davidson E R 1983 *Methods in Computational Molecular Physics (edited by Dierksen G H F and Wilson S)* (New York: Plenum) 95-113

[299] Liu B 1978 *Numerical Algorithms in Chemistry: Algebraic Methods (edited by Moler C and Shavitt I)* (Berkeley, CA: Lawrence Berkeley Laboratory) 49-53

[300] Wood D M and Zunger A 1985 A new method for diagonalizing large matrices *J. Phys. A-Math. Gen.* **18** 1343-1359

[301] Pulay P 1980 Convergence acceleration of iterative sequences - The case of SCF iteration *Chem. Phys. Lett.* **73** 393-398

[302] Fletcher R and Reeves C M 1964 Function minimization by conjugate gradients *Comput. J.* **7** 149-162

[303] Ochterski J W 1999 Vibrational Analysis in Gaussian *The Official Gaussian Website* 1-10

[304] Meot-Ner M 2005 The ionic hydrogen bond *Chem. Rev.* **105** 213-284

[305] Bernhard E 2012 wxDragon *Institut für Anorganische Chemie der RWTH: Aachen*

[306] Savin A, Jepsen O, Flad J, Andersen O K, Preuss H and Vonschnering H G 1992 Electron localization in solid-state structures of the elements - The diamond structure *Angew. Chem.-Int. Edit. Engl.* **31** 187-188

[307] Savin A 2005 The electron localization function (ELF) and its relatives: interpretations and difficulties *J. Mol. Struct. THEOCHEM* **727** 127-131

[308] Silvi B and Savin A 1994 Classification of chemical-bonds based on topological analysis of electron localization functions *Nature* **371** 683-686

[309] Terriberry T B, Cox D F and Bowman D A 2002 A tool for the interactive 3D visualization of electronic structure in molecules and solids *Comput. Chem.* **26** 313-319

[310] Mulliken R S 1955 Electron population analysis on LCAO-MO molecular wave functions. I *J. Chem. Phys.* **23** 1833-1840

[311] Reed A E, Curtiss L A and Weinhold F 1988 Intermolecular interactions from a natural bond orbital, donor-acceptor viewpoint *Chem. Rev.* **88** 899-926

[312] Hirshfeld F L 1977 Bonded-atom fragments for describing molecular charge-densities *Theor. Chim. Acta* **44** 129-138

[313] Bader R F W and Matta C F 2004 Atomic charges are measurable quantum expectation values: A rebuttal of criticisms of QTAIM charges *J. Phys. Chem. A* **108** 8385-8394

[314] Bader R F W 1991 A quantum theory of molecular structure and its applications *Chem. Rev.* **91** 893-928
[315] Besler B H, Merz K M and Kollman P A 1990 Atomic charges derived from semiempirical methods *J. Comput. Chem.* **11** 431-439
[316] Breneman C M and Wiberg K B 1990 Determining atom-centered monopoles from molecular electrostatic potentials. The need for high sampling density in formamide conformational analysis *J. Comput. Chem.* **11** 361-373
[317] Shao Y, Molnar L F, Jung Y, Kussmann J, Ochsenfeld C, Brown S T, Gilbert A T B, Slipchenko L V, Levchenko S V, O'Neill D P, DiStasio R A, Lochan R C, Wang T, Beran G J O, Besley N A, Herbert J M, Lin C Y, Van Voorhis T, Chien S H, Sodt A, Steele R P, Rassolov V A, Maslen P E, Korambath P P, Adamson R D, Austin B, Baker J, Byrd E F C, Dachsel H, Doerksen R J, Dreuw A, Dunietz B D, Dutoi A D, Furlani T R, Gwaltney S R, Heyden A, Hirata S, Hsu C P, Kedziora G, Khalliulin R Z, Klunzinger P, Lee A M, Lee M S, Liang W, Lotan I, Nair N, Peters B, Proynov E I, Pieniazek P A, Rhee Y M, Ritchie J, Rosta E, Sherrill C D, Simmonett A C, Subotnik J E, Woodcock H L, Zhang W, Bell A T, Chakraborty A K, Chipman D M, Keil F J, Warshel A, Hehre W J, Schaefer H F, Kong J, Krylov A I, Gill P M W and Head-Gordon M 2006 Advances in methods and algorithms in a modern quantum chemistry program package *Phys. Chem. Chem. Phys.* **8** 3172-3191
[318] Henkelman G, Arnaldsson A and Jonsson H 2006 A fast and robust algorithm for Bader decomposition of charge density *Comput. Mater. Sci.* **36** 354-360
[319] Jacquemin D, Le Bahers T, Adamo C and Ciofini I 2012 What is the "best" atomic charge model to describe through-space charge-transfer excitations? *Phys. Chem. Chem. Phys.* **14** 5383-5388
[320] Guerra C F, Handgraaf J W, Baerends E J and Bickelhaupt F M 2004 Voronoi deformation density (VDD) charges: Assessment of the Mulliken, Bader, Hirshfeld, Weinhold, and VDD methods for charge analysis *J. Comput. Chem.* **25** 189-210
[321] Sanville E, Kenny S D, Smith R and Henkelman G 2007 Improved grid-based algorithm for Bader charge allocation *J. Comput. Chem.* **28** 899-908
[322] Minami T, Miyata T and Yamamoto T 1998 Work function of transparent conducting multicomponent oxide thin films prepared by magnetron sputtering *Surf. Coat. Technol.* **108** 583-587
[323] Yang Z and Xiong S J 2011 Adsorption of Ag and Au atoms on wurtzite ZnO (0001) surface *Surf. Sci.* **605** 40-45
[324] Spencer M J S, Yarovsky I, Wlodarski W and Kalantar-zadeh K 2007 Density functional theory study of ZnO nanostructures for NO and NO_2 sensing *Transducers '07 and Eurosensors XXI, The 14th International Conference on Solid-State Sensors, Actuators and Microsystems, art. no.* 4300298 987-990
[325] Breedon M, Spencer M J S and Yarovsky I 2009 Adsorption of NO and NO_2 on the ZnO($2\bar{1}\bar{1}0$) surface: A DFT study *Surf. Sci.* **603** 3389-3399
[326] Lany S and Zunger A 2008 Assessment of correction methods for the band-gap problem and for finite-size effects in supercell defect calculations: Case studies for ZnO and GaAs *Phys. Rev. B* **78** 235104 (25pp)
[327] Lany S and Zunger A 2010 Many-body GW calculation of the oxygen vacancy in ZnO *Phys. Rev. B* **81** 113201 (4pp)
[328] Woll C 2007 The chemistry and physics of zinc oxide surfaces *Prog. Surf. Sci.* **82** 55-120
[329] Nyberg M, Nygren M A, Pettersson L G M, Gay D H and Rohl A L 1996 Hydrogen dissociation on reconstructed ZnO surfaces *J. Phys. Chem.* **100** 9054-9063

[330] Jang S H and Chichibu S F 2012 Structural, elastic, and polarization parameters and band structures of wurtzite ZnO and MgO *J. Appl. Phys.* **112** 073503 (6pp)
[331] D'Amico N R, Cantele G and Ninno D 2012 First-Principles Calculations of Clean and Defected ZnO Surfaces *J. Phys. Chem. C* **116** 21391-21400
[332] Filippetti A, Fiorentini V, Cappellini G and Bosin A 1999 Anomalous relaxations and chemical trends at III-V semiconductor nitride nonpolar surfaces *Phys. Rev. B* **59** 8026-8031
[333] Meyer B and Marx D 2003 Density functional study of the structure and stability of ZnO surfaces *Phys. Rev. B* **67** 035403 (11pp)
[334] Duke C B, Meyer R J, Paton A and Mark P 1978 Calculation of low energy electron diffraction intensities from ZnO ($10\bar{1}0$). II. Influence of calculational procedure, model potential, and second-layer structural distortions *Phys. Rev. B* **18** 4225-4240
[335] Spencer M J S, Wong K W J and Yarovsky I 2010 Density functional theory modelling of ZnO($10\bar{1}0$) and ZnO($2\bar{1}\bar{1}0$) surfaces: Structure, properties and adsorption of N_2O *Mater. Chem. Phys.* **119** 505-514
[336] Hill N A and Waghmare U 2000 First-principles study of strain-electronic interplay in ZnO: Stress and temperature dependence of the piezoelectric constants *Phys. Rev. B* **62** 8802-8810
[337] Hoang M T, Yvonnet J, Mitrushchenkov A and Chambaud G 2013 First-principles based multiscale model of piezoelectric nanowires with surface effects *J. Appl. Phys.* **113** 014309 (9pp)
[338] He M R, Yu R and Zhu J 2012 Subangstrom Profile Imaging of Relaxed ZnO($10\bar{1}$ 0) Surfaces *Nano Letters* **12** 704-708
[339] Sawai Y, Hazu K and Chichibu S F 2010 Surface stoichiometry and activity control for atomically smooth low dislocation density ZnO and pseudomorphic MgZnO epitaxy on a Zn-polar ZnO substrate by the helicon-wave-excited-plasma sputtering epitaxy method *J. Appl. Phys.* **108** 063541 (8pp)
[340] Labat F, Ciofini I and Adamo C 2009 Modeling ZnO phases using a periodic approach: From bulk to surface and beyond *J. Chem. Phys.* **131** 044708 (11pp)
[341] Prades J D, Cirera A, Morante J R and Comet A 2007 *Ab-initio* insights into the visible luminescent properties of ZnO *Thin Solid Films* **515** 8670-8673
[342] Cooke D J, Marmier A and Parker S C 2006 Surface structure of ($10\bar{1}0$) and ($11\bar{2}$ 0) surfaces of ZnO with density functional theory and atomistic simulation *J. Phys. Chem. B* **110** 7985-7991
[343] Claeyssens F, Freeman C L, Allan N L, Sun Y, Ashfold M N R and Harding J H 2005 Growth of ZnO thin films - experiment and theory *J. Mater. Chem.* **15** 139-148
[344] Catti M, Noel Y and Dovesi R 2003 Full piezoelectric tensors of wurtzite and zinc blende ZnO and ZnS by first-principles calculations *J. Phys. Chem. Solids* **64** 2183-2190
[345] Wander A and Harrison N M 2003 The structure of higher defective ZnO *Surf. Sci.* **529** L281-L284
[346] Whitmore L, Sokol A A and Catlow C R A 2002 Surface structure of zinc oxide ($10\bar{1}0$), using an atomistic, semi-infinite treatment *Surf. Sci.* **498** 135-146
[347] Beltran A, Andres J, Calatayud M and Martins J B L 2001 Theoretical study of ZnO ($10\bar{1}0$) and Cu/ZnO ($10\bar{1}0$) surfaces *Chem. Phys. Lett.* **338** 224-230
[348] Wander A and Harrison N M 2000 An *ab-initio* study of ZnO($10\bar{1}0$) *Surf. Sci.* **457** L342-L346

[349] Jaffe J E, Harrison N M and Hess A C 1994 *Ab-initio* study of ZnO $(10\bar{1}0)$ surface relaxation *Phys. Rev. B* **49** 11153-11158
[350] Kisi E H and Elcombe M M 1989 Upsilon-parameters for the wutzite structure of ZnS and ZnO using powder neutron-diffraction *Acta Crystallogr., Sect. C: Cryst. Struct. Commun.* **45** 1867-1870
[351] Albertsson J, Abrahams S C and Kvick A 1989 Atomic displacement, anharmonic thermal vibration, expansivity and pyroelectric coefficient thermal dependencies in ZnO *Acta Crystallogr., Sect. B: Struct. Sci.* **45** 34-40
[352] Wang Y R and Duke C B 1987 Surface reconstructions of ZnO cleavage faces *Surf. Sci.* **192** 309-322
[353] Blochl P E, Jepsen O and Andersen O K 1994 Improved tetrahedron method for Brillouin-zone integrations *Phys. Rev. B* **49** 16223-16233
[354] Diebold U, Koplitz L V and Dulub O 2004 Atomic-scale properties of low-index ZnO surfaces *Appl. Surf. Sci.* **237** 336-342
[355] Dulub O, Boatner L A and Diebold U 2002 STM study of the geometric and electronic structure of ZnO(0001)-Zn, $(000\bar{1})$-O, $(10\bar{1}0)$, and $(11\bar{2}0)$ surfaces *Surf. Sci.* **519** 201-217
[356] Wong K M, Alay-e-Abbas S M, Shaukat A, Fang Y and Lei Y 2013 First-principles investigation of the size-dependent structural stability and electronic properties of O-vacancies at the ZnO polar and non-polar surfaces *J. Appl. Phys.* **113** 014304 (11pp)
[357] Zhang H F, Lu S X, Xu W G and Yuan F 2013 First-principles study of electronic structures and photocatalytic activity of low-Miller-index surfaces of ZnO *J. Appl. Phys.* **113** 34903-34903
[358] Ding Y and Wang Z L 2007 Profile imaging of reconstructed polar and non-polar surfaces of ZnO *Surf. Sci.* **601** 425-433
[359] Wander A and Harrison N M 2000 An *ab-initio* study of ZnO$(11\bar{2}0)$ *Surf. Sci.* **468** L851-L855
[360] Jedrecy N, Gallini S, Sauvage-Simkin M and Pinchaux R 2000 The ZnO non-polar $(10\bar{1}0)$ surface: an X-ray structural investigation *Surf. Sci.* **460** 136-143
[361] Casarin M, Maccato C and Vittadini A 1998 Theoretical investigation of the chemisorption of H_2 and CO on the ZnO$(10\bar{1}0)$ surface *Inorg. Chem.* **37** 5482-5490
[362] Schröer P, Krüger P and Pollmann J 1994 Self-consistent electronic-structure calculations of the $(10\bar{1}0)$ surfaces of the wurtzite compounds ZnO and CdS *Phys. Rev. B* **49** 17092-17101
[363] Gopel W, Pollmann J, Ivanov I and Reihl B 1982 Angle-resolved photoemission from polar and non-polar zinc-oxide surfaces *Phys. Rev. B* **26** 3144-3150
[364] Duke C B, Lubinsky A R, Chang S C, Lee B W and Mark P 1977 Low energy electron diffraction analysis of the atomic geometry of ZnO $(10\bar{1}0)$ *Phys. Rev. B* **15** 4865-4873
[365] Lubinsky A R, Duke C B, Chang S C, Lee B W and Mark P 1976 Atomic geometry of low-index surfaces of ZnO - LEED analysis *J. Vac. Sci. Technol.* **13** 189-192
[366] Duke C B, Lubinsky A R, Lee B W and Mark P 1976 Atomic geometry of cleavage surfaces of tetrahedrally coordinated compound semiconductors *J. Vac. Sci. Technol.* **13** 761-768
[367] Wang Q and Jena P 2004 First-principles study of magnetism in $(11\bar{2}0)$ Zn1-xMnxO thin film *Appl. Phys. Lett.* **84** 4170-4172
[368] Janotti A and Van de Walle C G 2007 Native point defects in ZnO *Phys. Rev. B* **76** 165202 (22pp)

[369] Calzolari A and Catellani A 2009 Water Adsorption on Nonpolar ZnO($10\bar{1}0$) Surface: A Microscopic Understanding *J. Phys. Chem. C* **113** 2896-2902
[370] Kaewmaraya T, Pathak B, Araujo C M, Rosa A L and Ahuja R 2012 Water adsorption on ZnO($10\bar{1}0$): The role of intrinsic defects *Epl* **97** 17014 (5pp)
[371] Spencer M J S, Wong K W J and Yarovsky I 2012 Surface defects on ZnO nanowires: implications for design of sensors *J. Phys.Condens. Matter* **24** 305001 (12pp)
[372] Rusu C N and Yates J T 2001 N_2O adsorption and photochemistry on high area TiO_2 powder *J. Phys. Chem. B* **105** 2596-2603
[373] Oviedo J and Sanz J F 2005 N_2O decomposition on TiO_2(110) from dynamic first-principles calculations *J. Phys. Chem. B* **109** 16223-16226
[374] Sorescu D C and Yates J T 2002 First principles calculations of the adsorption properties of CO and NO on the defective TiO_2(110) surface *J. Phys. Chem. B* **106** 6184-6199
[375] Shultz A N, Hetherington W M, Baer D R, Wang L Q and Engelhard M H 1997 Comparative SHG and XPS studies of interactions between defects and N_2O on rutile TiO_2(110) surfaces *Surf. Sci.* **392** 1-7
[376] Henderson M A, Szanyi J and Peden C H F 2003 Conversion of N_2O to N_2 on TiO_2(110) *Catal. Today* **85** 251-266
[377] Pan X, Cai Q X, Chen W L, Zhuang G L, Li X N and Wang J G 2013 A DFT study of gas molecules adsorption on the anatase (001) nanotube arrays *Comput. Mater. Sci.* **67** 174-181
[378] Wanbayor R, Deak P, Frauenheim T and Ruangpornvisuti V 2012 First-principles investigation of adsorption of N_2O on the anatase TiO_2(101) and the CO pre-adsorbed TiO_2 surfaces *Comput. Mater. Sci.* **58** 24-30
[379] Zemva P, Lesar A, Kobal I and Senegacnik M 2001 Thermal decomposition of N_2O over ZnO: Kinetic isotope effects study *Langmuir* **17** 1543-1548
[380] Kanazawa E, Sakai G, Shimanoe K, Kanmura Y, Teraoka Y, Miura N and Yamazoe N 2001 Metal oxide semiconductor N_2O sensor for medical use *Sens. Actuator B: Chem.* **77** 72-77
[381] Tanaka K I and Blyholder G 1971 Photocatalytic reactions on semiconductor surfaces .1. Decomposition of nitrous oxide on zinc oxide *J. Phys. Chem.* **75** 1037-1043
[382] Miller T M and Grassian V H 1995 Environmental catalysis - Adsorption and decomposition of nitrous oxide on zirconia *J. Am. Chem. Soc.* **117** 10969-10975
[383] Lian J C, Kieseritzky E, Gonchar A, Sterrer M, Rocker J, Gao H J and Risse T 2010 N_2O Adsorption on the Surface of MgO(001) Thin Films: An Infrared and TPD Study *J. Phys. Chem. C* **114** 3148-3151
[384] Skoplyak O, Barteau M A and Chen J G 2008 Ethanol and ethylene glycol on Ni/Pt(111) bimetallic surfaces: A DFT and HREELS study *Surf. Sci.* **602** 3578-3587
[385] Kubo T, Ems T, Atli A, Aruga T, Takagi N and Nishijima M 1997 Adsorption and thermal decomposition of N_2O on Si(100): Electron energy loss spectroscopy and thermal desorption studies *Surf. Sci.* **382** 214-220
[386] Koel B, Panja C, Kim J and Samano E 2006 *Adsorbed Layers on Surfaces. Part 5: Adsorption of molecules on metal, semiconductor and oxide surfaces: CO_2, NO_2, SO_2, OCS, N_2O, O_3 on metal surfaces (edited by Bonzel H P)* (Springer) 170-242
[387] Huang H H, Seet C S, Zou Z and Xu G Q 1996 The adsorption of N_2O on clean and chemically modified Ru(001) surfaces *Surf. Sci.* **356** 181-188

[388] Wu S Y, Su C H, Chang J G, Chen H T, Hou C H and Chen H L 2011 Adsorption and dissociation of N_2O molecule on Fe(111) surface: A DFT study *Comput. Mater. Sci.* **50** 3311-3314
[389] Avery N R 1983 An EELS study of N_2O adsorption on Pt(111) *Surf. Sci.* **131** 501-510
[390] Kokalj A, Kobal I, Horino H, Ohno Y and Matsushima T 2002 Orientation of N_2O molecule on Pd(110) surface *Surf. Sci.* **506** 196-202
[391] Horino H, Rzeznicka I, Kokalj A, Kobal I, Ohno Y, Hiratsuka A and Matsushima T 2002 Two-directional N_2 desorption in thermal dissociation of N_2O on Rh(110), Ir(110), and Pd(110) at low temperatures *J. Vac. Sci. Technol., A: Vac. Surf. Films* **20** 1592-1596
[392] Matsushima T and Kokalj A 2007 Angular distributions of desorbing N_2 in thermal N_2O decomposition on Rh(100) *Surf. Sci.* **601** 3996-4000
[393] Manzhos S and Yamashita K 2010 A model for the dissociative adsorption of N_2O on Cu(100) using a continuous potential energy surface *Surf. Sci.* **604** 555-561
[394] Orita H and Itoh N 2004 Adsorption of N_2 and N_2O on Ni(755) surface: *Ab-initio* periodic density functional study *Surf. Sci.* **550** 166-176
[395] Paul J F, Perez-Ramirez J, Arnple F and Ricart J M 2004 Theoretical studies of N_2O adsorption and reactivity to N_2 and NO on Rh(111) *J. Phys. Chem. B* **108** 17921-17927
[396] Kaewruksa B, Wanbayor R and Ruangpornvisuti V 2012 Co-adsorptions of CO/N_2O, NO/NH_3, CO_2/N_2 and conversion of CO/N_2O to CO_2/N_2 on ZnO graphene-like nanosheet *J. Mol. Struct.* **1012** 50-55
[397] Liu E Z and Jiang J Z 2009 Magnetism of O-terminated ZnO(0001) with adsorbates *J. Phys. Chem. C* **113** 16116-16120
[398] Umbach E and Menzel D 1981 Horizontal and vertical configurations of molecular N_2O on W(110) and Ru(001) *Chem. Phys. Lett.* **84** 491-496
[399] Hussain G, Rahman M M and Sheppard N 1991 An infrared study of adsorption of N_2O on ZnO *Spectroc. Acta Pt. A-Molec. Biomolec. Spectr.* **47** 1525-1530
[400] Liao L, Lu H B, Li J C, He H, Wang D F, Fu D J, Liu C and Zhang W F 2007 Size Dependence of Gas Sensitivity of ZnO Nanorods *J. Phys. Chem. C* **111** 1900-1903
[401] Yuan Q Z, Zhao Y P, Li L M and Wang T H 2009 *Ab-initio* Study of ZnO-Based Gas-Sensing Mechanisms: Surface Reconstruction and Charge Transfer *J. Phys. Chem. C* **113** 6107-6113
[402] Kwak G and Yong K J 2008 Adsorption and reaction of ethanol on ZnO nanowires *J. Phys. Chem. C* **112** 3036-3041
[403] Vohs J M and Barteau M A 1989 Dehydration and dehydrogenation of ethanol and 1-propanol on the polar surfaces of zinc oxide *Surf. Sci.* **221** 590-608
[404] Barnes A J and Hallam H E 1970 Infra-red cryogenic studies. Part 5. Ethanol and ethanol-*d* argon matrices *Trans. Faraday Soc.* **66** 1932-1940
[405] Zhou X Y, Li J P, Ma M and Xue Q Z 2011 Effect of ethanol gas on the electrical properties of ZnO nanorods *Physica E* **43** 1056-1060
[406] Meyer B, Marx D, Dulub O, Diebold U, Kunat M, Langenberg D and Wöll C 2004 Partial Dissociation of Water Leads to Stable Superstructures on the Surface of Zinc Oxide *Angew. Chem. Int. Ed.* **43** 6641-6645
[407] Liu Y and Liu M L 2007 Ordered ZnO nanorods synthesized by combustion chemical vapor deposition *J. Nanosci. Nanotechnol.* **7** 4529-4533
[408] Durig J R, Deeb H, Darkhalil I D, Klaassen J J, Gounev T K and Ganguly A The r_0 structural parameters, conformational stability, barriers to internal rotation, and vibrational assignments for *trans* and *gauche* ethanol *J. Mol. Struct.* **985** 202-210

[409] Wang J, Wang Z, Huang B, Ma Y, Liu Y, Qin X, Zhang X and Dai Y 2012 Oxygen Vacancy Induced Band-Gap Narrowing and Enhanced Visible Light Photocatalytic Activity of ZnO *ACS Appl. Mater. Interfaces* **4** 4024-4030

[410] Branda M M, Rodriguez A H, Belelli P G and Castellani N J 2009 Ethanol adsorption on MgO surface with and without defects from a theoretical point of view *Surf. Sci.* **603** 1093-1098

[411] Lavrov E V, Herklotz F and Weber J 2009 Identification of two hydrogen donors in ZnO *Phys. Rev. B* **79** 165210 (13pp)

[412] Shi G A, Stavola M, Pearton S J, Thieme M, Lavrov E V and Weber J 2005 Hydrogen local modes and shallow donors in ZnO *Phys. Rev. B* **72** 195211 (8pp)

[413] Jokela S J and McCluskey M D 2005 Structure and stability of O-H donors in ZnO from high-pressure and infrared spectroscopy *Phys. Rev. B* **72** 113201 (4pp)

[414] McCluskey M D, Jokela S J, Zhuravlev K K, Simpson P J and Lynn K G 2002 Infrared spectroscopy of hydrogen in ZnO *Appl. Phys. Lett.* **81** 3807-3809

[415] Li F, Wang L, Dai J, Pu Y, Fang W and Jiang F 2007 Photoluminescence observations of hydrogen incorporation and outdiffusion in ZnO thin films *J.Lumin.* **124** 162-166

[416] Lindsay R, Muryn C A, Michelangeli E and Thornton G 2004 ZnO($000\bar{1}$)-O surface structure: hydrogen-free (1x1) termination *Surf. Sci.* **565** L283-L287

[417] Losurdo M and Giangregorio M M 2005 Interaction of atomic hydrogen with Zn-polar and O-polar ZnO surfaces *Appl. Phys. Lett.* **86** 091901-091903

[418] Yuri M S, Howard L M, David C L, Donald C R, Cole W L, Nelson Y G, Nancy C G, Larry E H, Shigeru N and Leonard J B 2004 Remote hydrogen plasma doping of single crystal ZnO *Appl. Phys. Lett.* **84** 2545-2547

[419] Tamaekong N, Liewhiran C, Wisitsoraat A and Phanichphant S 2009 Sensing Characteristics of Flame-Spray-Made Pt/ZnO Thick Films as H_2 Gas Sensor *Sensors* **9** 6652-6669

[420] Paraguay D F, Miki-Yoshida M, Morales J, Solis J and Estrada L W 2000 Influence of Al, In, Cu, Fe and Sn dopants on the response of thin film ZnO gas sensor to ethanol vapour *Thin Solid Films* **373** 137-140

[421] Lavrov E V, Borrnert F and Weber J 2005 Photoconductivity and infrared absorption study of hydrogen-related shallow donors in ZnO *Phys. Rev. B* **72** 085212 (8pp)

[422] Lavrov E V, Herklotz F and Weber J 2009 Identification of Hydrogen Molecules in ZnO *Phys. Rev. Lett.* **102** 185502 (4pp)

[423] Windisch C F, Exarhos G J, Yao C H and Wang L Q 2007 Raman study of the influence of hydrogen on defects in ZnO *J. Appl. Phys.* **101** 123711 (6pp)

[424] Du M H and Biswas K 2011 Anionic and Hidden Hydrogen in ZnO *Phys. Rev. Lett.* **106** 115502 (4pp)

[425] Stuart B 2000 *Kirk-Othmer Encyclopedia of Chemical Technology: Infrared Spectroscopy* (John Wiley & Sons Inc.) 1-14

[426] Krishnan D and Pradeep T 2009 Precursor-controlled synthesis of hierarchical ZnO nanostructures, using oligoaniline-coated Au nanoparticle seeds *J. Cryst. Growth* **311** 3889-3897

[427] Lo S S, Huang D, Tu C H and Jan D J 2009 Formation and Raman scattering of seed-like ZnO nanostructure *J. Raman Spectrosc.* **40** 1694-1697

[428] Lin K F, Cheng H M, Hsu H C and Hsieh W F 2006 Band gap engineering and spatial confinement of optical phonon in ZnO quantum dots *Appl. Phys. Lett.* **88** 263117 (3pp)

[429] Scepanovic M, Grujic-Brojcin M, Vojisavljevic K, Bernik S and Sreckovic T 2009 Raman study of structural disorder in ZnO nanopowders *J. Raman Spectrosc.* **41** 914-921

[430] Scepanovic M, Grujic-Brojcin M, Dohcevic-Mitrovic Z, Vojisavljevic K, Sreckovic T and Popovic Z V 2007 The effects of nonstoichiometry on optical properties of oxide nanopowders *Acta Phys. Pol. A* **112** 1013-1018

[431] Cusco R, Alarcon-Llado E, Ibanez J, Artus L, Jimenez J, Wang B G and Callahan M J 2007 Temperature dependence of raman scattering in ZnO *Phys. Rev. B* **75** 165202 (11pp)

[432] Wang X, Li Q Q, Liu Z B, Zhang J, Liu Z F and Wang R M 2004 Low-temperature growth and properties of ZnO nanowires *Appl. Phys. Lett.* **84** 4941-4943

[433] Xu X L, Lau S P, Chen J S, Chen G Y and Tay B K 2001 Polycrystalline ZnO thin films on Si (100) deposited by filtered cathodic vacuum arc *J. Cryst. Growth* **223** 201-205

[434] Ip K, Overberg M E, Heo Y W, Norton D P, Pearton S J, Stutz C E, Luo B, Ren F, Look D C and Zavada J M 2003 Hydrogen incorporation and diffusivity in plasma-exposed bulk ZnO *Appl. Phys. Lett.* **82** 385-387

[435] Kleinwechter H, Janzen C, Knipping J, Wiggers H and Roth P 2002 Formation and properties of ZnO nano-particles from gas phase synthesis processes *J. Mater. Sci.* **37** 4349-4360

[436] Li G R, Hu T, Pan G L, Yan T Y, Gao X P and Zhu H Y 2008 Morphology-function relationship of ZnO: Polar planes, oxygen vacancies, and activity *J. Phys. Chem. C* **112** 11859-11864

[437] Muruganandham M and Wu J J 2008 Synthesis, characterization and catalytic activity of easily recyclable zinc oxide nanobundles *Appl. Catal. B-Environ.* **80** 32-41

[438] Wang Y, Meyer B, Yin X, Kunat M, Langenberg D, Traeger F, Birkner A and Woll C 2005 Hydrogen induced metallicity on the ZnO($10\bar{1}0$) surface *Phys. Rev. Lett.* **95** 266104 (4pp)

[439] Vattuone L, Yeo Y Y and King D A 1996 Adatom bond energies and lateral interaction energies from calorimetry: NO, O2 and N2 adsorption on Ni{100} *J. Chem. Phys.* **104** (20) 8096-8102

[440] Angappane S, Selvi N R and Kulkarni G U 2009 ZnO(101) films by pulsed reactive crossed-beam laser ablation *Bull. Mat. Sci*. **32** (3) 253-258

[441] Atmospheric concentration of nitrous oxide (ppb) – European Environment Agency (EEA) [online] Available at: http://www.eea.europa.eu/data-and-maps/figures/atmospheric-concentration-of-n2o-ppb-1 [Accessed: 4 Nov 2013]